

Physics-based constitutive modelling for crystal plasticity finite element computation of cyclic plasticity in fatigue

THÈSE N° 7251 (2016)

PRÉSENTÉE LE 19 DÉCEMBRE 2016

À LA FACULTÉ DES SCIENCES ET TECHNIQUES DE L'INGÉNIEUR
LABORATOIRE DE MÉTALLURGIE MÉCANIQUE
PROGRAMME DOCTORAL EN SCIENCE ET GÉNIE DES MATÉRIAUX

ÉCOLE POLYTECHNIQUE FÉDÉRALE DE LAUSANNE

POUR L'OBTENTION DU GRADE DE DOCTEUR ÈS SCIENCES

PAR

Nicolò GRILLI

acceptée sur proposition du jury:

Prof. H. Frauenrath, président du jury
Prof. H. Van Swygenhoven, Dr K. Janssens, directeurs de thèse
Prof. F. Roters, rapporteur
Prof. T. Hochrainer, rapporteur
Prof. W. Curtin, rapporteur



ÉCOLE POLYTECHNIQUE
FÉDÉRALE DE LAUSANNE

Suisse
2016

Acknowledgements

In this section I want to acknowledge people who helped during the preparation of this thesis and who supported me during my stay in Switzerland. First, I would like to express my gratitude to my supervisor Dr. Koenraad Janssens and my thesis director Prof. Helena Van Swygenhoven who make this thesis possible. They instilled in me the critical thinking necessary to carry out scientific research.

Beside my supervisors, I would like to thank the rest of my thesis committee: Prof. Thomas Hochrainer, Prof. William Curtin and Prof. Franz Roters. I thank Prof. Thomas Hochrainer for the discussions we had during conferences about the higher dimensional dislocation dynamics model he is developing. That approach was the basis for the model developed in this thesis for cyclic fatigue. Prof. William Curtin followed my progresses regularly and this thesis has improved thanks to the feedback he provided during my annual reports. I thank Prof. Franz Roters for the great effort on developing the DAMASK code, which was used in this thesis. During my stay in Düsseldorf to learn that code, he helped me by answering all my questions. His articles about dislocation dynamics and crystal plasticity finite element method have constituted a basis for my work.

In Max Planck Institute for Iron Research in Düsseldorf I had to become familiar for the first time in my life with a large code such as DAMASK; I would like to thank the other people who helped me, in particular: Dr. Christoph Kords, Dr. Martin Diehl and Dr. Pratheek Shanthraj and Prof. Philip Eisenlohr.

A large part of this thesis would not have been possible without the experimental efforts carried out by Dr. Ainara Irastorza Landa and Dr. Jens Nellessen, I would like to thank them because they were able to keep a positive outlook during the difficulties encountered in their experimental projects. They have not been only colleagues, but also great friends. Many other researchers and technicians have been involved in the design and execution of the experiments, I would like to thank in particular: Dr. Steven Van Petegem, Dr. Stefanie Sandlöbes, Alex Bollhalder and Dr. Daniel Grolimund.

I would like to express my gratitude to my officemate Dr. Giacomo Facheris, he helped me learning how to use the Abaqus software in the first part of my PhD work. He and his family will always be great friends in my country. I would like to thank also the other italians working in the Nuclear Energy and Safety department, in particular: Dr. Marco Pecchia, Dr. Carlo Fiorina, Dr. Riccardo Puragliesi, Dr. Luca Podofilini, Dr. Davide Papini. Thanks to them I did not forget my language during my years in Switzerland.

In Paul Scherrer Institute I had the first occasion in my life to work in a highly multicultural

Acknowledgements

environment. I would like to thank all my colleagues in the LNM group and in the PEM-SYN group who shared their experiences with me, in particular: Juxing Bai, Dr. Pascal Grundler, Stefan Ritter, Hans-Peter Seifert, Dr. Guian Qian, Dr. Vicente Gonzalez Albuixech, Dr. Vicente Herrera Solaz, Dr. Supratik Roychowdhury, Serafin Knitel, Zaiqing Que, Markus Niffenegger, Dr. Sudhakar Rao, Dr. Philippe Spätig, Chen Wen, Dr. Cecile Marichal, Dr. Patrick Schloth, Dr. Chen Sun, Dr. Saba Zabihzadeh, Dr. Manas Upadhyay Vijay, Dr. Tobias Panzner.

I would like to thank all the people I met during my free time in Switzerland, especially people and clubs supporting and promoting cycling. In particular I would like to thank the Dirt Castle Crew in Lenzburg, #zhbmx and Pandapark Crew in Rüti for the great effort they put into building excellent bike facilities in their free time.

Finally, I would like to thank my parents and my whole family for their endless love and the logistics help they have given me for my move to Switzerland. They have always supported me and encourage me every day to follow my passions, even now that I am far away from home.

Lausanne, October 9, 2016

Nicolò Grilli

Abstract

Metal fatigue during cyclic loading puts an endurance limit on most of today's technology. It impacts the reliability of metallic components used for transportation, electronic devices and energy production because fatigue failure can occur without any apparent forewarning. This phenomenon limits the lifetime of many industrially manufactured items, whose periodic replacement affects the cost of everyday products. The problem of predicting fatigue failure in metals has been addressed using the finite element method, which can provide the stress and strain state of the material in complex geometries. Engineering models describing the material behaviour have been used to predict the damage accumulation, but microstructure and material design require constitutive models at the micrometre length scale, incorporating the physical processes in the material. This involves the study of dislocation dynamics and the formation of dislocation structures, which have been recognized as the key phenomena affecting the macroscopic fatigue behaviour of metals. This problem is computationally challenging, first because of the large number of state variables required to describe the dislocation behaviour, and second because the formation of dislocation structures takes place only after many deformation cycles. In this project a continuum dislocation-based model, specific for cyclic fatigue at the micrometre length scale, is developed. The main novelty is the prediction of 3D dislocation structures starting from a random initial dislocation distribution. In single slip deformation, the characteristic length scale and shape of dislocation structures are predicted using only physical parameters, such as the stacking fault energy, and without any fitting procedure. The model is implemented in a crystal plasticity finite element solver, describing all the slip systems. Therefore, it is possible to model polycrystalline structures and to study the orientation of multiple slip dislocation structures with respect to the loading direction. Compared with existing models, the implementation of the dislocation junction formation mechanism in a continuum framework is a step forward. A collaboration with another PhD student, carrying out electron channeling contrast imaging experiments on fatigued 316 stainless steel, has provided a validation of the model by direct comparison of experimental and simulated dislocation structures close to the specimen surface. The crystal lattice rotation is another variable that can be extracted from finite element simulations. The developed model correlates the forming dislocation structures with the lattice rotation around the coordinate axes. This allows the comparison with Laue microdiffraction experiments carried out on copper single crystal specimens by another PhD student at the SLS, the synchrotron at Paul Scherrer Institut. The dislocation-based model can calculate experimental observables, such as the rotation components and rotation gradients, as a function of the

Acknowledgements

simulated dislocation density in the specimen, which is not directly observable. This provides a validation of the constitutive equations at the micrometre length scale.

Keywords: Dislocations, Crystal Plasticity, Fatigue, Finite element method

Riassunto

La fatica dei metalli durante carichi ciclici pone un limite di resistenza nella maggior parte della tecnologia odierna. Ha un impatto sull'affidabilità dei componenti metallici usati per il trasporto, nei dispositivi elettronici e per la produzione di energia perché i guasti causati da fatica possono accadere senza nessun preallarme. Questo fenomeno limita la durata di molti manufatti industriali, la cui sostituzione periodica influenza il costo dei prodotti d'uso quotidiano. Il problema della predizione dei guasti causati da fatica è stato affrontato usando il metodo degli elementi finiti, che fornisce gli sforzi e le deformazioni del materiale in geometrie complesse. Modelli ingegneristici che descrivono il comportamento del materiale sono stati usati per predire l'accumulazione del danno, però lo sviluppo di materiali e microstrutture richiede modelli costitutivi alla scala del micrometro, che incorporino i processi fisici nel materiale. Questo implica lo studio della dinamica delle dislocazioni e della formazione di strutture di dislocazioni, che sono state riconosciute come i fenomeni fondamentali che influenzano il comportamento macroscopico dei metalli sottoposti a fatica. Questo problema è computazionalmente impegnativo, prima di tutto per il grande numero di variabili di stato necessarie per descrivere il comportamento delle dislocazioni e poi perché la formazione di strutture di dislocazioni ha luogo solo dopo molti cicli di deformazione. In questo progetto è stato sviluppato un modello del continuo basato sulle dislocazioni, specifico per la fatica ciclica alla scala del micrometro. L'innovazione principale consiste nella predizione di strutture di dislocazioni 3D partendo da una distribuzione iniziale casuale delle dislocazioni. In deformazione a scivolamento singolo, la lunghezza caratteristica e la forma delle strutture di dislocazioni sono predette usando solo parametri fisici, come l'energia di difetto d'impilaggio, e senza procedure di interpolazione. Il modello è implementato in un risolutore a elementi finiti della plasticità dei cristalli, che descrive tutti i sistemi di scivolamento. Quindi, è possibile simulare strutture policristalline e studiare l'orientamento delle strutture di dislocazioni in scivolamento multiplo rispetto alla direzione di carico. In confronto con modelli già esistenti, un passo in avanti è stata l'implementazione del meccanismo di formazione delle giunzioni di dislocazioni in un modello continuo. Una collaborazione con un altro studente di dottorato, che ha effettuato esperimenti usando il microscopio elettronico in contrasto di canalizzazione su campioni di acciaio inossidabile 316 sottoposti a fatica, ha fornito una validazione del modello confrontando direttamente le strutture di dislocazioni simulate e osservate nell'esperimento vicino alla superficie del campione. La rotazione del reticolo cristallino è un'altra variabile che può essere estratta dalle simulazioni a elementi finiti. Il modello sviluppato correla le strutture di dislocazioni in formazione con la rotazione del reticolo cristallino attorno

Riassunto

agli assi coordinati. Questo permette il confronto con esperimenti di microdiffrazione Laue effettuati da un altro studente di dottorato su campioni formati da un singolo cristallo di rame all'SLS, il sincrotrone all'istituto Paul Scherrer. Con il modello basato sulle dislocazioni si possono calcolare osservabili sperimentali, come le componenti della rotazione e i gradienti della rotazione, in funzione della densità di dislocazioni simulata nel campione, che non è direttamente osservabile. Questo fornisce una validazione delle equazioni costitutive alla scala del micrometro.

Parole chiave : Dislocazioni, Plasticità dei cristalli, fatica, metodo degli elementi finiti

Contents

| | |
|---|------------|
| Acknowledgements | i |
| Abstract (English/Italiano) | iii |
| List of figures | ix |
| List of tables | xix |
| Introduction | 1 |
| 0.1 Objectives and Project Framework | 1 |
| 0.2 Outline | 2 |
| 1 Review of Experimental Evidence and Computational Models | 5 |
| Review of Experimental Evidences and Computational Models | 5 |
| 1.1 Single Slip Dislocation Structures | 5 |
| 1.2 Multiple Slip Dislocation Structures | 10 |
| 1.3 Single slip mechanical properties | 16 |
| 1.4 Multiple slip mechanical properties | 18 |
| 1.5 Continuum dislocation-based models | 19 |
| 1.6 Dislocation-based models for cyclic fatigue | 19 |
| 1.7 The crystal plasticity finite element method | 26 |
| 2 Single slip dislocation-based model | 29 |
| Dislocation-based model for single slip cyclic fatigue | 29 |
| 2.1 Existing models for monotonic loads | 29 |
| 2.2 Single slip model for cyclic fatigue | 35 |
| 2.3 Eigenvalue analysis | 43 |
| 2.4 Single slip simulations | 46 |
| 2.5 Mechanical properties of the single slip model | 55 |
| 2.6 Persistent slip bands modelling | 57 |
| 3 Multiple slip dislocation-based model | 59 |

Contents

| | |
|--|------------|
| Dislocation-based model for multiple slip cyclic fatigue | 59 |
| 3.1 Multiple slip model based on edge and screw dislocation densities | 59 |
| 3.2 Multiple slip model based on dislocation junctions | 62 |
| 3.2.1 Two dislocation loops forming a dislocation junction | 65 |
| 3.3 Dislocation patterning and orientation analysis | 67 |
| 3.4 Polycrystal simulations | 69 |
| 3.4.1 Dislocation patterning in the $[3\ 29\ 1]$ -oriented grain | 73 |
| 3.4.2 Dislocation patterning in the $[\bar{1}\ 19\ 0]$ -oriented grain | 76 |
| 4 Comparison between simulation and synchrotron Laue microdiffraction experiments | 83 |
| Model validation using synchrotron Laue microdiffraction experiments | 83 |
| 4.1 Crystal lattice rotation in the CPFE framework | 83 |
| 4.2 Relationship between the rotation components and the dislocation content . . | 84 |
| 4.3 Laue microdiffraction and in-situ fatigue experiment | 86 |
| 4.4 Plastic strain and strain homogeneity in the analyzed area | 92 |
| 4.5 The influence of pre-existing lattice rotation on the evolving microstructure | 94 |
| 4.6 Lattice rotation from evolving dislocation structures | 97 |
| 4.7 Rotation gradients from accumulated dislocation structures | 102 |
| 4.8 Rotation gradients surrounding different vein structures | 107 |
| 4.9 Formation and dissociation of apparent GND density structures | 114 |
| 4.10 Discussion and conclusion | 124 |
| 5 Conclusions and Outlook | 125 |
| Conclusions and Outlook | 125 |
| A Equation summary | 127 |
| A.1 Single slip model for cyclic fatigue | 127 |
| A.2 Multiple slip model for cyclic fatigue | 129 |
| A.3 List of symbols | 131 |
| A.4 Quantities describing the stress-strain curve | 132 |
| Bibliography | 147 |
| Curriculum Vitae | 149 |

List of Figures

| | | |
|------|--|----|
| 1 | (a) Dipolar wall in copper fatigued into saturation at room temperature [Kuhlmann-Wilsdorf and Laird, 1977]; (b) examples of persistent slip bands embedded in a loop patch structure [Laird et al., 1986]; (c) Photograph of the surface of a specimen after $1.5 \cdot 10^4$ cycles at $\gamma_{pl} = 4.5 \cdot 10^{-3}$ [Winter, 1974]. | 2 |
| 1.1 | (a) Loop patches after 9 deformation cycles at $\gamma_{pl} = 7.5 \cdot 10^{-3}$ [Kuhlmann-Wilsdorf and Laird, 1977]; (b) vein-channel structure after thousands of cycles at $\gamma_{pl} = 1.25 \cdot 10^{-3}$ [Kuhlmann-Wilsdorf and Laird, 1977]; (c) schematic dislocation arrangement in the vein-channel structure [Suresh, 1998]. | 6 |
| 1.2 | (a) Veins observed on a plane perpendicular to the edge dislocation lines [Buchinger et al., 1985]; (b) vein alignment shown in (a); (c) boundary zone (dashed line) between a PSB and the matrix structure [Winter, 1978]. | 6 |
| 1.3 | (a) Dislocation structures in a Cu crystal fatigued at $\gamma_{pl} = 10^{-3}$ [Suresh, 1998]; (b) crystal sharp-corner fatigued at $\gamma_{pl} = 1.2 \cdot 10^{-3}$ to 5000 cycles [Basinski and Basinski, 1992]; (c) schematic dislocation arrangement in the PSB structure [Suresh, 1998]. | 6 |
| 1.4 | (a) Vein structures at $\gamma_{pl} = 1 \cdot 10^{-4}$ [Holzwarth and Eßmann]; (b) intersecting secondary glide can move primary dislocations [Kuhlmann-Wilsdorf and Laird, 1980]; (c) intersecting cross slip system creates prismatic loops [Li and Laird, 1994], at position B two arrays of prismatic loops have been divided. | 8 |
| 1.5 | Dislocation structures in Ni single crystals deformed at $\gamma_{pl} = 2 \cdot 10^{-3}$ [Schwab et al., 1996]. | 8 |
| 1.6 | Dislocation structures in Al single crystals deformed at $\tau_s = 4$ MPa [Zhai et al., 1996]. | 8 |
| 1.7 | Vein-channel structures and PSB in copper cyclically deformed at $T = 77.4$ K [Basinski et al., 1980]. | 9 |
| 1.8 | Effect of the crystal orientation on dislocation structures [Li et al., 2010]. | 10 |
| 1.9 | (a) Dislocation structures of [011] nickel at $\gamma_{pl} = 6.1 \cdot 10^{-4}$ viewed from $(\bar{1}\bar{1}\bar{1})$ [Buque, 2001]; (b) Geometrical configuration of slip bands (SB) and deformation bands (DB) [Li et al., 2002]. | 10 |
| 1.10 | (a) Forming deformation bands in a $[\bar{5} 12 20]$ copper single crystal deformed at $\gamma_{pl} = 8 \cdot 10^{-3}$ [Zhang et al., 2001]; (b) schematic representation of misaligned PSB walls during the formation of a deformation band. | 11 |

List of Figures

| | |
|---|----|
| 1.11 (a) Uncondensed labyrinth structures [Jin and Winter, 1984]; (b) Condensed labyrinth structures [Jin and Winter, 1984]. | 12 |
| 1.12 (a) Labyrinth walls with a prevalent (001) orientation [Jin and Winter, 1984]; (b) illustration of the geometry of labyrinth structures [Li et al., 2011]. | 12 |
| 1.13 (a) Vein structure of $[\bar{1}11]$ copper single crystal at $\gamma_{pl} = 1.84 \cdot 10^{-4}$ [Li et al., 2009]; (b) cell structures of copper single crystal on the (111) [Lepistö et al., 1984]. . . | 13 |
| 1.14 (a) Cell structures of copper single crystal on the $(13\bar{2})$ at $\gamma_{pl} = 4 \cdot 10^{-4}$ [Li et al., 2009]; (b) illustration of the geometry of cell structures [Li et al., 2011]. | 14 |
| 1.15 (a) Cell structures in a $[\bar{3}45]$ grain at $\gamma_{pl} = 3.8 \cdot 10^{-3}$ [Hu and Wang, 1997]; (b) labyrinth structures in a $[\bar{1}17]$ grain at $2.8 \cdot 10^{-4}$; (c) high angle grain boundary [Winter et al., 1981]. | 14 |
| 1.16 (a) Hysteresis loop evolution in copper single crystal at $\Delta\gamma_{pl} = 3 \cdot 10^{-3}$ for different values of the cumulative plastic strain $\gamma_{pl,cum}$ [Déprés et al., 2008]; (b) cyclic hardening curve at different imposed $\Delta\gamma_{pl}$ [Déprés et al., 2008]; (c) cyclic stress strain curve (CSSC) of copper single crystal [Mughrabi, 1978]. | 16 |
| 1.17 CSSC for nickel, copper and silver single crystals [Mughrabi et al., 1979]. | 17 |
| 1.18 Maximum stress τ_{max} , friction stress τ_f and backstress τ_b as a function of the number of cycles for 316L stainless steel deformed in single slip at $\gamma_{pl} = 1 \cdot 10^{-3}$ [Li and Laird, 1994]. | 17 |
| 1.19 Hardening curves for copper deformed at three different temperatures T in region B [Basinski et al., 1980]. | 18 |
| 1.20 (a) CSSC of double and multiple slip oriented Cu single crystals [Wang et al., 2001]; (b) variation of the crystal CSS curve with its location in the standard stereographic triangle [Wang et al., 2001]. | 18 |
| 1.21 Hardening curve of $[001]$ single crystal aluminium deformed at constant γ_{pl} . . . | 19 |
| 1.22 (a) Equivalence between a continuum distribution ρ and an ensemble of states with different number of dislocations. (b) Different states with different spatial positions of one dislocation that are equivalent to a component of the discrete ensemble. | 20 |
| 1.23 (a) State variables of the Kubin-Estrin model; (b) fit of the hysteresis stress-strain curve for Al [Estrin et al., 1996]. | 21 |
| 1.24 (a) Amplitude of the spatial pattern, plain lines are stable states, dashed lines are unstable ones [Walgraef and Aifantis, 1985]; (b) pattern developed in a 1D model [Schiller and Walgraef, 1988]; (c) simulated 2D dislocation patterning, primary slip directions are parallel to the diagonals of the box [Pontes et al., 2006]. | 22 |
| 1.25 (a) dislocation structures if dislocation multiplication is introduced without external stress; (b) dislocation structures with dislocation multiplication and a periodic external stress [Groma and Balogh, 1999]. | 24 |
| 1.26 (a) Taylor lattice and “loop-flipping” motion [Kuhlmann-Wilsdorf, 1979a]; (b) disintegration of a dipolar wall due to stress increase; (c) maximum stability stress of various dislocation configurations [Neumann, 1987]. | 25 |

| | |
|--|----|
| 1.27 (a) Stacking arrangement of dislocation loops in the DPP theory [Dickson et al., 1986b]; (b) single slip simulated microstructure after 25 cycles [Déprés, 2004]; (c) double slip dislocation microstructure [Déprés et al., 2004]. | 25 |
| 1.28 Scheme of the crystal plasticity finite element method, as implemented in DAMASK [Roters et al., 2012]. | 27 |
| 1.29 Control volume to calculate dislocation fluxes and unit normals pointing towards the neighbouring integration points [Roters, 2011]. | 28 |
| 2.1 Dislocation annihilation process [Roters et al., 2000]. | 30 |
| 2.2 (a) Expanding dislocation loop; (b) gliding motion of one screw dislocation and averaging volume for the Arsenlis multiplication law. | 31 |
| 2.3 (a) Dislocation dipole formation process; (b) Uniform dipole height distribution. | 32 |
| 2.4 (a) Representative volume and mesh used to test the existing physics-based model; (b) Dislocation dipole density in one element. | 34 |
| 2.5 Simulated stress-strain curve during cyclic fatigue at 0.2 % strain amplitude and $2 \cdot 10^{-3} \text{ s}^{-1}$ strain rate. | 35 |
| 2.6 (a) Freed dipoles for the Gaussian distribution; (b) dipole height distribution from experiments [Catalao et al., 2005]. | 36 |
| 2.7 (a) New dislocation multiplication law when one dislocation loop occupies more elements; (b)-(c) time evolution of “straight” and “curved” dislocation segments. | 36 |
| 2.8 (a) Angular intervals $\Delta\theta_{e+,s+}$ and $\Delta\theta_{e-,s+}$ used to define the dislocation densities in the model; (b) screw dislocation configuration inside a channel if the curvature radius is around half of the channel width. | 38 |
| 2.9 Case study of the new multiplication law using two interacting dislocation segments. | 40 |
| 2.10 (a) Double cross slip mechanism; (b) Time evolution of a “straight” dislocation segment during double cross slip; (c) dislocation loop expanding after a double cross slip event. | 41 |
| 2.11 Values of ω_q in (2.35) as a function of the patterning wavelength λ , different colors correspond to different eigenvalues. | 44 |
| 2.12 Values of ω_q in (2.35) as a function of the patterning wavelength λ for $\beta = 8 \cdot 10^{-9}$ and $\beta = 8 \cdot 10^{-7}$, different colors correspond to different eigenvalues. | 45 |
| 2.13 Values of ω_q in (2.35) as a function of the patterning wavelength λ for $\beta = 0$ | 45 |
| 2.14 Values of ω_q in (2.35) as a function of the patterning wavelength λ for $\gamma = 0.2\%$ and $\gamma = 0.3\%$, different colors correspond to different eigenvalues. | 46 |

List of Figures

| | |
|--|----|
| 2.15 (a) Edge dislocation density after 100 cycles using the new multiplication law; (b) product between the total “curved” and edge dislocation density after 100 cycles using the new multiplication law; the patterning is similar to the one in (a); (c) scatter plot of the “curved” dislocation density as a function of the edge dislocation density in every element; (d) edge dislocation density along the dashed line passing through the geometry in the inset. In (a) and (b) the scales are different because of the different magnitude of the edge and “curved” dislocation density. | 47 |
| 2.16 (a) Screw dislocation density after 100 cycles using the new multiplication law; (b) scatter plot of the edge dislocation density as a function of the product $ \nu_{e+,s+} \cdot (\rho_{s+} + \rho_{s-})$ at every integration point. | 49 |
| 2.17 (a) Edge dislocation density after 100 cycles using the new multiplication law and initial fluctuations of the initial dislocation density $\delta\rho = 15\%$. (b) Spectral density of ρ_e as a function of the wavelength. | 51 |
| 2.18 Averaged edge dislocation density after (a) monotonic deformation and (b) after 8 cycles using both 200 nm and 100 nm element size. | 51 |
| 2.19 (a) Simulated average dislocation density as a function of the cumulative shear strain for $\beta = 8 \cdot 10^{-8}$ (solid curve) and $\beta = 8 \cdot 10^{-9}$ (dashed curve); squares represent experimental points [Hancock and Grosskreutz, 1969], with a measurement error estimated at about 50%. (b) Simulated channel volume fraction as a function of the number of cycles; the error bar represents the saturation channel volume fraction in copper at the same saturation stress [Buchinger et al., 1985]. | 52 |
| 2.20 (a) Simulated average dislocation density for two different strain amplitudes; (b)-(c) edge dislocation density before ($N = 25$) and after ($N = 37$) a strain rate jump. | 53 |
| 2.21 Edge dislocation density after 100 cycles using (a) a lower cross slip coefficient $\beta = 8 \cdot 10^{-9}$; (b) a higher dislocation mobility $B = 100 (\mu\text{m}/\text{s})/\text{MPa}$ and (c) including secondary dislocations. | 53 |
| 2.22 (a) Solid line: depletion of the channel indicated by the circle in the inset. Dashed line: depletion of the channel with higher cross slip coefficient $\beta = 8 \cdot 10^{-8}$. (b) Hardening curves for $\beta = 8 \cdot 10^{-8}$ (dashed line) and $\beta = 8 \cdot 10^{-9}$ (solid line). | 54 |
| 2.23 (a) Hardening curve using the multiplication law for cyclic fatigue (2.15), averaged over the deforming surface; (b) hardening curve for two different values of the strain amplitude γ | 55 |
| 2.24 Maximum stress as a function of the number of cycles for different plastic strain amplitudes using (a) the Arsenlis multiplication law (2.5) and (b) the multiplication law for cyclic fatigue (2.15). Simulation are carried out using the parameters in Tab. 2.7. | 56 |
| 2.25 (a) Hardening curve without the introduction of secondary dislocations and strain $\gamma = 0.1\%$. (b)-(c) Hardening curve with the introduction of secondary dislocations and strain $\gamma = 0.1\%$ and $\gamma = 0.2\%$ respectively. | 57 |

| | |
|--|----|
| 2.26 (a) Interaction between two dipoles inside neighbouring elements; (b) dipoles distributed orthogonally with respect to the slip plane; (c) dipoles distributed along the slip plane; (d) stress-strain curves of the two configurations in (b) and (c). | 58 |
| 2.27 (a) Edge dislocation density after 30 cycles without the τ_{dipole} stress term. (b) Edge dislocation density after 20 cycles with the τ_{dipole} term. (c) τ_{dipole} in (2.41) calculated from the dislocation distribution in (b). | 58 |
| 3.1 Fraction of mobile dislocations in multiple slip. | 60 |
| 3.2 (a) Simulation of labyrinth structures after 30 deformation cycles. (b) Simulation of cell structures and (c) dislocation density on the two active coplanar slip systems. | 61 |
| 3.3 (a) Definition of the dislocation junction vector \vec{l}_{lock} and of the different dislocation densities. (b) Velocity vectors \vec{v}_{r+}^1 , \vec{v}_{r-}^1 and $\vec{v}_{//+}^1$ | 63 |
| 3.4 (a) The process of cross slip of a screw dislocation segment from one slip plane to another. (b) The resulting Frank-Read source generates new curved dislocation segments. | 64 |
| 3.5 (a) Displacement field along the z axis. (b) Evolution of the total dislocation density ρ of two dislocation loops forming a dislocation junction at the intersection of their slip planes. | 66 |
| 3.6 (a) Total dislocation density after 40 cycles in $[001]$ compression. (b) Orientation of the active slip systems. | 67 |
| 3.7 (a) Black and white conversion of the image in Fig. 3.6 used to calculate the 2D orientation distribution function and dislocation line orientation angle θ ; (b) corresponding 2D orientation distribution function and comparison with the edge-screw model. | 68 |
| 3.8 (a) ECCI configuration of a SEM microscope; (b) electron backscattered intensity as a function of the incidence angle for a perfect crystal [Goldstein et al., 2005]. | 70 |
| 3.9 (a) Lattice plane orientation around a dislocation and consequent BSE intensity. (b) Single dislocations imaged in a Si single crystal [Simkin and Crimp, 1999]. . | 70 |
| 3.10 (a) ECCI image taken in the centre of the $[3\ 29\ 1]$ -oriented grain after 50 cycles; (111) and $(\bar{1}\bar{1}1)$ slip plane traces are visible. (b) Simulation set-up of the polycrystalline structure (LD: loading direction). | 71 |
| 3.11 (a) ECCI image taken in the centre of the $[\bar{1}\ 19\ 0]$ -oriented grain after 100 cycles; (111) , $(\bar{1}\bar{1}1)$ and $(\bar{1}11)$ slip plane traces are visible. (b) Simulation set-up of the polycrystalline structure (LD: loading direction). | 72 |
| 3.12 (a) Mesh used for the simulation of the $[3\ 29\ 1]$ -oriented grain; (b) detail of the central part of the mesh; (c) simulated dislocation structures are analyzed in the upper part, where 200 nm elements are generated. | 72 |

List of Figures

| | |
|--|----|
| 3.13 (a) Total dislocation density in the centre of the $[3\ 29\ 1]$ -oriented grain after 50 cycles using the dislocation junction model. (b) Black and white conversion used to calculate the 2D orientation distribution function and dislocation line orientation angle θ | 74 |
| 3.14 (a) Total dislocation density in the centre of the $[3\ 29\ 1]$ -oriented grain after 50 cycles using the edge-screw dislocation model. (b) Black and white conversion used to calculate the 2D orientation distribution function and dislocation line orientation angle θ | 75 |
| 3.15 Maximum dislocation density ρ_{peak} in the centre of the $[3\ 29\ 1]$ -oriented grain after 50 cycles on all the slip systems using (a) the edge-screw model and (b) the dislocation junction model. | 75 |
| 3.16 (a) ECCI image in the centre of the $[3\ 29\ 1]$ -oriented grain processed using a Gaussian filter to remove slip lines, dislocation structures have a dark contrast. (b) 2D orientation distribution function for the edge-screw and the dislocation junction model. | 76 |
| 3.17 (a) Black and white conversion of the dislocation density in the centre of the $[3\ 29\ 1]$ -oriented grain (Fig. 3.14 (a)) for the dislocation junction model and (b) corresponding 2D orientation distribution function. | 77 |
| 3.18 (a) Total dislocation density in the centre of the $[\bar{1}\ 19\ 0]$ -oriented grain after 100 cycles using the dislocation junction model. (b) Black and white conversion used to calculate the 2D orientation distribution function and dislocation line orientation angle θ . (c) Maximum dislocation density ρ_{peak} in the centre of the $[\bar{1}\ 19\ 0]$ -oriented grain after 100 cycles on all the slip systems using the dislocation junction model. | 78 |
| 3.19 (a) ECCI image in the centre of the $[\bar{1}\ 19\ 0]$ -oriented grain processed using a Gaussian filter to remove slip lines, dislocation structures have a dark contrast, examples of oriented walls are enclosed by rectangles. (b) 2D orientation distribution function for the simulated dislocation density in Fig. | 79 |
| 3.20 (a) Orientation distribution functions of the image in Fig. 3.13 for five different values of L . (b) Orientation distribution functions of the image in Fig. 3.18 (a) for three different values of L | 79 |
| 4.1 Schematic process through which edge GNDs accumulate and the crystal lattice rotates. | 86 |
| 4.2 (a) Schematic drawing of the microXAS beamline; (b) deformation rig to apply cyclic deformation on the sample (courtesy of Ainara Irastorza). | 87 |
| 4.3 (a) Schematic view of the copper single crystal sample geometry and actuators; (b) shear zone, the thickness of different regions is reported [Irastorza-Landa et al., 2016]. | 88 |
| 4.4 Rotation θ_x around the x axis for different number of cycles N [Irastorza-Landa et al., 2016]. | 88 |

| | | |
|------|---|-----|
| 4.5 | Rotation θ_y around the y axis for different number of cycles N [Irastorza-Landa et al., 2016]. | 89 |
| 4.6 | Rotation θ_z around the z axis for different number of cycles N [Irastorza-Landa et al., 2016]. | 89 |
| 4.7 | Euler angle θ for different number of cycles N [Irastorza-Landa et al., 2016]. | 89 |
| 4.8 | Apparent GND density for different number of cycles N [Irastorza-Landa et al., 2016]. | 90 |
| 4.9 | Evolution of the apparent GND density in regions G , A and B (courtesy of Ainara Irastorza). | 91 |
| 4.10 | (a) Representative volume and boundary conditions; (b) refined mesh in the shear zone. | 92 |
| 4.11 | (a) Simulated shear distribution of the sample; (b) measured force as a function of the simulated shear in the thin area [Irastorza-Landa et al., 2016]. | 93 |
| 4.12 | (a) Simulated RGB rotation map, using (a) the phenomenological power law model and (b) the dislocation-based model for cyclic fatigue, of the upper part of the rectangular area analyzed by Laue microdiffraction at cycle 11; the red and blue features indicate that θ_x and θ_z are the dominant rotation components. | 95 |
| 4.13 | (a) Simulated and (b) experimental Euler angle θ map of the upper part of the rectangular area analyzed by Laue microdiffraction at cycle 11 (courtesy of Ainara Irastorza). | 96 |
| 4.14 | (a) C_{xyxy} component of the stiffness tensor; (b) stress tensor component σ_{xy} ; (c) cumulative plastic strain $\gamma_{p,cum}$ on the primary slip system. In (a) and (b) the scales are different because of the different magnitude and sign of C_{xyxy} and σ_{xy} | 97 |
| 4.15 | (a) Representative volume to simulate the lattice rotation along the edge dislocation line (section cut at $x = 0.4 \mu\text{m}$) and dislocation density after 50 cycles; (b) rotation along the z axis, averaged over the elements along the blue and green dashed lines in (a). | 98 |
| 4.16 | Lattice rotation θ_z in channels and dislocation structures. | 99 |
| 4.17 | Rotation along the z axis in the dislocation structures for (a) $\gamma_{xy} = 0.1 \%$ and (b) $\gamma_{xy} = 0.2 \%$ | 100 |
| 4.18 | (a) Representative volume to simulate the lattice rotation along the edge dislocation line; (b) rotation along the z axis, averaged over the elements along the blue and green dashed lines in (a); (c) the oscillation amplitude and phase of θ_z is similar in the two low density regions. | 100 |
| 4.19 | Rotation along (a) the y axis and (b) the x axis, averaged over the elements along the green dashed line in Fig. 4.18 (a). | 101 |
| 4.20 | Schematic relationship between edge GNDs, screw GNDs and lattice rotation around the slip plane normal (x axis). | 102 |
| 4.21 | 3D section view of the mesh used in the central part of the thin region for the dislocation based model simulation. | 103 |

List of Figures

| | |
|--|-----|
| 4.22 (a) Edge dislocation density in the centre of the geometry; (b) simulated component α_{yz} of the Nye tensor; (c) measured component α_{yz} of the Nye tensor at cycle 100 (courtesy of Ainara Irastorza). | 103 |
| 4.23 (a) Simulated component α_{xz} of the Nye tensor; (b) measured component α_{xz} of the Nye tensor at cycle 100, the green rectangle evidences features that are similar to the simulated ones (courtesy of Ainara Irastorza). | 104 |
| 4.24 Edge dislocation density at different depth z in the 200 nm elements of the 30 μm thin layer and corresponding rotation field θ_z | 105 |
| 4.25 Displacing rotation gradient, as in Fig. 4.24, and consequent α_{xz} Nye tensor component. | 106 |
| 4.26 (a) Representative volume and mesh; (b) part of the representative volume where the dislocation-based plasticity is used. | 107 |
| 4.27 Boundary condition used in the simulation. | 108 |
| 4.28 Shapes of the straight, Y-inclined, Y&X-inclined and two inclined veins used in the simulation. | 108 |
| 4.29 Simulated rotation component θ_z for the four vein shapes after one cycle. Different scales are used because of the different magnitude for the four vein shapes. | 110 |
| 4.30 Simulated rotation gradient components for the straight vein shape after one cycle. Different scales are used because of the different magnitude of the components. | 111 |
| 4.31 Simulated rotation gradient components for the Y-inclined vein shape after one cycle. Different scales are used because of the different magnitude of the components. | 111 |
| 4.32 Simulated rotation gradient components for the Y&X-inclined vein shape after one cycle. Different scales are used because of the different magnitude of the components. | 112 |
| 4.33 Simulated rotation gradient components for the two inclined veins shape after one cycle. Different scales are used because of the different magnitude of the components. | 112 |
| 4.34 Measured rotation gradients in radians per meter in region F of Fig. 4.7 (courtesy of Ainara Irastorza). | 113 |
| 4.35 Simulated apparent GND density after one cycle. | 114 |
| 4.36 Maximum and minimum values of the applied displacement as a function of the number of cycles N | 115 |
| 4.37 Relationship between the geometrically necessary edge dislocation density $\rho_{e,GND} = (\rho_{e+} - \rho_{e-})$ and the threshold stress on the primary slip system for two different values of the mobile dislocation density. | 117 |
| 4.38 Geometrically necessary edge dislocation density $\rho_{e,GND} = (\rho_{e+} - \rho_{e-})$, averaged over depth (z axis), at different number of cycles N and for different mobile and immobile dislocation densities. | 118 |

| | | |
|------|--|-----|
| 4.39 | Threshold stress τ_{th}^1 on the primary slip system at different number of cycles N and for different mobile and immobile dislocation densities. The last row shows τ_{th}^1 at cycle 50 with the same color scale. | 120 |
| 4.40 | Velocity at cycle 50 for different mobile and immobile dislocation densities. . . | 121 |
| 4.41 | Apparent GND density at different number of cycles N and for different values of the dislocation densities. | 122 |
| A.1 | Quantities describing the stress-strain hysteresis loops. | 132 |

List of Tables

| | | |
|-----|---|-----|
| 1.1 | Volume fraction of veins f_V for different values of γ_{pl} [Buchinger et al., 1985]. . . | 7 |
| 1.2 | Dislocation processes associated with the different coefficients in (1.2)-(1.4). . . | 21 |
| 1.3 | Dislocation processes associated with the different coefficients in (1.5)-(1.6). . . | 22 |
| 1.4 | Features table of the presented dislocation-based models for cyclic fatigue. . . . | 26 |
| 1.5 | Elastic constants for copper [Overton and Gaffney, 1955], aluminium [Vallin et al., 1964] and 316L steel [Reed and Horiuchi, 1983]. | 26 |
| 2.1 | Annihilation distances used for different materials [Basinski and Basinski, 1992], [Caillard and Martin, 1989], [Catalao et al., 2005]. | 30 |
| 2.2 | Peierls stress for different materials [Schoeck and Krystian, 2005], [Wang and Fang, 2000], [Misra et al., 2010]. | 33 |
| 2.3 | Simulation parameters. | 34 |
| 2.4 | Dislocation densities used for the cyclic fatigue multiplication law. | 37 |
| 2.5 | Material parameters to calculate the cross slip rate [Bonneville et al., 1988], [Groh et al., 2009], [Déprés et al., 2008]. | 41 |
| 2.6 | Material parameters to calculate the cross slip rate coefficient β | 43 |
| 2.7 | Initial dislocation densities and parameters for the simulations in Fig. 2.15. . . . | 48 |
| 3.1 | Dislocation densities used in the junction constitutive model. | 62 |
| 3.2 | Initial dislocation densities and parameters for the simulations in Fig. 3.6. . . . | 67 |
| 3.3 | Dislocation line orientation θ for different dislocation types, projected on the $x-z$ plane. | 68 |
| 3.4 | Initial dislocation densities and kinetics parameters in the simulations using the edge-screw and dislocation junction model. | 73 |
| 4.1 | Parameters for the phenomenological plasticity model in (4.14)-(4.15) [Déprés et al., 2008], [Dmitrieva et al., 2009]. | 93 |
| 4.2 | Initial dislocation densities for the simulations. | 109 |
| 4.3 | Initial dislocation densities for the simulations. | 115 |
| 4.4 | Summary of the results. | 123 |
| A.1 | Dislocation densities used for the single slip model for cyclic fatigue. | 127 |
| A.2 | Dislocation densities used in the junction constitutive model. | 129 |

Introduction

Cyclic fatigue of metals is defined as the change of a metallic material when a repeated strain or stress is applied to it [Suresh, 1998]. It is a phenomenon that puts an endurance limit on mechanical components, and therefore affects the cost and reliability of modern technology. The systematic study of fatigue began in the 19th century due to the increasing use of metallic structures for transportation and industrial applications [Wöhler, 1870]. The discovery that plastic strain in metals is the mechanism controlling fatigue failure led to the formulation of the Coffin-Manson relation [Manson, 1954], [Coffin, 1954], fundamental to predict with a certain degree of accuracy the lifetime of mechanical components. The arrangement of dislocations into structures during cyclic fatigue has been extensively studied during the 1970s using electron microscopy [Laird et al., 1986]. Understanding how these structures form is important because they are regarded as precursors of fatigue damage. Analytical models based on simplified arrangement of dislocations were proposed in the 1970s, for instance by [Kuhlmann-Wilsdorf and Laird, 1977], [Holt, 1970]. However, the dislocation structures have very different features depending on the material and on the load conditions, therefore more complex models, based on numerical simulations are necessary. The description of metal fatigue is challenging also because of its multiscale nature. Dislocations have a core, whose features depend on the specific interatomic interactions, but they interact like discrete line objects on the micrometre scale. On the other hand, well-developed dislocation structures are large compared to the distance between single dislocations and, therefore, they may be described by continuum models. Lastly, the development of persistent slip bands and cracks is visible at the macroscopic scale. Thus, metal fatigue shows very different features if imaged at different length scales, as shown in Fig. 1. The development of specific dislocation-based models for fatigue is fundamental to understand why and how the dislocation structures form. Moreover, such a model would be applied to materials and microstructure design.

0.1 Objectives and Project Framework

The main objective of this dissertation is to develop constitutive dislocation-based equations to be used in a crystal plasticity finite element (CPFE) solver to simulate cyclic plastic deformation, as occurs during cyclic fatigue in FCC metals. Copper, aluminium and 316L stainless steel are the materials of interest. Both single crystals and polycrystalline structures are simulated.

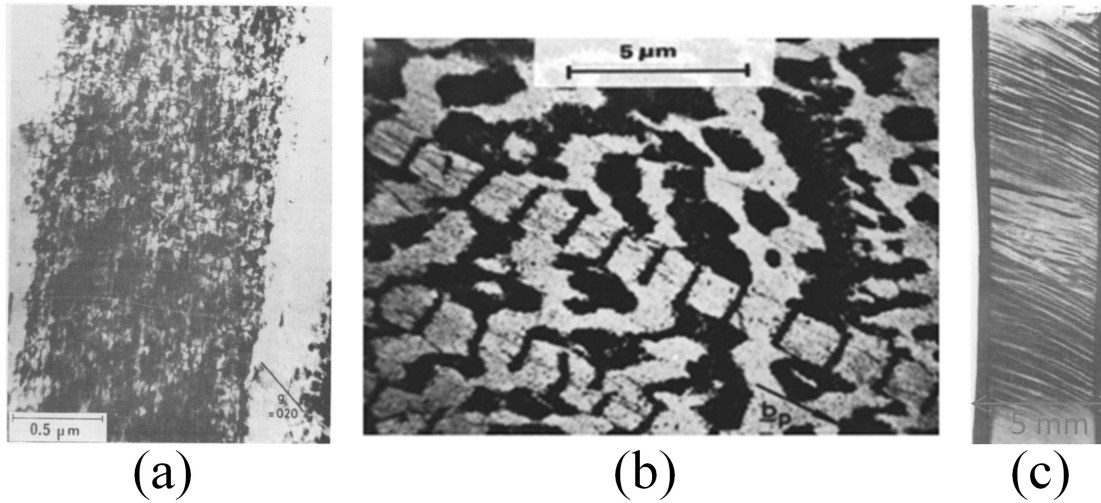


Figure 1 – (a) Dipolar wall in copper fatigued into saturation at room temperature [Kuhlmann-Wilsdorf and Laird, 1977]; (b) examples of persistent slip bands embedded in a loop patch structure [Laird et al., 1986]; (c) Photograph of the surface of a specimen after $1.5 \cdot 10^4$ cycles at $\gamma_{pl} = 4.5 \cdot 10^{-3}$ [Winter, 1974].

The developed models are implemented in the DAMASK framework of the Max Planck Institut für Eisenforschung [Roters et al., 2012], which allows users to introduce constitutive models into a crystal plasticity finite element code. This project involves a collaboration with two other PhD students: Ainara Irastorza-Landa, performing in-situ Laue microdiffraction experiments on fatigued copper single crystal samples at the Swiss Light Source, and Jens Nellessen, performing electron channeling contrast imaging (ECCI) experiments on 316L stainless steel polycrystalline samples at the Max Planck Institute for Iron Research [Nellessen et al., 2015].

0.2 Outline

- Chapter 1 contains a review of experimental evidence of dislocation structures and mechanical properties during cyclic fatigue. The existing knowledge on the origin of dislocation structure and their relationship with mechanical properties is discussed. Existing computational models and their limitations are also discussed.
- Chapter 2 presents the model that has been developed for single crystals oriented for single slip. Its ability to reproduce dislocation structures and mechanical properties is discussed. Tests of the model with different sets of material parameters are shown, in order to simulate the behaviour of different FCC metals.
- Chapter 3 presents the model that has been developed for multiple slip oriented crystals and its application to the simulation of 316L stainless steel polycrystals. Simulations are then compared with experimental results obtained using the electron channeling contrast imaging technique.

- Chapter 4 shows the application of the model to the simulation of Laue microdiffraction experiments, where the lattice rotation is the computed observable.

1 Review of Experimental Evidence and Computational Models

In this chapter a review of experimental evidences on dislocation structures and mechanical properties is reported. Dislocation structures are shown for single slip oriented crystals in section 1.1, for multiple slip oriented crystals in section 1.2, and the formation mechanisms are discussed. Mechanical properties and their relationship with dislocation structures are discussed in section 1.3 and 1.4 for single and multiple slip. Existing computational models are classified in section 1.6, while a brief introduction to the crystal plasticity finite element method used in this thesis is given in section 1.7.

1.1 Single Slip Dislocation Structures

Dislocation structures during cyclic fatigue have been studied using bright field transmission electron microscopy (TEM) [Laird et al., 1986] and the weak-beam technique [Sauzay and Kubin, 2011]. FCC metals, such as copper, have been extensively analysed due to the well-defined dislocation structures appearing after many deformation cycles. Positive and negative dislocations interact and form dislocation dipoles. After few cycles the so-called “loop patches” appear, as shown in Fig. 1.1 (a), which are constituted of edge dislocation dipoles and constitute barriers to the dislocation motion. After hundreds of cycles a stable configuration is reached, called “vein-channel structure”, as shown in Fig. 1.1 (b). Veins are high dislocation-density regions, oriented perpendicular to the Burgers vector, where mainly edge dislocations are present, having a density of the order of 10^{15} m^{-2} [Kuhlmann-Wilsdorf and Laird, 1980]. Screw dislocations connecting the veins have been imaged in the channels, where the dislocation density is of the order of 10^{12} m^{-2} [Buchinger et al., 1985]. These screw dislocations are relatively free to glide, due to the low dislocation density inside the channels, as shown in Fig. 1.1 (c). The observation on a plane perpendicular to the edge dislocation lines in Fig. 1.2 (a) shows that veins are cigar-shaped, they also tend to align along directions not contained in the primary glide plane, as depicted in Fig. 1.2 (b). The longer travelling path of dislocations during cyclic fatigue, compared to the case of monotonic load, leads to dislocation structures closer to their dynamic equilibrium configuration. For this reason, attempts have been made to describe veins as Taylor lattices [Kuhlmann-Wilsdorf, 2001]. If the plastic strain amplitude

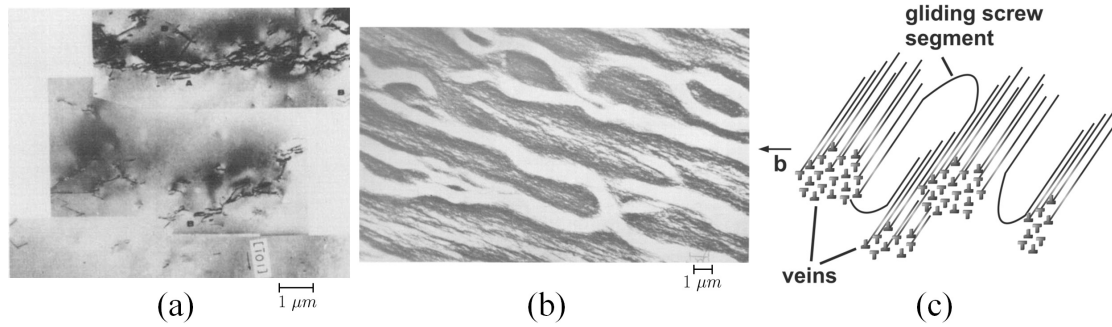


Figure 1.1 – (a) Loop patches after 9 deformation cycles at $\gamma_{pl} = 7.5 \cdot 10^{-3}$ [Kuhlmann-Wilsdorf and Laird, 1977]; (b) vein-channel structure after thousands of cycles at $\gamma_{pl} = 1.25 \cdot 10^{-3}$ [Kuhlmann-Wilsdorf and Laird, 1977]; (c) schematic dislocation arrangement in the vein-channel structure [Suresh, 1998].

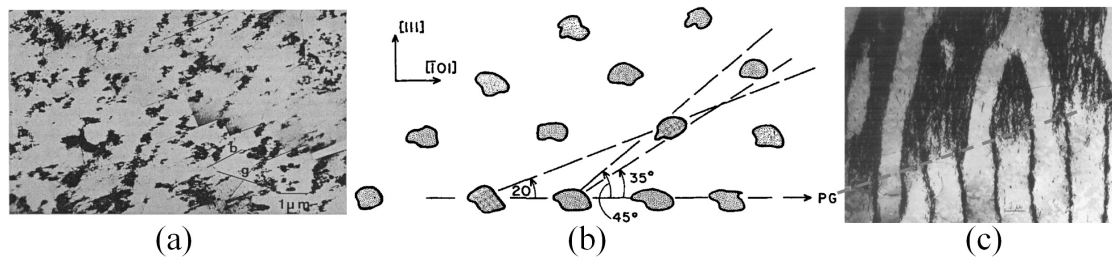


Figure 1.2 – (a) Veins observed on a plane perpendicular to the edge dislocation lines [Buchinger et al., 1985]; (b) vein alignment shown in (a); (c) boundary zone (dashed line) between a PSB and the matrix structure [Winter, 1978].

is in the interval $6 \cdot 10^{-5} < \gamma_{pl} < 7.5 \cdot 10^{-3}$, part of the vein-channel structures transforms into the so-called “persistent slip bands” (PSB), which take this name because of their recurring visibility after removal using electropolishing [Basinski and Basinski, 1992]. Each vein splits in two or three thinner walls and a sharp interface between the two structures appear, as shown in Fig. 1.2 (c). This transformation takes place on a large number of slip planes and

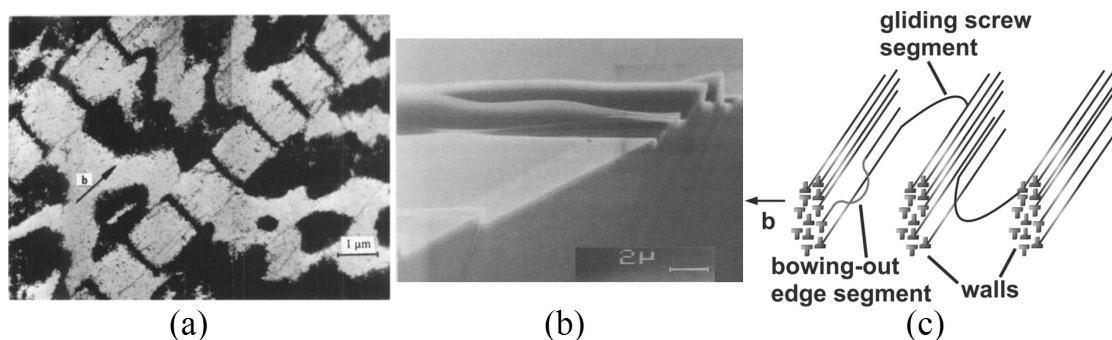


Figure 1.3 – (a) Dislocation structures in a Cu crystal fatigued at $\gamma_{pl} = 10^{-3}$ [Suresh, 1998]; (b) crystal sharp-corner fatigued at $\gamma_{pl} = 1.2 \cdot 10^{-3}$ to 5000 cycles [Basinski and Basinski, 1992]; (c) schematic dislocation arrangement in the PSB structure [Suresh, 1998].

1.1. Single Slip Dislocation Structures

the thin dislocation walls become equally spaced and arrange into a ladder-like shape with a rung spacing of $1.3 \mu\text{m}$, as shown in Fig. 1.3 (a). These walls are constituted mostly of edge dislocation dipoles, as depicted in Fig. 1.3 (c), and the dislocation density inside them is of the order of 10^{15} m^{-2} [Suresh, 1998]. The dipolar nature of veins and PSB walls is proven by the constant TEM background contrast from side to side of the walls. Using X-ray topography it was concluded that the density of GNDs amounts to only a few percent of the total dislocation density [Mughrabi and Obst, 2005]. The strain accommodated by PSB is usually much larger than the strain accommodated by the vein-channel structures and, after many cycles, surface extrusions appear at the intersection between the PSB and the crystal surface, as shown in Fig. 1.3 (b). These extrusions precede the nucleation of surface cracks. The transformation of veins into PSB walls begins with a decrease of the dislocation density in the inner part of veins, as shown in Fig. 1.4 (a). Secondary slip with a Burgers vector not contained in the primary slip systems has been proposed as a possible mechanism [Kuhlmann-Wilsdorf and Laird, 1980]. This would permit local mutual annihilation of opposite signed edge dislocations, as shown in Fig. 1.4 (b). A significant amount of dislocations with a non-primary Burgers vector is not always observed in copper [Antonopoulos and Winter, 1976]. However, experiments on stainless steel have shown many prismatic loops, i.e. formed by positive and negative edge dislocation segments connected by cross slip dislocations, which are likely to form if the cross slip system is active [Li and Laird, 1994]. This mechanism contributes to the dislocation annihilation and to the formation of low density dislocation channels, as shown in Fig. 1.4 (c).

Effect of strain amplitude. the increase of the average dislocation density with the plastic strain amplitude was noticed first from studies on the electrical resistivity [Polák, 1969]. TEM investigations of slices parallel to the active slip plane after plastic strain controlled tests have shown that, for $\gamma_{pl} < 6 \cdot 10^{-5}$, the volume fraction of veins f_V at saturation increases with γ_{pl} , as reported in Tab. 1.1.

| | | | | | | |
|---------------|-------------------|-------------------|---------------------|---------------------|-------------------|-------------------|
| γ_{pl} | $7 \cdot 10^{-6}$ | $1 \cdot 10^{-5}$ | $1.5 \cdot 10^{-5}$ | $2.2 \cdot 10^{-5}$ | $3 \cdot 10^{-5}$ | $6 \cdot 10^{-5}$ |
| f_V | 5 – 10% | 18 – 22% | 23 – 33% | ~ 40% | ~ 48% | ~ 50% |

Table 1.1 – Volume fraction of veins f_V for different values of γ_{pl} [Buchinger et al., 1985].

However the spacing between veins is not strongly affected by γ_{pl} and it turns out to be of the order of $1 \mu\text{m}$. For $6 \cdot 10^{-5} < \gamma_{pl} < 7.5 \cdot 10^{-3}$, the volume fraction of PSB increases linearly with γ_{pl} . For $\gamma_{pl} > 7.5 \cdot 10^{-3}$, multiple slip becomes important and the corresponding dislocation structures are described in section 1.2.

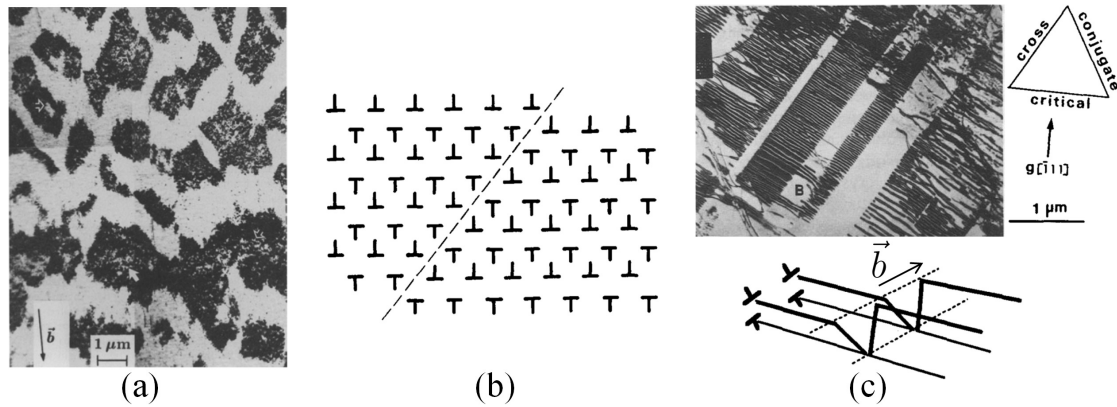


Figure 1.4 – (a) Vein structures at $\gamma_{pl} = 1 \cdot 10^{-4}$ [Holzwarth and Eßmann]; (b) intersecting secondary glide can move primary dislocations [Kuhlmann-Wilsdorf and Laird, 1980]; (c) intersecting cross slip system creates prismatic loops [Li and Laird, 1994], at position B two arrays of prismatic loops have been divided.

Effect of the material. Dislocation structures have been observed also in other FCC materials, such as aluminium, nickel and silver. For copper, aluminium and silver, vein-channel structures form and veins have a higher volume fraction if γ_{pl} increases. The value of γ_{pl} for which PSB appears in the material is between $\gamma_{pl} = 6 \cdot 10^{-5}$ and $\gamma_{pl} = 1 \cdot 10^{-4}$ for all these materials. The ratio τ_s/G between the threshold of the resolved shear stress for PSB formation and the shear modulus of the material has a value of $(6.5 \pm 0.5) \cdot 10^{-4}$ [Li et al., 2010]. The characteristic size of channels is of the order of $1 \mu\text{m}$ for these materials, as shown in Fig. 1.5 for Ni. Few publications are available about the dislocation structures of aluminium; ladder-like structures are typically not detected and, even at low resolved shear stress, cellular structures form, as shown in Fig. 1.6. Substitutional alloys of copper, where Al is added, show dislocations inside PSB walls that are stepped with respect to contiguous planes because of cross slip events [Laird et al., 1986].

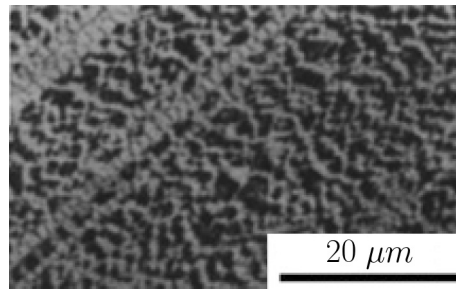


Figure 1.5 – Dislocation structures in Ni single crystals deformed at $\gamma_{pl} = 2 \cdot 10^{-3}$ [Schwab et al., 1996].

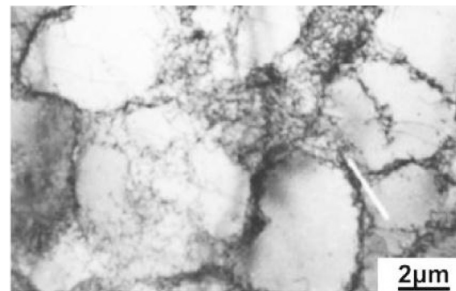


Figure 1.6 – Dislocation structures in Al single crystals deformed at $\tau_s = 4 \text{ MPa}$ [Zhai et al., 1996].

Effect of the temperature. Cyclic fatigue experiments at low temperatures were carried out on copper single crystals [Basinski et al., 1980]. As shown in Fig. 1.7, the main features of dislocation structures remain unchanged, apart from the spacing between dislocation walls of PSB, which reduces to $0.7 \mu\text{m}$ at $T = 77.4 \text{ K}$ and to $0.45 \mu\text{m}$ at $T = 4.2 \text{ K}$. The same trend has been observed at higher temperatures ($T = 600 \text{ K}$) in nickel single crystals [Schwab et al., 1996]. The temperature dependence of the PSB structures is in agreement with the proposed formation mechanism based on the activation of the cross slip system [Kuhlmann-Wilsdorf and Laird, 1980].

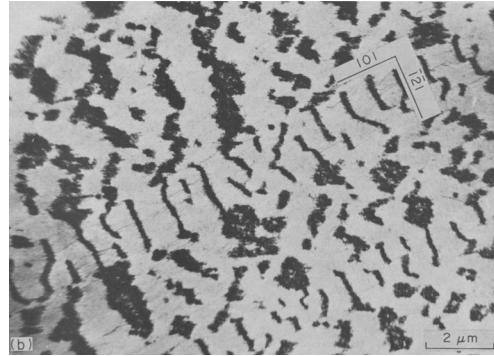


Figure 1.7 – Vein-channel structures and PSB in copper cyclically deformed at $T = 77.4 \text{ K}$ [Basinski et al., 1980].

Secondary dislocations. Secondary dislocations, belonging to the cross slip plane, are commonly observed also during single slip deformation of copper single crystals. Roughly equal numbers of primary and secondary dislocations have been imaged in the channels for $\gamma_{pl} < 6 \cdot 10^{-5}$ [Buchinger et al., 1985]. Appreciable quantities of secondary dislocations have been found in every dislocation wall only for $\gamma_{pl} > 6 \cdot 10^{-5}$ [Buchinger et al., 1985]. An increasing contribution of secondary slip is observed for $\gamma_{pl} > 2 \cdot 10^{-3}$ [Laird et al., 1986].

1.2 Multiple Slip Dislocation Structures

The kind of dislocation structures that are formed in multiple slip orientations is dictated by the interactions among dislocations belonging to different slip systems. The shape of these structures depends on the crystal orientation. As shown in Fig. 1.8 for copper single crystals under uniaxial compression, an orientation close to the $[001]$ leads to two families of perpendicular walls forming the so-called “labyrinth structure”, one close to the $[\bar{1}11]$ axis leads to hexagonal cells forming the so-called “cell structure”, and an orientation close to the $[011]$ axis leads to long dislocation walls forming the so-called “deformation bands”. PSB ladders are present in the material if the crystal orientation is contained in the grey area of the stereographic triangle in Fig. 1.8, but they are gradually converted into the labyrinth and cell structures when the orientation becomes closer to the $[001]$ and $[\bar{1}11]$ axes.

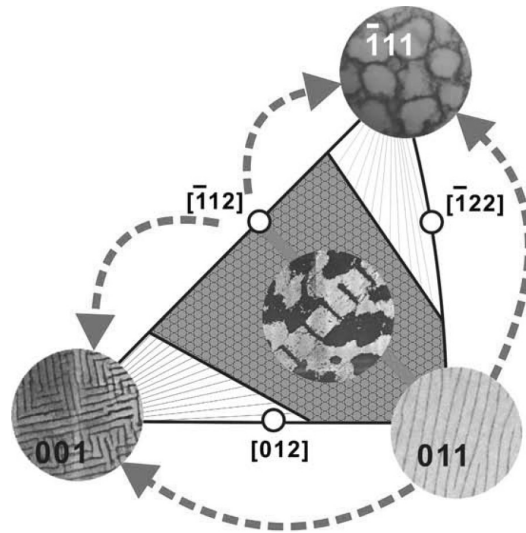


Figure 1.8 – Effect of the crystal orientation on dislocation structures [Li et al., 2010].

Deformation bands. In $[011]$ single crystals, apart from the PSB-vein structure, the so-called “deformation bands” appear, which are formed by dislocation walls longer than in PSB, as shown in Fig. 1.9 (a). The habit plane of these dislocation walls is $(\bar{1}01)$, which is perpendicular to the Burgers vector of the primary slip plane, as depicted in Fig. 1.9 (b). The characteristic distance between the walls is similar to the rung spacing of PSB. Deformation bands can accommodate more plastic deformation (up to $2 \cdot 10^{-2}$) than PSB [Zhang et al., 2001] and the intrusion-extrusion caused by them is stronger.

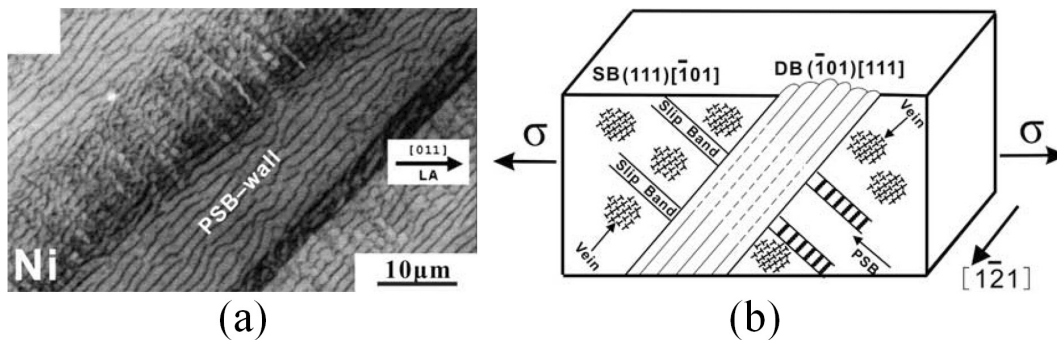


Figure 1.9 – (a) Dislocation structures of $[011]$ nickel at $\gamma_{pl} = 6.1 \cdot 10^{-4}$ viewed from $(\bar{1}\bar{1}\bar{1})$ [Buque, 2001]; (b) Geometrical configuration of slip bands (SB) and deformation bands (DB) [Li et al., 2002].

The formation of deformation bands is due to the locking of different PSB walls, initially misaligned, into longer dislocation structures, as represented in Fig. 1.10.

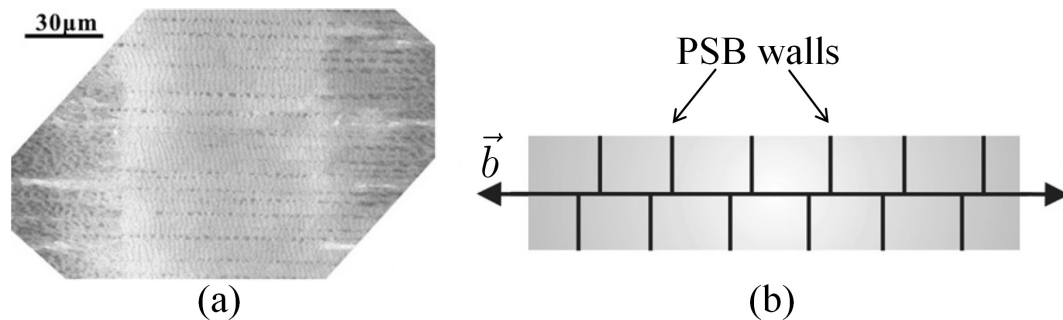


Figure 1.10 – (a) Forming deformation bands in a $[\bar{5} 12 20]$ copper single crystal deformed at $\gamma_{pl} = 8 \cdot 10^{-3}$ [Zhang et al., 2001]; (b) schematic representation of misaligned PSB walls during the formation of a deformation band.

Labyrinth structure. The activation of the critical slip systems during cyclic fatigue of $[001]$ single crystals is associated with the formation of labyrinth structures. For $\gamma_{pl} \approx 1 \cdot 10^{-4}$, only veins and PSB appear, while for $\gamma_{pl} \geq 2.5 \cdot 10^{-4}$ labyrinth structures were imaged [Li et al., 2011]. Some dislocation structures, referred as “uncondensed” labyrinths, are thicker and their edges are connected to forming labyrinth walls, as shown in Fig. 1.11 (a). If the strain amplitude is increased, the uncondensed structures evolve into “condensed” labyrinth structures. If imaged on a plane containing the load direction, for example (010) in Fig. 1.11 (a)-(b) and Fig. 1.12 (a), these structures are constituted of interconnected walls which appear parallel and perpendicular to the load direction.

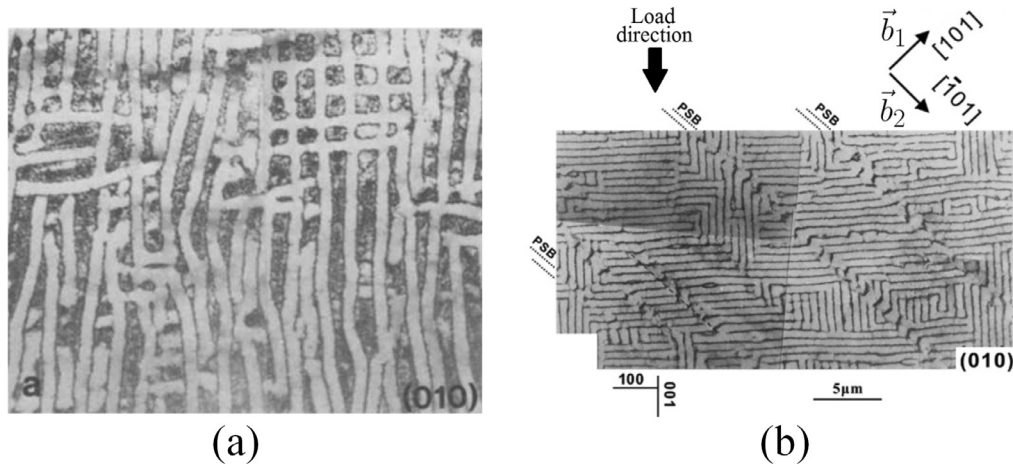


Figure 1.11 – (a) Uncondensed labyrinth structures [Jin and Winter, 1984]; (b) Condensed labyrinth structures [Jin and Winter, 1984].

Both sets of walls have the same regular spacing of around $0.5 \div 0.6 \mu\text{m}$. Longitudinal (100) walls are less common than the transverse (001) [Jin and Winter, 1984]. Two Burgers vectors are present in these structures: the (001) walls contain a preponderance of one particular Burgers vector in a ratio of around 2 : 1 and the (100) walls contain a similar preponderance of a different Burgers vector [Jin and Winter, 1984]. As shown in Fig. 1.11 (b), PSB ladders along the \vec{b}_2 direction are present, however their number is smaller than in single slip deformation at the same plastic strain amplitude. Labyrinth structures have been imaged also in single slip oriented crystals for $\gamma_{pl} \geq 2 \cdot 10^{-4}$ [Li et al., 2011].

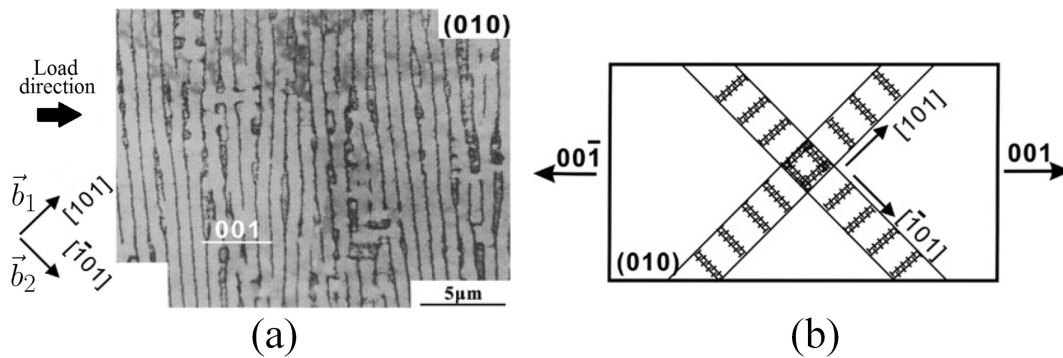


Figure 1.12 – (a) Labyrinth walls with a prevalent (001) orientation [Jin and Winter, 1984]; (b) illustration of the geometry of labyrinth structures [Li et al., 2011].

Both the conjugate and critical dislocation reactions take place in $[001]$ single crystals, forming Lomer-Cottrell and Hirth locks [Hirth, 1961]. However, the strength of the Lomer-Cottrell junction obstructs the dislocation motion and dislocations belonging to the primary and conjugate slip systems occupy separated regions [Jin, 1983]. The geometry of the labyrinth structure formation is depicted in Fig. 1.12 (b): the primary and secondary

dislocations, belonging to the critical system, with orthogonal Burgers vectors \vec{b}_1 and \vec{b}_2 respectively interact and form walls perpendicular to the sum and difference of the Burgers vectors. The wall orientations (001) and (100), once projected on the (010) plane, correspond also to the projected intersections between the primary and the critical slip planes, along which the dislocation junctions form.

Cell structure. The activation of the coplanar slip systems during cyclic fatigue of [111] single crystals is associated with the formation of cell structures. For $\gamma_{pl} \approx 2 \cdot 10^{-4}$, only veins appear, as shown in Fig. 1.13 (a), while for $\gamma_{pl} \geq 1 \cdot 10^{-3}$ cell structures were imaged [Li et al., 2009]. The intermediate formation of PSB ladders between these two strain amplitudes does not happen. As shown in Fig. 1.13 (b), on the primary slip plane (111) cell structures appear as irregular and anisotropic. The shape of these cells range from triangular to hexagonal, with a diameter of $1 \div 2 \mu\text{m}$, and most of the cell walls are perpendicular to the Burgers vectors of the three slip systems on the (111) plane. Screw dislocations appear along the edge of wall structures and connect them [Li et al., 2010].

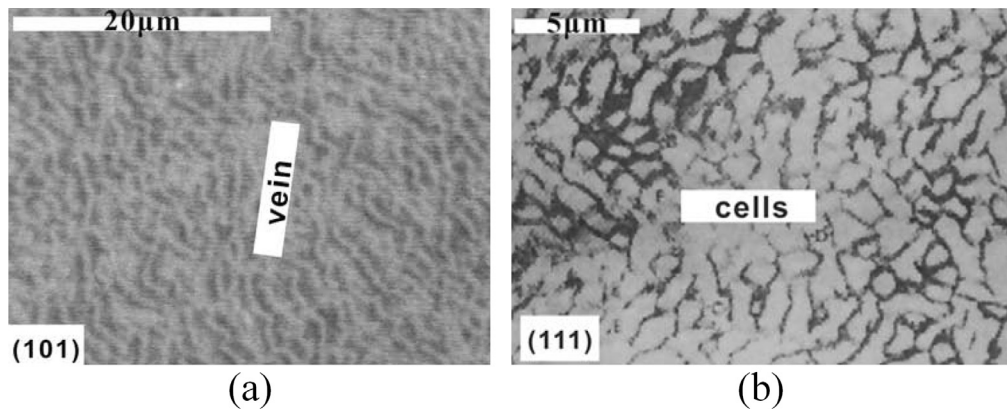


Figure 1.13 – (a) Vein structure of $[\bar{1}11]$ copper single crystal at $\gamma_{pl} = 1.84 \cdot 10^{-4}$ [Li et al., 2009]; (b) cell structures of copper single crystal on the (111) [Lepistö et al., 1984].

If images are taken on the $(13\bar{2})$ plane, as shown in Fig. 1.14 (a), it is visible that primary slip planes containing cells are not distributed uniformly, but they concentrate on well-defined slip bands [Li et al., 2010]. Cell structures have been imaged also in single slip oriented crystals for $\gamma_{pl} \geq 7.5 \cdot 10^{-3}$ [Li et al., 2011]. Both the conjugate and the coplanar dislocation reactions take place in [111] single crystals, forming Lomer-Cottrell and coplanar junctions. As for the labyrinth structure formation, the Lomer-Cottrell interaction is not contributing to the cell formation, whose geometry is depicted in Fig. 1.14 (b). The dislocations on the two active coplanar slip systems interact forming the third coplanar

dislocations. The three sets of dislocations form walls perpendicular to the respective Burgers vectors, where mainly edge dislocation dipoles are present.

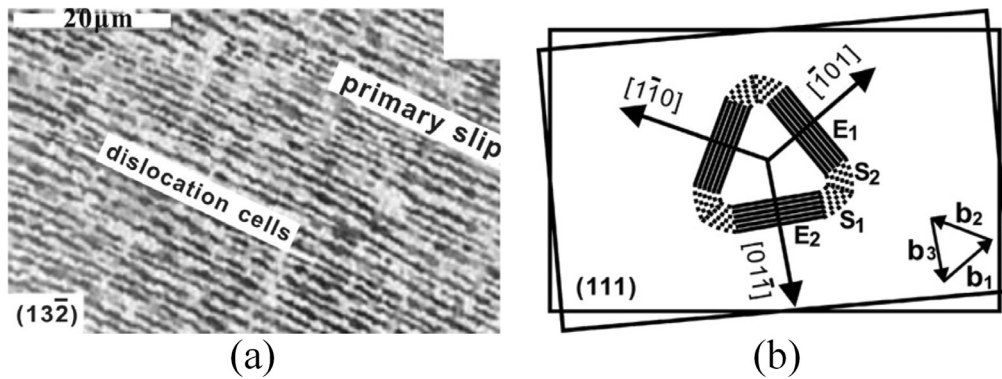


Figure 1.14 – (a) Cell structures of copper single crystal on the $(13\bar{2})$ at $\gamma_{pl} = 4 \cdot 10^{-4}$ [Li et al., 2009]; (b) illustration of the geometry of cell structures [Li et al., 2011].

Dislocation structures in polycrystals. The effect of grain boundaries on the dislocation structures has been studied on bicrystal specimens [Hu et al., 1996], [Hu and Wang, 1997], [Hu and Wang]. Multiple slip can be activated near the grain boundary also in the case where the corresponding monocrystalline components would undergo single slip only. Cell structures tend to form at γ_{pl} lower than an equally oriented single crystal: for example, the $[\bar{3}45]$ grain in [Hu and Wang, 1997] does not show vein structures for $\gamma_{pl} \geq 5 \cdot 10^{-4}$, but only cell structures, as shown in Fig. 1.15 (a), which are elongated along the primary slip direction. Labyrinth structures are commonly found in grains with an orientation close to $[001]$, as shown in Fig. 1.15 (b). Grain boundaries act as obstacles for dislocation structures, for example PSB are usually observed only on one side of high angle grain boundaries, as shown in Fig. 1.15 (c).

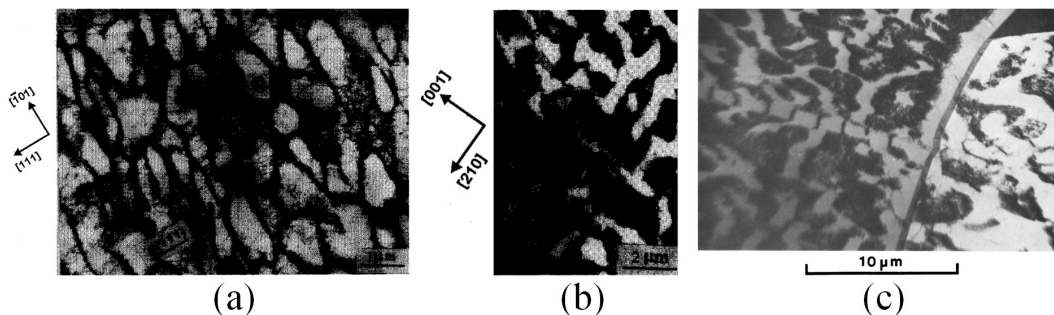


Figure 1.15 – (a) Cell structures in a $[\bar{3}45]$ grain at $\gamma_{pl} = 3.8 \cdot 10^{-3}$ [Hu and Wang, 1997]; (b) labyrinth structures in a $[\bar{1}17]$ grain at $2.8 \cdot 10^{-4}$; (c) high angle grain boundary [Winter et al., 1981].

Effect of the material. Silver single crystals oriented for multiple slip show similar dislocation structures as copper: labyrinth structures appear in $[001]$ -oriented crystals, cell structures in $[\bar{1}11]$ -oriented crystals and deformation bands in $[011]$ [Li et al., 2008]. Also nickel single crystals show labyrinth structures [Mecke et al., 1982] and deformation bands, but the $[\bar{1}11]$ orientation tends to form wall-like configurations, extended perpendicular to the tensile axis [Buque, 2001]. $[001]$ -oriented aluminium single crystals show well-developed labyrinth structures at 0.1 cumulative plastic strain $\gamma_{pl,cum}$ [Videm and Ryum, 1996], while copper shows well-developed structures at $\gamma_{pl,cum} = 0.5$ [Basinski and Basinski, 1992]. As stated for single slip orientation, PSB ladder structures have not been detected in multiple slip oriented aluminium.

1.3 Single slip mechanical properties

During cyclic loading of single slip oriented copper single crystals, rapid hardening occurs during the first tens of cycles until the resolved shear stress reaches a saturation value, as shown in Fig. 1.16 (a). The saturation is reached faster if the plastic strain amplitude γ_{pl} increases, thus the stress value depends on both γ_{pl} and the cumulative plastic strain $\gamma_{pl,cum}$, as shown in Fig. 1.16 (b). A plot of the resolved saturation stress as a function of γ_{pl} is called “cyclic stress-strain curve” (CSSC). It is shown in Fig. 1.16 (c) and it is divided into three regions, denoted by A, B and C. In region A ($\gamma_{pl} < 6 \cdot 10^{-5}$) the saturation stress increases with γ_{pl} and, as stated in section 1.1, this is correlated with an increase in the volume fraction of veins, where the motion of dislocations requires a higher stress. In region B ($6 \cdot 10^{-5} < \gamma_{pl} < 7.5 \cdot 10^{-3}$) the saturation stress is strain-independent and its value is around 28 MPa for copper. This is due to the two-phase structure: the softer ladder structure of PSB and the harder vein structure of the matrix. In region B the volume fraction of PSB increases, but the stress to move screw dislocations inside PSB channels remains the same because of their constant width [Suresh, 1998]. In region C, multiple slip becomes important and the saturation stress increases because of the interaction of primary and secondary slip systems.

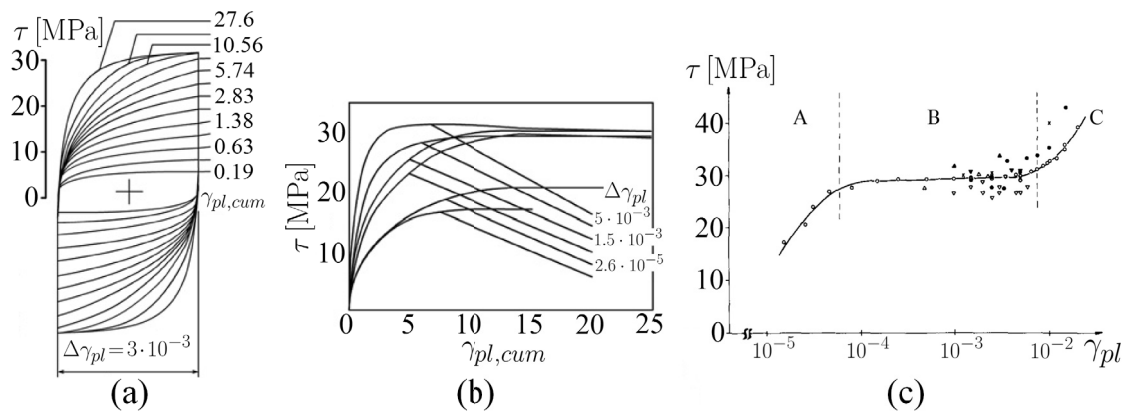


Figure 1.16 – (a) Hysteresis loop evolution in copper single crystal at $\Delta\gamma_{pl} = 3 \cdot 10^{-3}$ for different values of the cumulative plastic strain $\gamma_{pl,cum}$ [Déprés et al., 2008]; (b) cyclic hardening curve at different imposed $\Delta\gamma_{pl}$ [Déprés et al., 2008]; (c) cyclic stress strain curve (CSSC) of copper single crystal [Mughrabi, 1978].

Effect of the material. The CSSC of different FCC metals has the same features if the ratio between the saturation stress τ_{sat} and the shear modulus G is plotted as a function of the plastic strain amplitude, as shown in Fig. 1.17. In particular the threshold value of τ_{sat}/G for PSB formation has approximately the same value for copper, nickel and silver. Metals, such as aluminium, 316L stainless steel and Cu-16Al, show the so-called “softening” behaviour, which is a decrease of the maximum stress when the number of cycles increases. In annealed 316L stainless steel single crystals, softening is present from the first few cycles, as shown in Fig. 1.18, and this is associated with “dislocation starvation”, which means that not enough dislocations are available at the beginning of the test in order to accommodate the imposed plastic strain [Li and Laird, 1994]. The dislocation rearrangement, and the consequent formation of low density regions where dislocations can glide at lower stresses, is also regarded as a reason for mechanical softening [Pham et al., 2013]. The backstress τ_b , associated with barriers to dislocation motion, increases during cycling, while the friction stress τ_f decreases, as shown in Fig. 1.18. Details about how the backstress and friction stress are obtained from the stress-strain curves are explained in appendix A.4. The ratio between backstress and friction stress increases also with γ_{pl} for both 316L stainless steel and copper [Li and Laird, 1993], [Li and Laird, 1994].

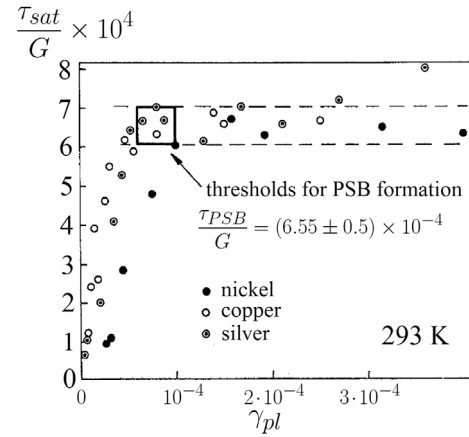


Figure 1.17 – CSSC for nickel, copper and silver single crystals [Mughrabi et al., 1979].

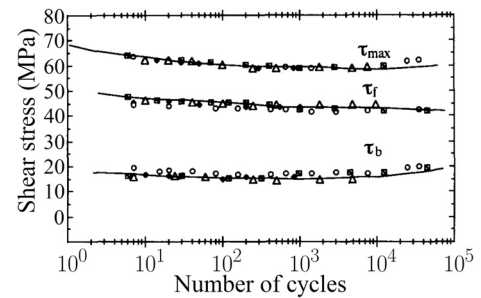


Figure 1.18 – Maximum stress τ_{max} , friction stress τ_f and backstress τ_b as a function of the number of cycles for 316L stainless steel deformed in single slip at $\gamma_{pl} = 1 \cdot 10^{-3}$ [Li and Laird, 1994].

Effect of temperature. At lower temperatures the saturation stress is higher, as shown in Fig. 1.19 for copper, and this is due to the length scale of the dislocation structures. For instance, in region B, 75 – 85% of the observed flow stress can be accounted for by the bow out stress of primary screw segments within the PSB [Basinski et al., 1980]. This bow out stress is inversely proportional to the PSB wall spacing, which decreases with temperature. The qualitative behaviour of the CSSC, with the three regions A, B and C shown in Fig. 1.16 (c), is similar at different temperatures [Hollmann, 2000], [Bretschneider et al., 1997].

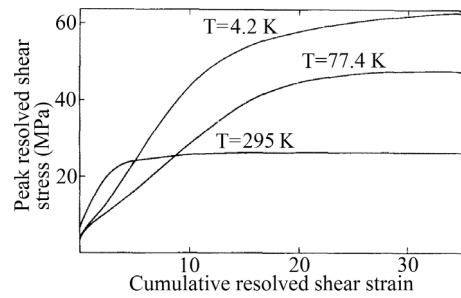
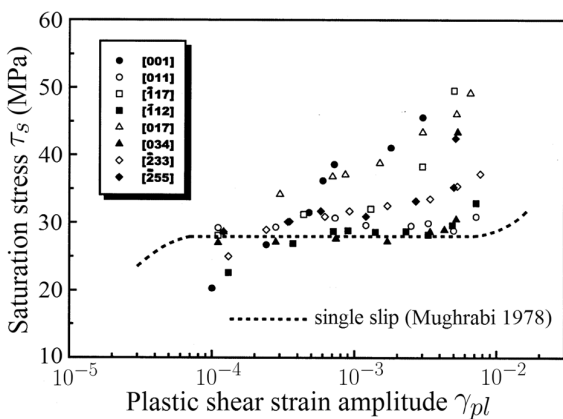


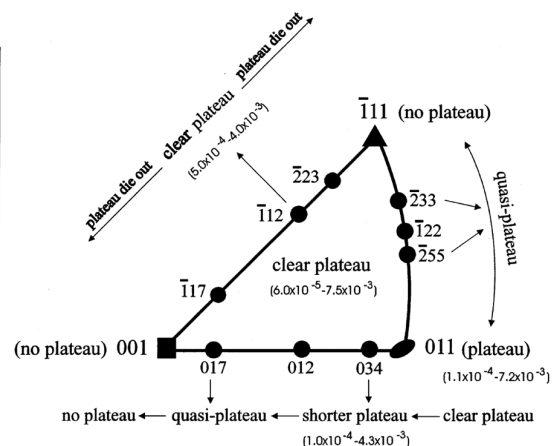
Figure 1.19 – Hardening curves for copper deformed at three different temperatures T in region B [Basinski et al., 1980].

1.4 Multiple slip mechanical properties

For multiple slip oriented single crystals the plateau in the cyclic stress strain curve is not always observed, as shown in Fig. 1.20 (a). Cu single crystals with 4 active slip systems ($[011]$), oriented for critical double slip ($[\bar{0}34]$) and conjugate double slip ($[\bar{1}12]$) show a clear plateau. By contrast, if the sample orientation gets closer to $[001]$ or $[\bar{1}11]$, the clear plateau fades away. Therefore, the region of the stereographic triangle where the plateau forms is correlated with the grey area of the stereographic triangle in Fig. 1.8, and therefore with the formation of PSB.



(a)



(b)

Figure 1.20 – (a) CSSC of double and multiple slip oriented Cu single crystals [Wang et al., 2001]; (b) variation of the crystal CSS curve with its location in the standard stereographic triangle [Wang et al., 2001].

Effect of the material. The effect of the orientation on the mechanical behaviour shown in Fig. 1.20 (b) has been found also in nickel [Buque, 2001] and silver [Li et al., 2008]. Aluminium [001] single crystals show mechanical softening, starting at a cumulative plastic strain around 0.1, as shown in Fig. 1.21. This corresponds to the beginning of the formation of labyrinth structures. Also polycrystalline 316L steel shows mechanical softening when dislocation rearrangement starts [Pham et al., 2013].

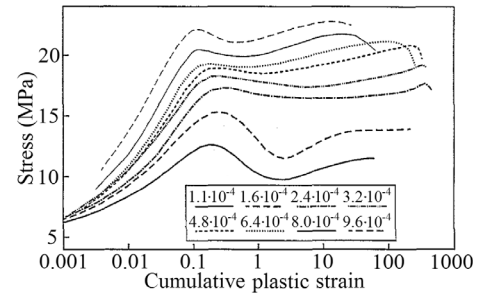


Figure 1.21 – Hardening curve of [001] single crystal aluminium deformed at constant γ_{pl} .

1.5 Continuum dislocation-based models

The description of systems of discrete dislocations using continuum densities is statistical. The dislocation density ρ is known with a certain spatial resolution, which is of the order of the element size used in the simulation. The dislocation density ρ does not contain information about the exact position of dislocations, but it represents an ensemble of systems of discrete dislocations [Groma, 1997]. This concept is explained in Fig. 1.22 (a) in 2D. Inside an area A , whose size is of the order of the spatial resolution, the number of dislocations is $\rho \cdot A$. This value can be non-integer because it is an average over the discrete ensemble, in which every component can have a different number of dislocations. For instance, in Fig. 1.22 (a) positive and negative edge dislocations have the same density: $\rho_{e+} \cdot A = \frac{1}{2}$ and $\rho_{e-} \cdot A = \frac{1}{2}$. In this case, the ensemble is constituted of four components: one containing a positive and a negative edge dislocation, two containing only one type of dislocation and one without dislocations. Furthermore, every component of the discrete ensemble represents different states in which the discrete dislocations have different spatial positions, as shown in Fig. 1.22 (b). This is because all these states are described by the same ρ and, in a statistical model, they are equally likely. A single simulation thus represents a set of discrete simulations. The rate equations describing the time evolution of ρ have to represent the evolution of the discrete ensemble. This implies that the average over the evolved discrete ensemble have to correspond to the evolved dislocation density. Such rate equations are presented in the following.

1.6 Dislocation-based models for cyclic fatigue

Simulation of cyclic fatigue with the aim of calculating the damage of materials has been carried out mostly using phenomenological material models [Lemaitre and Chaboche, 2002]. However the study of cyclic fatigue at the micrometer length scale requires a model with internal parameters representing dislocations. In this section existing models are divided

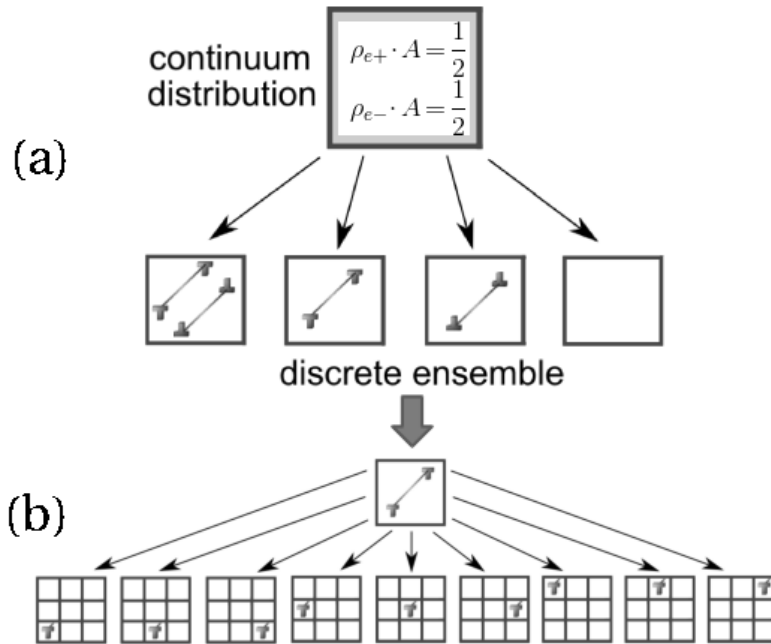


Figure 1.22 – (a) Equivalence between a continuum distribution ρ and an ensemble of states with different number of dislocations. (b) Different states with different spatial positions of one dislocation that are equivalent to a component of the discrete ensemble.

into different categories: composite models, reaction-diffusion models, self-consistent field models and discrete dislocation dynamics models.

Composite models. These models are based on the assumption that the behaviour of the high and low dislocation density regions can be treated separately. Two-phase models were initially developed to illustrate the mechanism by which the plastic strain is carried by the PSB. If f_{psb} is the PSB volume fraction, the plastic strain amplitude is expressed in terms of the law of mixtures:

$$\gamma_{pl} = f_{psb}\gamma_{psb} + (1 - f_{psb})\gamma_m, \quad (1.1)$$

where γ_{psb} and γ_m are the plastic strain accommodated by the PSB and the vein. As stated in section 1.1, f_{psb} increases linearly with γ_{pl} , suggesting that γ_{psb} and γ_m are constants. The volume fraction f_{psb} of the softer phase is adjusted in order to maintain a constant stress in the plateau of the cyclic stress-strain curve (region B) [Winter, 1974]. The Kubin-Estrin model is a composite model for the vein-channel structure that uses different state variables to model mobile dislocations in the channel (ρ_{mob}) and immobile dislocations in the veins (ρ_{imm}). As shown in Fig. 1.23 (a), immobile dislocations are divided into “recoverable” (ρ_r) and “non-recoverable” (ρ_{nr}), which cannot become mobile again after stress reversal. Three differential equations are necessary to describe the time

evolution of these state variables [Estrin, 1996]:

$$\dot{\rho}_r = C_5 \dot{\epsilon}_p \sqrt{\rho_{imm}} - C_2 \dot{\epsilon}_p \rho_r - C_6 \rho_r, \quad (1.2)$$

$$\dot{\rho}_{imm} = C \dot{\epsilon}_p + C_1 \dot{\epsilon}_p \sqrt{\rho_{imm}} - C_2 \dot{\epsilon}_p \rho_{imm} + C_3 \dot{\epsilon}_p \rho_{mob}, \quad (1.3)$$

$$\dot{\rho}_{mob} = -C \dot{\epsilon}_p - C_1 \dot{\epsilon}_p \sqrt{\rho_{imm}} - C_3 \dot{\epsilon}_p \rho_{mob} + C_4 \dot{\epsilon}_p (\rho_{imm}/\rho_{mob}) + C_7 \rho_r. \quad (1.4)$$

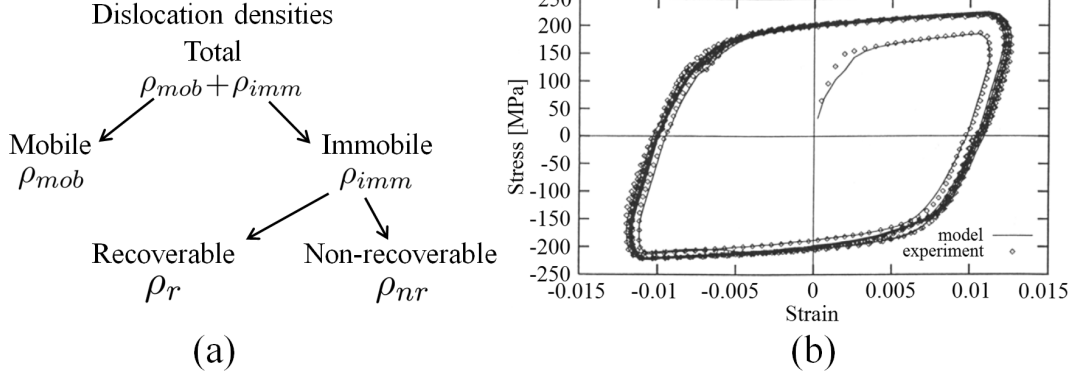


Figure 1.23 – (a) State variables of the Kubin-Estrin model; (b) fit of the hysteresis stress-strain curve for Al [Estrin et al., 1996].

Each term represents a different dislocation process, summarized in Tab. 1.2, and fitting coefficients are used.

| | | | |
|---------------------|----------|---------------|------------------|
| C | C_1 | C_2 | C_3 |
| multiplication | trapping | annihilation | dipole formation |
| C_4 | C_5 | C_6 | C_7 |
| dislocation sources | trapping | jog formation | remobilization |

Table 1.2 – Dislocation processes associated with the different coefficients in (1.2)-(1.4).

Reaction-diffusion models. These models introduce velocity gradient terms to describe the motion of dislocations and to predict the formation of dislocation structures starting from a random dislocation distribution [Dewel et al.]. In the Walgraef-Aifantis model, dislocations are divided into “slow” (S) and “fast” (F), but there is no a priori assumption on the spatial positions of these two types of dislocations. The evolution equations are [Walgraef and Aifantis, 1985]:

$$\dot{\rho}_S + \nabla \cdot \vec{j}_S = g(\rho_S) - \beta \rho_S + \gamma \rho_F \rho_S^2, \quad (1.5)$$

$$\dot{\rho}_F + \nabla \cdot \vec{j}_F = \beta \rho_S - \gamma \rho_F \rho_S^2, \quad (1.6)$$

where \vec{j}_S and \vec{j}_F are the dislocation fluxes and the meaning of the other terms is sum-

marized in Tab. 1.3. The multiplication-annihilation function $g(\rho_S)$ is zero if there is a balance between those two processes in the homogeneous steady state $\rho_{S,0}$, and a simple form used is $g(\rho_S) = a(\rho_{S,0} - \rho_S)$ [Schiller and Walgraef, 1988]. The dislocation fluxes are drift terms (first spatial derivatives), however they have been treated as diffusion terms (second spatial derivatives) because positive and negative dislocations during cyclic deformation have a back and forth motion. This motion causes a dislocation accumulation to spread with dislocations moving down the concentration gradient [Walgraef and Aifantis, 1986]. Two diffusion coefficients D_S and D_F for “slow” and “fast” dislocations are introduced. In this model both the terms representing the fluxes and the trapping of mobile dislocations (γ) are fundamental to obtain dislocation patterning. The characteristic pattern wavelength is [Schiller and Walgraef, 1988]:

$$\lambda_c = 2\pi \left(\frac{D_S D_F}{a\gamma\rho_{0,S}^2} \right)^{1/4}, \quad (1.7)$$

where $\rho_{0,S}$ is the “slow” dislocation density of the spatially uniform stationary state.

| $g(\rho_S)$ | β | γ |
|---------------------------------|----------------|----------|
| multiplication and annihilation | remobilization | trapping |

Table 1.3 – Dislocation processes associated with the different coefficients in (1.5)-(1.6).

The Walgraef-Aifantis model has been extended to 2D using two state variables for the “fast” dislocations belonging to the two slip systems [Pontes et al., 2006]. A 2D dislocation patterning arises from this model, with walls perpendicular to the two Burgers vectors, whose directions are chosen perpendicular, as shown in Fig. 1.24 (c). This is due to the flux terms used to model the motion of dislocations: fluxes are imposed along the two Burgers vectors and dislocations move away from emerging channels along the Burgers vector directions, leaving behind empty channels oriented as edge dislocations on the two slip systems. This is not consistent with the experimental observations of labyrinth structures presented in section 1.2, where the dislocation walls are perpendicular to the sum and difference of the Burgers vectors.

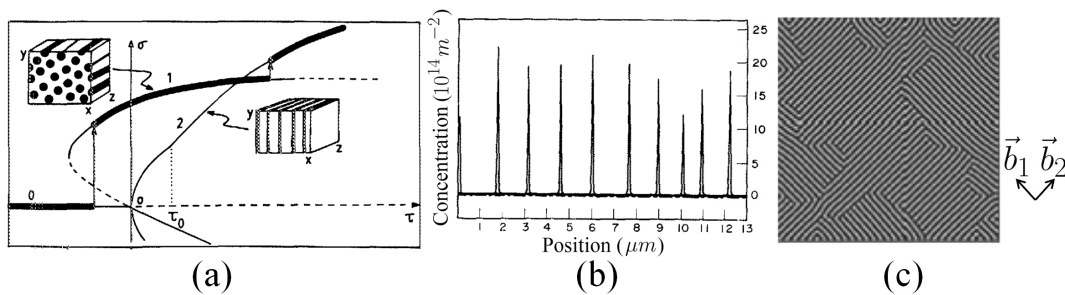


Figure 1.24 – (a) Amplitude of the spatial pattern, plain lines are stable states, dashed lines are unstable ones [Walgraef and Aifantis, 1985]; (b) pattern developed in a 1D model [Schiller and Walgraef, 1988]; (c) simulated 2D dislocation patterning, primary slip directions are parallel to the diagonals of the box [Pontes et al., 2006].

Self-consistent field models. These models propose a physics-based method to treat the dislocation interaction term (γ coefficient of the reaction diffusion models). A higher order distribution function $f_N(t, \vec{r}_1, \dots, \vec{r}_N)$ is defined for a system of N straight parallel dislocations, which represents the distribution function in the configurational space $(t, \vec{r}_1, \dots, \vec{r}_N)$ of the dislocation coordinates [Groma, 1997]. The dislocation density $\rho(r)$ of the reaction-diffusion models is found by integrating f_N over $(N - 1)$ coordinate variables. Approximations are needed for the correlation function $\rho_2(t, \vec{r}_1, \vec{r}_2)$, giving the probability that two interacting dislocations have coordinate vectors \vec{r}_1 and \vec{r}_2 . Existing simulations have neglected the correlation between dislocation positions or have estimated it using 2D discrete dislocation dynamics simulations [Groma et al., 2003]. In these models the dislocation motion is linearly proportional to the total stress on dislocations, which is given by [Groma et al., 2003]:

$$\tau(\vec{r}) = \int \tau_{ind}(\vec{r} - \vec{r}')(\rho_+(\vec{r}') - \rho_-(\vec{r}')) d\vec{r}' + \tau_{exp}, \quad (1.8)$$

$$\tau_{ind}(\vec{r}) = \frac{Gb}{2\pi(1-\nu)} \frac{x(x^2 - y^2)}{(x^2 + y^2)^2}, \quad (1.9)$$

where ρ_+ and ρ_- are the densities of positive and negative edge dislocations. 2D simulations have been carried out using this model to understand the origin of dislocation patterning. The main result is that a strong dislocation patterning appears only when a dislocation multiplication term, proportional to $\rho\tau^2$, is introduced, as shown in Fig. 1.25 (a). A periodic external stress can change the length scale of dislocation structures, as shown in Fig. 1.25 (b).

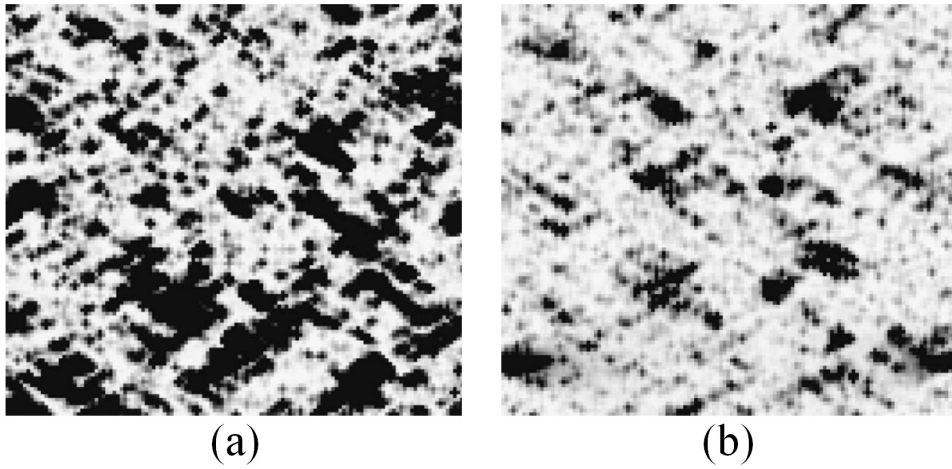


Figure 1.25 – (a) dislocation structures if dislocation multiplication is introduced without external stress; (b) dislocation structures with dislocation multiplication and a periodic external stress [Groma and Balogh, 1999].

Discrete dislocation dynamics (DDD). Taylor lattice models have been used to explain the basic properties of fatigue dislocation structures. The critical stress to split an edge dislocation dipole with height h is given by [Kuhlmann-Wilsdorf et al., 1952]:

$$\tau_h = \frac{Gb}{8\pi(1-\nu)h}, \quad (1.10)$$

and the same formula, apart from a proportionality coefficient, holds for a dislocation arrangement, as the one in Fig. 1.26 (a). The so-called “loop-flipping” mechanism, in which lines of positive and negative edge dislocations move along opposite directions, gives a contribution to the plastic strain accommodated by veins [Kuhlmann-Wilsdorf, 1979b]. Moreover, it is responsible for the creation of GND walls at the vein boundary and, therefore, for the backstress τ_B . According to the Taylor lattice model, τ_B is proportional to $\sqrt{\gamma_{pl,cum}}$ [Cheng and Laird, 1981], in agreement with experiments. The stability of dislocation dipole walls, shown in Fig. 1.26 (b), against disintegration due to stress increase has been studied [Neumann, 1987]. The maximum sustainable stress, as shown in Fig. 1.26 (c), is higher than the one of diamond-shaped Taylor lattices. Therefore this model indicates that thin PSB walls are tendentially more stable than veins.

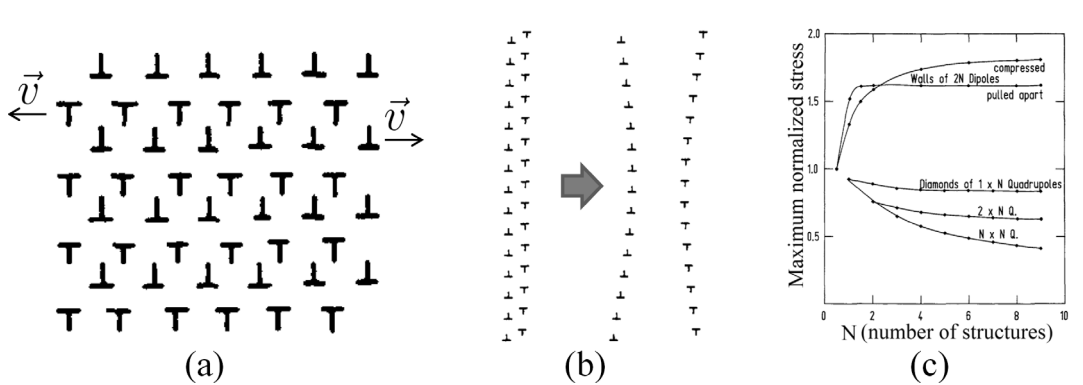


Figure 1.26 – (a) Taylor lattice and “loop-flipping” motion [Kuhlmann-Wilsdorf, 1979a]; (b) disintegration of a dipolar wall due to stress increase; (c) maximum stability stress of various dislocation configurations [Neumann, 1987].

The concept of low energy dislocation configurations has been applied also to multiple slip dislocation structures [Dickson et al., 1986a]. The so-called “double pseudo-polygonisation arrangement” theory (DPP) predicts energetically favourable wall orientations perpendicular to the directions that bisect the obtuse and acute angles between the edge dislocation lines on the two slip systems. These stacking directions (y and x axes in Fig. 1.27 (a)) for dislocation loops on the two slip systems favour the formation of edge dipoles, screw dipoles and dislocation junctions, which lower the interaction energy. 3D discrete dislocation dynamics simulations are computationally expensive and often use simplified boundary conditions, however they have been used to simulate the early fatigue cycles in a micrometre size grain. In single slip dislocation accumulations and development of dislocation dipole walls have been found, as shown in Fig. 1.27 (b). In multiple slip, a network of dislocations belonging to the two slip systems form, as shown in Fig. 1.27 (c).

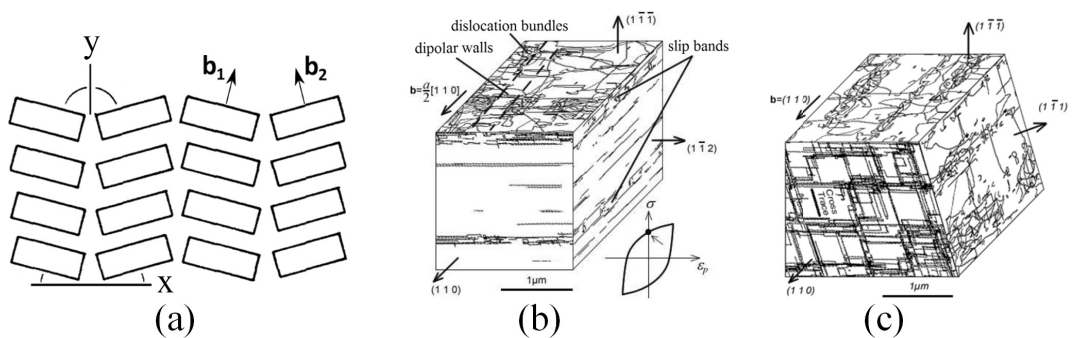


Figure 1.27 – (a) Stacking arrangement of dislocation loops in the DPP theory [Dickson et al., 1986b]; (b) single slip simulated microstructure after 25 cycles [Déprés, 2004]; (c) double slip dislocation microstructure [Déprés et al., 2004].

| | Patterning prediction | arbitrary boundary conditions | 3D | physics-based coefficients |
|-----------------------|-----------------------|-------------------------------|----|----------------------------|
| Composite models | × | × | × | × |
| Reaction-diffusion | ✓ | × | × | × |
| Self-consistent field | ✓ | × | × | ✓ |
| DDD | ✓ | × | ✓ | ✓ |

Table 1.4 – Features table of the presented dislocation-based models for cyclic fatigue.

1.7 The crystal plasticity finite element method

In the crystal plasticity finite element method (CPFEM) the plastic deformation induced by the activity on all the slip systems, and their specific geometry, is considered. The first CPFEM simulations date back to the 1980s [Peirce et al., 1982], but only recently the method has been applied to 3D simulations of single- and polycrystals with arbitrary boundary conditions, because the required computational resources are substantial [Roters, 2011]. The CPFEM considers all available slip systems to calculate the plastic velocity gradient:

$$\mathbf{L}_p = \sum_{\alpha=1}^n \dot{\gamma}_p^{\alpha}(\mathbf{S}) \mathbf{m}^{\alpha} \otimes \mathbf{n}^{\alpha}, \quad (1.11)$$

where \mathbf{m}^{α} is the slip direction and \mathbf{n}^{α} is the normal to the slip plane. This method has been implemented in a subroutine called DAMASK [Roters et al., 2012], used in our project, for commercial finite element software, like Abaqus. The FEM software, at each equilibrium iteration, provides a value for the total deformation gradient \mathbf{F} and requires a stress calculation (\mathbf{S}). Known \mathbf{F} , the task of the DAMASK subroutine is to find the elastic and plastic part \mathbf{F}_e and \mathbf{F}_p respectively by solving a self consistent loop, as shown in Fig. 1.28, with \mathbf{L}_p used as a predictor in the Newton-Raphson scheme. The elasticity matrix \mathbf{C} takes into account the crystal anisotropy and it is characterized by three constants C_{11} , C_{12} and C_{44} for FCC metals. The values of these constants for different materials are reported in Tab. 1.5.

| Material | C_{11} | C_{12} | C_{44} |
|------------|------------|------------|-----------|
| Copper | 168.75 GPa | 121.58 GPa | 75.68 GPa |
| Aluminium | 107.3 GPa | 60.8 GPa | 28.3 GPa |
| 316L steel | 206 GPa | 133 GPa | 119 GPa |

Table 1.5 – Elastic constants for copper [Overton and Gaffney, 1955], aluminium [Vallin et al., 1964] and 316L steel [Reed and Horiuchi, 1983].

1.7. The crystal plasticity finite element method

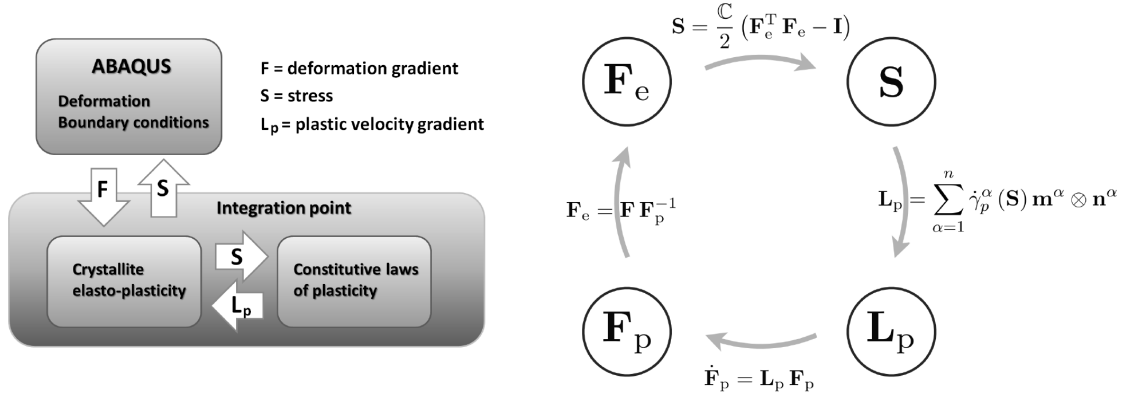


Figure 1.28 – Scheme of the crystal plasticity finite element method, as implemented in DAMASK [Roters et al., 2012].

This framework is highly suitable for physics-based theories because the plastic strain rate can be calculated using the Orowan kinetics law:

$$\dot{\gamma}_p^\alpha = \rho_{mob}^\alpha v b^\alpha, \quad (1.12)$$

where ρ_{mob}^α is the mobile dislocation density on the slip system α and v^α the corresponding dislocation velocity. The motion of dislocations between neighbouring elements is given by a flux term:

$$J_c^\alpha = -\nabla \cdot (\rho_c^\alpha \bar{v}_c^\alpha), \quad (1.13)$$

where \bar{v}_c^α is directed perpendicular to the line directions of dislocations on the slip plane α with character c . A finite volume discretization is used to calculate the spatial gradients in (1.13). Given an integration point $i0$, a hexahedral volume is defined, whose surfaces bisect the segments connecting $i0$ with its neighbouring integration points $i1, i2, i3, i4, i5, i6$. This control volume is represented as a grey hexahedra in Fig. 1.29. The unit normals of the surfaces are indicated as $\hat{n}_{i1}, \hat{n}_{i2}, \hat{n}_{i3}, \hat{n}_{i4}, \hat{n}_{i5}, \hat{n}_{i6}$ and the corresponding values of the areas as $A_{i1}, A_{i2}, A_{i3}, A_{i4}, A_{i5}, A_{i6}$. In a finite volume scheme, the flux term is approximated by a volume average of (1.13):

$$\frac{1}{V} \int_V \nabla \cdot (\rho_c^\alpha \bar{v}_c^\alpha) dV = \frac{1}{V} \oint_{\partial V} \rho_c^\alpha \bar{v}_c^\alpha \cdot \hat{n} dA = \frac{1}{V} \sum_{j=i1, \dots, i6} (\rho_c^\alpha \bar{v}_c^\alpha \cdot \hat{n}_j A_j), \quad (1.14)$$

where V is the grey volume in Fig. 1.29. Every term of the sum on the right hand side of (1.14) is calculated using the following first order approximation:

- if $\bar{v}_c^\alpha \cdot \hat{n}_j > 0$ at $i0$ (outgoing flux), then the values of \bar{v}_c^α and ρ_c^α are taken at the integration point $i0$;
- if $\bar{v}_c^\alpha \cdot \hat{n}_j < 0$ at $i0$ (incoming flux), then the values of \bar{v}_c^α and ρ_c^α are taken at the neighbour

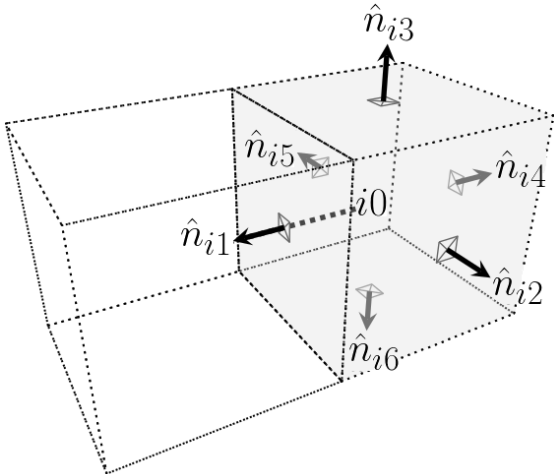


Figure 1.29 – Control volume to calculate dislocation fluxes and unit normals pointing towards the neighbouring integration points [Roters, 2011].

integration point j .

Evolution equations for the dislocation density during cyclic fatigue need to be implemented for this computational method, which can have all the features that other models are missing, as shown in Tab. 1.4.

2 Single slip dislocation-based model

In this chapter the dislocation-based CPFEE framework is applied to the simulation of cyclic fatigue in single crystals. The dislocation processes taken into account in the model are explained and new equations, specific for cyclic fatigue, are introduced to describe the dislocation multiplication and interaction. These modifications with respect to existing models lead to the prediction of the vein-channel structure starting from a randomly perturbed dislocation distribution. The resulting dislocation patterning is analyzed with different sets of material parameters in order to compare the behaviour of copper and aluminium. The influence of dislocation structures on the mechanical properties is shown. Mechanical softening and the strain amplitude dependence, predicted by the new model, are shown to be consistent with experimental results. Finally, a possible approach to predict the emergence of persistent slip bands during single slip deformation is presented.

2.1 Existing models for monotonic loads

Dislocation-based constitutive models for single slip describe the dislocation arrangement using several dislocation densities, describing different orientations of the dislocation line with respect to the Burgers vector [Sandfeld and Zaiser, 2015]. These models have been primarily applied to monotonic deformations [Leung and Ngan, 2016], for which the dislocation cell structure has been found [Xia and El-Azab, 2015]. Computationally efficient models used in the CPFEE framework consider signed edge and screw dislocation densities as state variables [Roters, 2011], [Kords, 2013]. Their dislocation line is perpendicular and parallel to the Burgers vector direction respectively, which is included in this computational framework for every slip system, as stated in section 1.7. The dislocation densities used in a continuum model can be thought as components of a state vector $\rho(\vec{r}, t)$, function of position and time. The time evolution can be described by rate equations:

$$\dot{\rho}(\vec{r}, t) = g(\rho(\vec{r}, t)) , \quad (2.1)$$

Chapter 2. Single slip dislocation-based model

where the function g is a sum of terms representing the dislocation processes, such as multiplication, annihilation and cross slip. In the following the dislocation processes considered in the constitutive model are explained.

Dislocation annihilation. In this process a positive and a negative dislocation (edge or screw character) meet and annihilate. This is possible, even if the two dislocations are not gliding exactly on the same slip plane, because of dislocation climb for edge dislocations and cross slip for screw dislocations. These processes are energetically favoured only when the distance between the two dislocation lines is lower than a characteristic length \check{d}^α [Hirth and Lothe, 1982], shown in Fig. 2.1, which is different for edge and screw dislocations. The flux per unit length of positive edge dislocations is $\rho_{e+}^\alpha |v_{e+}^\alpha|$, therefore the rate at which they cross the characteristic length $2\check{d}_e^\alpha$ for annihilation is $2\check{d}_e^\alpha \rho_{e+}^\alpha |v_{e+}^\alpha|$. The same holds for negative edge dislocations. The rate of encounters for edge (ρ_{e+}, ρ_{e-}) and screw (ρ_{s+}, ρ_{s-}) dislocations, causing annihilation, is given by:

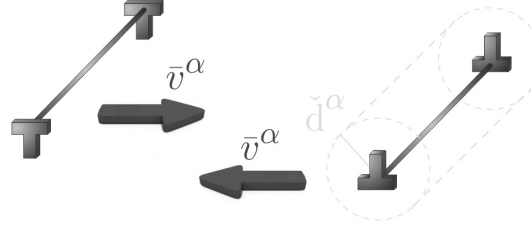


Figure 2.1 – Dislocation annihilation process [Roters et al., 2000].

$$\dot{\rho}_{e+,ann}^\alpha = \dot{\rho}_{e-,ann}^\alpha = -4\check{d}_e^\alpha \rho_{e+}^\alpha \rho_{e-}^\alpha |v_{e+}^\alpha|, \quad (2.2)$$

$$\dot{\rho}_{s+,ann}^\alpha = \dot{\rho}_{s-,ann}^\alpha = -4\check{d}_s^\alpha \rho_{s+}^\alpha \rho_{s-}^\alpha |v_{s+}^\alpha|. \quad (2.3)$$

The annihilation distance for edge dislocations is determined by equating the attractive stress between a positive and negative dislocation with the osmotic force, associated with the free energy change when a vacancy is formed, which depends on the vacancy diffusion coefficient [Hirth and Lothe, 1982]. The annihilation distance for screw dislocations is determined by equating the attractive stress between a positive and negative dislocation with the critical stress to induce a cross slip event [Basinski and Basinski, 1992]. The values used in the simulations of this thesis for different materials are reported in Tab. 2.1.

| Material | \check{d}_e^α | \check{d}_s^α |
|------------|----------------------|----------------------|
| Copper | 1.6 nm | 50 nm |
| Aluminium | 1.6 nm | 50 nm |
| 316L steel | 1.3 nm | 50 nm |

Table 2.1 – Annihilation distances used for different materials [Basinski and Basinski, 1992], [Caillard and Martin, 1989], [Catalao et al., 2005].

Dislocation multiplication. One of the first equations developed to describe the length increase of dislocation lines is the Kocks-Mecking equation [Mecking and Kocks, 1981], which states that:

$$\left(\frac{\partial \rho}{\partial \gamma_{pl}} \right)_{mult} = k_1 \sqrt{\rho}, \quad (2.4)$$

where ρ is the total dislocation density and k_1 is a constant. Models considering edge and screw dislocations are usually based on the Arsenlis multiplication law [Arsenlis and Parks, 2002], which holds if the averaging volume to obtain a continuum description is larger than the characteristic size of a dislocation loop, which should be contained inside one element of the mesh. As dislocation lines need to remain connected, moving screw dislocations, with characteristic lengths \bar{l}_{s+} and \bar{l}_{s-} , create new edge dislocations, and edges create screws, as shown in Fig. 2.2 (a). For example the multiplication law for ρ_{e+}^α is:

$$\dot{\rho}_{e+,mult}^\alpha = \frac{\rho_{s+}^\alpha |v_{s+}^\alpha|}{\bar{l}_{s+}} + \frac{\rho_{s-}^\alpha |v_{s-}^\alpha|}{\bar{l}_{s-}}. \quad (2.5)$$

Dislocation multiplication in the vein-channel structure is caused by moving screw dislocations inside channels, producing new edge dislocations at the location of the *vein-channel interface*, as shown in Fig. 2.2 (b). These screw dislocations can be considered to be the expanding dislocation loops in the Arsenlis model.

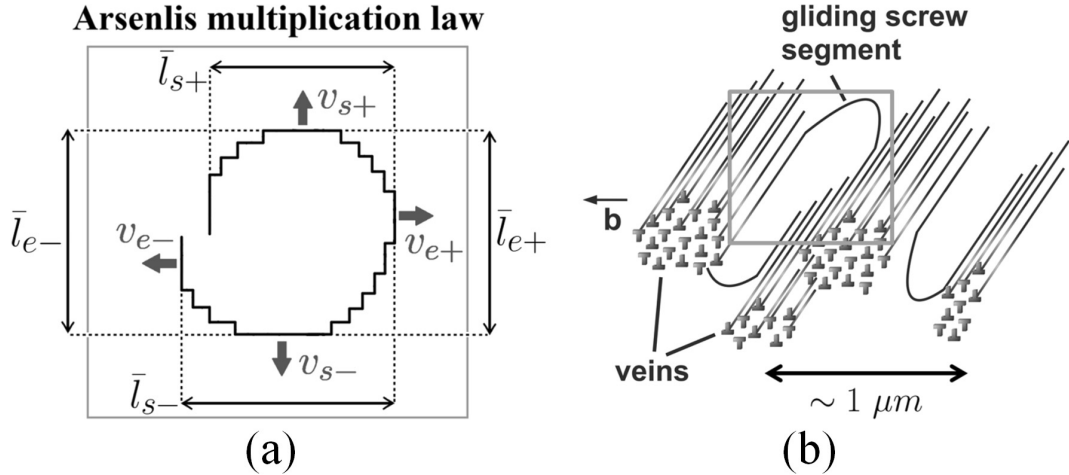


Figure 2.2 – (a) Expanding dislocation loop; (b) gliding motion of one screw dislocation and averaging volume for the Arsenlis multiplication law.

Therefore, the Arsenlis law is valid when the averaging volume in the simulation is larger than the channel width.

Dislocation dipoles. During single slip deformation of pure crystals the major interaction mechanism is the formation of dislocation dipoles [Roters, 2011]. As for annihilation, the formation of a dipole takes place if the distance between two opposite signed dislocations is lower than the so-called *dipole stability height* \hat{d}_e^α [Roters et al., 2000], as shown in Fig. 2.3 (a), but larger than the annihilation distance \check{d}_e^α . The dipole stability height in (1.10) depends on the dislocation character and the applied stress. As for annihilation, the flux per unit length of positive edge dislocations is $\rho_{e+}^\alpha |v_e^\alpha|$, therefore the rate at which they cross the characteristic distance $2(\hat{d}_e^\alpha - \check{d}_e^\alpha)$ for dipole formation is $2(\hat{d}_e^\alpha - \check{d}_e^\alpha) \rho_{e+}^\alpha |v_e^\alpha|$. For example, the dipole formation rate for positive edge dislocations is:

$$\dot{\rho}_{e+,dip,form}^\alpha = 4(\hat{d}_e^\alpha - \check{d}_e^\alpha) \rho_{e+}^\alpha \rho_{e-}^\alpha |v_e^\alpha|. \quad (2.6)$$

A stress increase causes the dislocations to be freed and the rate of this process is determined by a dipole height distribution function. In existing dislocation-based models this distribution is assumed uniform [Roters et al., 2012], as shown in Fig. 2.3 (b), and it leads to a dissociation rate:

$$\dot{\rho}_{e+,dip,diss}^\alpha = -\frac{\rho_{e+,dip}^\alpha}{\hat{d}_e^\alpha} \frac{d(\hat{d}_e^\alpha)}{dt} = \frac{\rho_{e+,dip}^\alpha}{|\tau^\alpha|} \frac{d|\tau^\alpha|}{dt}, \quad (2.7)$$

where $\rho_{e+,dip}^\alpha$ is the dipole density, $d(\hat{d}_e^\alpha)/dt$ is the derivative of the dipole stability distance with respect to time and $d|\tau^\alpha|/dt$ is the derivative of the resolved shear stress with respect to time.

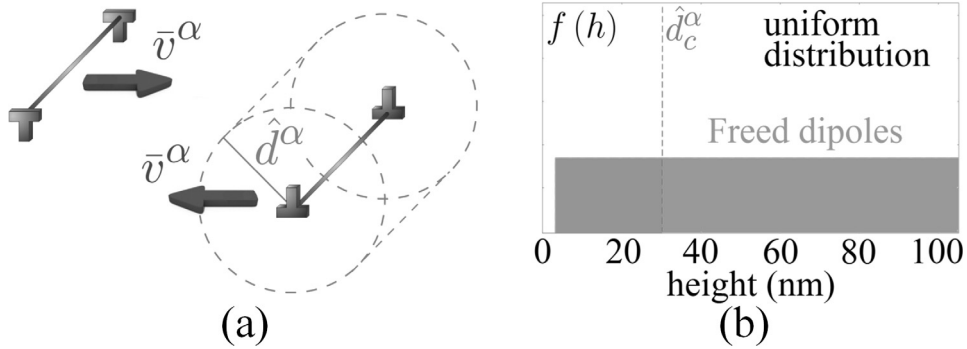


Figure 2.3 – (a) Dislocation dipole formation process; (b) Uniform dipole height distribution.

Dislocation kinetics. The velocity of mobile dislocations is assumed to grow linearly with the applied stress in all our simulations. This approximation has been widely used for the

simulation of FCC crystals [der Giessen and Needleman, 1995]:

$$v^\alpha = B\tau_{\text{eff}}^\alpha = B(|\tau^\alpha| - \tau_{th}^\alpha - \tau_p), \quad (2.8)$$

where B is the drag coefficient, τ^α is the resolved shear stress on the slip system α , τ_{th} is the threshold stress for dislocation motion and τ_p is the Peierls stress, whose values for different materials are reported in Tab. 2.2.

| Material | Copper | Aluminium | 316L steel |
|----------|---------|-----------|------------|
| τ_p | 0.5 MPa | 2.83 MPa | 0.112 MPa |

Table 2.2 – Peierls stress for different materials [Schoeck and Krystian, 2005], [Wang and Fang, 2000], [Misra et al., 2010].

Kinetics equation (2.8) holds for both edge and screw dislocations. The threshold stress τ_{th}^α is given by dislocation interactions on various slip systems:

$$\tau_{th}^\alpha = Gb \sqrt{\sum_{\beta=1}^{12} \xi^{\alpha\beta} \rho^\beta}, \quad (2.9)$$

where $\xi^{\alpha\beta}$ is the matrix representing the strength of interactions between dislocations of slip systems α and β [Arsenlis and Parks, 2002]. In strain controlled simulations the dislocation velocity is determined by the applied plastic strain rate, as stated by the Orowan's law (1.12); the higher the plastic strain rate, the higher the dislocation velocity. The simulation timestep dt should satisfy the Courant–Friedrichs–Lewy condition $vdt < C_{max}\Delta x$, where C_{max} is a constant and Δx is the distance between two integration points [Courant et al., 1928]. This condition limits the computational feasibility of dislocation dynamics simulations and, usually, discrete simulations use higher strain rates (typically 10^4 s^{-1} [Fivel, 2008]) than in experiments in order to reach the desired strain amplitude in a reduced number of simulation steps. The dislocation velocity can also be limited by using higher dislocation densities than in pristine materials [Déprés, 2004]. In this case, given the plastic strain rate, the dislocation velocity is reduced, as stated by the Orowan's law (1.12). Another upper limit of the dislocation velocity is given by the shear sound velocity [Hirth and Lothe, 1982]. A decrease of the total dislocation density in certain elements during the formation of dislocation structures is observed because of dislocation fluxes, leading to very high values of the dislocation velocity, as determined by (2.8). For this reason a maximum velocity v_{max} is set in our simulations to prevent numerical divergence without decreasing dt . This choice does not affect simulation results, provided that the resolved shear stress $|\tau^\alpha|$ in (2.8) is not much higher than $(\tau_{th}^\alpha + \tau_p)$, because in that case the dislocation velocity, and consequently the plastic strain rate in low dislocation density regions, would be underestimated.

Chapter 2. Single slip dislocation-based model

| | | | | |
|------------------|------------------|------------------|------------------------------|----------------|
| $\rho_{e+}(t=0)$ | $\rho_{e-}(t=0)$ | $\rho_{s+}(t=0)$ | $\rho_{s-}(t=0)$ | \bar{l}_{e+} |
| $1.0 \mu m^{-2}$ | $1.0 \mu m^{-2}$ | $1.0 \mu m^{-2}$ | $1.0 \mu m^{-2}$ | $10 \mu m$ |
| \bar{l}_{e-} | \bar{l}_{s+} | \bar{l}_{s-} | B | v_{max} |
| $10 \mu m$ | $10 \mu m$ | $10 \mu m$ | $5 \cdot 10^4 (\mu m/s)/MPa$ | $1 m/s$ |

Table 2.3 – Simulation parameters.

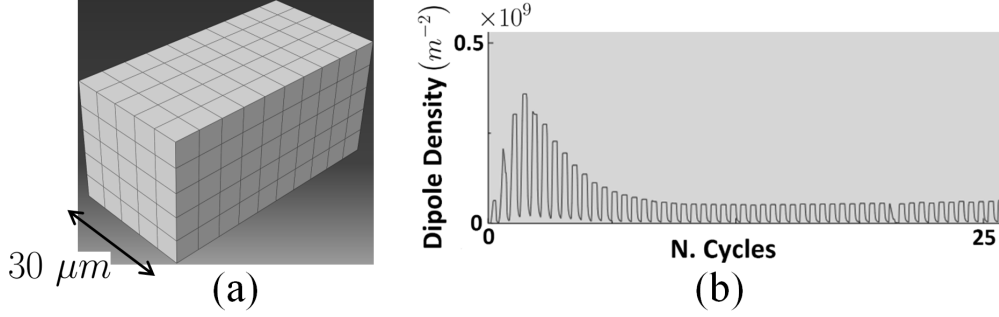


Figure 2.4 – (a) Representative volume and mesh used to test the existing physics-based model; (b) Dislocation dipole density in one element.

Using the aforementioned dislocation processes cyclic deformation simulations have been carried out in a small representative volume as shown in Fig. 2.4 (a), and using the parameters in Tab. 2.3. The characteristic behaviour of the dislocation dipole density, shown in Fig. 2.4 (b), is ruled by the two mechanisms (formation and dissociation) described by (2.6) and (2.7). Dipoles, created by glide when the stress is maximum, are almost completely eliminated in the next half cycle because of dissociation by stress increase. This is due to the assumption made in existing models of uniform dipole height distribution [Roters et al., 2012]. When the stress goes from zero to its maximum value, the majority of dipoles are freed, as can be seen in Fig. 2.3 (b). Such dipole density oscillations preclude the identification of dislocation structures in the model. The multiplication and annihilation laws (2.5) and (2.2)-(2.3) predict a monotonic increase of dislocation density until the two mechanisms are balanced. In this case the edge and screw dislocation density at saturation become:

$$\rho_e(\text{saturation}) = 2.8 \cdot 10^{14} \text{ m}^{-2}, \quad (2.10)$$

$$\rho_s(\text{saturation}) = 9.1 \cdot 10^{13} \text{ m}^{-2}. \quad (2.11)$$

These densities are spread uniformly throughout the model because the Arsenlis multiplication law is based on averaging volumes larger than the channel spacing. Edge dislocations are created wherever screw ones are present, according to (2.5), thus any initial inhomogeneities in the edge dislocation density is removed. This prevents the formation of dislocation patterning, leading to a high and homogeneous threshold stress, and to an elastic shakedown at saturation, as shown by the hardening curve in Fig. 2.5, simulated at 0.2 % strain amplitude. This is not experimentally observed at that strain amplitude and the lack of low density channels, accommodating plastic strain, is causing this inconsistency.

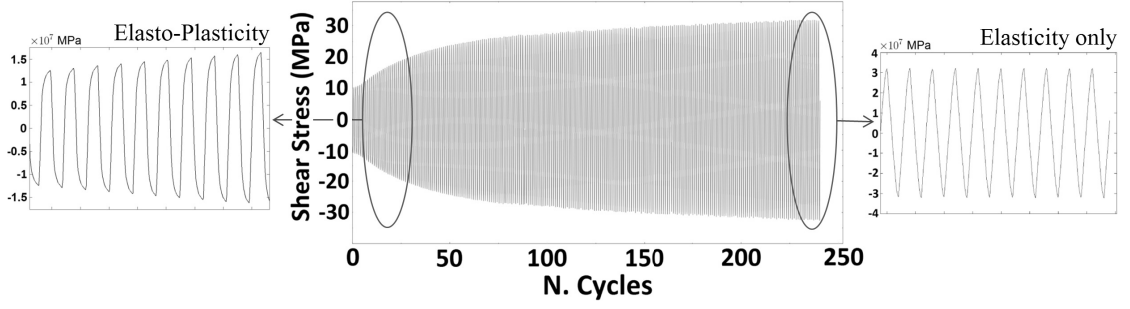


Figure 2.5 – Simulated stress-strain curve during cyclic fatigue at 0.2 % strain amplitude and $2 \cdot 10^{-3} \text{ s}^{-1}$ strain rate.

2.2 Single slip model for cyclic fatigue

In this section the new laws, developed for cyclic fatigue, are applied to the simulation of single slip deformation of single crystals.

Gaussian dipole distance distribution. To calculate the fraction of mobile dislocations a Gaussian dipole distance distribution is used, as shown in Fig. 2.6 (a). Indeed, it has been shown experimentally (Fig. 2.6 (b)) and confirmed by discrete dislocation dynamics [Déprés et al., 2008] that during cyclic deformation the fraction of dislocations forming a dipole with height h (and stability distance given by (1.10)) is given by the distribution:

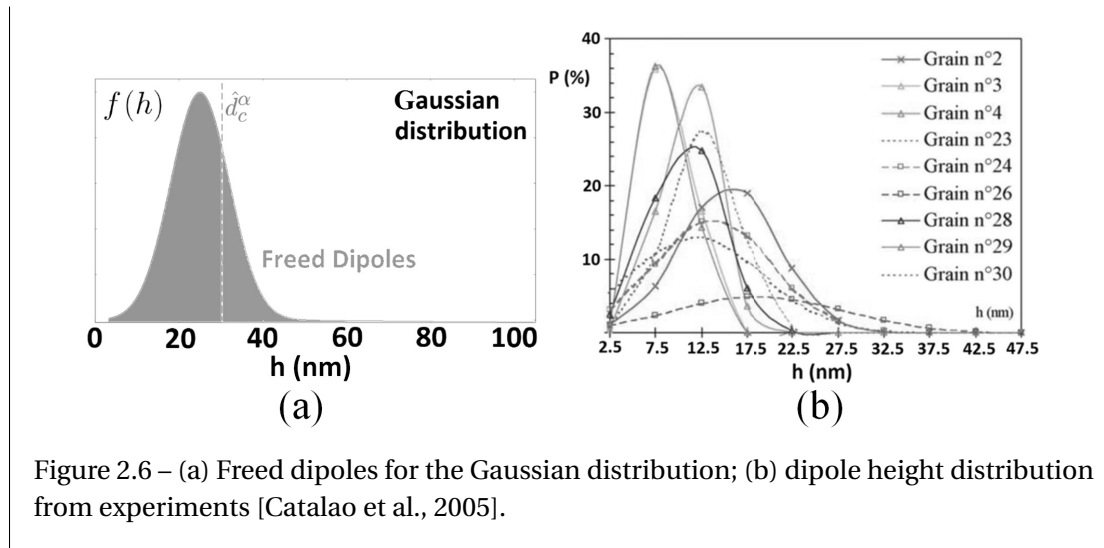
$$f_c(h) \propto \exp\left(-\left(\frac{h - \bar{h}_c}{0.467\bar{h}_c}\right)^2\right), \quad (2.12)$$

where c is the dislocation character (edge or screw). The mean \bar{h}_c of the Gaussian distribution as a function of the total dislocation density $\rho_{total,c}$ with character c [Catalao et al., 2005] is:

$$\bar{h}_e = \frac{1}{8\pi\alpha(1-\nu)\sqrt{\rho_{total,e}}}, \quad (2.13)$$

$$\bar{h}_s = \frac{1}{8\pi\alpha\sqrt{\rho_{total,s}}}, \quad (2.14)$$

where $\alpha \approx 0.3$ is a constant. Dislocations in veins, where the density is higher, have a smaller mean distance \bar{h}_c than in channels. By introducing the actual Gaussian distribution not all dipoles are freed when the stress is increased from zero to its maximum value, as shown in Fig. 2.6 (a).



Dislocation multiplication law for cyclic plasticity. When a finite element size is chosen smaller than $1 \mu\text{m}$, which is the characteristic spacing between two veins (Fig. 2.2), a loop dislocation segment occupies several neighbouring elements, as shown in Fig. 2.7 (a). The dislocation orientation becomes important and separate geometrical configurations, which are indicated as “straight” and “curved” in Fig. 2.7, need to be considered. Assuming that the dislocation speed is approximately constant within a single element, and assuming that the segments are convex, “straight” dislocation segments entering an element from opposite sides (Fig. 2.7 (b)) do not generate longer dislocation segments when they travel through the element. This is because the two intersections of the dislocation segment with the element boundary (dashed circles in Fig. 2.7 (b)) move at the same speed in the same direction, thus the “straight” segment keeps approximately the same shape while moving. By contrast, dislocation segments which enter the element from neighbouring sides (“curved” in Fig. 2.7 (c)) increase their length during motion (dislocation multiplication) because the two intersections of the dislocation segment with the element boundaries (dashed circles in Fig. 2.7 (c)) move in different directions while the segment must remain connected.

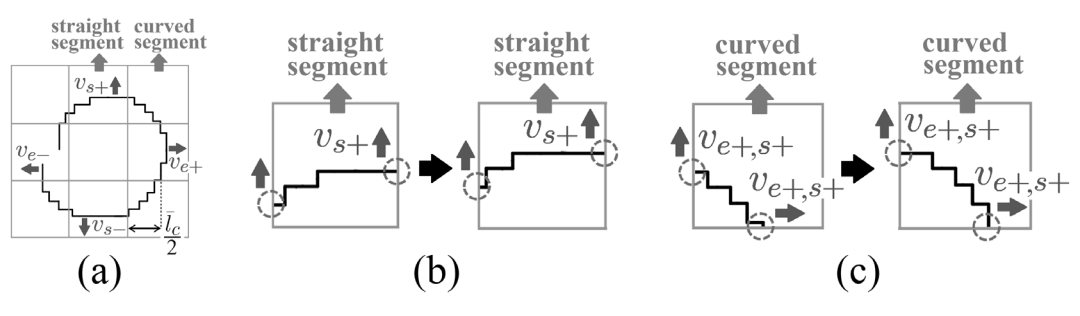


Figure 2.7 – (a) New dislocation multiplication law when one dislocation loop occupies more elements; (b)-(c) time evolution of “straight” and “curved” dislocation segments.

The multiplication law we propose for cyclic plasticity differentiates between these two types of dislocation segments. A total of 8 density variables, listed in Tab. 2.4, are thereby introduced. The 4 densities in the top row are used to describe “straight” segments, the other 4 densities describe “curved” ones. For example, the density $\rho_{e+,s+}$ describes segments that are formed from positive edge and screw dislocations.

| | | | |
|----------------|----------------|----------------|----------------|
| ρ_{e+} | ρ_{e-} | ρ_{s+} | ρ_{s-} |
| $\rho_{e+,s+}$ | $\rho_{e+,s-}$ | $\rho_{e-,s+}$ | $\rho_{e-,s-}$ |

Table 2.4 – Dislocation densities used for the cyclic fatigue multiplication law.

In terms of dislocation structures, “curved” dislocations are expected to be located close to the vein-channel interface. For one “curved” dislocation segment of the type $\rho_{e+,s+}$, as in Fig. 2.7 (c), the increase rate of the length of positive edge dislocation line is given by the velocity $|v_{e+,s+}|$. The same can be stated for segments of the type $\rho_{e+,s-}$. The number of “curved” segments of the type $\rho_{e+,s+}$ per unit volume is the ratio between their density $\rho_{e+,s+}$ and their average length \bar{l}_c . Therefore the multiplication law for ρ_{e+} is:

$$\dot{\rho}_{e+,mult} = \frac{\rho_{e+,s+}|v_{e+,s+}|}{\bar{l}_c} + \frac{\rho_{e+,s-}|v_{e+,s-}|}{\bar{l}_c}. \quad (2.15)$$

Similar equations hold for the other “straight” dislocation densities. This multiplication law can be derived from the general continuum dislocation dynamics theory [Hochrainer et al., 2014], whose state variable is a dislocation density $\rho(p, \varphi)$ that measures, at a point with coordinates p , the area density of dislocations with line direction $\mathbf{l}(\varphi) = (\cos \varphi, \sin \varphi, 0)$. The following time evolution equation holds [Hochrainer et al., 2014]:

$$\partial_t \rho(p, \varphi) = -\nabla \cdot (\rho(p, \varphi) \vec{v}(p, \varphi)) - \partial_\varphi (\rho(p, \varphi) \omega_\varphi(p, \varphi)) + v(p, \varphi) q(p, \varphi), \quad (2.16)$$

where $q(p, \varphi)$ is the curvature density and $\omega_\varphi(p, \varphi)$ is the angular velocity. An integration of $\rho(p, \varphi)$ over specific angular intervals, using weight functions, can be used to define a set of state variables for a constitutive theory. In the so-called *simplified continuum dislocation dynamics* (sCDD) the first-order terms of the Fourier expansion of $\rho(p, \varphi)$ are used as state variables [Hochrainer et al., 2014], while in this thesis a simplifying assumption on the dislocation curvature is taken because of the specific dislocation structure geometry in Fig. 2.8 (a). An angle $\Delta\theta_{e+,s+}$, whose value is close to $\pi/2$, has been chosen to define $\rho_{e+,s+}$ and a corresponding angular interval $[\theta_1, \theta_2] = [-\pi/4 - \Delta\theta_{e+,s+}/2, -\pi/4 + \Delta\theta_{e+,s+}/2]$:

$$\rho_{e+,s+}(p) = \int_{\theta_1}^{\theta_2} \rho(p, \varphi) d\varphi. \quad (2.17)$$

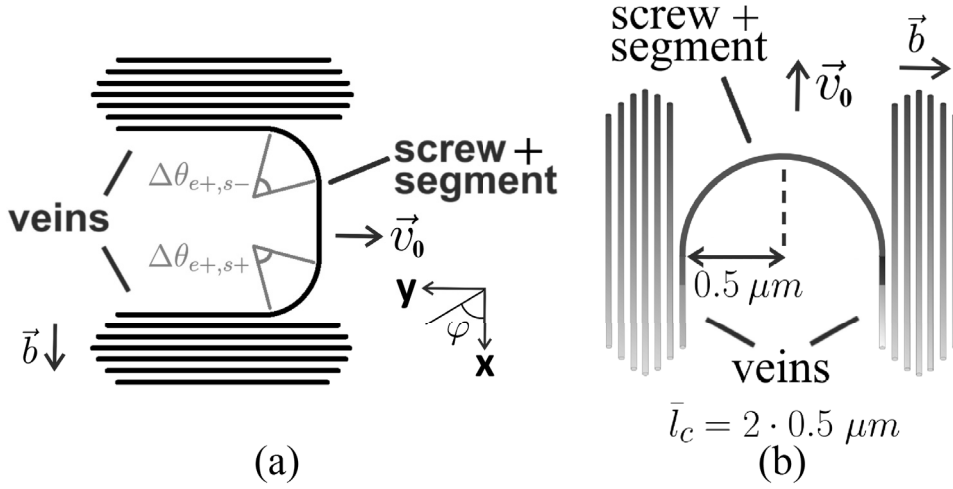


Figure 2.8 – (a) Angular intervals $\Delta\theta_{e+,s+}$ and $\Delta\theta_{e-,s+}$ used to define the dislocation densities in the model; (b) screw dislocation configuration inside a channel if the curvature radius is around half of the channel width.

Integrating (2.16) on the same interval:

$$\dot{\rho}_{e+,s+} = - \int_{\theta_1}^{\theta_2} \nabla \cdot (\rho(p, \varphi) \vec{v}(p, \varphi)) d\varphi - \left| \rho(p, \varphi) \omega_\varphi(p, \varphi) \right|_{\theta_1}^{\theta_2} + \int_{\theta_1}^{\theta_2} q(p, \varphi) v(p, \varphi) d\varphi. \quad (2.18)$$

The main hypothesis introduced is a constant value $\bar{k} = (\pi/2) / \bar{l}_c$ of the average curvature in the interval $[\theta_1, \theta_2]$. In order to satisfy that hypothesis it is necessary that the dislocation velocity decreases, reaching zero, toward the vein-channel interface because of the interaction between the moving curved dislocation and the vein. A simple assumption, which satisfies also the time evolution equation of the dislocation curvature [Hochrainer et al., 2014], is $v = -v_0 \sin \varphi$. The third term on the right-hand side of (2.18) becomes:

$$-v_0 \int_{\theta_1}^{\theta_2} q(p, \varphi) \sin \varphi d\varphi = v_0 \bar{k} \left(\frac{\rho_{e+,s+}(p)}{\pi/2} \right). \quad (2.19)$$

This term gives the contribution of the loop expansion of curved dislocations. The angular velocity is $\omega_\varphi(p, \varphi) = -\hat{\nabla}_{\mathbf{L}} v$, which is the directional derivative of the scalar velocity along the generalized line direction [Hochrainer et al., 2014]. The generalized line direction is defined for a dislocation as a 6D vector $\mathbf{L} = (\mathbf{I}(\varphi), \mathbf{k}(\varphi))$, where $\mathbf{I}(\varphi)$ is the line direction and $\mathbf{k}(\varphi)$ is the curvature vector, which is the unit normal vector of the dislocation line multiplied by the scalar curvature. In this particular case, ω_φ is given by:

$$\omega_\varphi(p, \varphi) = -\bar{k} \partial_\varphi v = \bar{k} v_0 \cos \varphi, \quad (2.20)$$

hence it is finite at θ_2 but zero at θ_1 . Thus the second term on the right-hand side of (2.18) is:

$$|\rho(p, \varphi) \omega_\varphi(p, \varphi)|_{\theta_1}^{\theta_2} = v_0 \bar{k} \left(\frac{\rho_{e+,s+}(p)}{\pi/2} \right), \quad (2.21)$$

which is exactly cancelled out by the term in (2.19). This implies that the time evolution of $\rho_{e+,s+}$ is given by the flux term only. The evolution equation of a density of “straight” dislocations, for instance ρ_{e+} , can be found similarly by integrating 2.16 on an interval $[\theta_2, \theta_3] = [-\pi/4 + \Delta\theta_{e+,s+}/2, \pi/4 - \Delta\theta_{e+,s-}/2]$:

$$\dot{\rho}_{e+}(p) = - \int_{\theta_2}^{\theta_3} \nabla \cdot (\rho(p, \varphi) \bar{v}(p, \varphi)) d\varphi - |\rho(p, \varphi) \omega_\varphi(p, \varphi)|_{\theta_2}^{\theta_3}. \quad (2.22)$$

The third term on the right-hand side of (2.16) is absent because, in this angular interval, the curvature is zero. Using (2.21) and the corresponding equation for $\rho_{e+,s-}$, one finds:

$$\dot{\rho}_{e+}(p) = - \int_{\theta_2}^{\theta_3} \nabla \cdot (\rho(p, \varphi) \bar{v}(p, \varphi)) d\varphi + \frac{v_0 \rho_{e+,s+}(p)}{\bar{l}_c} + \frac{v_0 \rho_{e+,s-}(p)}{\bar{l}_c}. \quad (2.23)$$

The last two terms represent the new multiplication law (2.15), while the first term is the dislocation flux of positive edge dislocations, also considered in the model.

Determination of the value of the average curvature from first principle would require computationally expensive simulations using the higher order dislocation density theory [Hochrainer et al., 2014]. However, microscopy images [Winter, 1978], [Winter et al., 1981], [Kuhlmann-Wilsdorf and Laird, 1977] show screw dislocations nearly straight in the middle of the channel. The channel width is around 1 μm , therefore, using a value $\bar{l}_c = 1 \mu\text{m}$, screw dislocations would have a circular shape inside the channels, as shown in Fig. 2.8 (b). This is not consistent with experimental observations, therefore an upper limit is:

$$\bar{l}_c \ll 1 \mu\text{m}. \quad (2.24)$$

The new multiplication law is tested on a simple system with two interacting dislocation segments, as shown in Fig. 2.9. One straight edge dislocation is kept immobile. A second dislocation segment has a edge part, forming a dislocation dipole with the first dislocation, and a screw part. “Curved” dislocation density is present at the intersection between the edge and the screw segment. When a resolved shear stress is applied the screw dislocation move towards the left in Fig. 2.9. Therefore the edge dislocation density increases in the elements that contain the immobile edge segment and, after the transit of the “curved” density, it has doubled in value. This indicates that two edge dislocations are present in those elements and this reproduces the behaviour of the equivalent discrete system.

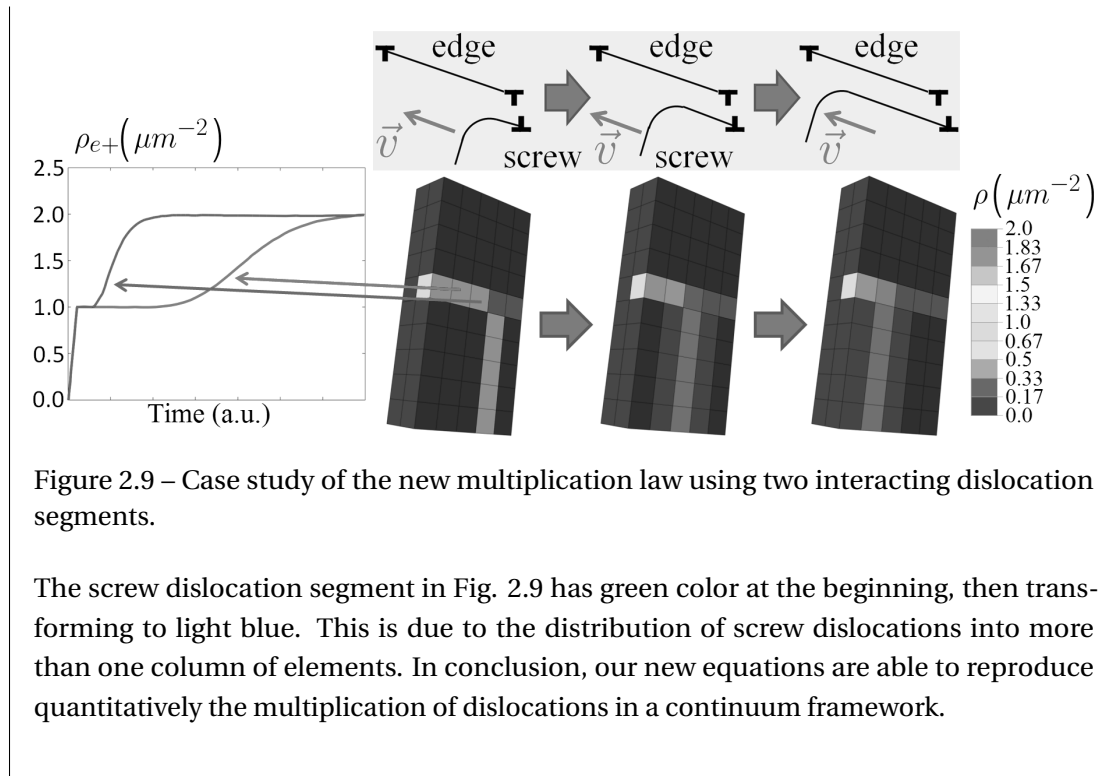


Figure 2.9 – Case study of the new multiplication law using two interacting dislocation segments.

The screw dislocation segment in Fig. 2.9 has green color at the beginning, then transforming to light blue. This is due to the distribution of screw dislocations into more than one column of elements. In conclusion, our new equations are able to reproduce quantitatively the multiplication of dislocations in a continuum framework.

Cross slip law. The new multiplication law (2.15) does not predict an increase of the “curved” dislocation densities because the annihilation laws (2.2)-(2.3) are applied to both “straight” and “curved” segments. The complete annihilation of oppositely signed “curved” dislocations, which would interrupt the dislocation multiplication process, is prohibited by cross slip. Therefore one needs to introduce this process in the model equations. The double cross slip process has been recognized as a major multiplication mechanism in FCC metals [Bitzek et al., 2008], [Messerschmidt and Bartsch, 2003]. A simple model for double cross slip needs to consider that the process occurs at locations where screw dislocations are present. A length w of such dislocations on the primary slip system transfers to a parallel slip plane and then it multiplies as a Frank-Read source, as depicted in Fig. 2.10 (a). In terms of the dislocation densities defined in Tab. 2.4, this mechanism converts a length w of a “straight” screw segment into a dislocation loop formed by “curved” segments, as shown in Fig. 2.10 (b), whose average length is \bar{l}_c .

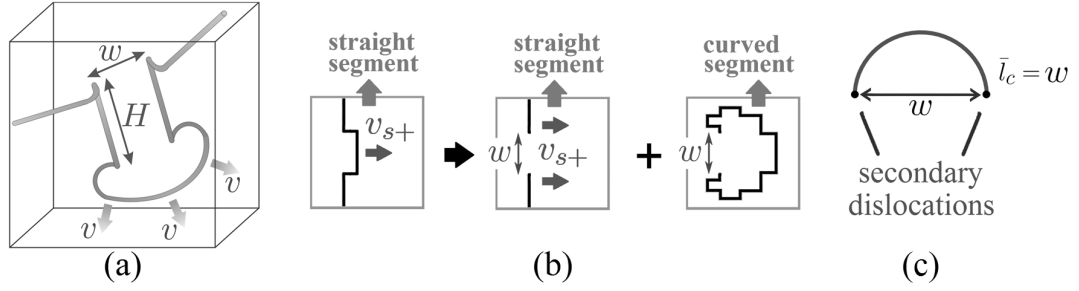


Figure 2.10 – (a) Double cross slip mechanism; (b) Time evolution of a “straight” dislocation segment during double cross slip; (c) dislocation loop expanding after a double cross slip event.

The cross slip rate is given by [Vegge et al., 2000]:

$$R = \nu \exp\left(-\frac{\tau_{III} V_{act}}{kT}\right) = \nu \exp\left(-\frac{\Delta G}{kT}\right), \quad (2.25)$$

where τ_{III} is the stage three stress, V_{act} is the activation volume, ν is the attack frequency and ΔG is the activation energy. Parameters used in our simulations for different materials are reported in Tab. 2.5.

| Material | τ_{III} | V_{act} | ΔG |
|------------|--------------|-----------------------------------|------------|
| Copper | 37 MPa | $4.97 \cdot 10^{-27} \text{ m}^3$ | 1.15 eV |
| Aluminium | 15 MPa | $8.84 \cdot 10^{-27} \text{ m}^3$ | 0.829 eV |
| 316L steel | 56 MPa | $5 \cdot 10^{-27} \text{ m}^3$ | 1.75 eV |

Table 2.5 – Material parameters to calculate the cross slip rate [Bonneville et al., 1988], [Groh et al., 2009], [Déprés et al., 2008].

The width w in Fig. 2.10 depends on the applied stress, however it is typically lower than 100 nm [Escaig, 1968] and thus the double cross slip can be described using a local law in our model if an element size of around 200 nm is used. The same is true for the height H [Appel et al., 1982]. The attack frequency $\nu \approx 2 \cdot 10^{15} \text{ s}^{-1}$ has been deduced from molecular dynamics simulations [Vegge et al., 2000]. Once the double cross slip process has taken place, the curved segment expands, as shown in Fig. 2.10 (b), until a dislocation loop, whose average length is \bar{l}_c , is formed. The double cross slip mechanism usually emits only a single new dislocation loop [Messerschmidt and Bartsch, 2003], therefore the number of loops created per unit volume during an infinitesimal time interval dt is:

$$\frac{d\rho_{cs}}{w} = \frac{(\rho_{s+} + \rho_{s-}) R dt}{w}, \quad (2.26)$$

where $d\rho_{cs}$ is the density of screw dislocation segments that cross slipped. The density of new “curved” dislocations is:

$$d\rho_{e+,s+,cs} = \frac{\bar{l}_c d\rho_{cs}}{w} = \frac{(\rho_{s+} + \rho_{s-}) \bar{l}_c R dt}{w}, \quad (2.27)$$

and similar equations hold for the other “curved” densities. The length w is stress dependent, but typically of the same order as the dissociation width [Escaig, 1968], which can be estimated by $w \approx 44b$. Therefore:

$$\dot{\rho}_{e+,s+,cs} = \left(\frac{\bar{l}_c R}{44b} \right) \cdot (\rho_{s+} + \rho_{s-}) . \quad (2.28)$$

Multiplying and dividing (2.28) by the dislocation velocity $|v_{e+,s+}|$:

$$\dot{\rho}_{e+,s+,cs} = \left(\frac{\bar{l}_c}{|v_{e+,s+}|} \right) \left(\frac{R}{44} \right) \frac{|v_{e+,s+}|}{b} \cdot (\rho_{s+} + \rho_{s-}) . \quad (2.29)$$

The fraction $\bar{l}_c/|v_{e+,s+}|$ is the characteristic expansion time t_c for a dislocation loop, created by double cross slip. In the following we assume this fraction is a constant because the maximum shear stress, and consequently the maximum dislocation velocity, does not change significantly after the hardening stage in the first cycles. In our single slip simulations, a characteristic velocity $|v_{e+,s+}| \approx 1 \mu\text{m/s}$ follows from the chosen strain rate. Defining:

$$\beta = \frac{R t_c}{44} , \quad (2.30)$$

the following cross slip equation can be obtained:

$$\dot{\rho}_{e+,s+,cs} = \frac{\beta |v_{e+,s+}|}{b} \cdot (\rho_{s+} + \rho_{s-}) . \quad (2.31)$$

For every cross slip event a line length $2H$ of secondary dislocations is created, as depicted in Fig. 2.10 (a). During an infinitesimal time interval dt , the number of these events per unit volume is given by (2.26). Therefore, the density increase of secondary dislocations is:

$$d\rho_{sec} = 2H \left(\frac{d\rho_{cs}}{w} \right) . \quad (2.32)$$

Using (2.26) and (2.32), a rate equation for the secondary dislocation density ρ_{sec} can be found:

$$\dot{\rho}_{sec} = \frac{2HR}{w} (\rho_{s+} + \rho_{s-}) . \quad (2.33)$$

The characteristic value $H \approx 100 \text{ nm}$ [Appel et al., 1982] has been used in our simulations. The double cross slip mechanism imposes a lower limit for the average segment length \bar{l}_c . Equation (2.27) is valid if the curved part of the dislocation loop in Fig. 2.10 (b), for instance the part representing $\rho_{e+,s+}$, has average length \bar{l}_c . This length cannot be smaller than the diameter of a circle, whose radius is $w/2$, because, as shown in Fig. 2.10 (c), the curved segment connects the two secondary dislocations. Therefore, a lower limit for copper is:

$$\bar{l}_c \gg w \approx 0.011 \mu\text{m} . \quad (2.34)$$

In our simulations a value $\bar{l}_c = 0.1 \mu\text{m}$, intermediate between the two limits (2.24) and (2.34), has been chosen. As a consequence, a characteristic expansion time $t_c \approx 0.1 \text{ s}$ in (2.30) is used in our simulations.

The values of the cross slip coefficient β in (2.31) for different materials are reported in Tab. 2.6.

| Material | β |
|------------|----------------------|
| Copper | $8 \cdot 10^{-8}$ |
| Aluminium | $2.6 \cdot 10^{-2}$ |
| 316L steel | $1.7 \cdot 10^{-18}$ |

Table 2.6 – Material parameters to calculate the cross slip rate coefficient β .

The uncertainty on β is due to the experimental errors of τ_{III} , around $\pm 3 \%$, and V_{act} , around $\pm 4 \%$ [Bonneville et al., 1988]. An error of $\pm 7 \%$ of the product $\tau_{III}V_{act}$ is increased by the exponential function in (2.25) and thus we expect an uncertainty of one order of magnitude on β .

The constitutive equations of the single slip model for cyclic fatigue are summarized in appendix A.1.

2.3 Eigenvalue analysis

A condition for the appearance of dislocation patterning from a randomly perturbed, initially homogeneous distribution of dislocations, is the instability of the stationary state [Groma and Balogh, 1999]. If ρ_0 is the stationary state of the function g in (2.1), then $g(\rho_0) = 0$. The stationary state corresponds to a uniformly dislocation filled system. Near equilibrium a Fourier component of the solution can be written as:

$$\rho(\vec{r}, t) = \rho_0 + \Delta\rho \cdot \exp(\omega_q t + i\vec{q} \cdot \vec{r}), \quad (2.35)$$

where \vec{q} represents a specific spatial wavelength while ω_q gives the time evolution: if $\omega_q > 0$ a particular wavelength of the solution is increasing its amplitude and eventually a patterning can form, while if $\omega_q < 0$ a spatially uniform solution arises. The amplitude $\Delta\rho$ is a vector constituted of fluctuations of all the dislocation densities of the model:

$$\Delta\rho = (\Delta\rho_{e+}, \Delta\rho_{e-}, \Delta\rho_{s+}, \Delta\rho_{s-}, \Delta\rho_{e+,s+}, \Delta\rho_{e+,s-}, \Delta\rho_{e-,s+}, \Delta\rho_{e-,s-}). \quad (2.36)$$

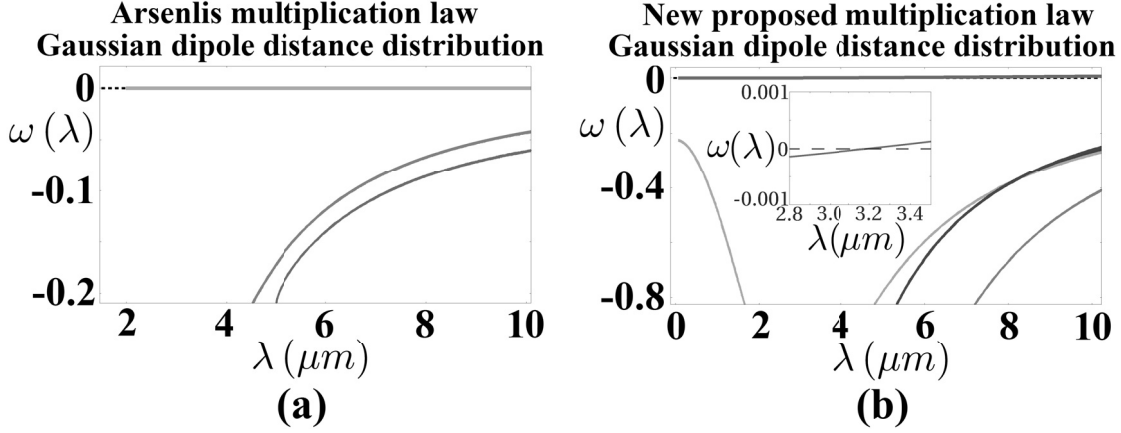


Figure 2.11 – Values of ω_q in (2.35) as a function of the patterning wavelength λ , different colors correspond to different eigenvalues.

If the solution (2.35)-(2.36) is introduced into the time evolution equation (2.1) and only first order terms in $\Delta\rho$ are considered, then the following eigenvalue problem is obtained:

$$\omega_q \begin{pmatrix} \Delta\rho_{e+} \\ \Delta\rho_{e-} \\ \Delta\rho_{s+} \\ \Delta\rho_{s-} \\ \Delta\rho_{e+,s+} \\ \Delta\rho_{e+,s-} \\ \Delta\rho_{e-,s+} \\ \Delta\rho_{e-,s-} \end{pmatrix} = \mathbf{M} \cdot \begin{pmatrix} \Delta\rho_{e+} \\ \Delta\rho_{e-} \\ \Delta\rho_{s+} \\ \Delta\rho_{s-} \\ \Delta\rho_{e+,s+} \\ \Delta\rho_{e+,s-} \\ \Delta\rho_{e-,s+} \\ \Delta\rho_{e-,s-} \end{pmatrix}, \quad (2.37)$$

where the components of the 8x8 matrix \mathbf{M} are given by:

$$\mathbf{M}_{ij} = \frac{\partial g_i}{\partial \rho_j}, \quad (2.38)$$

where i and j are the indices of the vectors $\dot{\rho}$ and ρ in (2.1). The eigenvalue problem 2.37 has been solved numerically. The eight eigenvalues ω_q are functions of the spatial wavelength $\lambda = \frac{2\pi}{|\vec{q}|}$, which is present in the matrix \mathbf{M} because of the spatial derivatives introduced by the flux term in (1.13). They are calculated in Fig. 2.11 (a) using the Arsenlis multiplication law (2.5), and in Fig. 2.11 (b) using both the new multiplication law (2.15) and cross slip law (2.5). In both cases the annihilation laws (2.2)-(2.3) and the Gaussian dipole distance distribution (2.12) have been used. Copper parameters are used in the analysis and the strain amplitude is $\gamma = 0.1\%$. It is evident that all the eigenvalues for the Arsenlis law are negative, apart from a zero eigenvalue which corresponds to a fluctuation of screw densities only, and thus no patterning can arise from an initial uniform dislocation distribution. That is not the case for the new multiplication law, for which one of the eigenvalues is positive above a certain λ , as shown in the inset of Fig. 2.11 (b). That eigenvalue remains positive even if the value of β is increased or

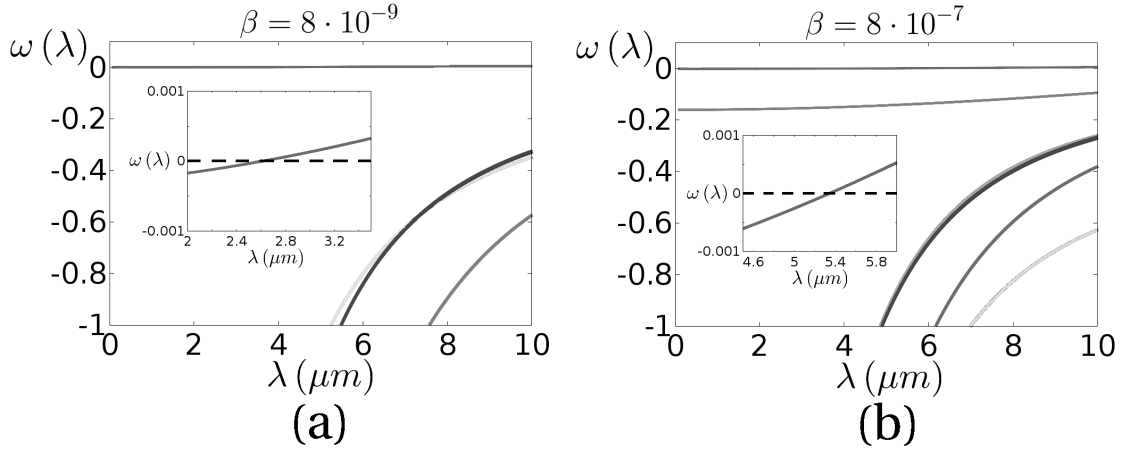


Figure 2.12 – Values of ω_q in (2.35) as a function of the patterning wavelength λ for $\beta = 8 \cdot 10^{-9}$ and $\beta = 8 \cdot 10^{-7}$, different colors correspond to different eigenvalues.

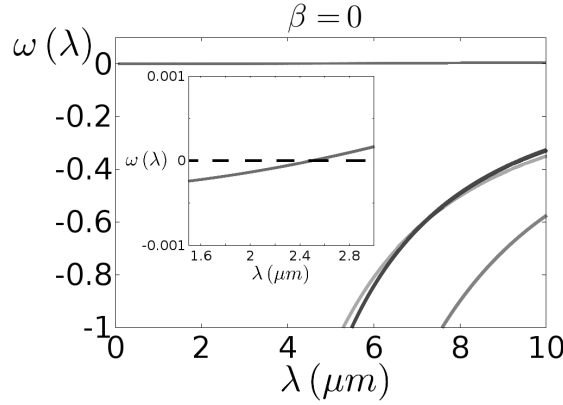


Figure 2.13 – Values of ω_q in (2.35) as a function of the patterning wavelength λ for $\beta = 0$.

decreased by an order of magnitude with respect to the one for copper, as shown in Fig. 2.12. This shows that our theory can predict dislocation patterning without fine tuning β , which has a large uncertainty. This eigenvalue analysis has shown that the Arsenlis law is not suitable to model patterning because it leads to a spatially uniform dislocation distribution. By contrast the new multiplication law has a positive eigenvalue and thus a spatially periodic solution can arise. The cross slip coefficient affects the values of ω_q in (2.35), as shown in Fig. 2.12. However, if the model is used without cross slip ($\beta = 0$), one positive eigenvalue is still present, as shown in Fig. 2.13. This indicates that the new multiplication law is sufficient to predict dislocation patterning. A specific value for the developing wavelength cannot be deduced from Fig. 2.11 (b) and a simulation in the time domain is necessary. However, eigenvalue analyses using different model parameters can show which wavelengths λ increase their amplitudes. In Fig. 2.14 the values of ω_q are shown for two different strain amplitudes γ . The eigenvalue that becomes positive cross the $\omega_q = 0$ axis at a wavelength $\lambda \approx 2.2 \mu\text{m}$ for $\gamma = 0.2\%$ and $\lambda \approx 1.8 \mu\text{m}$ for $\gamma = 0.3\%$. The same eigenvalue becomes positive at $\lambda \approx 3.2 \mu\text{m}$ for $\gamma = 0.1\%$, as shown in Fig. 2.11 (b). These different analyses are consistent with the similitude principle, according to

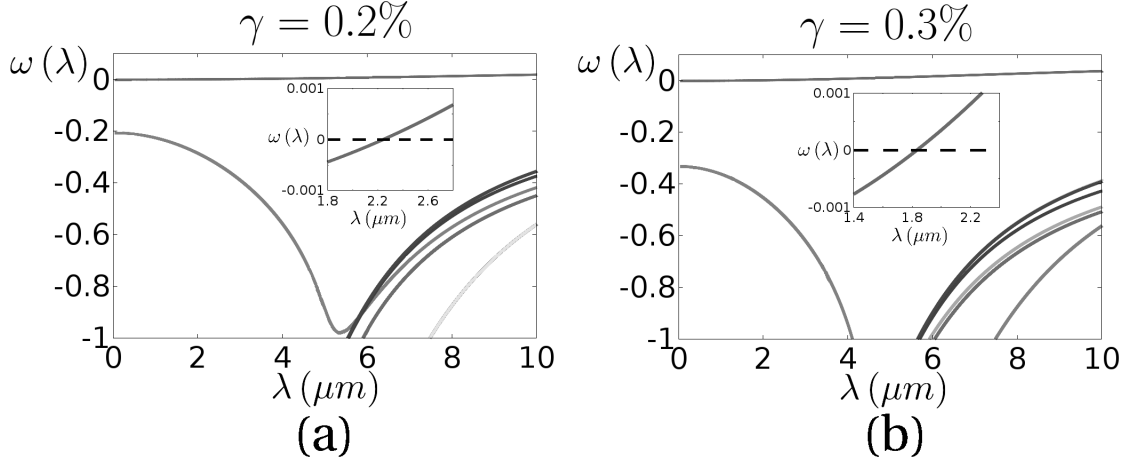


Figure 2.14 – Values of ω_q in (2.35) as a function of the patterning wavelength λ for $\gamma = 0.2\%$ and $\gamma = 0.3\%$, different colors correspond to different eigenvalues.

which the characteristic wavelength of dislocation structures during cyclic fatigue is inversely proportional to the loading amplitude [Sauzay and Kubin, 2011].

2.4 Single slip simulations

Cyclic deformation simulations of a copper single crystal oriented for single slip have been carried out using an element size of 200 nm on a parallelepiped geometry whose size is 12 μm along the x and y directions and 0.6 μm along z , as shown in Fig. 2.15. The slip plane (111) is oriented perpendicular to the z axis and the Burgers vector along the x axis. Cyclic shear deformation with a strain amplitude $\gamma_{xz} = 0.1\%$ is applied along the Burgers vector direction, as shown in Fig. 2.15 (a). The strain rate is 10^{-3} s^{-1} . Periodic boundary conditions are used for dislocation fluxes along the y axis and the secondary dislocation density in (2.33) is not included. Average values of initial dislocation densities and kinetic parameters in the simulations are summarized in Tab. 2.7. Random fluctuations of $\delta\rho = 50\%$ are added to this uniform distribution. These fluctuations depend on the spatial position and they are generated randomly using the method described in the following. A random Halton sequence [Halton, 1964] of 2-dimensional vectors $(\text{rnd}_1, \text{rnd}_2)$ in $(0, 1) \times (0, 1)$ is generated. For every 2-dimensional vector of the sequence, the condition:

$$\text{rnd}_2 < \exp\left(-\frac{1}{2} [3(2 \cdot \text{rnd}_1 - 1)]^2\right), \quad (2.39)$$

is checked. If (2.39) is satisfied, then the initial dislocation density with character c at the integration point i is:

$$\rho_c(i) = \rho_c(t=0) \cdot [1 + \delta\rho(3(2 \cdot \text{rnd}_1 - 1))]. \quad (2.40)$$

2.4. Single slip simulations

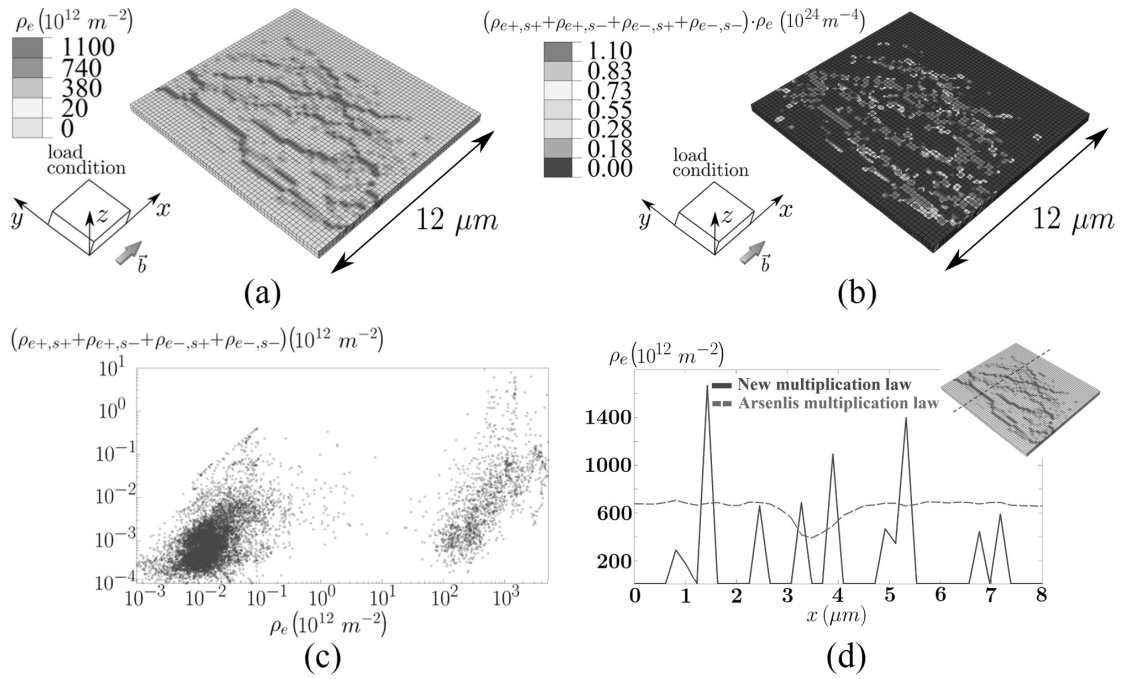


Figure 2.15 – (a) Edge dislocation density after 100 cycles using the new multiplication law; (b) product between the total “curved” and edge dislocation density after 100 cycles using the new multiplication law; the patterning is similar to the one in (a); (c) scatter plot of the “curved” dislocation density as a function of the edge dislocation density in every element; (d) edge dislocation density along the dashed line passing through the geometry in the inset. In (a) and (b) the scales are different because of the different magnitude of the edge and “curved” dislocation density.

Chapter 2. Single slip dislocation-based model

The integration point index i is the same as in the input file of the finite element solver (Abaqus) and it is increased until the dislocation density is assigned to all the integration points. According to (2.39)-(2.40) the dislocation density fluctuations at the integration points have a Gaussian distribution with standard deviation $\delta\rho$. At every integration point, the fluctuation $\delta\rho$ is the same for every dislocation type in the model. Thus, the Kröner-Nye tensor of the initial dislocation distribution is zero at every point and connectivity of dislocation lines is satisfied.

| | |
|---|---|
| $\rho_{e+}(t=0) = 1.0 \mu\text{m}^{-2}$ | $\rho_{e-}(t=0) = 1.0 \mu\text{m}^{-2}$ |
| $\rho_{s+}(t=0) = 1.0 \mu\text{m}^{-2}$ | $\rho_{s-}(t=0) = 1.0 \mu\text{m}^{-2}$ |
| $\rho_{e+,s+}(t=0) = 0.01 \mu\text{m}^{-2}$ | $\rho_{e+,s-}(t=0) = 0.01 \mu\text{m}^{-2}$ |
| $\rho_{e-,s+}(t=0) = 0.01 \mu\text{m}^{-2}$ | $\rho_{e-,s-}(t=0) = 0.01 \mu\text{m}^{-2}$ |
| $B = 1.0 (\mu\text{m/s})/\text{MPa}$ | $v_{max} = 10 \mu\text{m/s}$ |
| $\bar{l}_{e+} = 1.0 \mu\text{m}$ | $\bar{l}_{e-} = 1.0 \mu\text{m}$ |
| $\bar{l}_{s+} = 1.0 \mu\text{m}$ | $\bar{l}_{s-} = 1.0 \mu\text{m}$ |

Table 2.7 – Initial dislocation densities and parameters for the simulations in Fig. 2.15.

In Fig. 2.15 (a) accumulations of edge dislocations are visible in regions oriented perpendicular to the Burgers vector. The dislocation density reaches values of the order of 10^{15} m^{-2} inside the walls and $10^{11} \div 10^{12} \text{ m}^{-2}$ inside channels. These densities are similar to the ones observed experimentally, as stated in section 1.1. A characteristic micrometre spacing among dislocation walls emerges. This length scale is predicted using only physics-based parameters and it compares well with the observed channel width (Fig. 1.1 (b) and Fig. 1.2 (c)). The characteristic in-plane bending of veins along the Burgers vector is also reproduced. By contrast, using the Arsenlis multiplication law (2.5), the edge dislocation density grows uniformly. This can be seen in Fig. 2.15 (d), where the edge dislocation density after 100 cycles along the dashed line passing through the geometry in the inset is shown for the two multiplication laws. This is because the Arsenlis law, applied with an element size smaller than a channel, predicts that new edge dislocations are continuously produced inside channels and thus it would remove any initial inhomogeneities in the edge dislocation density. In Fig. 2.15 (b) the product between the edge and the total “curved” dislocation density, responsible for the multiplication, is shown: the spatial variations are similar to those of the edge dislocation density in Fig. 2.15 (a). Some additional accumulations of “curved” dislocations are present inside channels; however, there is a spatial correlation between the edge dislocation density and the total “curved” dislocation density after 100 cycles. This can be seen in Fig. 2.15 (c), where the total “curved” dislocation density is plotted against the edge dislocation density for every element in the geometry. The points concentrate in two regions, one on the left, containing elements inside channels (low ρ_e), and one on the right, containing elements inside veins (high ρ_e). The right region shows, in average, higher values of the total “curved” dislocation density. Therefore, “curved” dislocations are concentrated where veins are present and the dislocation multiplication takes place mostly at the vein-channel interface, as shown in Fig. 2.2 (b). The distribution of screw dislocations does not show patterning in the Burgers

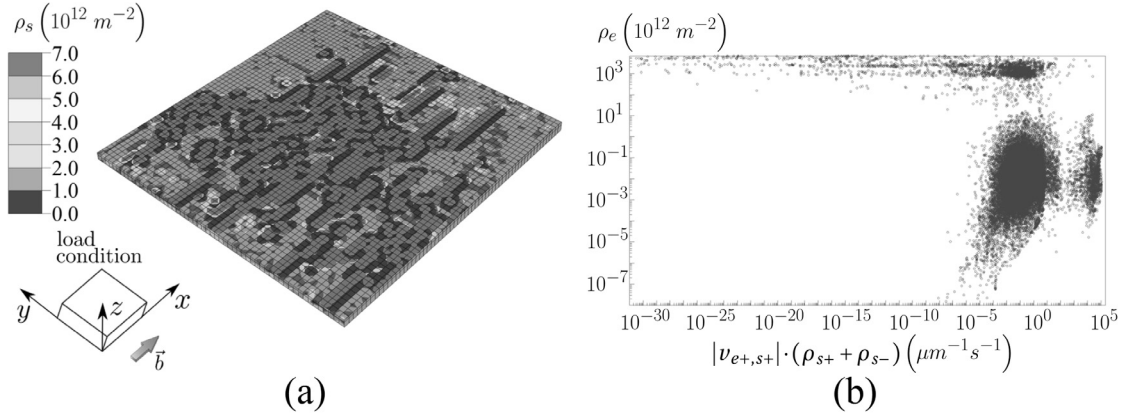


Figure 2.16 – (a) Screw dislocation density after 100 cycles using the new multiplication law; (b) scatter plot of the edge dislocation density as a function of the product $|v_{e+,s+}| \cdot (\rho_{s+} + \rho_{s-})$ at every integration point.

vector direction and turns out to be uncorrelated with the edge dislocation density, as shown in Fig. 2.16 (a). The dynamics of dislocation structure formation the simulations suggest are as follow: regions where edge dislocations accumulate are more resistant against dipole splitting because the mean \bar{h}_c of the Gaussian distribution in Fig. 2.6 (a) decreases with increasing total dislocation density. Edge dislocations then move from low density regions (channels) to high density ones (veins), and channels are not refilled with edge dislocations because the “curved” dislocations tend to concentrate near the vein-channel interface. According to (2.31), the “curved” dislocations are created by cross slip mainly where both a high screw dislocation density and dislocation velocity are present. This can be seen by plotting ρ_e as a function of the product $|v_{e+,s+}| \cdot (\rho_{s+} + \rho_{s-})$ at every integration point, as shown in Fig. 2.16 (b). The points with a lower value of ρ_e , representing channels, have, in average, a higher value of the product $|v_{e+,s+}| \cdot (\rho_{s+} + \rho_{s-})$, proportional to the production rate of “curved” dislocations. Once created, “curved” dislocations move from low density regions to high density ones, where their velocity decreases.

The dislocation structure formation in this statistical framework has to be interpreted using the ensemble introduced in section 1.5. Since the dislocation density is the average over the discrete ensemble, many components of this ensemble have to contain high and low dislocation density regions, at the same position where they appear in the continuum simulation. Therefore, a single simulation run represents an average of the results of multiple discrete simulations.

The mesh size dependence has been tested on a $4 \mu\text{m} \times 4 \mu\text{m} \times 1 \mu\text{m}$ geometry deformed at 0.1% strain with both 200 nm and 100 nm element size. The parameters are the same as in Tab. 2.7. The Burgers vector is along the y axis and the slip plane normal along the z axis. The edge dislocation density is averaged along the x axis. In Fig. 2.18 (a) the averaged edge dislocation density after monotonic deformation is shown. The mesh size dependence is visible at the boundary, where large gradients of the edge dislocation density are present. These gradients are due to the stress free boundary condition and the consequent low dislocation velocity,

leading to dislocation accumulation. After 8 cycles, as shown in Fig. 2.18 (b), the simulation made with 100 nm elements shows more features, even if the spatially averaged value of the edge dislocation density agrees with the 200 nm elements simulation. This shows that dislocation patterning appears also using a smaller element size.

In the simulation in Fig. 2.15 (a), the dislocation walls have a typical length of around 400 nm along the Burgers vector direction (x axis). Therefore, they occupy two elements along that axis. Since linear elements are used, the dislocation density as a function of the x coordinate has triangular peaks, as shown in Fig. 2.15 (d). This simulation cannot predict the exact density distribution of dislocation walls along the Burgers vector direction, which is not necessarily linear. However, it predicts the maximum value of the dislocation density in the centre of the wall. By contrast, the low dislocation density channels have a larger characteristic size, around $1 \mu\text{m}$. The dislocation density in these channels is low and the continuum model predicts that less than one dislocation is present in some elements. As explained in section 1.5, those elements represent an ensemble where some components do not contain dislocations at that specific spatial position. As shown by the electron microscopy images in section 1.1, channels are occupied by single dislocations, whose spacing is of the order of $1 \mu\text{m}$, larger than the element size in the simulations. Therefore, ensemble components in which no dislocations are present in certain elements are realistic. The statistical continuum models used in these simulations are not able to find the position of single dislocations in the channels, but only to determine their density.

As shown by the simulation in Fig. 2.15 (a), an element size larger than $1 \mu\text{m}$ would prevent the observation of dislocation patterning because the element size would be larger than the spacing between neighbouring dislocation walls. Similarly, an element size smaller than 10 nm would not be suitable because the details of the dislocation core are not included in the model.

The simulation in Fig. 2.15 has been carried out also with $\delta\rho = 15\%$ random fluctuations, added to the initial uniform dislocation distribution. In Fig. 2.17 (a), accumulations of edge dislocations are visible with a characteristic shape and length scale comparable to the patterning in Fig. 2.15 (a). The spectral density obtained using the Fourier transform of the edge dislocation density in Fig. 2.15 (a) ($\delta\rho = 50\%$) and 2.17 (a) ($\delta\rho = 15\%$) is shown in Fig. 2.17 (b). The Fourier transform is calculated along the x axis and the spectral density is averaged over the y and z axis. The comparison between the two spectral densities in Fig. 2.17 (b) shows that the characteristic wavelength of dislocation structures depends mainly on the equation system and not on the initial condition. However, the specific position of dislocation walls is different in the two simulations with $\delta\rho = 50\%$ and $\delta\rho = 15\%$.

The dependence on the cross slip coefficient β of the rate at which the average dislocation density increases is illustrated in Fig. 2.19 (a). The solid curve ($\beta = 8 \cdot 10^{-8}$) is the average value predicted by our model using copper parameters [Bonneville et al., 1988]. Due to the large uncertainty in the value of the β , a lower limit of the predicted average dislocation density is given by the dashed curve ($\beta = 8 \cdot 10^{-9}$) in Fig. 2.19 (a). Transmission electron microscopy measurements of the dislocation density in copper [Hancock and Grosskreutz, 1969] fit inside the interval between the solid and the dashed curve in Fig. 2.19 (a). Considering that the

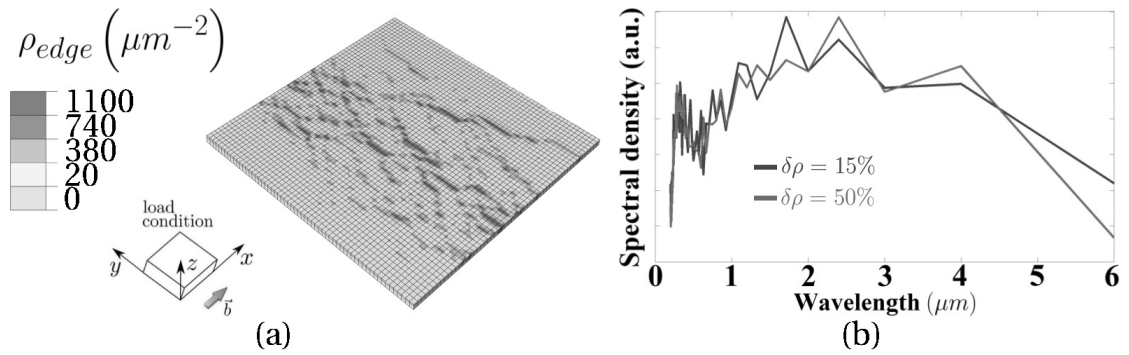


Figure 2.17 – (a) Edge dislocation density after 100 cycles using the new multiplication law and initial fluctuations of the initial dislocation density $\delta\rho = 15\%$. (b) Spectral density of ρ_e as a function of the wavelength.

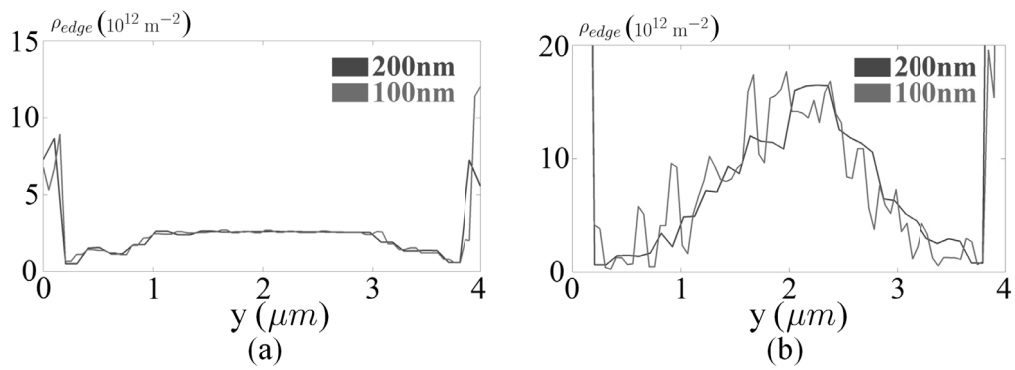


Figure 2.18 – Averaged edge dislocation density after (a) monotonic deformation and (b) after 8 cycles using both 200 nm and 100 nm element size.

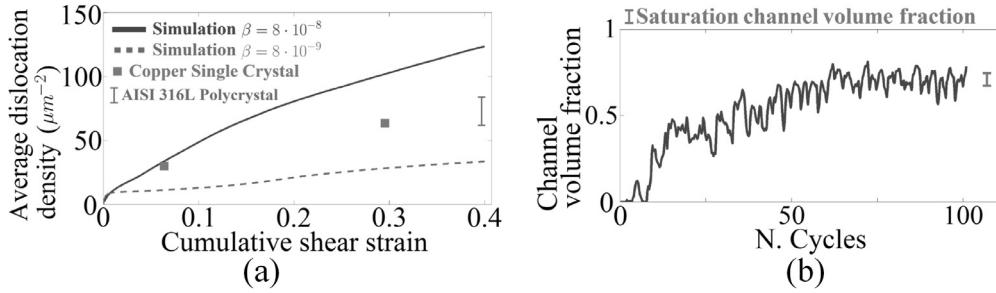
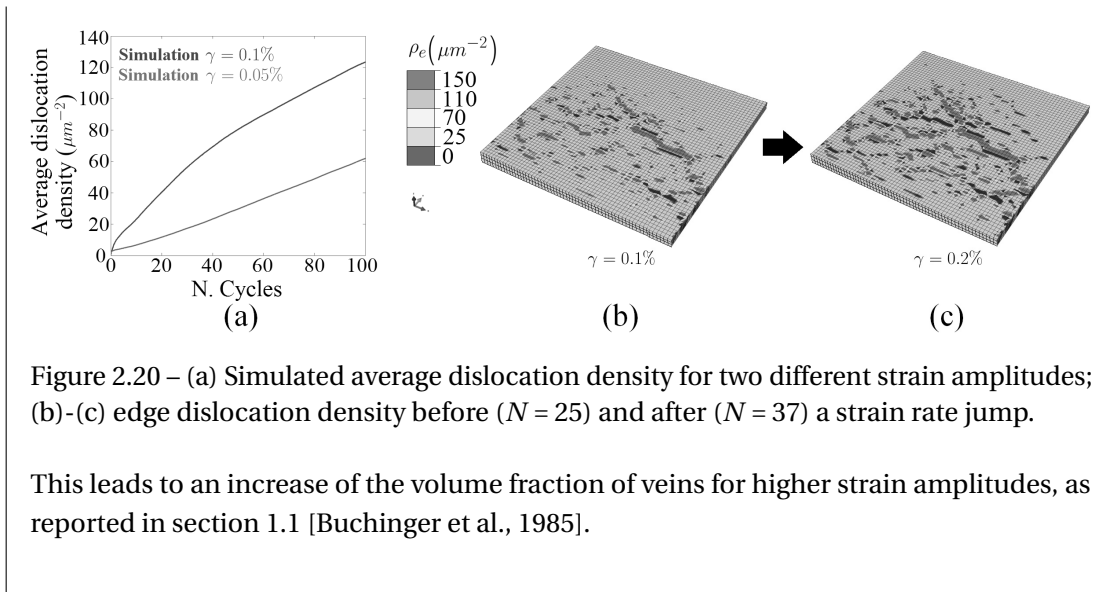


Figure 2.19 – (a) Simulated average dislocation density as a function of the cumulative shear strain for $\beta = 8 \cdot 10^{-8}$ (solid curve) and $\beta = 8 \cdot 10^{-9}$ (dashed curve); squares represent experimental points [Hancock and Grosskreutz, 1969], with a measurement error estimated at about 50%. (b) Simulated channel volume fraction as a function of the number of cycles; the error bar represents the saturation channel volume fraction in copper at the same saturation stress [Buchinger et al., 1985].

experimental error is about 50%, our predicted average dislocation density compares well with experiments. Once dislocation structures are formed, there is a sharp interface between low and high dislocation density regions: channels are almost empty of edge dislocations while inside veins $\rho_e > 1 \cdot 10^{14} \text{ m}^{-2}$. Thus, it is possible to set a threshold edge dislocation density $\rho_{e,th}$ (e.g. $\rho_{e,th} = 1 \cdot 10^{11} \text{ m}^{-2}$) and to define the volume fraction of channels as the fraction of integration points where $\rho_e < \rho_{e,th}$. The channel volume fraction as a function of the number of cycles at 0.1% strain amplitude is shown in Fig. 2.19 (b) and its value at saturation agrees with the experimental one [Buchinger et al., 1985]. The simulated saturation value of the channel volume fraction does not change significantly if $\rho_{e,th}$ is chosen from the interval $1 \cdot 10^{11} \text{ m}^{-2} \leq \rho_{e,th} \leq 5 \cdot 10^{12} \text{ m}^{-2}$.

Effect of strain amplitude. In our model the average dislocation density after a certain number of cycles increases with the strain amplitude, as shown in Fig. 2.20 (a). This is coherent with the experimental results reported in section 1.1 [Polák, 1969]. To understand the effect of the strain amplitude on the dislocation structures a simulation with strain jump is shown in Fig. 2.20. The simulation geometry is the same as the one in Fig. 2.15 and the parameters the same as in Tab. 2.7. The strain amplitude is $\gamma = 0.1\%$ until cycle $N = 30$, then it is suddenly increased to $\gamma = 0.2\%$. In Fig. 2.20 (b)-(c) the edge dislocation density at $N = 25$ and $N = 37$ cycles is shown. Some of the previously formed small veins disappear and the dislocations rearrange, while the larger veins increase their dimensions. The channels become shorter, satisfying the similitude principle [Sauzay and Kubin, 2011].



Effect of the material. Performing simulations with different sets of parameters is useful to determine the model predictions for different FCC materials. The parameter that affects more the shape, volume fraction and channel width of dislocation structures is the cross slip coefficient β . A lower cross slip rate leads to less developed dislocation structures, a smaller average dislocation density and an increased channel width. This is shown in Fig. 2.21 (a) where the simulation setup is the same as the one in Fig. 2.15 and the cross slip coefficient is one order of magnitude lower ($\beta = 8 \cdot 10^{-9}$). This is consistent with results found by discrete [Devincre and Kubin, 1997] and continuum [Xia and El-Azab, 2015] dislocation dynamics, where, in the absence of cross slip, no dislocation storage occurs in the material and cell structures do not form. The same simulation as in Fig. 2.15 has been made with a 100 times higher dislocation mobility. As shown in Fig. 2.21 (b), a smaller spacing between adjacent dislocation walls is obtained. Dislocation patterning after 100 cycles, using copper parameters and including secondary dislocations, results in slightly shorter channel widths, as shown in Fig. 2.21 (c), than the patterning without secondary dislocations in Fig. 2.15.

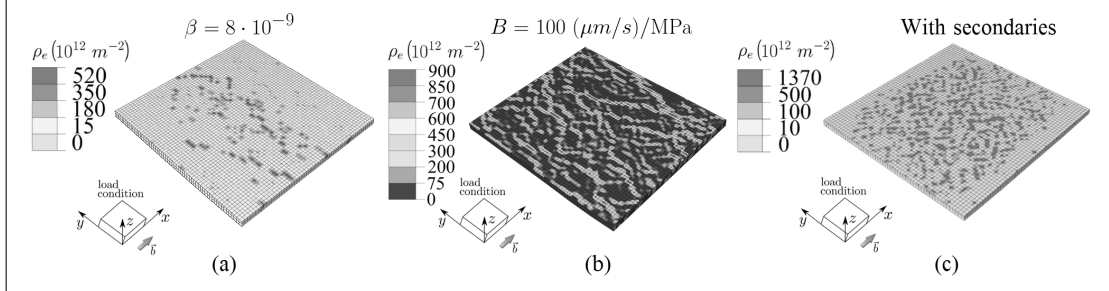


Figure 2.21 – Edge dislocation density after 100 cycles using (a) a lower cross slip coefficient $\beta = 8 \cdot 10^{-9}$; (b) a higher dislocation mobility $B = 100 (\mu\text{m}/\text{s})/\text{MPa}$ and (c) including secondary dislocations.

A general criterion to find out the effect of parameters on the patterning wavelength can be deduced from the Walgraef-Aifantis model. Equation (1.7) implies that stronger interactions among dislocations lead to a shorter wavelength of dislocation structures. Accordingly, the more dislocations are free to move, the longer is the patterning wavelength. Using this criterion we can interpret all the above results. If the cross slip coefficient β decreases, then the dislocation density grows at lower rate and the threshold stress to remobilize dislocations inside walls is lower; therefore more dislocations are mobile and larger channels form. To explain the shorter channels in Fig. 2.21 (b), one should note that, in a strain controlled simulation, if the dislocation mobility increases, then the resolved stress decreases because, according to Orowan's law, a lower stress is needed to accommodate the imposed plastic strain. Thus fewer dislocations are free to move and the wavelength of dislocation structures decreases. The shorter channels in Fig. 2.21 (c) are due to the stronger interactions among dislocations when secondary dislocations are present. In general, our simulations have shown that the patterning wavelength is shorter whenever the average dislocation density is higher.

If the cross slip coefficient is lower, edge dislocations transfer faster from channels to veins because of the lower dislocation density and the consequent lower mutual interactions. This can be seen in Fig. 2.22 (a) where the solid line represents the edge dislocation density in an element contained in the circle in the inset while the dashed line shows the same quantity in a channel in Fig. 2.15 (a) ($\beta = 8 \cdot 10^{-8}$).

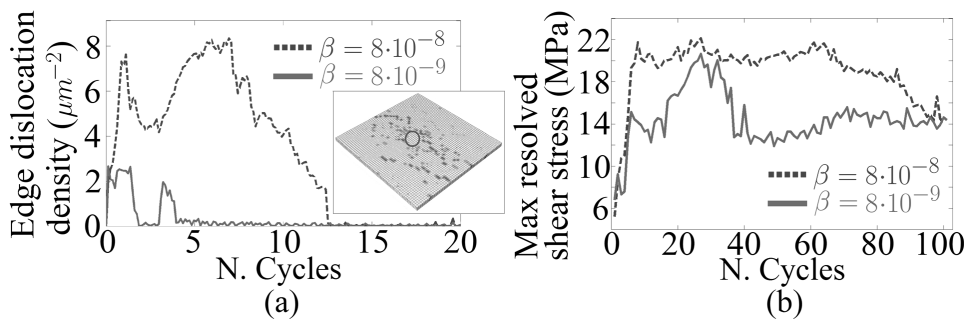


Figure 2.22 – (a) Solid line: depletion of the channel indicated by the circle in the inset. Dashed line: depletion of the channel with higher cross slip coefficient $\beta = 8 \cdot 10^{-8}$. (b) Hardening curves for $\beta = 8 \cdot 10^{-8}$ (dashed line) and $\beta = 8 \cdot 10^{-9}$ (solid line).

This property is confirmed by TEM analyses of different materials. For instance, the dislocation structures in aluminium and copper reach a comparable state when the cumulative plastic shear strain reaches 0.1 [Videm and Ryum, 1996] in aluminium, and 0.5 [Basinski and Basinski, 1992] in copper.

As stated in section 1.1, at higher temperature the characteristic length scale of dislocation

2.5. Mechanical properties of the single slip model

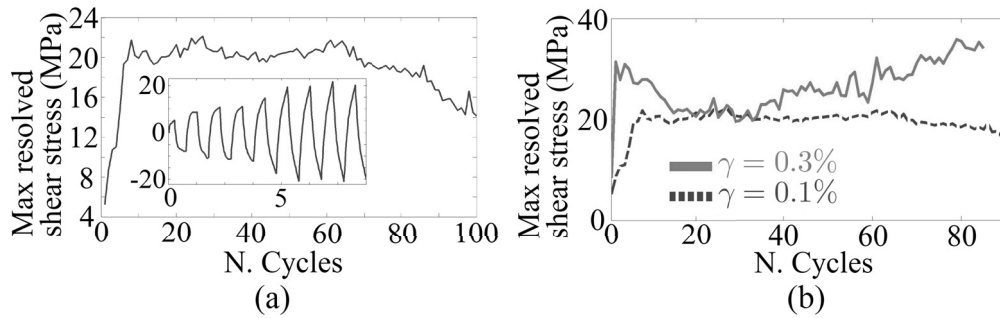


Figure 2.23 – (a) Hardening curve using the multiplication law for cyclic fatigue (2.15), averaged over the deforming surface; (b) hardening curve for two different values of the strain amplitude γ .

structures increases. This is consistent with our results and with (1.7) if one assumes that the increased annihilation rate leads to a lower average dislocation density.

2.5 Mechanical properties of the single slip model

The flow stress as a function of the number of cycles is shown in Fig. 2.23 (a). Initially hardening is observed, followed by a stagnation in the flow stress characterized by some fluctuations and followed by a softening. This softening can be explained by the influence of regions, forming after many cycles, with low dislocation density, as shown in Fig. 2.22 (a), where screw dislocations can glide easily. If the strain amplitude γ is higher, as shown in Fig. 2.23 (b), the softening is more evident because the higher stress causes a faster decrease of the edge dislocation density inside the channels. Because of the absence of dislocation patterning, softening cannot be predicted when using the Arsenlis multiplication law (2.5), as shown in Fig. 2.5. For different plastic strain amplitudes the flow stress as a function of the number of cycles predicted using the multiplication law for cyclic fatigue (2.15) and the Arsenlis multiplication law (2.5) is shown in Fig. 2.24. The Arsenlis multiplication law predicts a spatially uniform dislocation density at saturation whose value is given by the balance between dislocation multiplication and annihilation, as stated in (2.10) and (2.11). Both those processes are directly proportional to the dislocation velocity $|v|$, which, according to Orowan's law (1.12), is directly proportional to the plastic strain rate. When rate equations for dislocation multiplication (2.5) and annihilation (2.2)-(2.3) are equated, the dislocation density at saturation is determined only by the material parameters \bar{l}_{e+} , \bar{l}_{e-} , \bar{l}_{s+} , \bar{l}_{s-} , \check{d}_e , \check{d}_s and not by the plastic strain amplitude γ_{pl} . Therefore the flow stress at saturation, which is determined by the total dislocation density, does not depend on γ_{pl} , as shown in Fig. 2.24 (a). Using the multiplication law for cyclic fatigue (2.15) the saturation stress increases with γ_{pl} because of the presence of dislocation structures, whose volume fraction depends on γ_{pl} , as shown in Fig. 2.20. The strain amplitude dependence of the saturation stress compares well with existing experimental

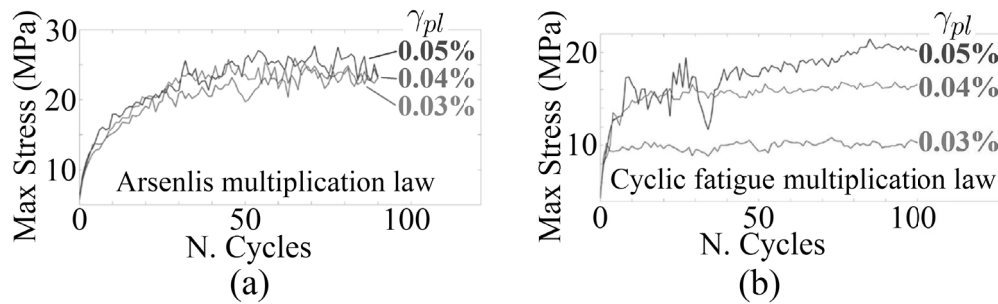


Figure 2.24 – Maximum stress as a function of the number of cycles for different plastic strain amplitudes using (a) the Arsenlis multiplication law (2.5) and (b) the multiplication law for cyclic fatigue (2.15). Simulation are carried out using the parameters in Tab. 2.7.

data for copper [Déprés et al., 2008] and aluminium [Videm and Ryum, 1996], as shown in section 1.3.

Effect of the material. As shown in Fig. 2.22, mechanical softening is caused by the depletion of channels and the faster this phenomenon develops, the stronger the mechanical softening becomes. Indeed a more pronounced mechanical softening is present if the cross slip coefficient β is lower, as shown in Fig. 2.22 (b). Aluminium exhibits softening, the hardening curve having a local minimum between 0.5 and 5 cumulative plastic shear strain [Videm and Ryum, 1996], as shown in Fig. 1.21, while copper hardening saturates only when the cumulative plastic shear strain reaches values around 10 [Déprés et al., 2008], as shown in Fig. 1.16 (b). The computational results in Fig. 2.22 (b) are in contrast to the experimental knowledge that aluminium, which has a higher cross slip coefficient, shows more pronounced cyclic softening. Every dislocation based model able to predict patterning presents this inconsistency because a faster depletion of channels for a lower multiplication rate is predicted. The introduction of secondary dislocations in our model has shown to solve this problem. During the formation of vein-channel structures, the additional hardening provided by secondary dislocations increases the number of dislocations stopped inside veins and, therefore, leads to a faster dislocation structure formation. This effect is more evident using aluminium parameters because its cross slip coefficient is higher than that of copper, as shown in Tab. 2.6. Including secondary dislocations, mechanical softening appears in aluminium but not in copper while the opposite holds true without secondary dislocations, as shown in Fig. 2.25.

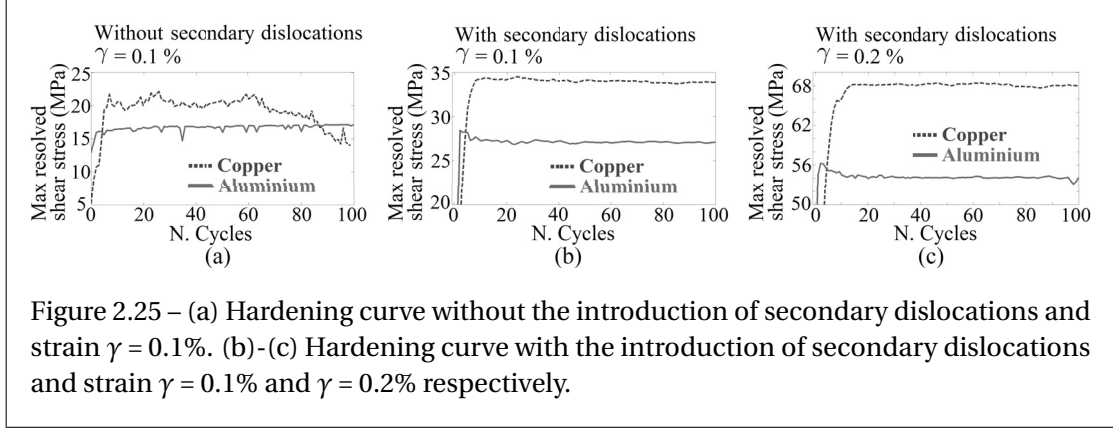


Figure 2.25 – (a) Hardening curve without the introduction of secondary dislocations and strain $\gamma = 0.1\%$. (b)-(c) Hardening curve with the introduction of secondary dislocations and strain $\gamma = 0.1\%$ and $\gamma = 0.2\%$ respectively.

2.6 Persistent slip bands modelling

A dipole-dipole interaction term has been introduced to reproduce the stability of dislocation dipole walls, as shown in Fig. 1.26 (b)-(c) [Neumann, 1987]. This interaction is caused by the combination of attractive forces, among opposite signed dislocations (red arrows in Fig. 2.26 (a)), and repulsive ones (green arrows in Fig. 2.26 (a)). This attractive interactions affect dislocation dipoles on neighbouring elements along the slip plane normal and can be modelled in our continuum framework using an additinal stress term:

$$\tau_{\text{dipole}} = \frac{Gb}{2\pi(1-\nu)} \cdot \left(\frac{N_{\text{dipole}} \bar{h}}{D^2} \right), \quad (2.41)$$

where N_{dipole} is the number of dipoles in one element, \bar{h} is the average dipole height, given by (2.13), and D is the distance between the two elements. This term is significant only when the dislocation density reaches a high value, after many deformation cycles. Tests on simple geometries are made using the configurations in Fig. 2.26 (b) and (c), where dislocations are distributed horizontally and vertically with respect to the Burgers vector \vec{b} . When shear stress is applied, the wall configuration turns out to be more stable because it has a higher yield point (Fig. 2.26 (d)) and a consequent lower dislocation flux. This is due to the attractive interaction (2.41) among dislocation dipoles in the wall configuration. Cyclic shear simulations using copper parameters have been carried out both with and without the interaction term in (2.41) on a $4 \mu\text{m} \times 4 \mu\text{m} \times 0.6 \mu\text{m}$ parallelepiped geometry. The crystal orientation is the same as in Fig. 2.15, the strain amplitude $\gamma = 0.1\%$, and the initial dislocation densities are the same reported in Tab. 2.7. Without the dipole interaction term τ_{dipole} , a single dislocation structure forms in the centre of the geometry, as shown in Fig. 2.27 (a). Two channels with low dislocation density are present and dislocation accumulations at the boundary are caused by stress free boundary conditions. If the τ_{dipole} term is introduced, dislocation walls are spread throught the geometry and they are shorter along the \vec{b} vector direction. This shows that such an interaction term can change the shape of dislocation structures after many cycles and lead

Chapter 2. Single slip dislocation-based model

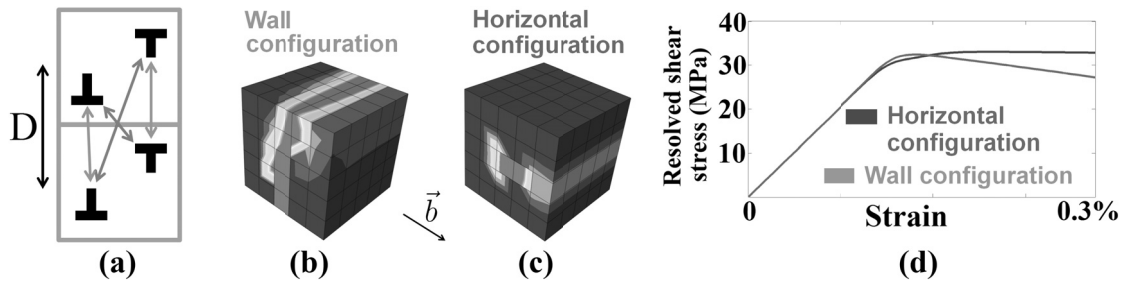


Figure 2.26 – (a) Interaction between two dipoles inside neighbouring elements; (b) dipoles distributed orthogonally with respect to the slip plane; (c) dipoles distributed along the slip plane; (d) stress-strain curves of the two configurations in (b) and (c).

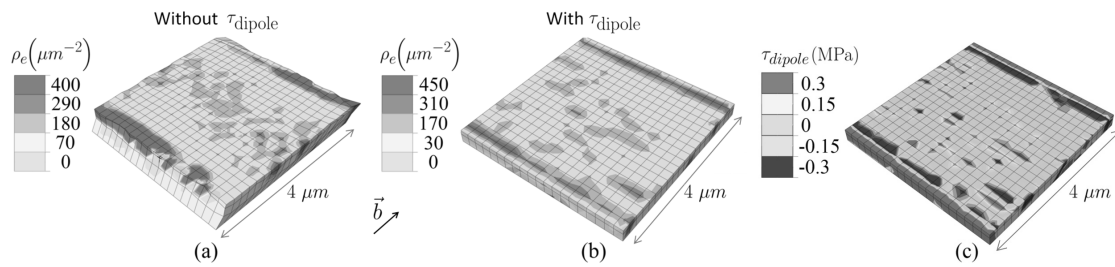


Figure 2.27 – (a) Edge dislocation density after 30 cycles without the τ_{dipole} stress term. (b) Edge dislocation density after 20 cycles with the τ_{dipole} term. (c) τ_{dipole} in (2.41) calculated from the dislocation distribution in (b).

to thinner dislocation walls, more similar to persistent slip band walls.

3 Multiple slip dislocation-based model

In this chapter the dislocation-based CPFE framework is applied to the simulation of cyclic fatigue in single- and polycrystals oriented for multiple slip. The single slip model is extended to multiple slip, first considering edge and screw dislocations as state variables and then taking into account of the formation of dislocation junctions in a continuum framework. These two approaches are compared with the single crystal simulations and an analysis based on the orientation distribution function. In a case study of a polycrystal, electron channeling contrast images of cyclically deformed austenitic stainless steel samples [Nellesen et al., 2015] are used to validate the developed model. By comparison with predictions of existing models it is shown that the introduction of dislocation junctions is necessary to correctly predict the orientation of dislocation structures.

3.1 Multiple slip model based on edge and screw dislocation densities

The single slip model for cyclic plasticity explained in section 2.2 has been extended to multiple slip with the following modifications to dislocation processes:

- **dislocation annihilation:** equations (2.2)-(2.3) are used independently for the different slip systems α . The annihilation process on one slip system does not affect the others.
- **dislocation multiplication and cross slip:** the new multiplication law (2.15) and the cross slip law (2.29) are used independently for the different slip systems, which means the processes on one slip system do not affect the others.
- **dislocation interactions:** the threshold stress equation (2.9) is used as the average value of the Gaussian distribution to determine the fraction of mobile edge and screw dislocations, as shown in Fig. 3.1. In the single slip model a distribution of the dipole height is used (section 2.2), while in multiple slip the Gaussian curve represents a distribution of the interaction strength between two dislocations, as done in [Déprés

et al., 2008]. Thus, given an external resolved shear stress τ_i on the i -th slip system, the fraction of mobile edge and screw dislocations can be approximated using the blue area under the Gaussian curve in Fig. 3.1. The threshold stress equation (2.9) implies that dislocations on one slip system have an influence on the others. Using this approach, the orientation dependence of the yield point, corresponding to the stress value at which most dislocations become mobile, of different single crystalline materials can be predicted [Arsenlis and Parks, 2002]. The Gaussian distribution function used is [Déprés et al., 2008]:

$$f_c(\tau_i) \propto \exp\left(-\left(\frac{\tau_i - \bar{\tau}_i^c}{0.467\bar{\tau}_i^c}\right)^2\right), \quad (3.1)$$

where c is the dislocation character. The mean $\bar{\tau}_i^c$ of the Gaussian distribution as a function of the dislocation density ρ_c^i with character c on the i -th slip system is given by (2.9). Because of its statistical nature, this approach is suitable for high dislocation densities, when many dislocations are present at one integration point. For materials with a low cross slip coefficient (e.g. 316L steel), this leads to high values of the fraction of mobile dislocations and to a less pronounced dislocation patterning. This is because the value of the dislocation density is low in the first cycles, of the order of $1.0 \mu\text{m}^{-2}$, the average number of dislocation lines in a 200 nm size element is lower than one. A high value of the fraction of mobile dislocations also leads to more dislocation exiting the geometry, given that free surface conditions are used. For this reason, when simulating 316L steel, all dislocations are assumed mobile only when the resolved shear stress becomes higher than the threshold stress in (2.9) [der Giessen and Needleman, 1995].

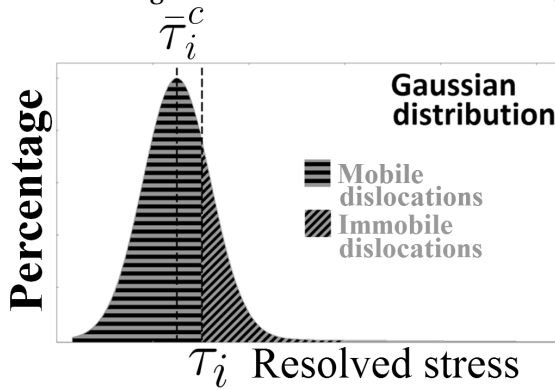


Figure 3.1 – Fraction of mobile dislocations in multiple slip.

The motion of dislocations between neighbouring elements is given by the flux term in (1.13) for every slip system and the kinetics law used is (2.8).

A cyclic compression simulation on a parallelepiped geometry whose size is $4 \mu\text{m}$ along the x and y directions and $1 \mu\text{m}$ along z is done. The element size is 200 nm, which is the same used in the single slip simulations presented in section 2.2. The load direction is $[100]$ and the applied displacement is $0.008 \mu\text{m}$, in order to induce a 0.2% strain amplitude. Copper

3.1. Multiple slip model based on edge and screw dislocation densities

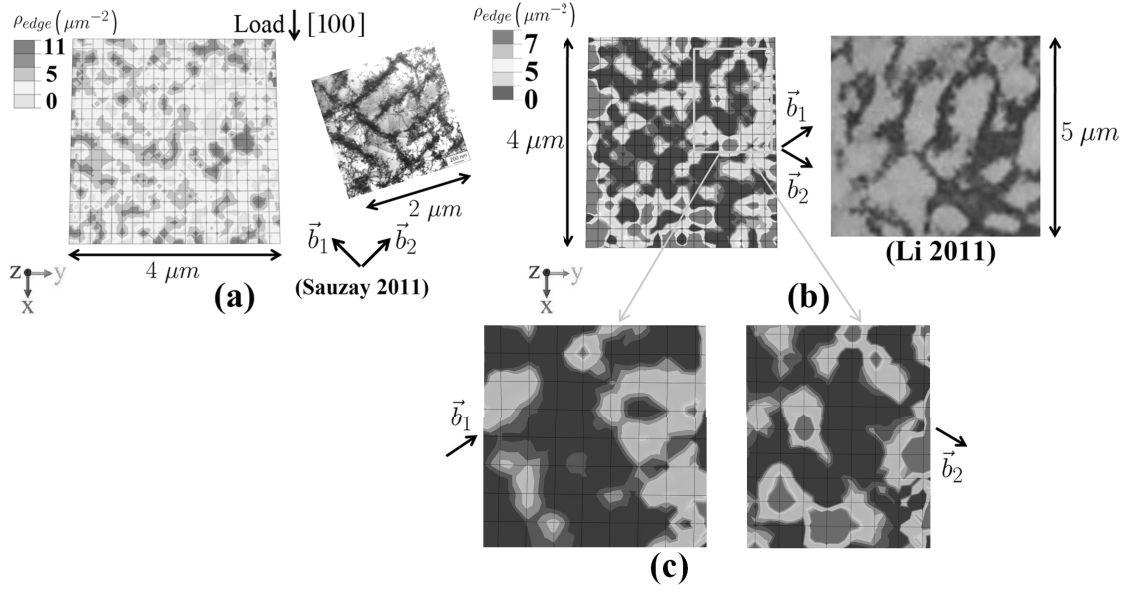


Figure 3.2 – (a) Simulation of labyrinth structures after 30 deformation cycles. (b) Simulation of cell structures and (c) dislocation density on the two active coplanar slip systems.

parameters are used and all the 12 slip systems are considered. Periodic boundary conditions for dislocation fluxes are used along all the axes and the secondary dislocation density in (2.33) is not included. Average values of initial dislocation densities and kinetic parameters in the simulation are summarized in Tab. 2.7. Random fluctuations of 50% are added to this uniform distribution. The total dislocation density ρ in the centre of the parallelepiped after 30 deformation cycles is shown in Fig. 3.2 (a). Dislocation walls form perpendicular to two direction, \vec{b}_1 and \vec{b}_2 , oriented at 45 degrees with respect to the load direction. These directions correspond to Burgers vectors of four active critical slip systems (interacting by Hirth locks [Martínez et al., 2008]): $[110](1\bar{1}1)$, $[110](1\bar{1}\bar{1})$, $[1\bar{1}0](111)$ and $[1\bar{1}0](11\bar{1})$. As stated in section 1.6 for the Walgraef-Aifantis model, this is due to the motion of edge dislocations along a direction perpendicular to the Burgers vector. This is not consistent with the experimental observation in Fig. 1.11 (b), where labyrinth walls form parallel and perpendicular to the load direction. In the simulation of Fig. 3.2 (b), dislocation walls do not align with the Hirth junction direction, which would be $[010]$ if projected on the observation plane. Thus, it appears necessary to introduce dislocation junctions and their specific geometrical configuration. The proposed method will be explained in section 3.2. The characteristic length scale of the labyrinth structures shown by the simulation is close to the experimental one, as shown in Fig. 3.2 (a) [Sauzay and Kubin, 2011].

The same simulation is made with a different load condition in order to activate two coplanar slip systems. A cyclic shear deformation is applied, reaching an amplitude $\gamma_{yz} = 0.1\%$. The total dislocation density ρ is shown in Fig. 3.2 (b). The two Burgers vectors \vec{b}_1 and \vec{b}_2 belong to the two most active slip systems, whose dislocation densities are shown in Fig. 3.2 (c). The orientation of channels is typically perpendicular to the respective Burgers vectors. These two coplanar slip systems account for the majority of dislocations, while dislocations do not

multiply on the third coplanar slip system. Even if the simulated dislocation walls in Fig. 3.2 (b) have a cell-like shape, similar to the one observed experimentally [Li et al., 2011], dislocations in the third coplanar system are not produced because of the absence of coplanar junction formation, in contrast to the experimental evidences explained in section 1.2. Also in this case, the introduction of dislocation junctions is necessary.

3.2 Multiple slip model based on dislocation junctions

The dislocation junction formation in the continuum dislocation dynamics framework is introduced by combining edge and screw dislocation densities into a density aligned with dislocation junctions. As for the single slip model, multiple dislocation densities are used to differentiate between the orientations of a dislocation line. The state variables can be defined starting from the higher order dislocation density $\rho^\alpha(p, \varphi)$ of the continuum dislocation dynamics theory [Hochrainer et al., 2014], which quantifies the density of dislocations at a point p on the slip system α with line direction oriented at an angle φ with respect to the Burgers vector. Integration of $\rho^\alpha(p, \varphi)$ over prescribed angular intervals as defined in the following, leads to different dislocation densities. In case two slip systems are active, for which the slip plane normals are \mathbf{n}_1 and \mathbf{n}_2 , the dislocation junction vector \vec{l}_{lock} can be defined as $\vec{l}_{\text{lock}} = (\hat{\mathbf{n}}_1 \times \hat{\mathbf{n}}_2)$, as shown in Fig. 3.3 (a). Dislocation segments orthogonal to \vec{l}_{lock} are included in the dislocation densities $\rho_{\Gamma+}^\alpha$ and $\rho_{\Gamma-}^\alpha$, as shown in Fig. 3.3 (a). This orientation corresponds to dislocations gliding inside channels between neighbouring dislocation walls formed by Hirth locks in labyrinth dislocation structures Li et al. [2011]. The positive or negative sign depends on the position of the dislocation line in a clockwise oriented dislocation loop. Similarly $\rho_{\parallel+}^\alpha$ and $\rho_{\parallel-}^\alpha$ are defined as the densities of dislocation segments parallel to \vec{l}_{lock} . These dislocations have the same orientation as dislocation junctions. General dislocations, with an orientation intermediate between Γ and \parallel , are included in other dislocation densities. For instance by integrating $\rho^\alpha(p, \varphi)$ over the angular interval $\Delta\theta_{\parallel+, \Gamma-}$ shown in Fig. 3.3 (a), which includes orientations intermediate between positive \parallel and negative Γ , the density $\rho_{\parallel+, \Gamma-}^\alpha$ can be defined. The 8 different densities used in the model are listed in Tab. 3.1.

| | | | |
|------------------------------|------------------------------|------------------------------|------------------------------|
| $\rho_{\parallel+}$ | $\rho_{\parallel-}$ | $\rho_{\Gamma+}$ | $\rho_{\Gamma-}$ |
| $\rho_{\parallel+, \Gamma+}$ | $\rho_{\parallel+, \Gamma-}$ | $\rho_{\parallel-, \Gamma+}$ | $\rho_{\parallel-, \Gamma-}$ |

Table 3.1 – Dislocation densities used in the junction constitutive model.

If more than two slip systems are active, a fixed reference slip system is chosen to define the dislocation junction vector \vec{l}_{lock} , ρ_{\parallel} and ρ_{Γ} dislocations. The velocity vectors of different dislocation densities are orthogonal to the corresponding dislocation lines; for instance the velocity vectors $\vec{v}_{\Gamma+}^1$, $\vec{v}_{\Gamma-}^1$ and $\vec{v}_{\parallel+}^1$ are depicted in Fig. 3.3 (b). Other dislocation densities have velocity vectors oriented at 45 or 135 degrees, respectively, with \vec{l}_{lock} ; for instance $\rho_{\parallel+, \Gamma+}^\alpha$ has velocity vector $(\vec{v}_{\parallel+}^\alpha + \vec{v}_{\Gamma+}^\alpha)$. This definition of dislocation densities is suitable for modelling

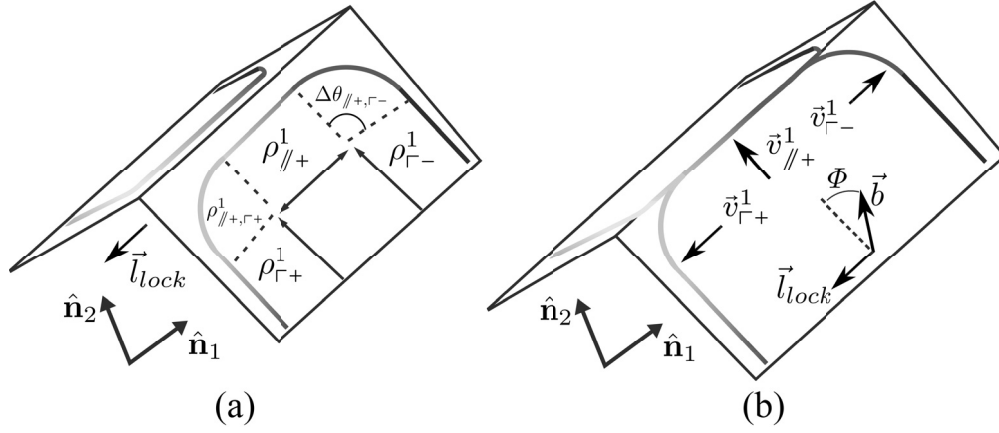


Figure 3.3 – (a) Definition of the dislocation junction vector \vec{l}_{lock} and of the different dislocation densities. (b) Velocity vectors $\vec{v}_{\Gamma+}^1$, $\vec{v}_{\Gamma-}^1$ and $\vec{v}_{\parallel+}^1$.

the dynamics of dislocation junctions in labyrinth dislocation structures, since under an applied stress the dislocations $\rho_{\Gamma+}^\alpha$ and $\rho_{\Gamma-}^\alpha$ move along \vec{l}_{lock} , as shown in Fig. 3.3 (b), while the dislocations $\rho_{\parallel+}^\alpha$ and $\rho_{\parallel-}^\alpha$ can interact and form immobile junctions. The choice of a fixed reference slip system allow to model at the same time all dislocation junction types between that reference system and all the others. Therefore this slip system has to be the most active slip system, with the highest value of the dislocation density, to predict the actual dislocation junctions in the material.

Dislocation multiplication law for the junction constitutive model. A multiplication law, formally similar to the one used for the single slip model, can be written in terms of the dislocation densities in Tab. 3.1. The dislocation loop in Fig. 3.3 (b) has to remain connected, therefore a new dislocation line is created that lengthens the dislocation junction during the motion of $\rho_{\Gamma+}^\alpha$ and $\rho_{\Gamma-}^\alpha$. This dislocation multiplication process is accounted for by the dislocation curvature density Hochrainer et al. [2007], which concentrates between \parallel and Γ dislocation segments, for instance in $\rho_{\parallel+, \Gamma+}^1$ in Fig. 3.3 (a). As a consequence the densities $\rho_{\parallel+}^\alpha$, $\rho_{\parallel-}^\alpha$, $\rho_{\Gamma+}^\alpha$ and $\rho_{\Gamma-}^\alpha$ do not participate in the dislocation multiplication process because they are constituted of dislocation segments with zero curvature. A curved dislocation segment, such as $\rho_{\parallel+, \Gamma+}^\alpha$, is always connected to one \parallel and one Γ segment and its motion creates new \parallel dislocation lines at a rate given by the velocities $|\vec{v}_{\Gamma+}^\alpha|$ and $|\vec{v}_{\Gamma-}^\alpha|$. The number of these curved segments per unit volume is given by the ratio between the corresponding density and a fixed average segment length $\bar{\Lambda}$, for instance $\rho_{\parallel+, \Gamma+}^\alpha / \bar{\Lambda}$. The dislocation multiplication law can be written as:

$$\dot{\rho}_{\parallel+, mult}^\alpha = \frac{\rho_{\parallel+, \Gamma+}^\alpha |\vec{v}_{\Gamma+}^\alpha|}{\bar{\Lambda}} + \frac{\rho_{\parallel+, \Gamma-}^\alpha |\vec{v}_{\Gamma-}^\alpha|}{\bar{\Lambda}}. \quad (3.2)$$

Similar equations for $\dot{\rho}_{\parallel-,mult}^\alpha$, $\dot{\rho}_{\parallel+,mult}^\alpha$ and $\dot{\rho}_{\parallel-,mult}^\alpha$ can be obtained by substituting the curved densities in (3.2) $\rho_{\parallel+, \Gamma+}^\alpha$ and $\rho_{\parallel+, \Gamma-}^\alpha$ with the two curved densities with $\parallel-, \Gamma+$ or $\parallel-, \Gamma-$ into the subscript. The value of $\bar{\Lambda}$ chosen for our simulations is $0.1 \mu\text{m}$, so that a curved dislocation segment has a length corresponding to the distance between two neighbouring integration points. This is the same value used for \bar{l}_c in the single slip model, whose lower and upper bounds are described in section 2.2.

Cross slip law for the junction constitutive model. The cross slip law is implemented as in the single slip model. However, the screw dislocation density is not a state variable in the junction constitutive model and it has to be expressed as a function of the dislocation densities in Tab. 3.1. The motion of screw dislocations on secondary slip planes and their consequent multiplication as Frank-Read sources Bitzek et al. [2008], Messerschmidt and Bartsch [2003] is shown in Fig. 3.4 (a).

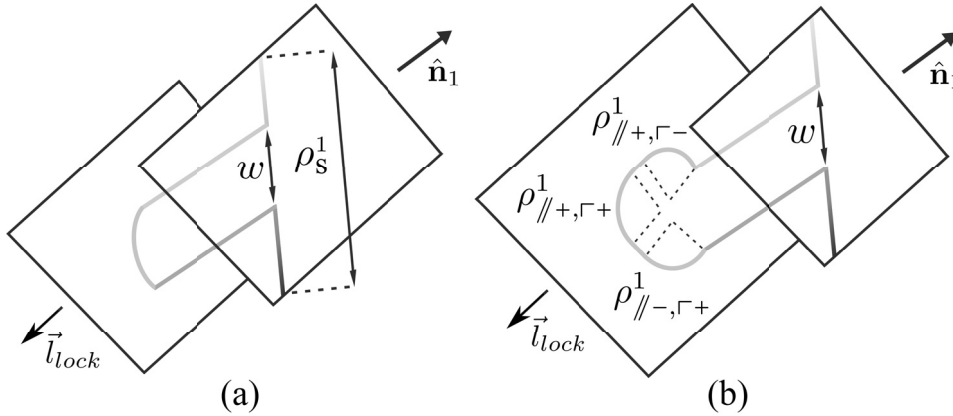


Figure 3.4 – (a) The process of cross slip of a screw dislocation segment from one slip plane to another. (b) The resulting Frank-Read source generates new curved dislocation segments.

This process generates new curved dislocation segments at a rate R given by (2.25) and the same attack frequency $\nu = 2 \cdot 10^{15} \text{ s}^{-1}$ as in single slip is used [Vegge et al., 2000]. The value used for the width w is the same as in the single slip model, $w \approx 44b$. The density of new “curved” dislocations is given by an expression similar to (2.27):

$$d\rho_{\parallel+, \Gamma+, cs} = \frac{\bar{\Lambda} d\rho_{cs}}{w} = \frac{(\rho_{s+} + \rho_{s-}) \bar{\Lambda} R dt}{w}, \quad (3.3)$$

where $d\rho_{cs}/w$ is the number of loops created per unit volume during an infinitesimal time dt , as in (2.26). Similar equations hold for the other “curved” densities. The same

3.2. Multiple slip model based on dislocation junctions

characteristic expansion time $t_c \approx 0.1s$ for a dislocation loop is used, as for the single slip simulations. The cross slip coefficient β is defined by (2.30) and the following cross slip equation can be obtained:

$$\dot{\rho}_{//+, \Gamma+, cs}^\alpha = \frac{\beta |v_{//+, \Gamma+}|}{b} \cdot (\rho_{s+} + \rho_{s-}) . \quad (3.4)$$

The screw dislocation densities ρ_{s+} and ρ_{s-} are obtained by projecting $//$ and Γ dislocation segments along the Burgers vector:

$$\rho_{s+}^\alpha = \rho_{\Gamma+}^\alpha \cos \Phi + \rho_{//+}^\alpha \sin \Phi , \quad (3.5)$$

$$\rho_{s-}^\alpha = \rho_{\Gamma-}^\alpha \cos \Phi + \rho_{//+}^\alpha \sin \Phi , \quad (3.6)$$

where $0 \leq \Phi \leq \pi/2$ is the angle represented in Fig. 3.3 (b):

$$\sin \Phi = \left| \frac{\vec{l}_{\text{lock}} \cdot \vec{b}}{\|\vec{l}_{\text{lock}}\| \cdot \|\vec{b}\|} \right| , \quad (3.7)$$

where $\|\vec{l}_{\text{lock}}\|$ and $\|\vec{b}\|$ are the norms of \vec{l}_{lock} and \vec{b} .

Annihilation law for the junction constitutive model. The annihilation rate is proportional to the product of opposite signed edge and screw dislocation densities, as expressed by (2.2) and (2.3) for every slip system. The projection equations (3.5) and (3.6) are used. For instance, the annihilation rate of $\rho_{//+}$ dislocations is given by:

$$\dot{\rho}_{//+, \text{ann}}^\alpha = -4 \hat{d}_s \rho_{s-}^\alpha \cdot (\rho_{//+}^\alpha \sin \Phi) \cdot |\vec{v}_s^\alpha| - 4 \hat{d}_e \rho_{e-}^\alpha \cdot (\rho_{//+}^\alpha \cos \Phi) \cdot |\vec{v}_s^\alpha| . \quad (3.8)$$

The two terms in (3.8) take into account the annihilation of screw and edge parts of $\rho_{//+}$ dislocation segments.

The constitutive equations of the multiple slip model for cyclic fatigue based on dislocation junctions are summarized in appendix A.2.

3.2.1 Two dislocation loops forming a dislocation junction

To illustrate the junction constitutive model in the presence of dislocations belonging to two different slip systems, we simulate the motion of two dislocation loops on intersecting

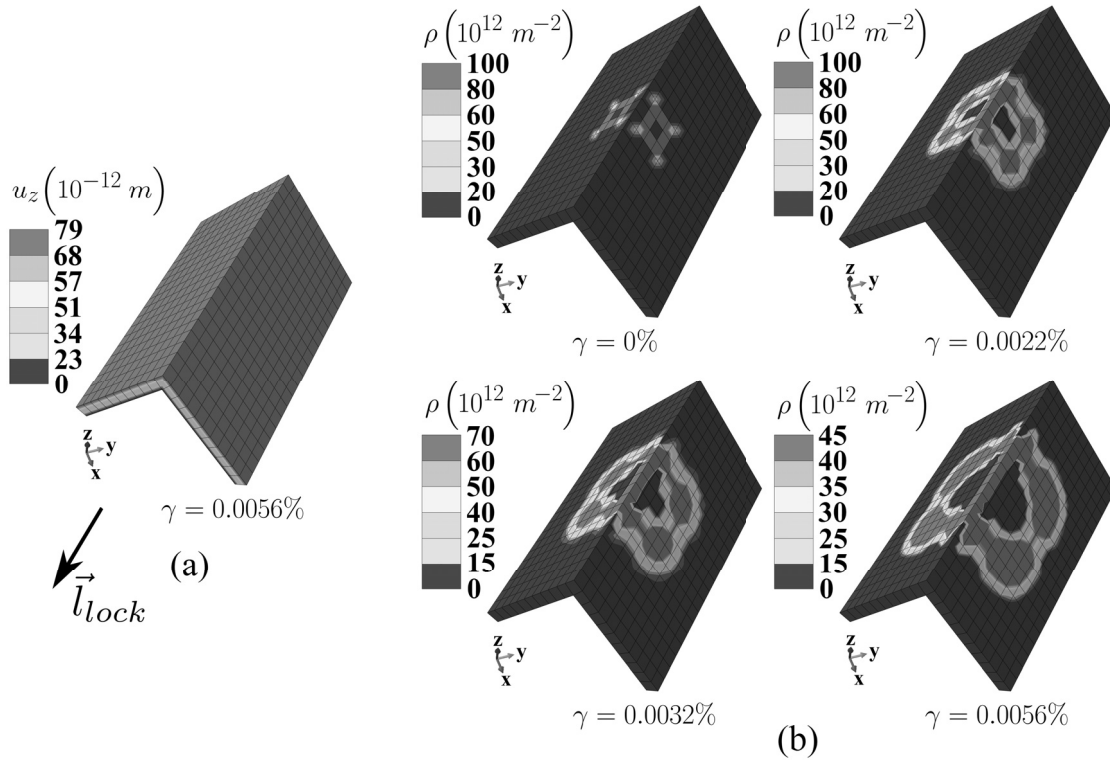


Figure 3.5 – (a) Displacement field along the z axis. (b) Evolution of the total dislocation density ρ of two dislocation loops forming a dislocation junction at the intersection of their slip planes.

slip planes. The model geometry is constituted of two planes with a thickness of 200 nm, corresponding to one single element, that intersect along a line of elements, as shown in Fig. 3.5 (a). These planes correspond to the (111) and $(\bar{1}\bar{1}1)$ slip planes of the FCC crystal and the angle between them is around 109° . A displacement along the z axis is imposed on the upper surfaces of the two planes while the lower surfaces are held fixed; the resulting z component of the displacement is shown in Fig. 3.5 (a). Using these boundary conditions, the resolved shear stress on the two slip systems is uniform. Fig. 3.5 (b) shows the evolution of the total dislocation density ρ on the two slip systems during changes in the resolved shear strain γ . The initial dislocation density of the two loops is set at $10^{14} m^{-2}$, thus each integration point, having a distance of 100 nm, contains the equivalent of a single dislocation. The two dislocation loops expand until they meet at the intersection of the two planes, where a dislocation junction is formed. The $\rho_{//+}^\alpha$ dislocation density becomes immobile due to the threshold stress (2.9), used in the dislocation junction model. Without this interaction the dislocation density would exit the geometry. The sections of the loops that do not form the junction expand further and a new dislocation line is created at the connections between $//$ and Γ segments, as predicted by the multiplication law (3.2). This simulation is made without the cross slip process described by (3.4).

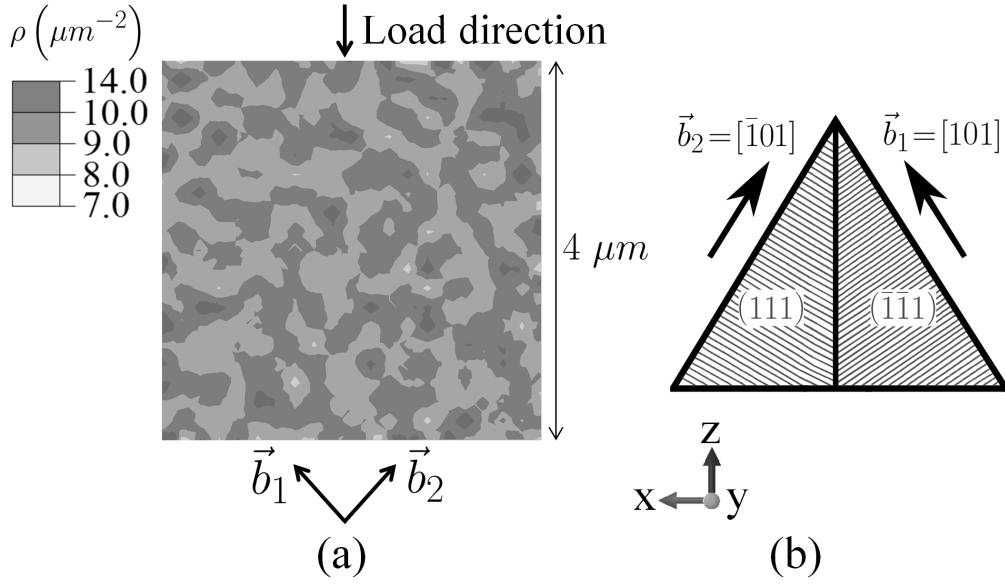


Figure 3.6 – (a) Total dislocation density after 40 cycles in [001] compression. (b) Orientation of the active slip systems.

3.3 Dislocation patterning and orientation analysis

The dislocation junction model is applied to the simulation of cyclic [001] compression using copper parameters. The geometry and element size is the same as in Fig. 3.2 (a). The load direction is [001] and the applied displacement is $0.004 \mu\text{m}$, in order to induce a $\varepsilon_{zz} = 0.1\%$ strain amplitude. Only two slip systems (critical double slip) are activated: $[101](\bar{1}\bar{1}\bar{1})$ and $[\bar{1}01](111)$. Their geometry and Burgers vectors \vec{b}_1 and \vec{b}_2 are shown in Fig. 3.6. Periodic boundary conditions for dislocation fluxes are used along all the axes and the secondary dislocation density in (2.33) is not included. Average values of initial dislocation densities and kinetic parameters in the simulation are summarized in Tab. 3.2.

| | |
|--|--|
| $\rho_{//+}(t=0) = 1.0 \mu\text{m}^{-2}$ | $\rho_{//-}(t=0) = 1.0 \mu\text{m}^{-2}$ |
| $\rho_{\Gamma+}(t=0) = 1.0 \mu\text{m}^{-2}$ | $\rho_{\Gamma-}(t=0) = 1.0 \mu\text{m}^{-2}$ |
| $\rho_{//+, \Gamma+}(t=0) = 0.01 \mu\text{m}^{-2}$ | $\rho_{//+, \Gamma-}(t=0) = 0.01 \mu\text{m}^{-2}$ |
| $\rho_{//-, \Gamma+}(t=0) = 0.01 \mu\text{m}^{-2}$ | $\rho_{//-, \Gamma-}(t=0) = 0.01 \mu\text{m}^{-2}$ |
| $B = 1.0 (\mu\text{m/s})/\text{MPa}$ | $v_{max} = 10 \mu\text{m/s}$ |

Table 3.2 – Initial dislocation densities and parameters for the simulations in Fig. 3.6.

The total dislocation density ρ in the centre of the parallelepiped after 40 deformation cycles is shown in Fig. 3.6 (a). Comparing this result with the dislocation pattern in Fig. 3.2, it can be seen that the wall orientation is not at 45° with respect to the load direction using the dislocation junction model. A quantitative analysis of the orientation of walls is possible using the 2D orientation distribution function [Gasparyan and Ohanyan, 2015], [Lu and Torquato,

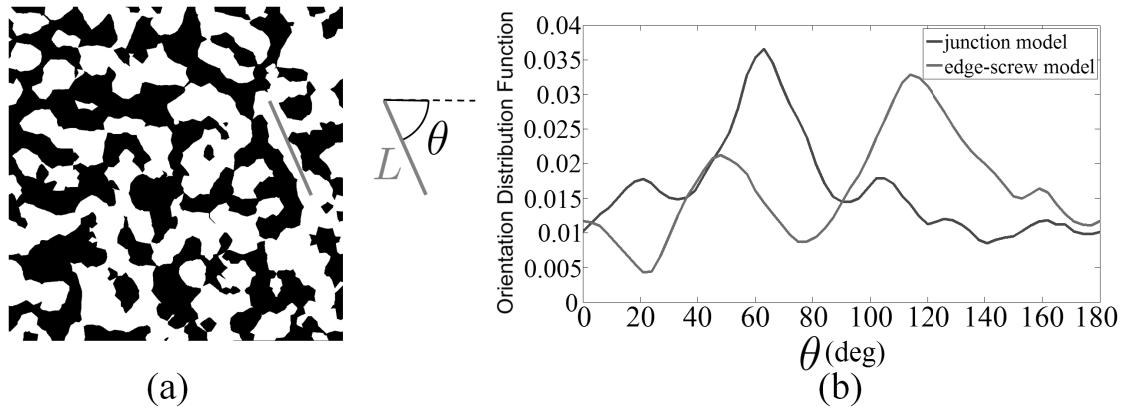


Figure 3.7 – (a) Black and white conversion of the image in Fig. 3.6 used to calculate the 2D orientation distribution function and dislocation line orientation angle θ ; (b) corresponding 2D orientation distribution function and comparison with the edge-screw model.

1992]. First the simulated pattern images are converted into black and white using a threshold value for the total dislocation density. For instance, a black and white conversion of the dislocation pattern in Fig. 3.6 (a) is shown in Fig. 3.7 (a). White and black areas correspond to high and low dislocation density areas. The 2D orientation distribution function is defined as the probability that a segment of length L , oriented at an angle θ with respect to the horizontal, lie completely inside the white area, representing dislocation structures. Such a segment is shown in red in Fig. 3.7 (a). θ is a variable of the 2D orientation distribution function, while the length L is kept fixed. The 2D orientation distribution function is calculated by counting the fraction of segments with length L and orientation θ that fit inside the white area, among all possible segments with this orientation fitting inside the figure. The result calculated for the junction model (Fig. 3.6) and for the edge-screw model (section 3.1) is shown in Fig. 3.7 (b) for $L = 760$ nm. For the edge-screw model, two peaks of the curve in Fig. 3.7 (b) are reached at different values of θ , one between $40^\circ < \theta < 60^\circ$ and the other between $110^\circ < \theta < 130^\circ$. For the dislocation junction model, a main peak is reached between $60^\circ < \theta < 70^\circ$. As stated in section 3.1, in the edge-screw model the dislocation walls tend to align to the orientation of edge dislocations. As reported in Tab. 3.3, edge dislocation lines are oriented at $\theta = 45^\circ$ and $\theta = 135^\circ$, which are close to the values of the peaks of the green curve in Fig. 3.7 (b). The broadening of the peak is due to the width of the dislocation structures. Indeed segments with length L with slightly different orientations can fit inside the same vein. This broadening decreases if the segment length L is increased.

| Slip system | $[101](\bar{1}\bar{1}1)$ | $[\bar{1}01](111)$ |
|-----------------|--------------------------|--------------------|
| ρ_e | 135° | 45° |
| ρ_s | 45° | 135° |
| $\rho_{//}$ | 0° | 0° |
| ρ_{Γ} | 63° | 117° |

Table 3.3 – Dislocation line orientation θ for different dislocation types, projected on the $x - z$ plane.

The peak between $60^\circ < \theta < 70^\circ$ in the blue curve in Fig. 3.7 (b) corresponds to $\rho_{\bar{r}}$ dislocations of the $[101](\bar{1}\bar{1}1)$ slip system, which is 63° , as reported in Tab. 3.3. Therefore the predictions of the two models are different; the dislocation junction model predicts that $\rho_{\bar{r}}$ dislocations move away from forming low density regions along directions parallel to the dislocation junction vector $\vec{l}_{\text{lock}} = [1\bar{1}0]$ between these two slip planes. Thus, dislocation walls form perpendicular to \vec{l}_{lock} and this orientation is at around $\theta = 63^\circ$ for the slip system $[101](\bar{1}\bar{1}1)$. The wall orientation found in Fig. 3.6 (a) is more similar to the experimental results on $[001]$ single crystals shown in section 1.2 (Fig. 1.11 (a)) with respect to the edge-screw model simulation. This is because the edge-screw model, as shown in Fig. 3.2 (a), predicts dislocation walls perpendicular to the Burgers vector directions and this is in contradiction to the experimental observation in Fig. 1.12 (a).

3.4 Polycrystal simulations

Both the multiple slip edge-screw model and the dislocation junction model are applied to the simulation of fatigue experiments on polycrystalline 316 austenitic stainless steel, where the electron channeling contrast imaging (ECCI) technique [Zaefferer and Elhami, 2014] is used. These experiments have been carried out at the Max Planck Institut for Iron Research by Jens Nellessen [Nellessen et al., 2015]. In the following the principles of the ECCI technique are briefly explained.

Electron Channeling Contrast Imaging. This experimental analysis is performed in a scanning electron microscope (SEM) and uses a backscattered electron (BSE) detector. Typically, a low tilt configuration of the sample is employed, as shown in Fig. 3.8 (a). The backscattered intensity of a perfect crystal is a function of the incidence angle θ , as shown in Fig. 3.8 (b). The sample is usually oriented close to the Bragg diffraction angle θ_B in order to maximize the derivative of the backscattered intensity with respect to θ .

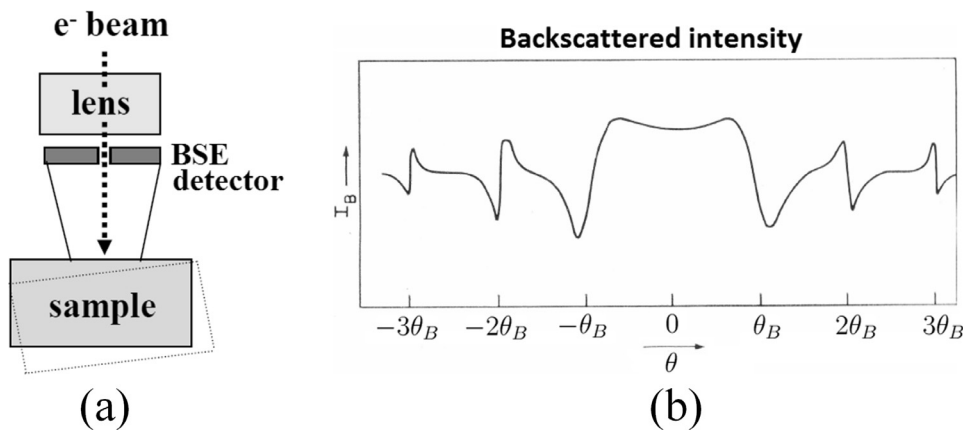


Figure 3.8 – (a) ECCI configuration of a SEM microscope; (b) electron backscattered intensity as a function of the incidence angle for a perfect crystal [Goldstein et al., 2005].

A dislocation close to the specimen surface creates a distortion of lattice planes. These planes deviate with respect to the Bragg condition. Therefore, a dislocation produces a contrast in the BSE intensity constituted by a positive and a negative intensity peak, as shown in Fig. 3.9 (a). An example of the contrast produced by single dislocations in a single crystal is shown in Fig. 3.9 (b).

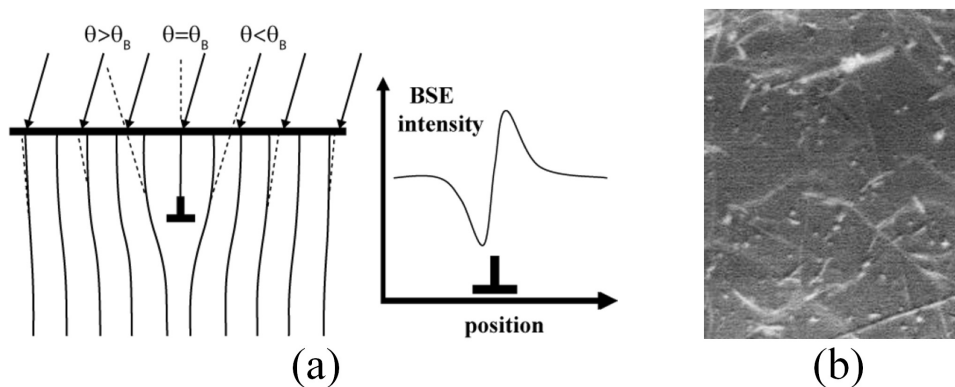


Figure 3.9 – (a) Lattice plane orientation around a dislocation and consequent BSE intensity. (b) Single dislocations imaged in a Si single crystal [Simkin and Crimp, 1999].

The advantages of ECCI over transmission electron microscopy (TEM) are the easier sample preparation and the larger analysed areas. The electron beam has usually an energy in the interval $10 \div 30$ KeV, for which the electron penetration depth in steel is typically around 400 nm [Drouin et al., 2007]. This is also the characteristic depth at which dislocations can be imaged. ECCI enables the observation of dislocations with different Burgers vectors.

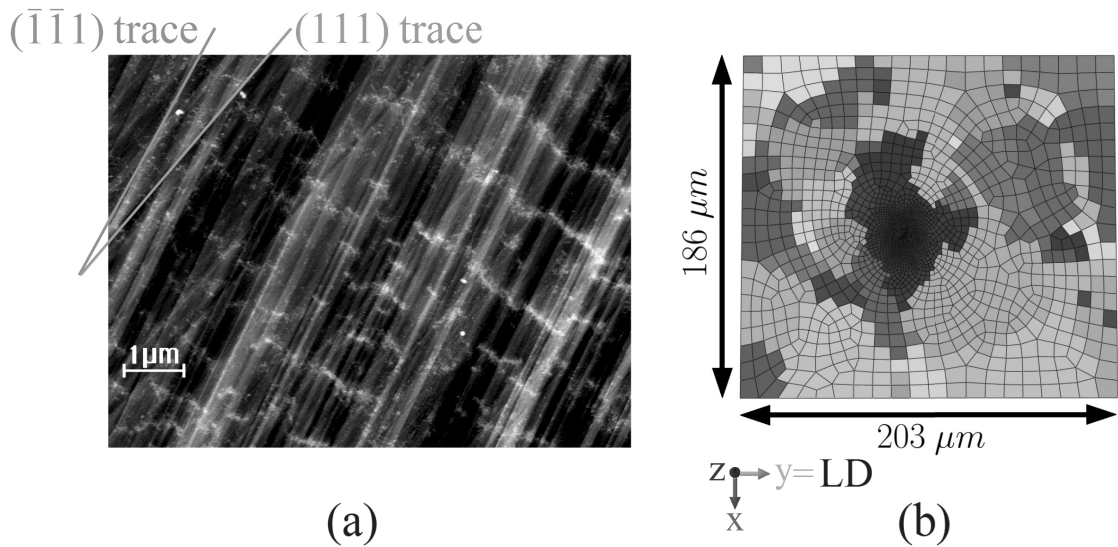


Figure 3.10 – (a) ECCI image taken in the centre of the $[3\ 29\ 1]$ -oriented grain after 50 cycles; (111) and $(\bar{1}\bar{1}\bar{1})$ slip plane traces are visible. (b) Simulation set-up of the polycrystalline structure (LD: loading direction).

Bone-shaped specimens are characterized using EBSD; they have a gauge length of 8 mm, a width of 2 mm and a thickness of 1 mm. The microstructure is fully austenitic with an average grain size of $60\ \mu\text{m}$ and random crystallographic texture. The specimens are deformed cyclically up to 100 cycles using a tensile-compression module under displacement control ($100\ \mu\text{m}$) with a strain rate of $0.5 \cdot 10^{-3}\ \text{s}^{-1}$. In situ DIC measurements [Raabe et al., 2001] are used to determine the local strain distribution. Two grains, whose orientations are close to $[3\ 29\ 1]$ and $[\bar{1}\ 19\ 0]$, are selected and analyzed by ECCI. Evidence of oriented dislocation walls are provided by ECCI observations, as shown in Fig. 3.10 (a) and 3.11 (a). EBSD data are used to build the corresponding polycrystal geometries in Fig. 3.10 (b) and 3.11 (b), whose dimensions are $6\ \mu\text{m} \times 203\ \mu\text{m} \times 186\ \mu\text{m}$ and $6\ \mu\text{m} \times 195\ \mu\text{m} \times 182\ \mu\text{m}$, and to assign the proper stiffness tensor to every grain depending on the orientation. The mesh used (Fig. 3.10 (b) and 3.11 (b)) is coarser in the grains surrounding the central one and refined in the centre, where $200\ \text{nm}$ elements are generated inside a parallelepiped with dimensions $4\ \mu\text{m} \times 4\ \mu\text{m}$ and depth $0.6\ \mu\text{m}$, close to the upper surface. Details of the mesh are shown in Fig. 3.12. The strain in the central grain is determined by the polycrystalline structure and by the boundary conditions, and can be predicted using this meshing technique. Dislocation structures are analyzed in the upper part of the central grain, where the mesh is refined, as shown in Fig. 3.12 (c). In the simulations a pure tension-compression cyclic deformation, with a period of $0.004\ \text{s}$ and a displacement amplitude of $1.48\ \mu\text{m}$ (Fig. 3.10 (b)) and $1.43\ \mu\text{m}$ (Fig. 3.11 (b)), is applied along the loading direction (LD). The deformation amplitude is chosen such that the local strain amplitude in the central grain is 0.95% , as measured by in situ DIC, and the strain rate is $9.5\ \text{s}^{-1}$. The strain rate in the simulation is higher than the experimental one in order to reduce the computational time. In a strain controlled test, the distance travelled by dislocations depends only on the strain increment if the dislocation density and stress distribution are

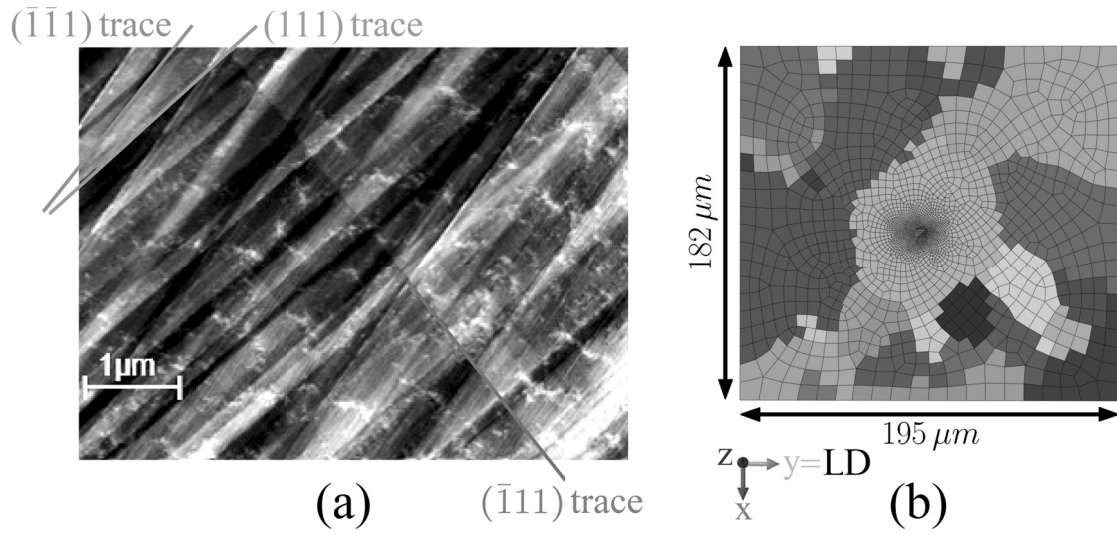


Figure 3.11 – (a) ECCI image taken in the centre of the $[\bar{1}190]$ -oriented grain after 100 cycles; (111) , $(\bar{1}\bar{1}1)$ and $(\bar{1}11)$ slip plane traces are visible. (b) Simulation set-up of the polycrystalline structure (LD: loading direction).

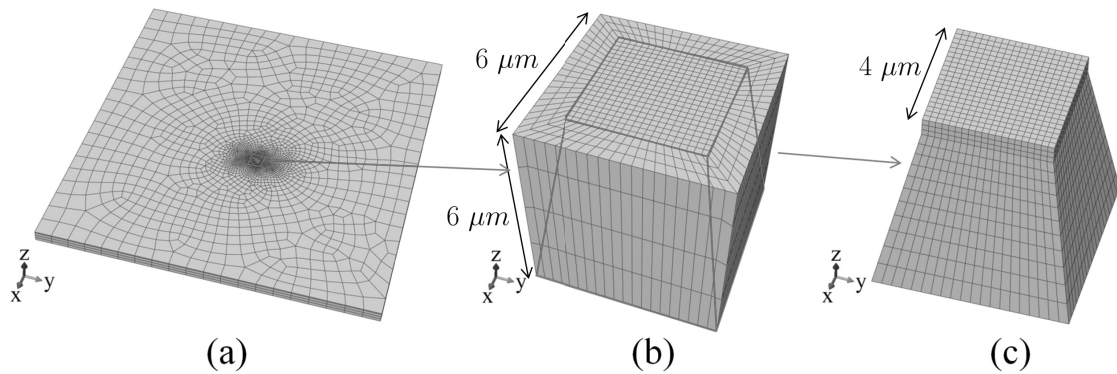


Figure 3.12 – (a) Mesh used for the simulation of the $[3291]$ -oriented grain; (b) detail of the central part of the mesh; (c) simulated dislocation structures are analyzed in the upper part, where 200 nm elements are generated.

3.4. Polycrystal simulations

| Edge-screw model | | Dislocation junction model | |
|---|---|--|--|
| $\rho_{e+} = 1 \cdot 10^{13} \text{ m}^{-2}$ | $\rho_{e-} = 1 \cdot 10^{13} \text{ m}^{-2}$ | $\rho_{//+} = 1 \cdot 10^{13} \text{ m}^{-2}$ | $\rho_{//-} = 1 \cdot 10^{13} \text{ m}^{-2}$ |
| $\rho_{s+} = 1 \cdot 10^{13} \text{ m}^{-2}$ | $\rho_{s-} = 1 \cdot 10^{13} \text{ m}^{-2}$ | $\rho_{\Gamma+} = 1 \cdot 10^{13} \text{ m}^{-2}$ | $\rho_{\Gamma-} = 1 \cdot 10^{13} \text{ m}^{-2}$ |
| $\rho_{e+,s+} = 1 \cdot 10^{11} \text{ m}^{-2}$ | $\rho_{e+,s-} = 1 \cdot 10^{11} \text{ m}^{-2}$ | $\rho_{//+, \Gamma+} = 1 \cdot 10^{11} \text{ m}^{-2}$ | $\rho_{//+, \Gamma-} = 1 \cdot 10^{11} \text{ m}^{-2}$ |
| $\rho_{e-,s+} = 1 \cdot 10^{11} \text{ m}^{-2}$ | $\rho_{e-,s-} = 1 \cdot 10^{11} \text{ m}^{-2}$ | $\rho_{//-, \Gamma+} = 1 \cdot 10^{11} \text{ m}^{-2}$ | $\rho_{//-, \Gamma-} = 1 \cdot 10^{11} \text{ m}^{-2}$ |
| $B = 100 \text{ } (\mu\text{m/s})/\text{MPa}$ | $v_{max} = 1000 \text{ } \mu\text{m/s}$ | $B = 100 \text{ } (\mu\text{m/s})/\text{MPa}$ | $v_{max} = 1000 \text{ } \mu\text{m/s}$ |

Table 3.4 – Initial dislocation densities and kinetics parameters in the simulations using the edge-screw and dislocation junction model.

uniform. This is because, according to Orowan's law (1.12), the plastic strain rate is directly proportional to the dislocation velocity. When dislocation non-uniformities are present, the dislocation configuration can be affected by the strain rate if the effective shear stress τ_{eff} , defined in (2.8), becomes comparable with the difference between the threshold stress τ_{th}^{α} in low and high dislocation density regions. This is due to the additional stress necessary to move dislocations in low dislocation density regions, compared with the threshold stress τ_{th}^{α} , during a higher strain rate simulation. This higher stress can move dislocations in high dislocation density regions at a strain amplitude smaller than in lower strain rate simulations. The typical effective resolved shear stress in our simulations is around 20 MPa, while the difference in threshold stress is around 100 MPa. Additionally, experimental investigations made at a deformation frequency around 1 Hz [Laird et al., 1986] and around 0.01 Hz [Pham et al., 2011] show a similar geometry of the labyrinth structures. It is worth to note that our strain rate is smaller than the one used in discrete dislocation dynamics simulations, which is typically around 10^4 s^{-1} [Fivel, 2008]. Average values of initial dislocation densities in the simulations and kinetics parameters are summarized in Tab. 3.4. Random non-uniformities of 10% are added. The $6 \text{ } \mu\text{m}$ thickness, shown in Fig. 3.12 (b), of the representative volumes is chosen based on the typical dislocation travel distance. If the initial dislocation densities in Tab. 3.4 are used in Orowan's law (1.12), then the dislocation travel distance is around $1 \text{ } \mu\text{m}$ and the surface effects due to dislocations exiting the geometry through the bottom surface of the representative volumes in Fig. 3.10 (b) and Fig. 3.11 (b) are minimized. The typical dislocation velocity, according to the imposed strain rate and Orowan's law (1.12), is around $10^3 \text{ } \mu\text{m/s}$, which corresponds to the limit imposed on the dislocation velocity. Thus, the velocity limit does not affect the behaviour of dislocations, apart from those in elements where the dislocation density becomes temporary close to zero, as stated in section 2.1.

3.4.1 Dislocation patterning in the $[3\ 29\ 1]$ -oriented grain

The slip traces visible in Fig. 3.10 (a) belong to (111) and $(\bar{1}\bar{1}1)$ planes. As revealed by Schmid factor analysis, the two most active slip systems are $[01\bar{1}](111)$ and $[011](\bar{1}\bar{1}1)$. This last slip system is taken as reference to define the dislocation junction vector \vec{l}_{lock} in Fig. 3.3 (a). The simulated total dislocation density after 50 cycles in the central grain is shown in

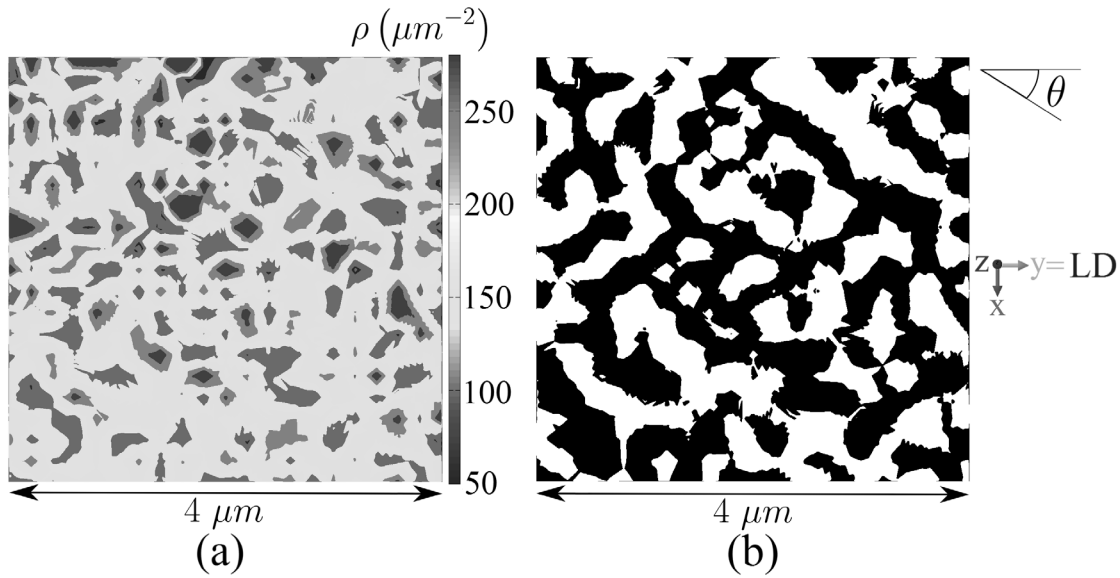


Figure 3.13 – (a) Total dislocation density in the centre of the $[3\ 29\ 1]$ -oriented grain after 50 cycles using the dislocation junction model. (b) Black and white conversion used to calculate the 2D orientation distribution function and dislocation line orientation angle θ .

Fig. 3.13 (a) using the dislocation junction model and in Fig. 3.14 (a) using the edge-screw model. Dislocation walls separated by low dislocation density regions are observed using both models. This density has been found by averaging the total dislocation density at a depth of 100 nm and 300 nm, i.e. in the centre of the two elements that are closest to the upper surface in Fig. 3.12 (c), this in order to be comparable to the analysis depth of ECCI experiments. Indeed, the penetration depth of 30 keV electrons, used in the experiments, is around 400 nm Drouin et al. [2007] and the dislocation contrast decays exponentially with depth Zaerrerer and Elhami [2014]. The maximum dislocation density within the dislocation structures ρ_{peak} for all the slip systems is shown in Fig. 3.15 (a) for the edge-screw model and in Fig. 3.15 (b) for the dislocation junction model. This quantity represents the contribution of the different slip systems to the formation of dislocation structures. The slip systems $[011](\bar{1}\bar{1}\bar{1})$ and $[110](\bar{1}\bar{1}\bar{1})$ have higher ρ_{peak} for the edge-screw model, while the slip systems $[1\bar{1}0](111)$ and $[011](\bar{1}\bar{1}\bar{1})$ give the major contribution for the dislocation junction model. In Fig. 3.13 (b) and 3.14 (b) the dislocation line orientation angle θ for edge, screw, \parallel and Γ dislocations is reported. A quantitative analysis of the orientation of walls is made using the 2D orientation distribution function [Gasparyan and Ohanyan, 2015]. The black and white conversion of the simulated images is shown in Fig. 3.13 (b) and Fig. 3.14 (b). The value of the dislocation density in the white regions is greater than $175\ \mu\text{m}^{-2}$. This value has been selected to identify connected walls.

The 2D orientation distribution as a function of the angle θ is shown in Fig. 3.16 (b) for the dislocation junction model (continuous line) and for the edge-screw model (dashed line). A fixed length of about $L = 780\ \text{nm}$ is used. The choice of L in an interval between 620 nm and 940 nm does not affect the position of the maxima of the 2D orientation distribution function,

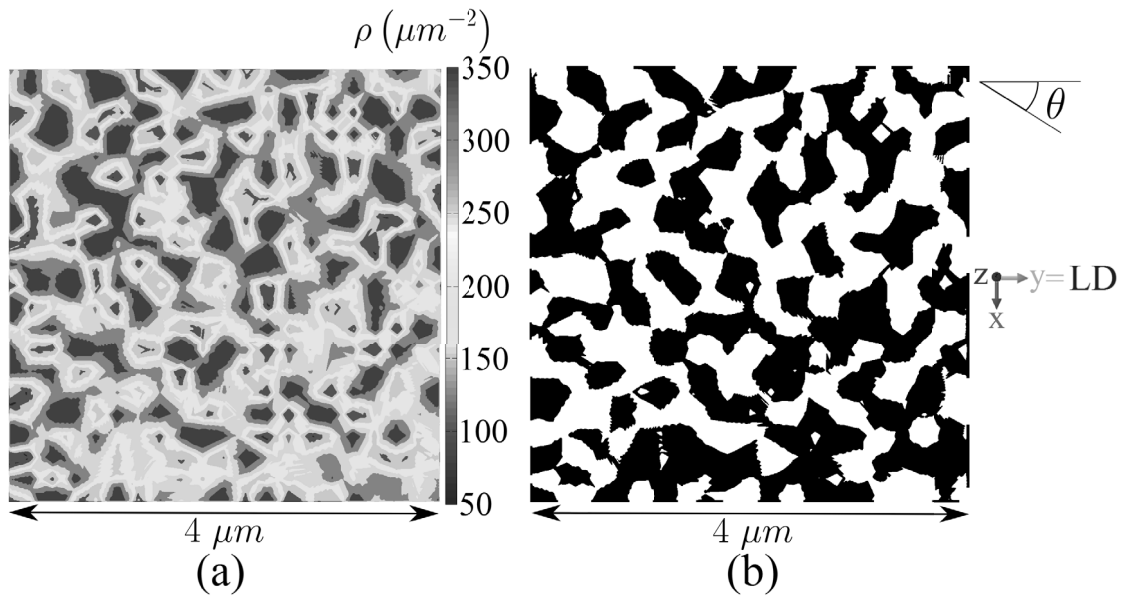


Figure 3.14 – (a) Total dislocation density in the centre of the $[3\ 29\ 1]$ -oriented grain after 50 cycles using the edge-screw dislocation model. (b) Black and white conversion used to calculate the 2D orientation distribution function and dislocation line orientation angle θ .

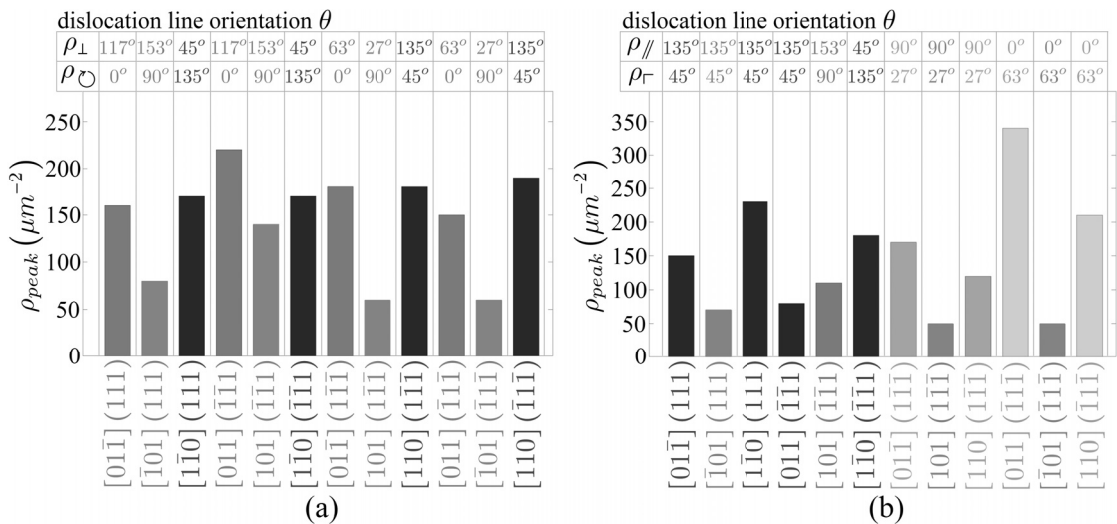


Figure 3.15 – Maximum dislocation density ρ_{peak} in the centre of the $[3\ 29\ 1]$ -oriented grain after 50 cycles on all the slip systems using (a) the edge-screw model and (b) the dislocation junction model.

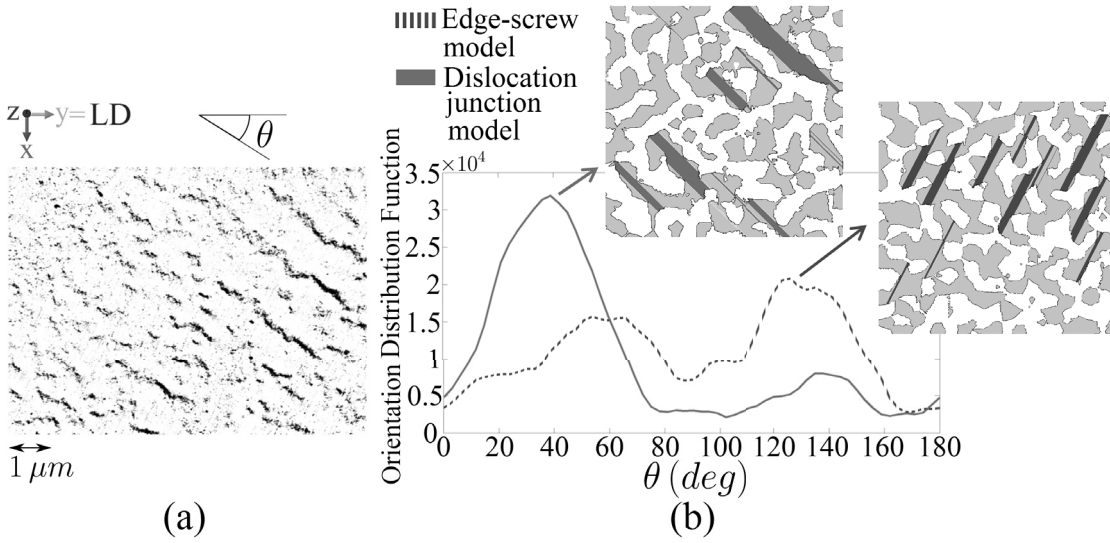


Figure 3.16 – (a) ECCI image in the centre of the $[3\ 29\ 1]$ -oriented grain processed using a Gaussian filter to remove slip lines, dislocation structures have a dark contrast. (b) 2D orientation distribution function for the edge-screw and the dislocation junction model.

as shown in Fig. 3.20 (a). The 2D orientation distribution function has the highest peak around 40 degrees for the dislocation junction model, an orientation close to Γ segments of the slip systems $[1\bar{1}0](111)$ and $[011](\bar{1}\bar{1}\bar{1})$, and around 120 degrees for the edge-screw model, an orientation close to the edge segments of the slip systems $[011](\bar{1}\bar{1}\bar{1})$ and $[110](\bar{1}\bar{1}\bar{1})$. The line segments oriented at $\theta = 45^\circ$ for the dislocation junction model and at $\theta = 117^\circ$ for the edge-screw model are shown in Fig. 3.16 (b). In the filtered ECCI image in Fig. 3.16 (a) dislocation walls are mainly parallel to the $[110]$ direction, in better agreement with the results of the dislocation junction model.

If the value of the dislocation density in the white regions is increased to $225\ \mu\text{m}^{-2}$, then these regions appear unconnected, as shown in Fig. 3.17 (a). This can be explained by the element size (200 nm), which is comparable to the experimentally observed thickness of labyrinth walls [Jin and Winter, 1984]. The corresponding 2D orientation distribution as a function of the angle θ is shown in Fig. 3.17 (b) for the dislocation junction model. Two different values of L (500 nm and 700 nm) are used. Two peaks around 50 and 120 degrees are present for $L = 500$ nm, which are similar to the ones in Fig. 3.16 (b), while the maximum of the distribution is at $\theta = 0^\circ$. However, for $L = 700$ nm, the 2D orientation distribution function is zero almost everywhere and no orientations can be identified. This justifies the choice of the threshold density $175\ \mu\text{m}^{-2}$ to identify dislocation walls with a length comparable to the one in the ECCI image in Fig. 3.16 (a).

3.4.2 Dislocation patterning in the $[\bar{1}\ 19\ 0]$ -oriented grain

The slip traces visible in Fig. 3.11 (a) belong to (111) , $(\bar{1}\bar{1}\bar{1})$ and $(\bar{1}11)$ planes. By contrast, the two slip systems with the highest Schmid factor (0.429) are $[011](1\bar{1}\bar{1})$ and $[0\bar{1}\bar{1}](\bar{1}11)$. The

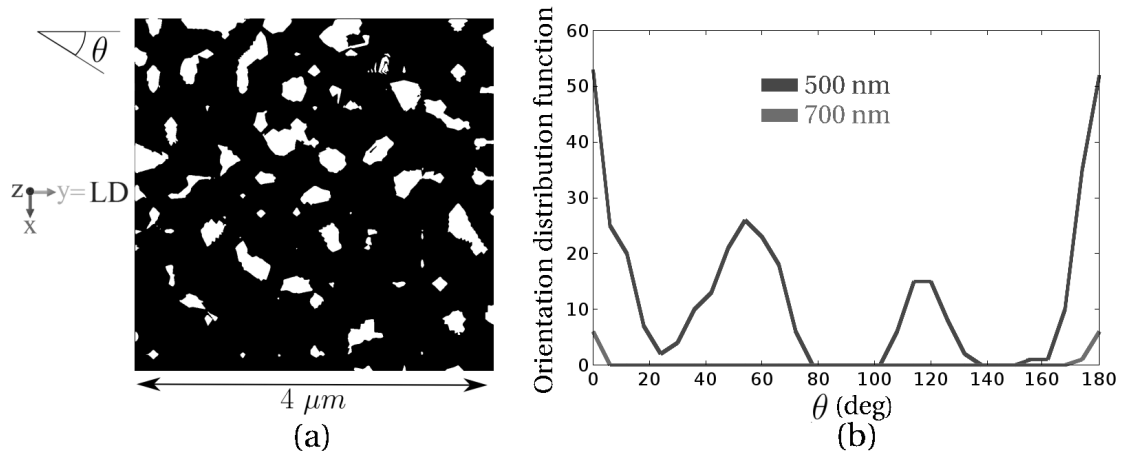


Figure 3.17 – (a) Black and white conversion of the dislocation density in the centre of the $[3\ 29\ 1]$ -oriented grain (Fig. 3.14 (a)) for the dislocation junction model and (b) corresponding 2D orientation distribution function.

two slip systems with the second highest Schmid factor (0.406) $[1\bar{1}0](111)$ and $[1\bar{1}0](\bar{1}\bar{1}1)$ are likely to be active. This last slip system is taken as reference to define the dislocation junction vector \vec{l}_{lock} . The simulated total dislocation density after 100 cycles in the central grain is shown in Fig. 3.18 (a) using the dislocation junction model. The maximum dislocation density ρ_{peak} is shown in Fig. 3.18 (b) and it is highest for the slip systems $[1\bar{1}0](111)$ and $[1\bar{1}0](\bar{1}\bar{1}1)$. Thus, CPFÉ simulations can predict the activation of these two collinear slip systems and show that the influence of neighbouring grains is changing the slip activity in the central one with respect to an equally oriented single crystal. Indeed, active slip systems interacting by the collinear interaction are not commonly observed in copper single crystals [Devincre et al., 2006], [Devincre et al., 2005]. When the two collinear slip systems are active, the dislocation junction model and the edge-screw model are identical because screw and \parallel dislocation lines coincide. The 2D orientation distribution function for the $[\bar{1}\ 19\ 0]$ -oriented grain is shown in Fig. 3.19 (b), where a length of about $L = 860$ nm is used. The choice of L in an interval between 780 nm and 940 nm does not affect the position of the maxima of the 2D orientation distribution function, as shown in Fig. 3.20 (b). Four maxima around 0° , 45° , 63° , 135° are present. The $\theta = 45^\circ$ and $\theta = 135^\circ$ orientations correspond to \parallel and Γ dislocations of the two active collinear slip systems. In the filtered ECCI image in Fig. 3.19 (a) several orientations of the dislocation walls are visible: 0° coincides with the orientation of Γ dislocations of the $[011](\bar{1}\bar{1}1)$ slip system, 27° and 90° with Γ and \parallel dislocations on the $(1\bar{1}\bar{1})$ slip plane. Some other walls with an orientation around 170° can also be identified.

In the following the simulation results are compared with the existing dislocation-based models described in section 1.6 and 3.1.

Comparison between the junction model and the edge-screw models. The simulation

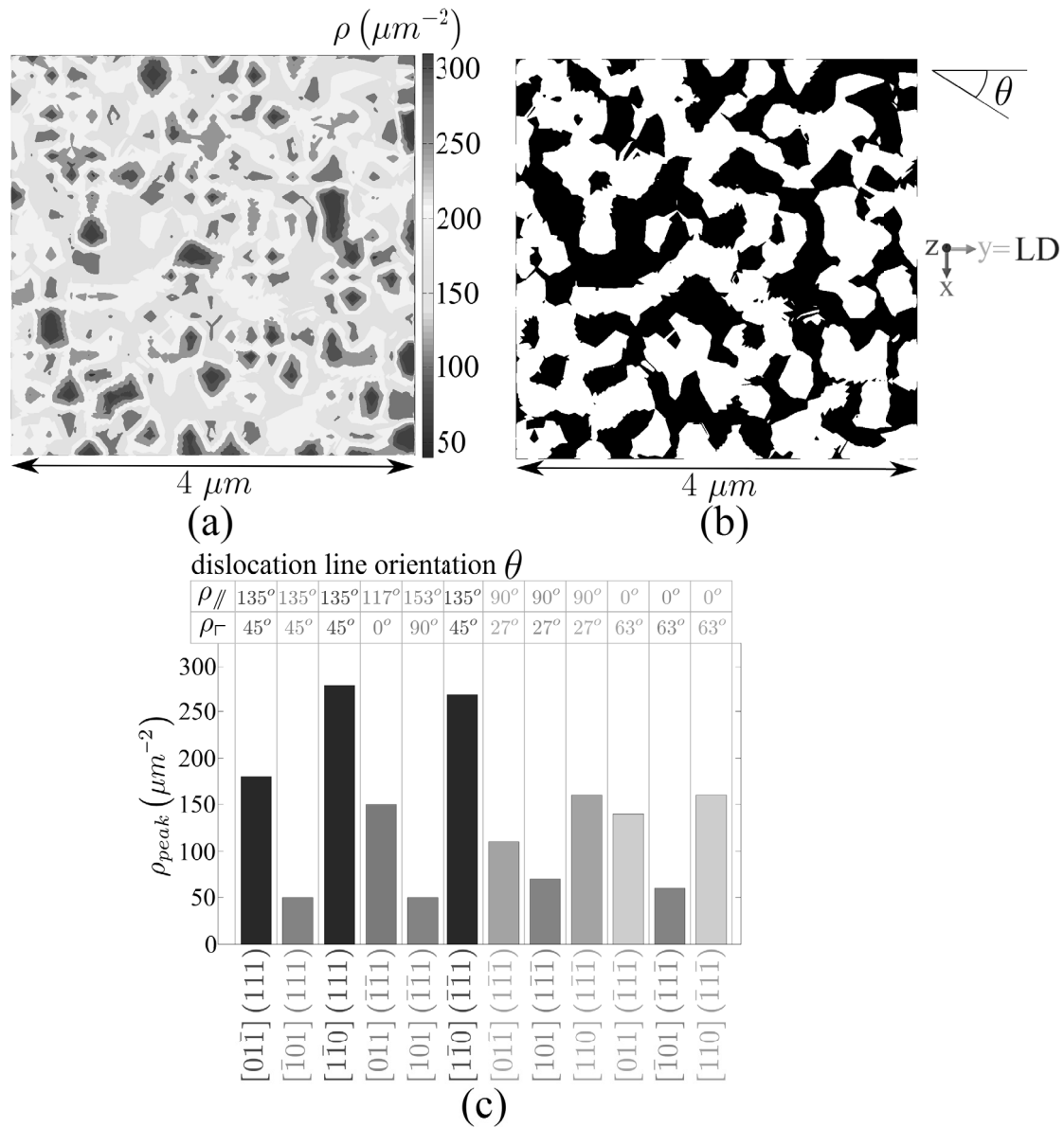


Figure 3.18 – (a) Total dislocation density in the centre of the $[\bar{1} 19 0]$ -oriented grain after 100 cycles using the dislocation junction model. (b) Black and white conversion used to calculate the 2D orientation distribution function and dislocation line orientation angle θ . (c) Maximum dislocation density ρ_{peak} in the centre of the $[\bar{1} 19 0]$ -oriented grain after 100 cycles on all the slip systems using the dislocation junction model.

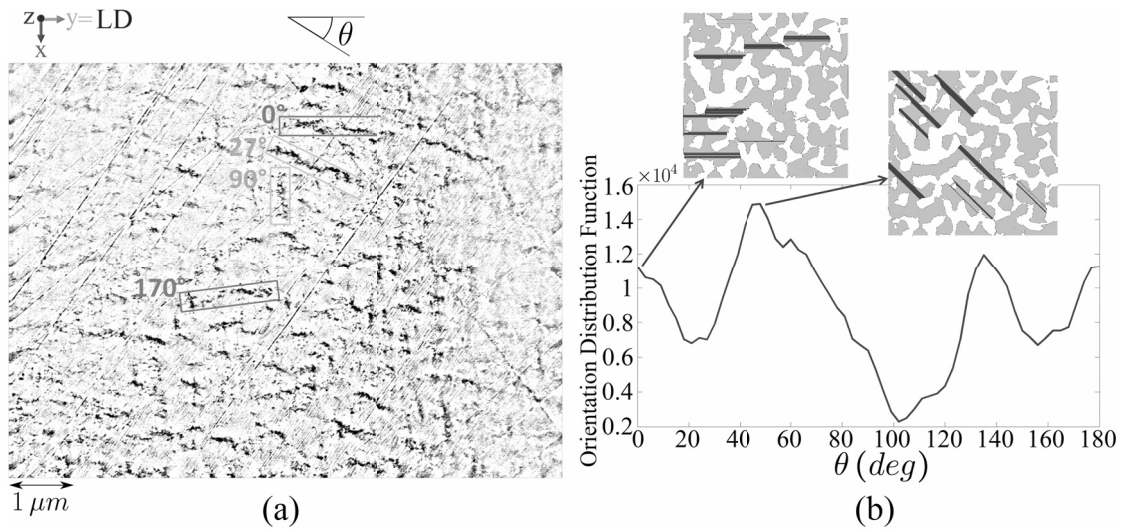


Figure 3.19 – (a) ECCI image in the centre of the $[\bar{1} 19 0]$ -oriented grain processed using a Gaussian filter to remove slip lines, dislocation structures have a dark contrast, examples of oriented walls are enclosed by rectangles. (b) 2D orientation distribution function for the simulated dislocation density in Fig. 3.18 (a).

3.18 (a).

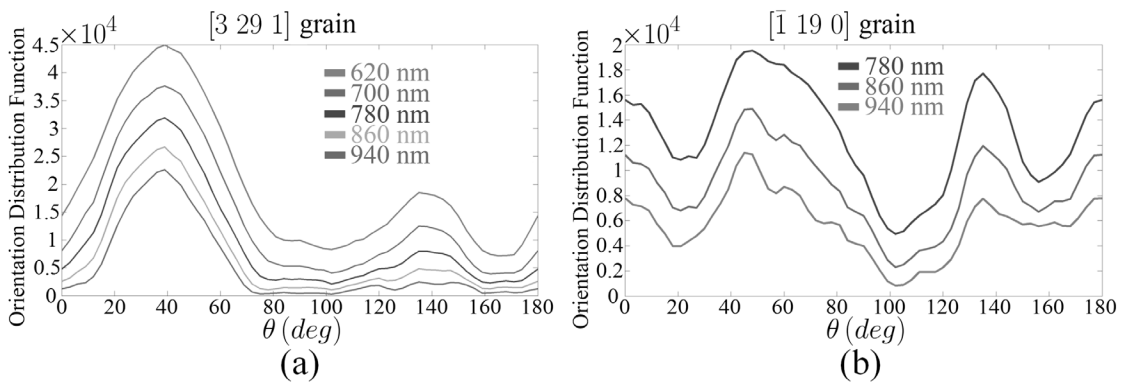


Figure 3.20 – (a) Orientation distribution functions of the image in Fig. 3.13 for five different values of L . (b) Orientation distribution functions of the image in Fig. 3.18 (a) for three different values of L .

of the $[3\ 29\ 1]$ -oriented grain can be used to distinguish between the predictions of the dislocation junction and the edge-screw model, explained in section 3.1. When using the edge-screw model, walls parallel to the edge dislocation segments of the two slip systems with highest Schmid factor form (Fig. 3.15 (a) and 3.16 (b)), which are mostly constituted by edge dislocations. This is due to the high density of edge dislocations on the active slip systems after many cycles. Indeed, the annihilation distance for edge dislocations \hat{d}_e is lower than for screw dislocations, as reported in Tab. 2.1. Edge dislocations move along their Burgers vector and interact, forming dislocation walls. Thus, the simulated channels tend to assume the shape of edge dislocation segments that moved away. By contrast, the dislocation junction model predicts that $\rho_{//}$ and ρ_{\perp} dislocation densities have the same order of magnitude after many cycles because their annihilation rate equations, like (3.8), involve both distances \hat{d}_e and \hat{d}_s . ρ_{\perp} dislocations of the slip systems $[01\bar{1}](111)$ and $[011](\bar{1}\bar{1}1)$ get away from forming low density regions along directions parallel to the dislocation junction vector between these two slip planes, which in this case is $\vec{l}_{lock} = [1\bar{1}0]$. Thus, many dislocation walls form perpendicular to \vec{l}_{lock} and this orientation is at around $\theta = 45^\circ$ to the loading direction, in agreement with the experimental results in Fig. 3.16 (a) and by L'Esperance et al. [L'Esperance et al., 1986], who found wall orientations intermediate between $\{100\}$ and $\{210\}$.

In the $[\bar{1}\ 19\ 0]$ -oriented grain, the $\theta = 90^\circ$ orientation is explained by the model as dislocation junctions at the intersection between the $(\bar{1}\bar{1}1)$ and the $(\bar{1}11)$ slip planes. The predicted $\theta = 45^\circ$ orientation corresponds to Γ dislocations of the two active collinear slip systems and the closest observed orientation is at around $\theta = 27^\circ$, as shown in Fig. 3.19 (a), which coincides with the orientation of Γ dislocations on the $(1\bar{1}\bar{1})$ slip plane. The dominant $\theta = 0^\circ$ orientation in the experimental image in Fig. 3.19 (a), compared with the 2D orientation distribution function in Fig. 3.19 (b), can be due to the lack of dislocation junctions between the slip planes (111) and $(1\bar{1}\bar{1})$ in the model, forming dislocation walls with $\theta = 0^\circ$ orientation. Indeed the slip system $[1\bar{1}0](\bar{1}\bar{1}1)$, and not $[1\bar{1}0](111)$, is taken as reference to define the dislocation junction vector \vec{l}_{lock} . A model with more state variables for every slip system would be required to capture all possible dislocation junctions. For instance, one dislocation density could be defined for every couple of slip systems to describe dislocation segments aligned with the corresponding dislocation junction. The activity of the $(1\bar{1}\bar{1})$ slip system can also be underestimated in the simulation because the subsurface microstructure is not considered.

Comparison with reaction-diffusion models. The reaction-diffusion approaches presented in section 1.6 model the motion of dislocations using diffusion and flux terms in the constitutive equations. In the model by Pontes et al. [Pontes et al., 2006], the motion of dislocations on two slip systems takes place along the two orthogonal Burgers vectors respectively. Consequently low density regions form perpendicular to the Burgers vector directions and not, as observed experimentally, perpendicular to the dislocation junction line. The lack of dislocation junctions in the model, therefore, leads to incorrect predictions. Reaction-diffusion models are valuable to understand the characteristic length scale of dislocation structures, which is determined by the balance between dislocation interaction strength and dislocation mobility. According to (1.7), the distance between dislocation walls increases if the coefficient γ that determines the amount of immobile dislocations, called pinning rate in their model, or the homogeneous steady state dislocation density $\rho_{0,S}$ decreases. This applies also to our simulations: the small annihilation distance for edge dislocations \hat{d}_e leads to a higher homogeneous steady state dislocation density in the edge-screw model than in the dislocation junction model. Therefore a larger length scale is predicted by the dislocation junction model. Additionally, a higher average dislocation density is predicted by the edge-screw model, as shown by the higher volume fraction of dislocation structures in Fig. 3.14 (a) than in Fig. 3.13 (a). The characteristic distance between dislocation walls is in the range $0.3 \div 0.6 \mu\text{m}$ for the edge-screw model in Fig. 3.14 (a) and $0.6 \div 0.8 \mu\text{m}$ for the dislocation junction model in Fig. 3.13 (a), which better agrees with the experimental image in Fig. 3.16 (a).

Comparison with the double pseudo-polygonisation arrangement theory. The double pseudo-polygonisation (DPP) arrangement theory of Dickson [Dickson et al., 1986a], explained in section 1.6, predicts energetically favourable wall orientations perpendicular to the directions that bisect the obtuse and acute angles between the edge dislocation lines on the two slip systems. According to Table 1 in Dickson et al. [1986a] these directions are $[001]$ and $[\bar{2}10]$ for the $[3\ 29\ 1]$ -oriented grain. This second type of walls is oriented at $\theta = 27^\circ$ with the loading direction, similar to the value $\theta = 45^\circ$ predicted using the dislocation junction model. Therefore, the experimental image in Fig. 3.16 (a) cannot be used to discriminate between the Dickson's theory and the dislocation junction model. However, the edge-screw model predicts $\theta = 117^\circ$ as the main wall orientation, which is not observed experimentally.

The simulation of the $[\bar{1}\ 19\ 0]$ -oriented grain is used to examine the case of two active collinear slip systems on conjugate slip planes, in our case $[1\bar{1}0](111)$ and $[1\bar{1}0](\bar{1}\bar{1}1)$, not considered by the DPP theory of Dickson et al. [Dickson et al., 1986a]. By applying

the DPP theory criterion, the dislocation walls result perpendicular to $[001]$ and $[110]$. This second type of walls would be oriented at $\theta = 135^\circ$ with the loading direction but they are not evident in the experimental image in Fig. 3.19 (a), being $\theta = 170^\circ$ the closest visible orientation. The $\theta = 135^\circ$ orientation corresponds to one of the four maxima of the 2D orientation distribution function in Fig. 3.19 (b) and these walls are constituted by // dislocations forming collinear junctions. However, the collinear junction involves an annihilation of dislocation segments along the intersection of the two slip planes (111) and $(\bar{1}\bar{1}1)$ [Madec et al., 2003] and this can explain why this orientation is not visible in the experiment. Dislocation walls oriented at $\theta = 0^\circ$ are predicted by the dislocation junction model as formed by dislocations on the $(\bar{1}\bar{1}1)$ slip plane, while the DPP theory criterion is not able to explain them.

Comparison with the Li formation mechanism. The formation mechanism of dislocation structures proposed by Li [Li et al., 2011], shown in Fig. 1.12 (b), does not predict walls perpendicular to the $[\bar{2}10]$ or $[1\bar{1}0]$ direction. This theory predicts that the interaction of edge dislocations of the two mainly active slip systems creates walls perpendicular to the sum and difference of the two Burgers vectors, which in our case are $[001]$ and $[010]$. Walls perpendicular to the $[010]$ direction ($\theta = 90^\circ$ orientation) are more common for the edge-screw model than for the dislocation junction model, as shown by the 2D orientation distribution function in Fig. 3.16 (b), but they are not observed in the experimental image in Fig. 3.16 (a). By contrast, our dislocation junction model predicts that dislocation walls are formed when Γ dislocations move and interact forming immobile structures. This behaviour cannot be captured by models based solely on edge and screw dislocations.

In conclusion, the developed junction model predicts dislocation walls, arising from a random initial dislocation distribution, oriented parallel to the $[110]$ direction, which were not captured by existing reaction-diffusion models Pontes et al. [2006] and by low energy theories. The interpretation of electron channeling contrast imaging analyses of fatigued austenitic steel is improved, because our model identifies the interactions that cause the formation of this type of observed dislocation walls as the interactions between dislocations parallel and perpendicular to the dislocation junction line. The introduction of the dislocation junction mechanism is shown to be essential in continuum constitutive equations when describing fatigue on a sub-micrometer length scale.

4 Comparison between simulation and synchrotron Laue microdiffraction experiments

In this chapter the single and multiple slip edge-screw dislocation-based models are used to predict the crystal lattice rotation at the sub-dislocation structure length scale. For validation, the results are compared to Laue microdiffraction experiments carried out on copper single crystals [Irastorza-Landa et al., 2016]. First, the methods to calculate the crystal lattice rotation in the CPFEE framework and in the experiment are explained and compared. The relationship between the rotation components and the dislocation content is expressed in terms of the Kröner-Nye tensor. The experiment has revealed misoriented regions influenced by pre-existing plastic deformations. This has motivated specific calculations. The effect of the initial crystal lattice orientation, induced by these pre-existing deformations, on the subsequent evolution is studied using a phenomenological plasticity model and interpreted with the stiffness tensor. The correlation between dislocation patterning and crystal rotation is studied using a refined mesh and the dislocation based model. A highly misoriented area found in the experiment is explained with the behaviour of immobile dislocation clusters with different shapes. Finally, the interpretation of the simulation results is discussed and compared with previous X-ray experiments on cyclically deformed samples [Mughrabi and Obst, 2005].

4.1 Crystal lattice rotation in the CPFEE framework

Using CPFEE method one can compute the components of the crystal lattice rotation by polar decomposition of the elastic strain gradient. The plastic deformation gradient \mathbf{F}_p does not incorporate a rotation, while the elastic deformation gradient \mathbf{F}_e can be decomposed as [Eberl et al., 2002]:

$$\mathbf{F}_e = \mathbf{R}_e \cdot \mathbf{U}_e , \quad (4.1)$$

where \mathbf{R}_e is a rotation matrix and \mathbf{U}_e represents a pure stretching. According to Euler's rotation theorem, \mathbf{R}_e can be represented by a rotation vector $\hat{\mathbf{e}}$ and a rotation angle θ . The rotation

Chapter 4. Comparison between simulation and synchrotron Laue microdiffraction experiments

components are defined as:

$$\theta_x = \theta \cdot \hat{\mathbf{e}}_x, \quad (4.2)$$

$$\theta_y = \theta \cdot \hat{\mathbf{e}}_y, \quad (4.3)$$

$$\theta_z = \theta \cdot \hat{\mathbf{e}}_z. \quad (4.4)$$

In case of small rotation angles, as for the Laue microdiffraction experiment, θ_x , θ_y and θ_z represent the values of three different rotations around the coordinate axes x , y and z , whose composition gives the total rotation. This approximation is in general not true for large rotations [Goldstein et al., 2000], because in 3D they are not commutative. The rotation components θ_x , θ_y and θ_z are the observables of the Laue microdiffraction experiments.

4.2 Relationship between the rotation components and the dislocation content

The elastic strain gradient \mathbf{F}_e can be decomposed in the sum of an elastic strain tensor ε_{ij}^e (representing a stretching) and a lattice rotation tensor ω_{ij}^e (representing a spin) [McHugh, 2004]. This last tensor is related to the rotation components in (4.2)-(4.4) by:

$$\omega_{ij}^e = -\varepsilon_{ijk} \theta_k, \quad (4.5)$$

where ε_{ijk} is the permutation symbol. As shown by Kröner [E., 1955], considering the lattice mismatch produced by a set of N dislocations (indexed by n), there is a relationship between their Burgers vectors b_i^n , their dislocation lines l_i^n and the curl of the elastic deformation gradient:

$$\sum_{n=1}^N b_i^n l_k^n \delta(\vec{x} - \vec{x}^n) = - \sum_{l,j=1}^3 \varepsilon_{klj} \frac{\partial \mathbf{F}_{e,ij}}{\partial x_l}. \quad (4.6)$$

The left hand side of (4.6) is referred as the Kröner-Nye tensor and indicated as α_{ik} . In the absence of an elastic strain tensor ($\varepsilon_{ij}^e = 0$), which is a realistic condition at zero stress, there is a simplified relationship between the Kröner-Nye tensor and the rotation components [Pantleon, 2008]:

$$\alpha_{xy} = k_{yx} = \frac{\partial \theta_y}{\partial x}, \quad (4.7)$$

$$\alpha_{xz} = k_{zx} = \frac{\partial \theta_z}{\partial x}, \quad (4.8)$$

4.2. Relationship between the rotation components and the dislocation content

$$\alpha_{yx} = k_{xy} = \frac{\partial \theta_x}{\partial y}, \quad (4.9)$$

$$\alpha_{yz} = k_{zy} = \frac{\partial \theta_z}{\partial y}, \quad (4.10)$$

$$\alpha_{zz} = -k_{xx} - k_{yy}. \quad (4.11)$$

These equations allow to find the five accessible Kröner-Nye tensor components using only derivatives along x and y . This allows an estimation of Kröner-Nye tensor components using EBSD [Pantleon, 2008] or transmission X-rays analysis [Larson et al., 2008]. The approximation used in (4.7)-(4.11) is valid if ε_{ij}^e is much smaller than ω_{ij}^e , which does not contribute to the stress tensor.

The same procedure to find these accessible components can be carried out using CPFÉ simulations: first the rotation components (4.2)-(4.4) are found from the elastic deformation gradient \mathbf{F}_e , then the rotation gradients and Kröner-Nye tensor components in (4.7)-(4.11) are calculated. With this method, the α_{ij} components, that would be found if the real specimen has the same elastic and plastic strain state of the virtual one, can be calculated. Therefore, the comparison between the α_{ij} found in experiments and simulations is not subject to the approximation ($\varepsilon_{ij}^e = 0$), while this is the case for the interpretation of rotation gradients in terms of GND density.

A simple case to understand the relationship between rotation components and dislocations is shown in Fig. 4.1. The crystal lattice rotation is caused by gradients of the plastic strain along the Burgers vector direction [Arsenlis and Parks, 1999]. Three regions with different plastic behaviours are represented using three parallelepipeds. If the central region does not accommodate plasticity because inside it the motion of dislocations is prevented, then a gradient of the plastic strain γ_p^α along the Burgers vector direction (y axis) is present. Edge dislocations, moving in the two lateral regions, stop when they reach the interface with the central region, as shown in Fig. 4.1, and they form walls constituted of signed edge dislocations, called geometrically necessary dislocations (GNDs). Therefore, GNDs appear at the interface between high and low plastic strain regions in order to maintain continuity in the crystal. The mathematical relationship between the plastic strain and the edge GND density is:

$$\rho_{e,GND}^\alpha b = -\nabla \gamma_p^\alpha \cdot \mathbf{m}^\alpha. \quad (4.12)$$

The displacement continuity between the high and low plastic strain region leads to a crystal lattice rotation, as shown in Fig. 4.1. This rotation compensates for the strain incompatibility and it has opposite sign in the high and low plastic strain regions. For instance, in equation (4.6) and in the idealized case represented in Fig. 4.1, only edge dislocations are present (only

Chapter 4. Comparison between simulation and synchrotron Laue microdiffraction experiments

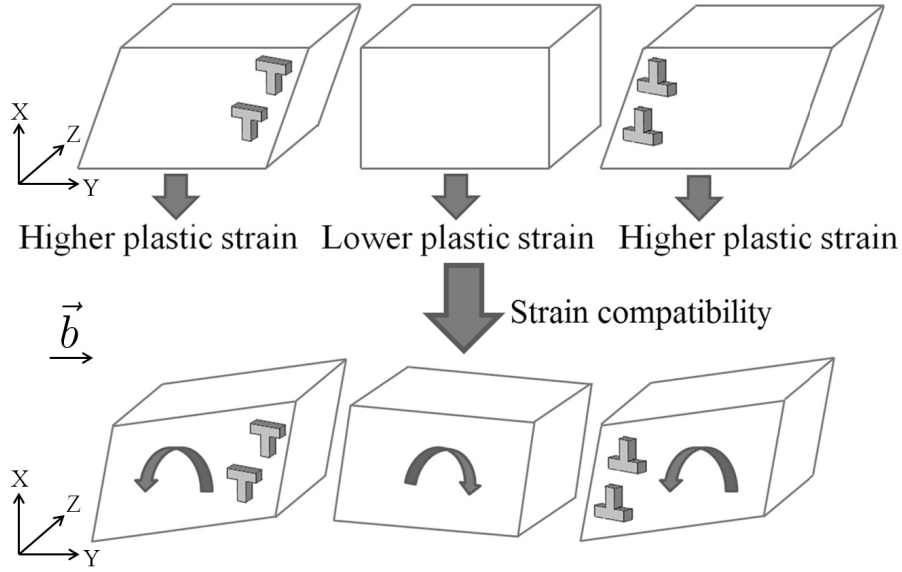


Figure 4.1 – Schematic process through which edge GNDs accumulate and the crystal lattice rotates.

α_{yz} is non zero) and only the component $\omega_{xy}^e = \theta_z$ has a gradient along the Burgers vector direction (y). In the lower part of Fig. 4.1 the approximation $\varepsilon_{ij}^e = 0$ is valid, if no external constraints are imposed on the relaxed configuration. The two higher plastic strain regions accommodate plastic strain and rotation, while the lower plastic strain region accommodates only rotation. Both plastic deformation and rotation do not contribute to the stress tensor, therefore the stress equilibrium condition between the lower and the higher plastic strain regions is satisfied. In this case the rotation component θ_z is equal to the accommodated plastic strain amplitude γ_p^α in the higher plastic strain regions. As shown in the following, the experimental rotation angle reaches a value $\theta_z \approx 0.25^\circ = 0.0044$ radians, while the plastic strain amplitude γ_p^α goes up to $0.295\% = 0.00295$. Using this simplified comparison, a difference of around 30% between the Nye tensor components and the rotation gradients can be expected. Another quantity that will be used in the following is the so-called “apparent” GND density that is the sum of all available components of α_{ij} [Gupta and Agnew, 2010]:

$$\rho_{app} = \frac{1}{b} \cdot (|\alpha_{xy}| + |\alpha_{xz}| + |\alpha_{yx}| + |\alpha_{yz}| + |\alpha_{zz}|) . \quad (4.13)$$

This quantity includes different types of dislocations, it can be seen as an upper limit of the GND content of the material or a lower limit of the total dislocation density [Kysar et al., 2010].

4.3 Laue microdiffraction and in-situ fatigue experiment

In this section the experimental results of the Laue microdiffraction experiments on copper single crystals using synchrotron X-rays [Van Swygenhoven and Van Petegem, 2010] are shown.

4.3. Laue microdiffraction and in-situ fatigue experiment

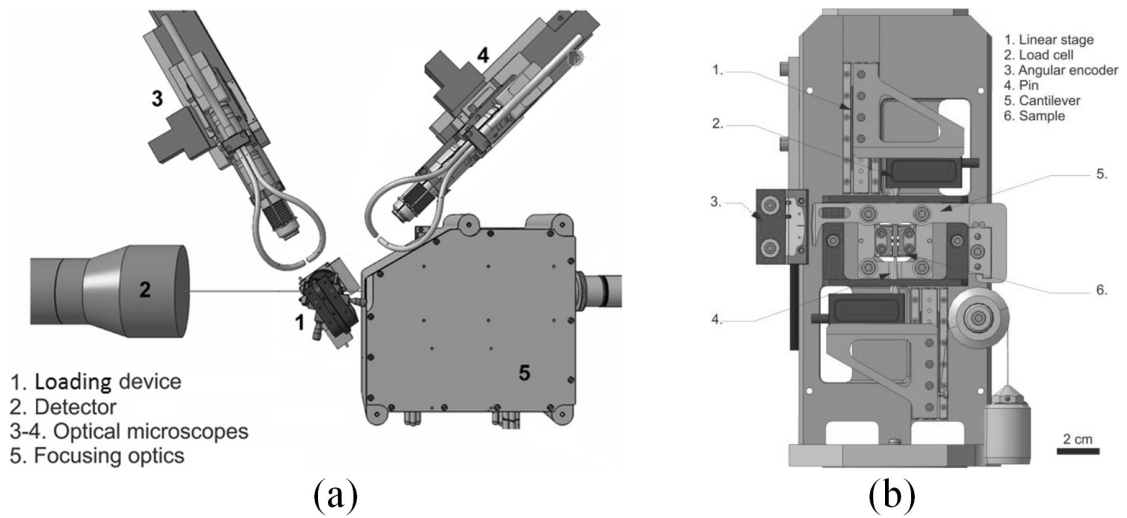


Figure 4.2 – (a) Schematic drawing of the microXAS beamline; (b) deformation rig to apply cyclic deformation on the sample (courtesy of Ainara Irastorza).

These experiments have been carried out at the microXAS beamline of the Swiss Light Source of the Paul Scherrer Institut by Ainara Irastorza-Landa [Irastorza-Landa et al., 2016]. In the following the principles of the Laue microdiffraction technique and experimental details are briefly explained. The synchrotron radiation, once focused by a pair of Kirkpatrick-Baez mirrors, can reach a submicrometre spot size. Bragg diffraction takes place in the single crystal copper sample and the image is recorded in transmission geometry by a photoluminescence detector, as shown in Fig. 4.2 (a). The Laue pattern of the undeformed samples is constituted of sharp peaks at specific azimuthal and tangential angles θ and Φ , which move, broaden and split once deformation occurs. The cyclic deformation is applied by the deformation rig shown in Fig. 4.2 (b), compatible with in-situ Laue microdiffraction experiments. The sample, shown in Fig. 4.3, has two external immobile parts, fixed by bolts, and a central mobile region. The load cell acts on this central part, inducing shear strain in two “shear zones”, magnified in Fig. 4.3 (b). During deformation the shear strain is concentrated in the $150 \mu\text{m}$ thick region. The single slip crystal orientation is such that the x axis is perpendicular to the (111) plane and the y axis is parallel to the $[\bar{1}01]$ Burgers vector. Picosecond pulse laser ablation has been applied to this region to form the circular $30 \mu\text{m}$ thick region in Fig. 4.3 (b) [Guitton et al., 2015]. The diameter is around $300 \mu\text{m}$ and Laue microdiffraction is applied in this region after cyclic deformation. The sample is scanned along the x and y axes in Fig. 4.3 (b), in a rectangular area with dimensions $10 \mu\text{m} \times 25 \mu\text{m}$. The beam direction is along the z axis. The experimental rotation components are calculated using a template-matching technique [Gupta and Agnew, 2010], [Hofmann et al., 2012]. This is a refinement procedure yielding an orientation matrix that represents the average crystal orientation within the illuminated volume. First an average orientation is calculated, then virtual diffraction patterns are generated by rotating around the x , y and z axes with a step size of 0.03° . For every virtual diffraction pattern, the diffraction spots are calculated and it is checked if the experimental intensity in those spots is higher

Chapter 4. Comparison between simulation and synchrotron Laue microdiffraction experiments

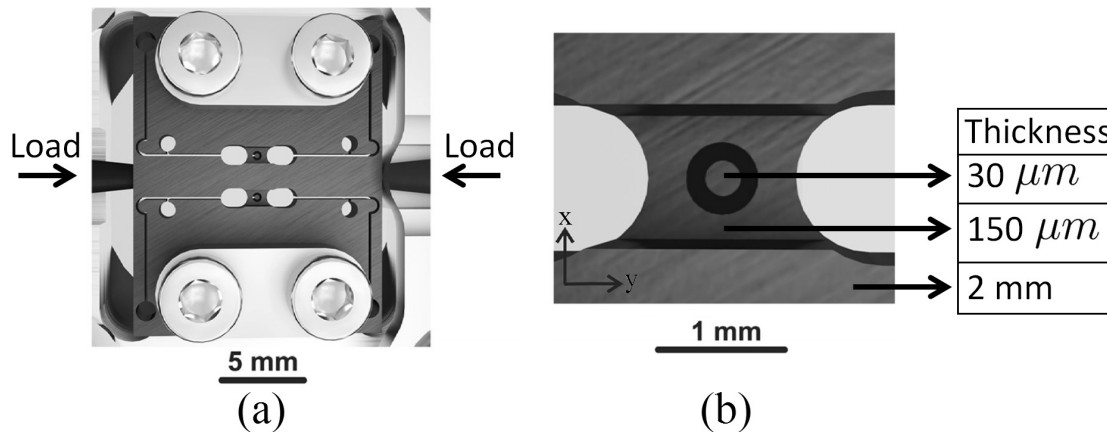


Figure 4.3 – (a) Schematic view of the copper single crystal sample geometry and actuators; (b) shear zone, the thickness of different regions is reported [Irastorza-Landa et al., 2016].

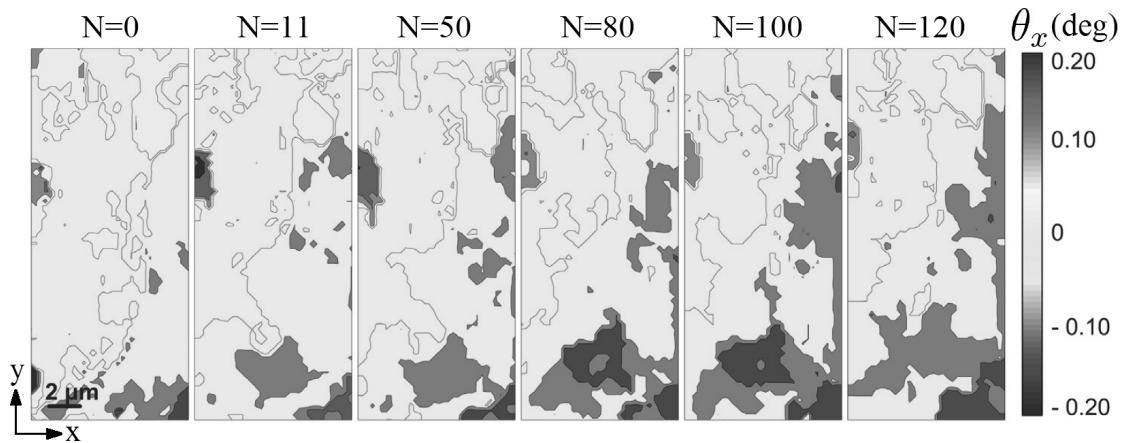


Figure 4.4 – Rotation θ_x around the x axis for different number of cycles N [Irastorza-Landa et al., 2016].

than 20% of the maximum peak intensity. In this case, the rotation angles around the x , y and z axes are saved. Misorientation angles θ_x , θ_y and θ_z are calculated with respect to a point whose orientation does not change sensibly after 120 cycles. This point corresponds to coordinates $x = 5.9 \mu m$ and $y = 12.7 \mu m$ and it is selected as a reference point. The Euler angle θ and the apparent GND density are calculated as in (4.2)-(4.4) and (4.13).

The misorientation angles θ_x , θ_y and θ_z at different number of cycles are shown in Fig. 4.4, 4.5 and 4.6. The Euler angle θ at different number of cycles is shown in Fig. 4.7. Some misoriented regions are present at cycle 0 because of pre-existing plastic deformations. These are indicated with the letters **A**, **B**, **C**, **D** and **E** in Fig. 4.7. In the first 80 cycles the distribution of the misorientation θ changes continuously. The feature in region **A** disappears, the ones in regions **B** and **D** fragment while the rotation in region **C** increases until cycle 50, then it decreases. Between cycle 80 and 120, new features appear, as shown in Fig. 4.7. In region **F** and **B**, two highly misoriented regions form. As shown in Fig. 4.4, 4.5 and 4.6, the rotation around the

4.3. Laue microdiffraction and in-situ fatigue experiment

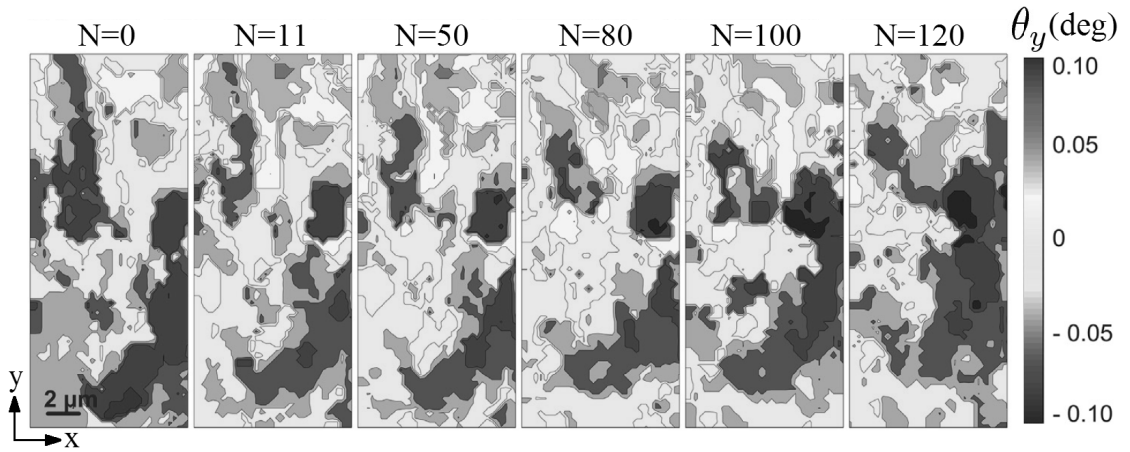


Figure 4.5 – Rotation θ_y around the y axis for different number of cycles N [Irastorza-Landa et al., 2016].

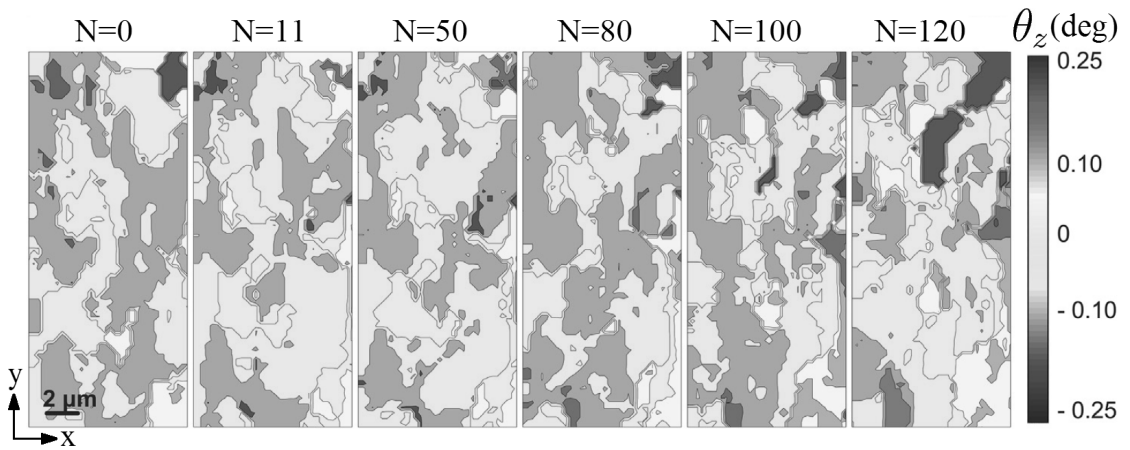


Figure 4.6 – Rotation θ_z around the z axis for different number of cycles N [Irastorza-Landa et al., 2016].

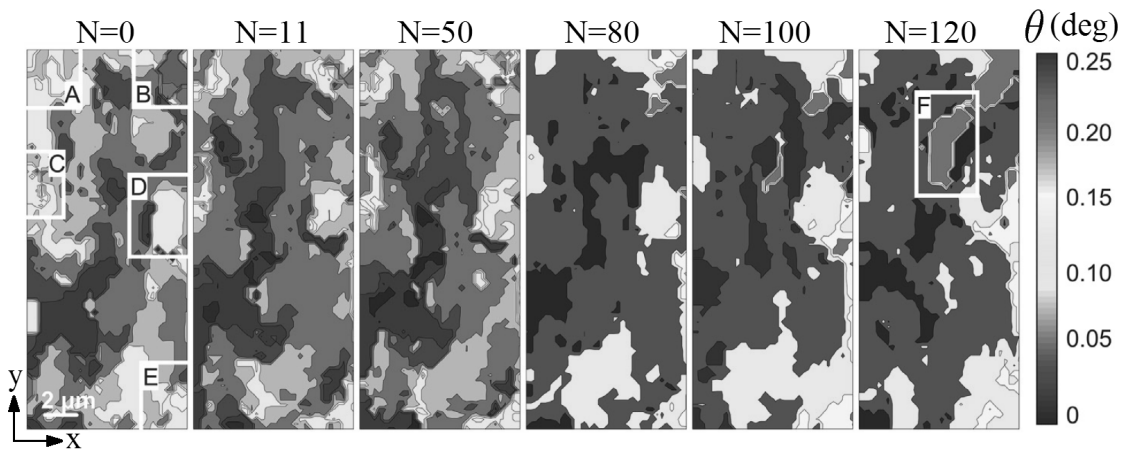


Figure 4.7 – Euler angle θ for different number of cycles N [Irastorza-Landa et al., 2016].

Chapter 4. Comparison between simulation and synchrotron Laue microdiffraction experiments

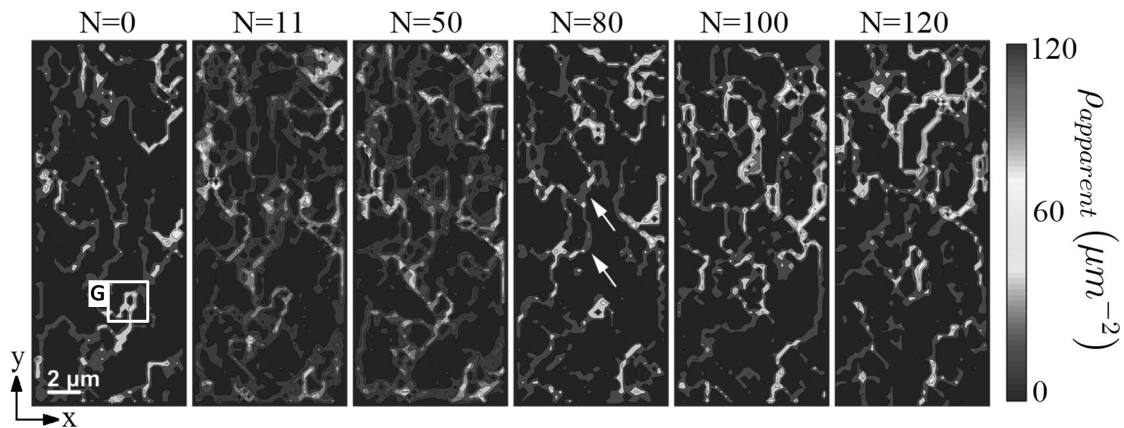


Figure 4.8 – Apparent GND density for different number of cycles N [Irastorza-Landa et al., 2016].

z and x axes are more pronounced than the rotation around the y axis. Highly misoriented regions after cycle 80 (**F** and **B**) are rotated mainly around the z axis.

The apparent GND density ρ_{app} , calculated using (4.13), at different number of cycles is shown in Fig. 4.8. Already at cycle 0 several traces with non-zero ρ_{app} can be observed. For instance, region **B**, corresponding to the initial red feature of the θ_z field in Fig. 4.6, is surrounded by apparent GND walls at cycle 0. During the first 50 cycles both formation and dissociation of apparent GND walls are observed. For instance, dissociation is visible in the lower part of Fig. 4.8 (region **G**). The highly misoriented region **F** does not contain apparent GNDs in the initial cycles, but a stable structure form after deformation. The apparent GND density ρ_{app} is particularly high at the interface of this highly misoriented region compared to the rest of the analyzed area. Also regions **B** and **D** are surrounded by some GND walls after deformation. Fig. 4.9 shows the details of the evolution of apparent GND traces of some regions in Fig. 4.7 and 4.8:

- Region **G**: initial traces disappear upon cycling;
- Region **A**: initial traces redistribute and a region free of apparent GND on the left side is formed after 120 cycles;
- Region **B**: high density initial apparent GND are present; they redistribute upon cycling and do not disappear.

Simulations are carried out in the next sections to address the following questions, suggested by the experimental results:

- Section 4.4: what is the plastic strain and the strain homogeneity in the analyzed area?
- Section 4.5: Does the pre-existing rotation affect the time evolution of the microstructure?

4.3. Laue microdiffraction and in-situ fatigue experiment

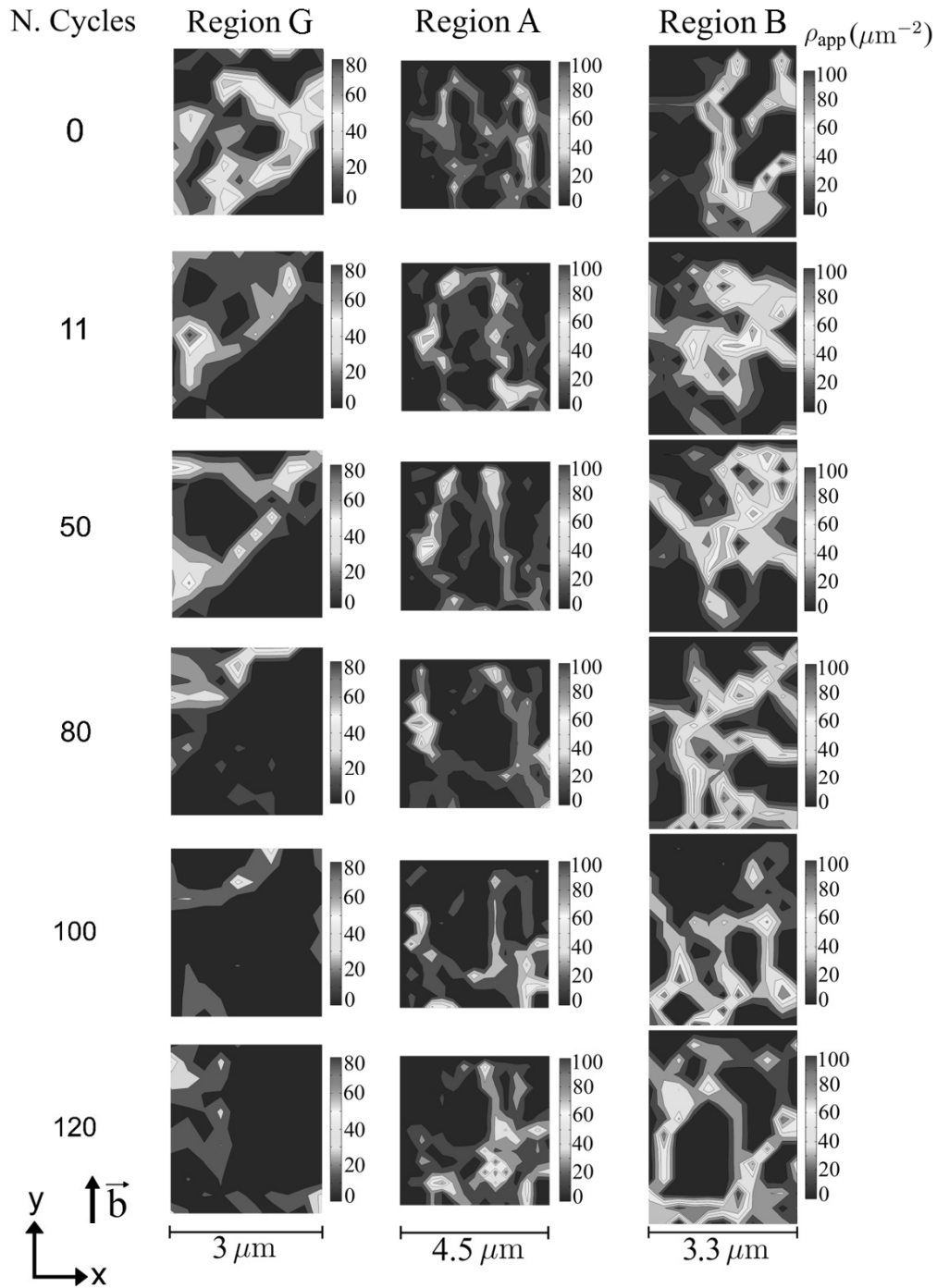


Figure 4.9 – Evolution of the apparent GND density in regions **G**, **A** and **B** (courtesy of Ainara Irastorza).

Chapter 4. Comparison between simulation and synchrotron Laue microdiffraction experiments

- Section 4.6: How is the lattice rotation affected by the evolving dislocation structures?
- Section 4.6: Which boundary condition and representative volume are necessary to predict the correct magnitude of the rotation components?
- Section 4.7 and 4.8: How does the shape of accumulated dislocation structures affect the rotation gradients?
- Section 4.8: Is the predicted apparent GND density comparable to experiments?
- Section 4.9: Is the simulation able to reproduce the formation and dissociation of apparent GND density structures?

4.4 Plastic strain and strain homogeneity in the analyzed area

In this section a phenomenological power law plasticity model is used to simulate the full geometry of the sample during in-situ fatigue experiments. The aim is to quantify the plastic strain applied in the thin area, which cannot be measured in the experiment, and the strain homogeneity in the analyzed area. The representative volume used in the CPFÉ simulations is shown in Fig. 4.10 (a). This represents only half of the real geometry, symmetric displacement boundary conditions are applied on the upper surface in Fig. 4.10 (a). The surface in contact with the bolts, indicated by green arrows in Fig. 4.10 (a), is set at zero displacement. The magnitude of the applied displacement is measured by the actuator and used in the simulation [Irastorza-Landa et al., 2016]. The same crystal orientation as in the experiment is used, therefore a single slip system is active. A refined mesh is used in the shear zone, as shown in Fig. 4.10 (b), where the plasticity concentrates. The surrounding region can be meshed with

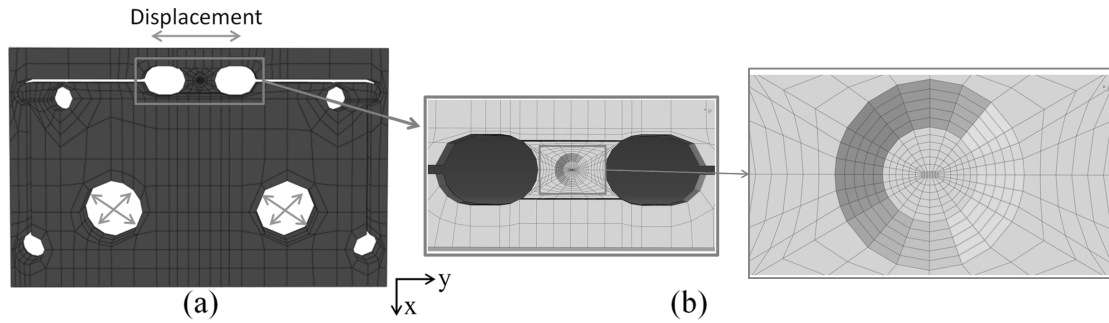


Figure 4.10 – (a) Representative volume and boundary conditions; (b) refined mesh in the shear zone.

coarser elements since it remains elastic.

The phenomenological constitutive model is based on the description of Hutchinson [Hutchinson, 1976]. The plastic strain rate of every slip system is given by:

$$\dot{\gamma}_p^\alpha = \dot{\gamma}_0 \left| \frac{\tau^\alpha}{g^\alpha} \right|^n \text{sgn}(\tau^\alpha), \quad (4.14)$$

4.4. Plastic strain and strain homogeneity in the analyzed area

where $\dot{\gamma}_0$ is a reference shear rate, τ^α is the resolved shear stress of the α -th slip system and n is the stress exponent. g^α is a variable representing the slip resistance of the α -th slip system and it evolves according to:

$$\dot{g}^\alpha = \sum_{\beta=1}^{12} h_0 h_{\alpha\beta} \left| 1 - \frac{g^\beta}{g_\infty} \right|^a \operatorname{sgn} \left(1 - \frac{g^\beta}{g_\infty} \right), \quad (4.15)$$

where h_0 , a are parameters and $h_{\alpha\beta}$ is the hardening matrix [Diehl et al., 2016], representing the interaction among slip systems. The parameters used for copper are derived from stress-strain curves obtained in pure shear experiments [Dmitrieva et al., 2009] and are listed in Tab. 4.1.

| $\dot{\gamma}_0$ | n | $g(t=0)$ | g_∞ | h_0 | a |
|------------------|-----|----------|------------|---------|------|
| 0.1 | 20 | 10 MPa | 30 MPa | 100 MPa | 0.01 |

Table 4.1 – Parameters for the phenomenological plasticity model in (4.14)-(4.15) [Déprés et al., 2008], [Dmitrieva et al., 2009].

The simulated force is calculated using a surface average of the stress component σ_{xy} over the displaced surface in Fig. 4.10 (a). This force is matched to the experimental one and the resulting strain field γ_{xy} is shown in Fig. 4.11 (a). The strain reaches a value of 1.05% in the centre of the representative volume, where the rectangular area analyzed by Laue microdiffraction lies. In Fig. 4.11 (a), a strain uniformity within 10% is present in the analyzed area.

The experiment has been carried out with different imposed displacements for different

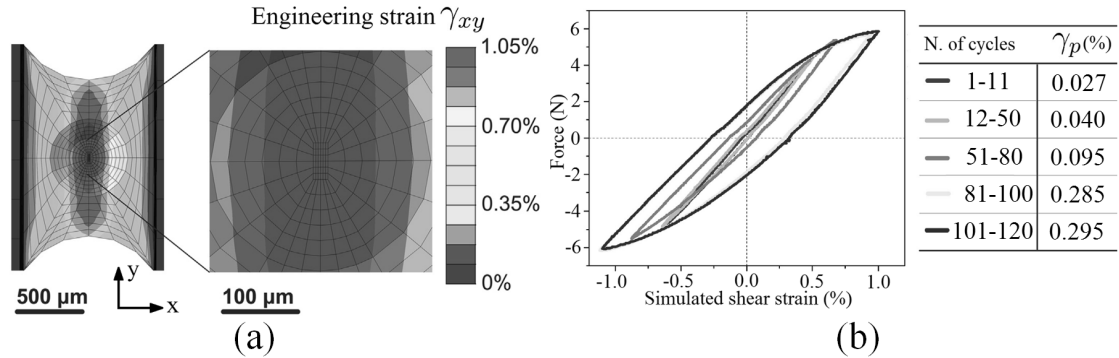


Figure 4.11 – (a) Simulated shear distribution of the sample; (b) measured force as a function of the simulated shear in the thin area [Irastorza-Landa et al., 2016].

interval of the cycle number, as shown in Fig. 4.11 (b). The simulation has shown that the shear strain can be approximated as $\gamma = \Delta/D$, where Δ is the displacement of the actuator and D is the diameter of the thin part ($300 \mu\text{m}$). Thus, a plot of the measured force as a function of the calculated shear stress can be made, as shown in Fig. 4.11 (b). Then the plastic strain has been calculated as suggested in Suresh's book [Suresh, 1998]: first the hysteresis loops

Chapter 4. Comparison between simulation and synchrotron Laue microdiffraction experiments

of the force-strain curve is drawn, as in Fig. 4.11 (b), then the plastic part of the shear strain is calculated as the width of one loop along the zero force ($F = 0$) axis. The plastic strain amplitude at different number of cycles is reported in Fig. 4.11 (b). It considerably increases after cycle 80, leading to a larger force-strain hysteresis. In conclusion, the simulation has given an estimation of the plastic strain amplitude and its homogeneity in the analyzed area.

4.5 The influence of pre-existing lattice rotation on the evolving microstructure

The phenomenological power law model (4.14)-(4.15) has been used to study, at the micrometre length scale, the effect of the initial crystal orientation, induced by pre-existing plastic deformations, on the rotation components after cyclic deformation. The aim is to show that the model predictions at a length scale of the order of $10 \mu\text{m}$ are affected by the stiffness tensor of initially misoriented regions. A comparison with the dislocation-based model introduced in section 2.2 is made.

The mesh used for the phenomenological power law model is the same as in Fig. 4.10, except for the central part of the thin area. In that part, cubic elements with a $0.5 \mu\text{m}$ size are used in a parallelepiped region with size $10 \mu\text{m} \times 25 \mu\text{m} \times 30 \mu\text{m}$ along the x , y and z axes. The mesh used for the dislocation-based model is the same as in Fig. 4.21.

The rotation of the initial crystal, as measured in the experiment, is not uniform, but initial misorientations are present, as shown by the components θ_x , θ_y and θ_z in Fig. 4.4, 4.5 and 4.6. This initial rotation has been incorporated in the simulation: first the components θ_x , θ_y and θ_z are converted into Bunge angles (ϕ_1, θ, ϕ_2) at every point in the x and y plane, then a rotation matrix $\mathbf{R}_0(x, y)$ is calculated and assigned as initial value for the plastic deformation gradient \mathbf{F}_p . This rotation is assumed uniform in depth (along the z axis).

An analysis based on a RGB (red-green-blue) representation of the simulated rotation components is carried out. The rotation components θ_x , θ_y and θ_z , with respect to the reference point mentioned in section 4.3, are first averaged over depth (arithmetic average over the z axis) to model the behaviour of X-rays penetrating the thin layer. Then, the Euler vector $\hat{\mathbf{e}}$ in (4.2)-(4.4) is found. The Euler vector components $\hat{\mathbf{e}}_x$, $\hat{\mathbf{e}}_y$ and $\hat{\mathbf{e}}_z$, whose values are in the interval $[-1; 1]$, are mapped linearly to the interval $[0; 255]$ (8-bit color intensity). A color map is built using these numbers as intensities of red, green and blue. This method allows to evidence around which coordinate axis the rotation is dominant. The result is shown in Fig. 4.12 at cycle 11 in the upper part of the geometry using the phenomenological power law model and the dislocation-based model for cyclic fatigue. The main features are the following:

- the white-pink area on the upper right, corresponding to the initial misoriented region **B** in Fig. 4.6 and 4.7;
- the two regions on the left and right of the area in Fig. 4.12 (a)-(b), where red-pink is the dominant color;

4.5. The influence of pre-existing lattice rotation on the evolving microstructure

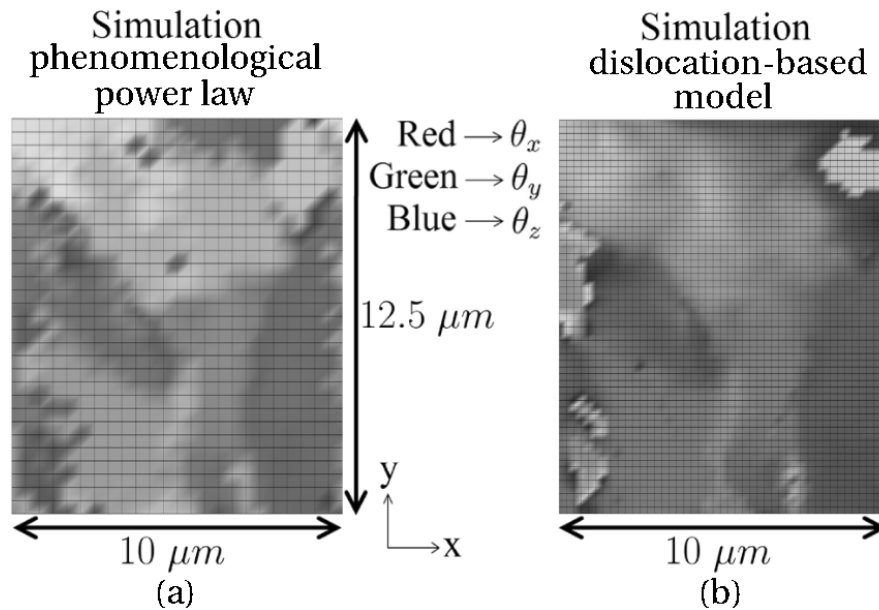


Figure 4.12 – (a) Simulated RGB rotation map, using (a) the phenomenological power law model and (b) the dislocation-based model for cyclic fatigue, of the upper part of the rectangular area analyzed by Laue microdiffraction at cycle 11; the red and blue features indicate that θ_x and θ_z are the dominant rotation components.

- the central part, where blue is the dominant color.

For instance, the left red-pink region is comparable with the red feature in the θ_x field at cycle 11 in Fig. 4.4, corresponding to region **C** in Fig. 4.7. The RGB map in Fig. 4.12 indicates that the dominant rotation components are θ_x (red) and θ_z (blue), as also measured in [Mughrabi, 2006]. The RGB maps obtained using the phenomenological power law model and the dislocation-based model are similar. Therefore, at a length scale of the order of $10 \mu\text{m}$, the magnitude of the rotation components is not determined by the dislocation structures. As will be shown in the rest of this chapter, dislocation structures influence the rotation components, even in absence of initial misorientations, at a smaller length scale.

The comparison between the measured and simulated Euler angle θ in (4.2)-(4.4) is shown in Fig. 4.13:

- also in this map a highly rotated region is present on the upper right of the area, corresponding to region **B** in Fig. 4.7;
- some of the yellow features on the left side, corresponding to regions **A** and **C** in Fig. 4.7, having a Euler angle in the interval $0 \div 0.15$ degrees, are present in both experiment and simulation.

The simulated angular interval has the same order of magnitude as in the experiment and it is determined by the applied displacement. These results suggest that the knowledge of the

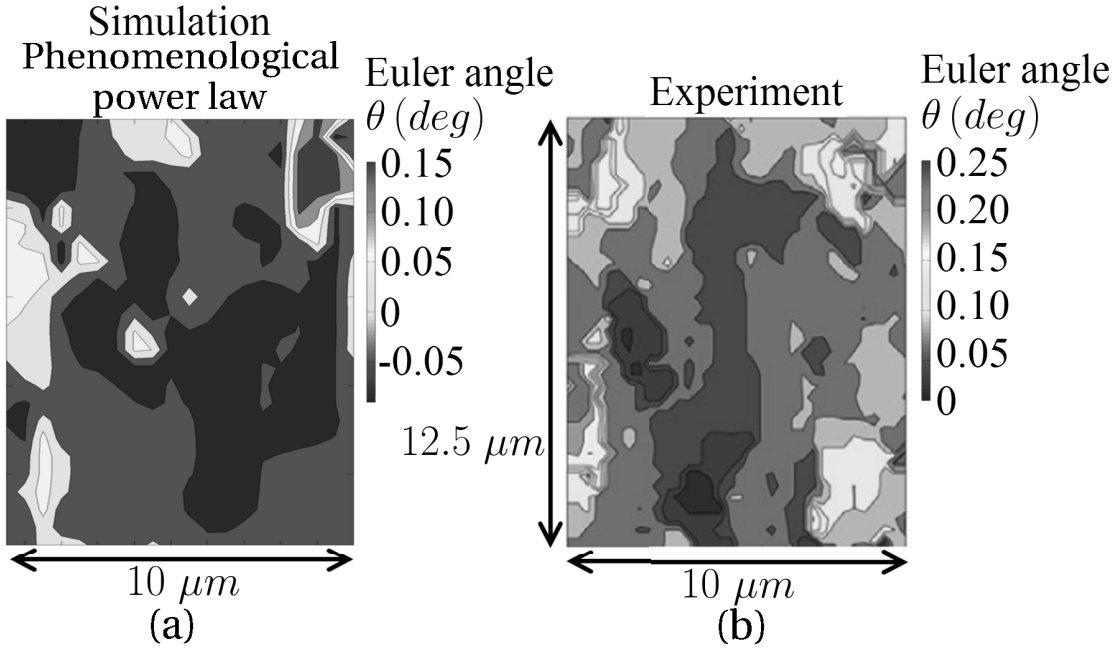


Figure 4.13 – (a) Simulated and (b) experimental Euler angle θ map of the upper part of the rectangular area analyzed by Laue microdiffraction at cycle 11 (courtesy of Ainara Irastorza).

initial microstructure is essential to predict the time evolution of the rotation components. Therefore it has been necessary to further analyze the simulation made with the phenomenological model, to understand the origin of high and low rotation regions. The stress tensor component σ_{xy} , corresponding to the resolved shear stress on the primary slip system, is strongly correlated with the cumulative plastic shear strain on that system, as shown in Fig. 4.14 (b)-(c). Regions where the absolute value of this resolved stress is higher have higher $\gamma_{p,cum}$, as predicted by the phenomenological model in (4.14). This affects the evolution of the rotation components. Some regions with lower absolute value of σ_{xy} , such as the red feature on the lower right of Fig. 4.14 (b), are correlated with a lower value of the stiffness tensor component C_{xyxy} (blue region in Fig. 4.14 (a)). The stiffness tensor is calculated using the initial orientation. At every coordinate (x, y) its value is given by:

$$\mathbf{C}_{ijkl}(x, y) = \mathbf{R}_{0,ia}(x, y) \mathbf{R}_{0,jb}(x, y) \mathbf{R}_{0,kc}(x, y) \mathbf{R}_{0,ld}(x, y) \mathbf{C}_{0,abcd}, \quad (4.16)$$

where \mathbf{R}_0 is the lattice rotation matrix and $\mathbf{C}_{0,abcd}$ is the stiffness matrix of FCC copper in the undeformed lattice reference system. In this specific specimen geometry, the component C_{xyxy} is the proportionality coefficient between the highest strain component ε_{xy} and the stress component σ_{xy} . Therefore, in this strain controlled test, regions with lower stiffness component are expected to have a lower stress magnitude. This is true for the lower part of the area in Fig. 4.14 (a) and (b). Therefore, the stiffness component C_{xyxy} affects strongly the shear stress. By comparing Fig. 4.14 (a) with the initial rotation components in Fig. 4.4, 4.5 and 4.6, one can observe a correlation between the stiffness component C_{xyxy} , θ_x and θ_y

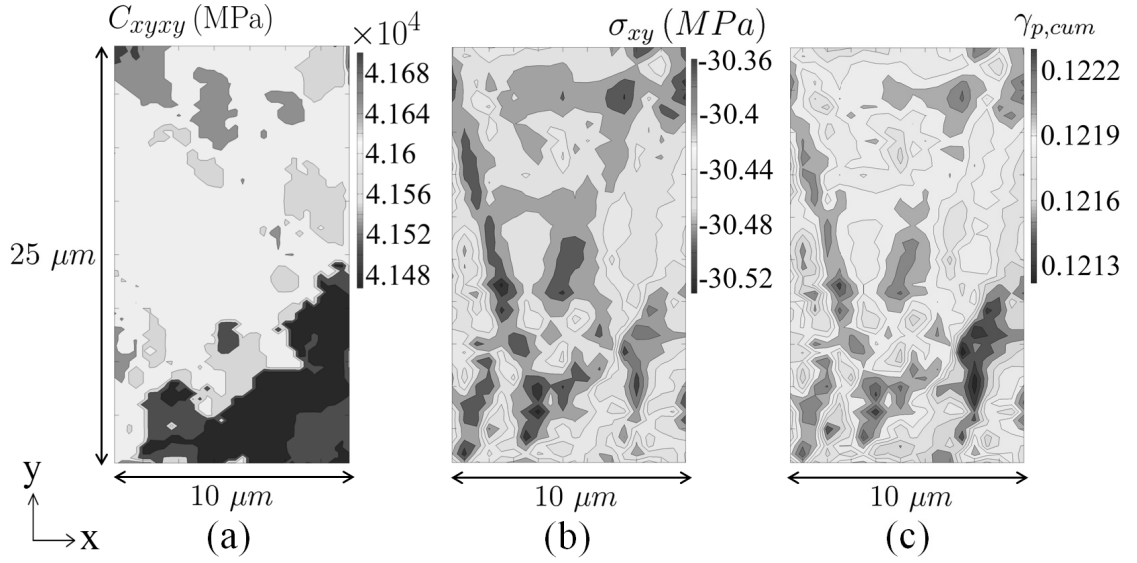


Figure 4.14 – (a) C_{xyxy} component of the stiffness tensor; (b) stress tensor component σ_{xy} ; (c) cumulative plastic strain $\gamma_{p,cum}$ on the primary slip system. In (a) and (b) the scales are different because of the different magnitude and sign of C_{xyxy} and σ_{xy} .

in the lower part of the area. The low value of the stiffness component C_{xyxy} in that area is due to these initial rotation components. The stiffness component C_{xyxy} can affect the time evolution of the rotation components:

- the θ_x rotation component in Fig. 4.4 shows expanding blue regions in the lower part of the area, where C_{xyxy} is lower;
- regions **B** and **D** in Fig. 4.7, where the value of θ_z increases after many cycles, are associated with areas having a lower value of C_{xyxy} compared with the surrounding regions, as shown by the two light blue regions in the upper right part of the area in Fig. 4.14 (a).

The phenomenological model is also able to predict that θ_x and θ_z are the main rotation components, as shown by the red and blue features in Fig. 4.12 (a)-(b).

In conclusion, the comparison between simulation and experiment has shown that, at a length scale of the order of $10 \mu\text{m}$, the rotation components are strongly affected by the initial misorientation, present because of plastic deformation probably induced during manufacturing. To understand the behaviour after cyclic deformation an analysis of the local elastic stiffness tensor is necessary.

4.6 Lattice rotation from evolving dislocation structures

In this section the single slip dislocation-based model in section 2.2 is used to study the correlation between evolving dislocation structures and rotation components. Simulations

Chapter 4. Comparison between simulation and synchrotron Laue microdiffraction experiments

are carried out first in a smaller representative volume to understand the effect of boundary condition and averaging over depth (z axis).

During cyclic fatigue, the dislocation structures represent a barrier for the motion of dislocations. Thus, it is expected that signed gliding dislocations are blocked and form accumulations of GNDs. As stated in section 1.1, GNDs amount to only a few percent of the total dislocation density. This information was found by analyzing the broadening of X-ray rocking curves of cyclically deformed samples [Mughrabi, 2006]. Using the assumption that equally spaced dislocation walls form, which are impenetrable for dislocations, Mughrabi estimated that at most 5% of the total dislocation density is constituted of GNDs [Mughrabi and Obst, 2005]. However, these analytical models do not give insight into the time evolution of the rotation. The main rotation components during cyclic fatigue of copper found using Berg-Barrett X-ray topographs are along the edge dislocation line ($[\bar{1}\bar{2}1]$) and the slip plane normal ($[111]$) [Mughrabi, 2006]. The dislocation walls used in the Mughrabi's assumption are infinite along the edge dislocation line ($[\bar{1}\bar{2}1]$) (z axis in Fig. 4.1), thus the only non-zero rotation component is θ_z and the rotation along the slip plane normal cannot be calculated.

To understand the effect of dislocation structures in our single slip model (section 2.2), a

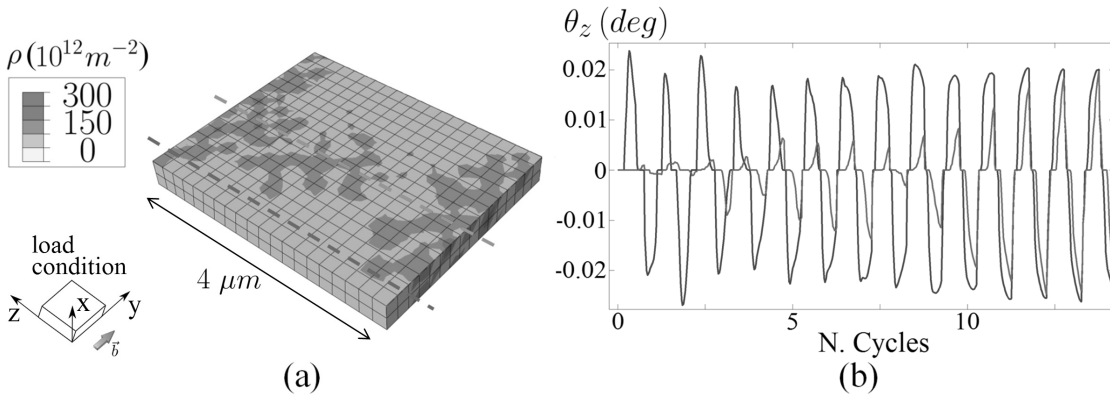


Figure 4.15 – (a) Representative volume to simulate the lattice rotation along the edge dislocation line (section cut at $x = 0.4 \mu\text{m}$) and dislocation density after 50 cycles; (b) rotation along the z axis, averaged over the elements along the blue and green dashed lines in (a).

cyclic shear simulation is carried out on a parallelepiped geometry with size $4 \mu\text{m}$ along the y and z directions and $1 \mu\text{m}$ along x . 200 nm elements are used and the load conditions are the same as in Fig. 2.15, with a strain amplitude $\gamma_{xy} = 0.1\%$. Periodic boundary conditions for the dislocation fluxes are used, and the initial dislocation densities are the same as in Tab. 2.7. The slip plane (111) is oriented perpendicular to the x axis and the Burgers vector along the y axis. The strain rate is 10^{-3} s^{-1} . The rotation θ_z is averaged over the elements along the dashed green and blue lines in Fig. 4.15 (a), which are in the middle of the representative volume, at a depth of $x = 0.5 \mu\text{m}$. Dislocation patterns form after 50 cycles in the central part of this geometry, where the green dashed line is chosen, as shown in Fig. 4.15 (a). The blue dashed line is chosen along a low dislocation density region, representing a channel. The θ_z rotation is shown in Fig. 4.15 (b). It reaches values around 0.02° inside forming channels. Along the

4.6. Lattice rotation from evolving dislocation structures

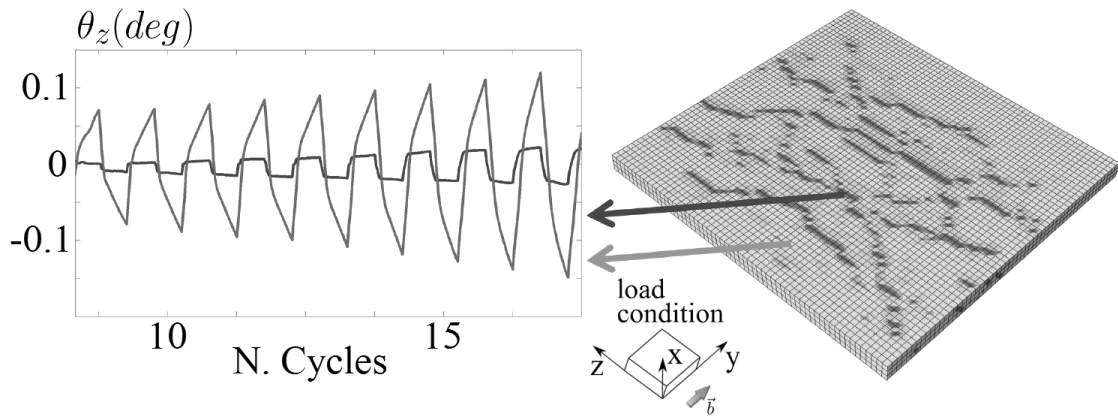


Figure 4.16 – Lattice rotation θ_z in channels and dislocation structures.

green dashed line θ_z has lower values in the first cycles and a phase difference with respect to the blue line is present. This difference tends to disappear after many cycles as an effect of the averaging procedure. The simulated values of θ_z are smaller than the experimental ones in Fig. 4.6 because of the smaller strain amplitude in this simulation compared with the experiment. A higher and persistent difference of the rotation θ_z in dislocation structures and channels can be seen if the rotation is selected only in a single element. This is shown in Fig. 4.16 for the $12 \mu\text{m} \times 12 \mu\text{m} \times 0.6 \mu\text{m}$ representative volume analyzed in section 2.2. The value of θ_z selected in a single channel element at a distance of around $1 \mu\text{m}$ from the closest dislocation structure can reach 0.1° , while inside the dislocation structure the rotation is smaller. Also in this case a phase difference is present. These simulations indicate that the formation of dislocation structures can induce highly misoriented regions in the θ_z rotation component, as the ones shown in Fig. 4.6, but also that this effect can be partially hidden by the averaging along depth (z axis).

Simulations with different strain amplitudes are carried out to understand the effect on the lattice rotation. If the strain amplitude is increased, the magnitude of the rotation θ_z in the dislocation structures increases only slightly, as shown in Fig. 4.17. In the idealized picture in Fig. 4.1, a double value of the plastic strain in the high plastic strain regions would lead to a double value of the rotation around the edge dislocation lines. However, θ_z in Fig. 4.17 does not scale linearly with γ_{xy} because the representative volume is constrained on the upper surface, therefore free rotations of the elements around the z axis are prevented.

In the idealized picture in Fig. 4.1, if the same plastic strain amplitude is present in the two high plastic strain regions, then the same magnitude of the rotation is expected. In Fig. 4.18 (a), the central region, where dislocation structures are present, is surrounded by two low density regions, where the green and blue dashed lines are drawn. If the rotation is averaged along these lines, then a difference of the maximum and minimum value of θ_z is present, as shown in Fig. 4.18 (b)-(c). The oscillation amplitude of θ_z is similar in the two low density regions and no large phase difference is present, in agreement with the simplified model in Fig. 4.1. Additionally, a drift of the average value of θ_z is present, as shown in Fig. 4.18 (b), which can be due to an asymmetry of the plastic strain accommodated in the two channels.

Chapter 4. Comparison between simulation and synchrotron Laue microdiffraction experiments

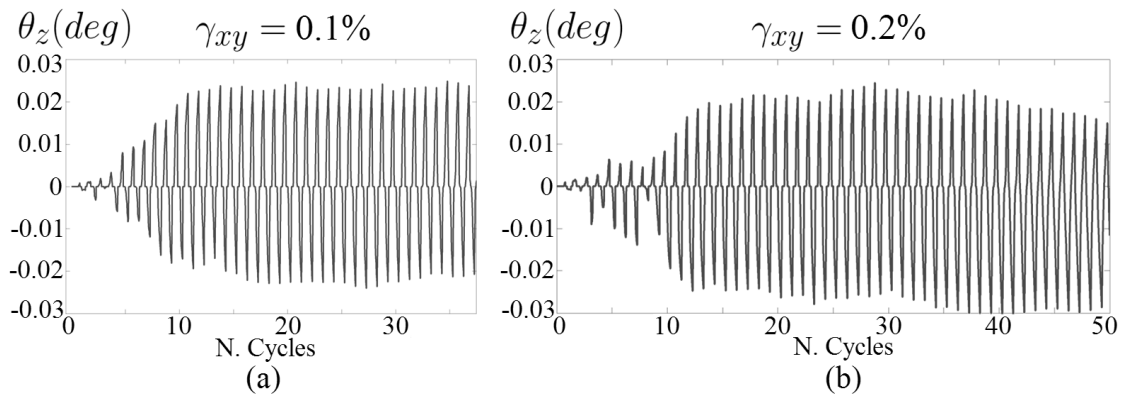


Figure 4.17 – Rotation along the z axis in the dislocation structures for (a) $\gamma_{xy} = 0.1\%$ and (b) $\gamma_{xy} = 0.2\%$.

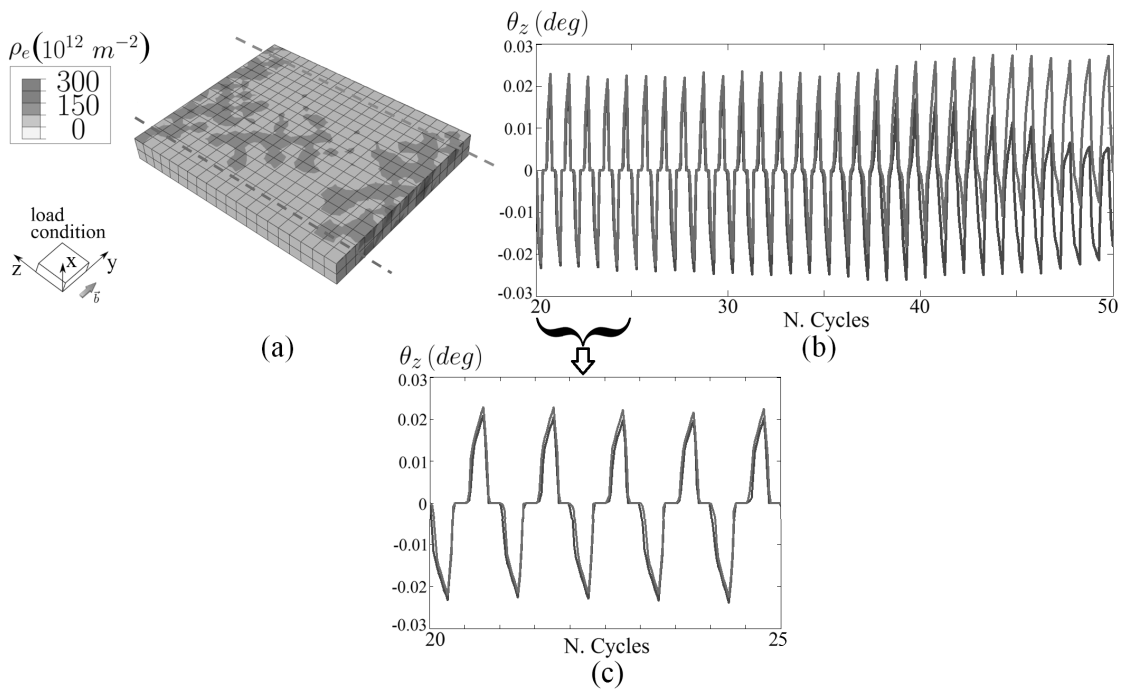


Figure 4.18 – (a) Representative volume to simulate the lattice rotation along the edge dislocation line; (b) rotation along the z axis, averaged over the elements along the blue and green dashed lines in (a); (c) the oscillation amplitude and phase of θ_z is similar in the two low density regions.

4.6. Lattice rotation from evolving dislocation structures

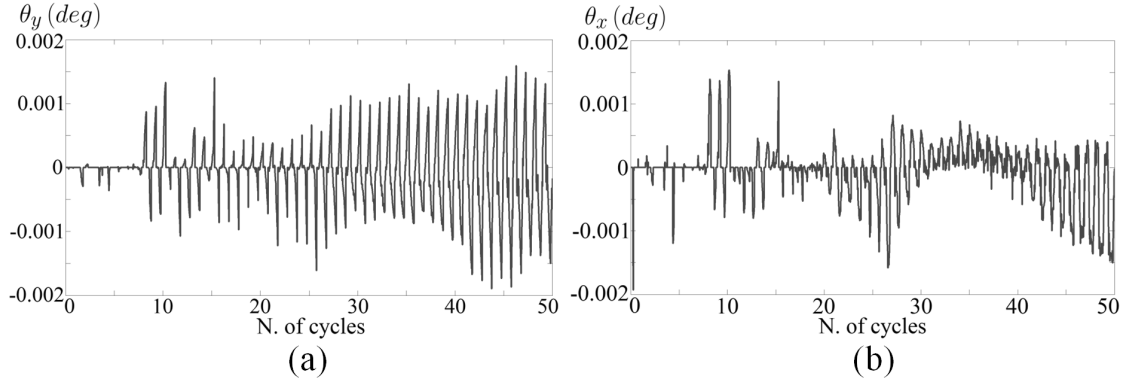


Figure 4.19 – Rotation along (a) the y axis and (b) the x axis, averaged over the elements along the green dashed line in Fig. 4.18 (a).

Free boundary condition are set on the two surfaces perpendicular to the y axis, therefore they do not cause boundary effects in the two low density regions. In the experiment (Fig. 4.6), the rotation component θ_z has also different values around the highly misoriented region F in Fig. 4.7, ranging between -0.05° and 0.05° .

The other two components of the rotation θ_x and θ_y , averaged along the elements indicated by the green dashed line in Fig. 4.18 (a), are shown in Fig. 4.19. In this simulation the components θ_x and θ_y have a magnitude that is smaller by approximately a factor 20 compared with θ_z . This is due to the single slip load in this simulation and the dominant γ_{xy} strain component. Therefore, this simulated volume, smaller than the experimentally analyzed volume by approximately a factor 500, cannot reproduce the higher values of θ_x and θ_y found in the experiment (Fig. 4.4 and 4.5) because the boundary condition is more restrictive than in the experiment.

However the components θ_x and θ_y are not zero because of the three dimensional character of the simulation. In the idealized picture in Fig. 4.1, if the lower plastic strain region is uniform in depth (representing a straight dislocation structure along the edge dislocation line direction), the only rotation component would be θ_z . However this condition is not satisfied in the simulation in Fig. 4.18 (a) because the dislocation structures are bent and not straight along the z axis. The origin of θ_x can be understood from the scheme in Fig. 4.20. If the lower plastic regions are not uniform along the z axis, there is a gradient of the plastic strain component $\gamma_{p,yx}$ because the plastic deformation increases along the z axis from the lower to the higher plastic strain region. In terms of GNDs this is associated to the presence of both edge and screw accumulations at the interface between the low and high plastic strain regions, as shown in Fig. 4.20. With zero applied stress, the displacement continuity between the high and low plastic strain region leads to a crystal lattice rotation around the x axis, as shown in Fig. 4.20. In terms of (4.6), the presence of screw GNDs, represented by the α_{yy} component of the Nye tensor, leads to a gradient of the component $\omega_{yz}^e = -\theta_x$. The relationship between the vein bending on the slip plane and the rotation components will be further discussed later in this chapter.

Chapter 4. Comparison between simulation and synchrotron Laue microdiffraction experiments

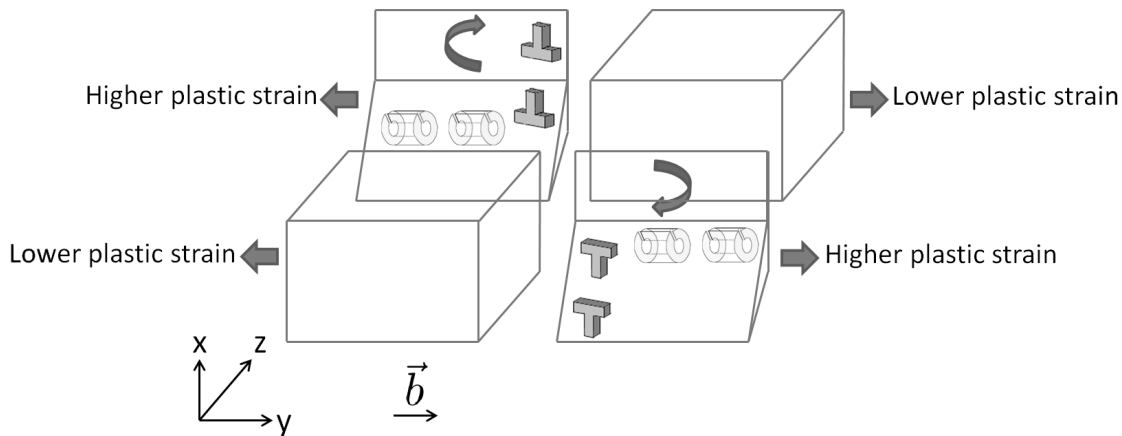


Figure 4.20 – Schematic relationship between edge GNDs, screw GNDs and lattice rotation around the slip plane normal (x axis).

4.7 Rotation gradients from accumulated dislocation structures

The dislocation-based model, applied to the specimen geometry, can clarify some micrometre scale features of the Nye tensor observed in the experiment. As shown in section 2.2 a 200 nm mesh size is necessary to resolve dislocation structures in the single slip model. Therefore, a parallelepiped, with dimensions $0.2 \mu\text{m} \times 4 \mu\text{m} \times 1 \mu\text{m}$ along the coordinate axes, formed by 200 nm elements is included in the thin area, as shown in Fig. 4.21. The mesh becomes gradually coarser in the surrounding region to allow the application of the dislocation-based model to this large geometry. Even if the 200 nm region is short along the x axis, patterning of edge dislocations is reproducible because their dislocation line is along z and the Burgers vector is along y . Thus, the 200 nm element regions can be thought as the representative volume used in the simple shear simulation in section 2.2, which is also short ($0.6 \mu\text{m}$) along the direction perpendicular to the slip plane.

The simulation is carried out with the same deformation amplitude as in the experiment, copper parameters are used and the initial dislocation densities are the same as in Tab. 2.7. The crystal lattice orientation is the same as in the experiment. The strain rate used is 10^3 s^{-1} . Dislocation fluxes are allowed at the surface and the transmissivity factor is 1. This means that every dislocation reaching the surface and moving towards the surface normal can exit the representative volume. For this crystal orientation this happens mainly for positive and negative screw dislocations because their velocity vector is directed along the z axis in Fig. 4.21. This leads to dislocation structures with a lower value of the maximum dislocation density compared to the simulation with periodic fluxes in Fig. 2.15 (a).

Dislocation patterning appears after 50 deformation cycles, as shown by the edge dislocation density in Fig. 4.22 (a). The rotation components, averaged over the z axis, and the rotation gradient k_{zy} , corresponding to the Nye tensor component α_{yz} in the approximations (4.7)-(4.11), are calculated. The result is shown in Fig. 4.22 (b): couples of positive and negative peaks are present in the same positions as veins because, as shown in section 4.6, the motion of positive

4.7. Rotation gradients from accumulated dislocation structures

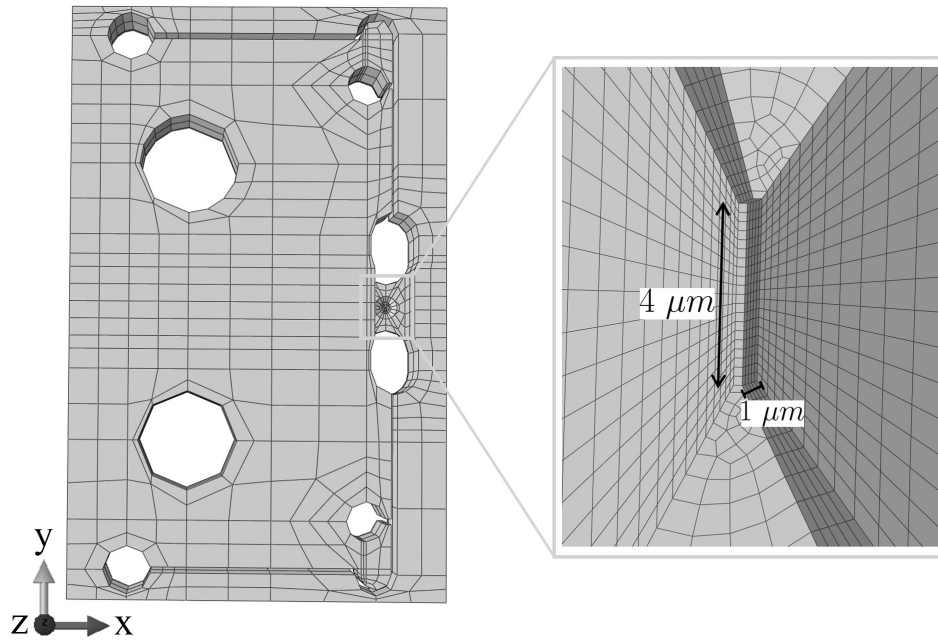


Figure 4.21 – 3D section view of the mesh used in the central part of the thin region for the dislocation based model simulation.

and negative GNDs is stopped by dislocation structures. These GNDs on the primary slip system are in this case represented by α_{yz} . Experimental data in Fig. 4.22 (c) show also positive and negative peaks after 100 cycles in region F in Fig. 4.7, whose spacing is of the order of $1 \mu\text{m}$. In the simulations, positive and negative peaks are not always visible in correspondence of a vein because of the average over depth. As it will be shown in the following, dislocation structures change position along the z axis. Therefore positive and negative edge GNDs on the opposite side of a vein can remove the features observed in α_{yz} .

The same procedure described above for α_{yz} is applied to the calculation of the α_{xz} component of the Nye tensor. The simulation after 50 deformation cycles in Fig. 4.23 shows features

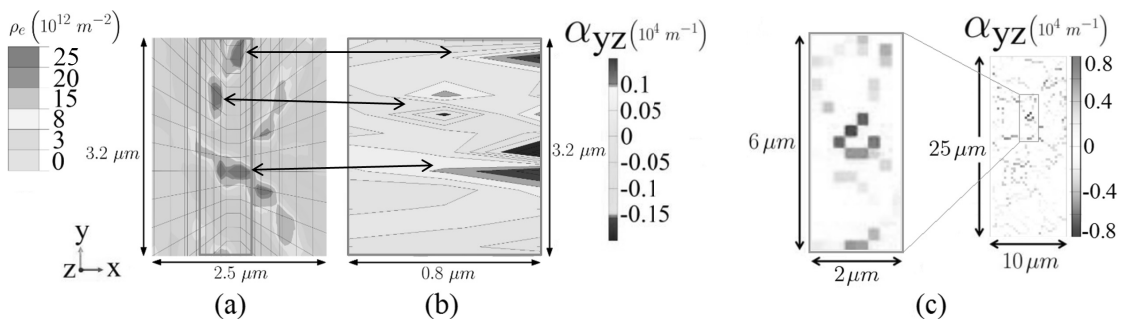


Figure 4.22 – (a) Edge dislocation density in the centre of the geometry; (b) simulated component α_{yz} of the Nye tensor; (c) measured component α_{yz} of the Nye tensor at cycle 100 (courtesy of Ainara Irastorza).

Chapter 4. Comparison between simulation and synchrotron Laue microdiffraction experiments

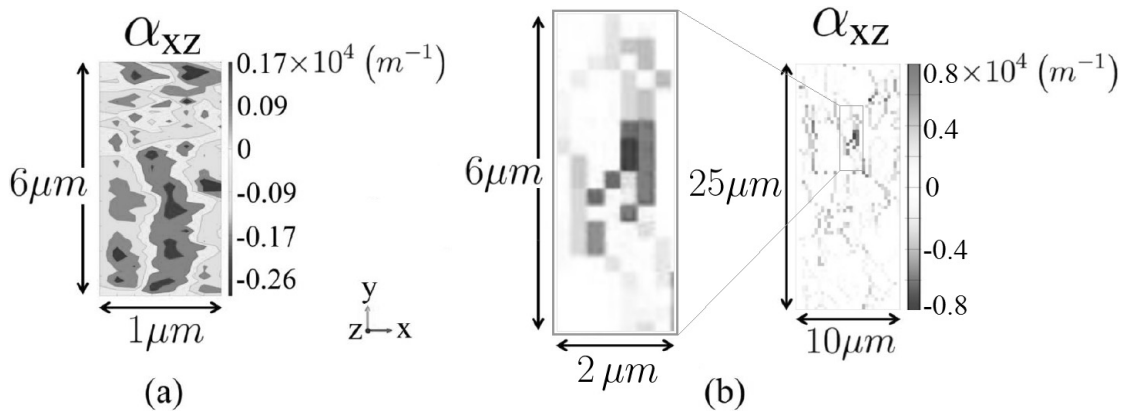


Figure 4.23 – (a) Simulated component α_{xz} of the Nye tensor; (b) measured component α_{xz} of the Nye tensor at cycle 100, the green rectangle evidences features that are similar to the simulated ones (courtesy of Ainara Irastorza).

elongated along the Burgers vector direction (y axis). A similar elongation is observed after 100 cycles in region **F** in Fig. 4.7 of the experimental map, as shown in Fig. 4.23 (b). The α_{xz} component of the Nye tensor is not directly related to GNDs on the primary slip system but it reflects the rotation gradient along the slip plane normal direction (x axis). As shown in the following, this rotation gradient is connected with the displacement of the veins along the depth (z axis).

4.7. Rotation gradients from accumulated dislocation structures

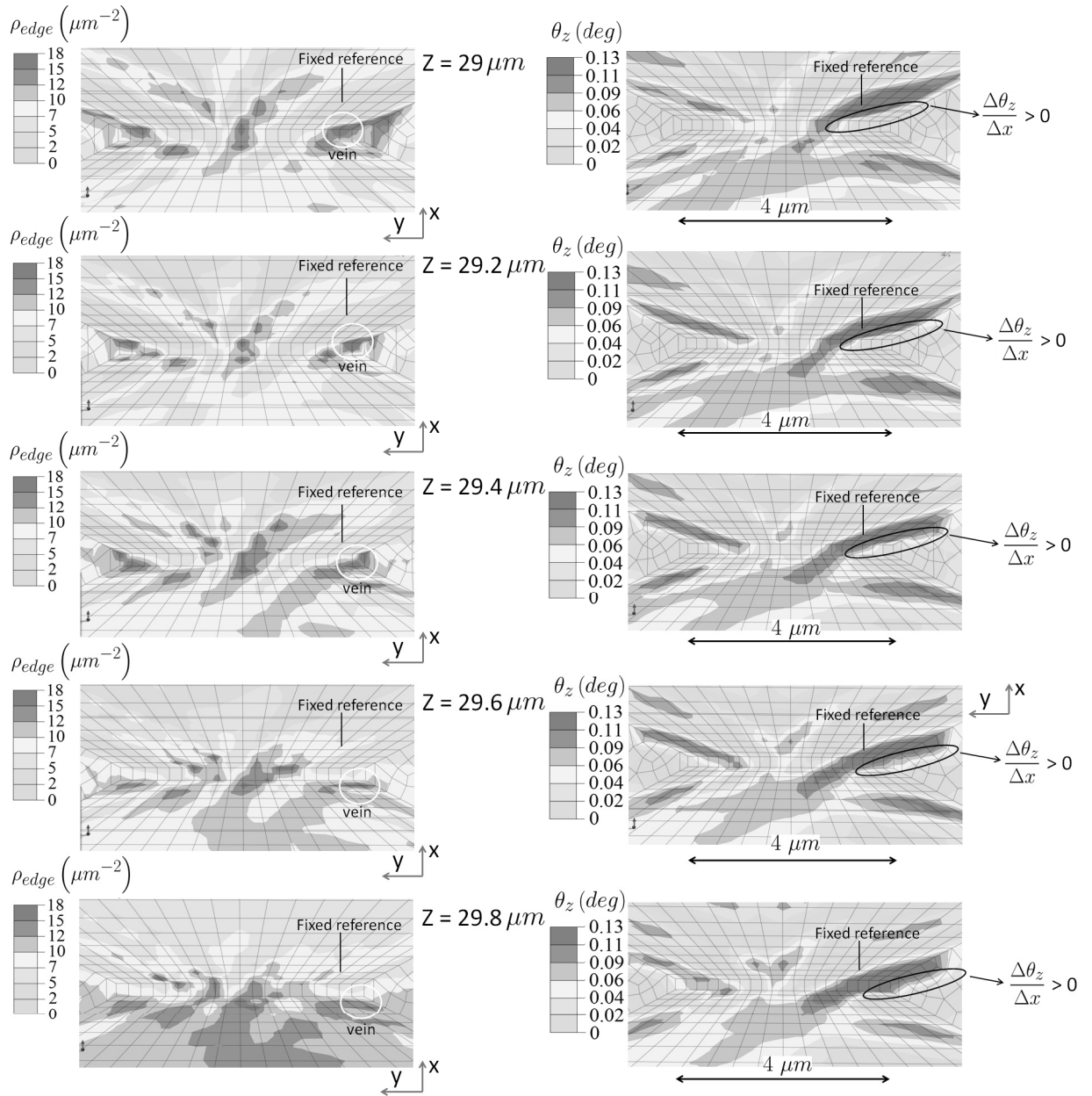


Figure 4.24 – Edge dislocation density at different depth z in the $200\ \text{nm}$ elements of the $30\ \mu\text{m}$ thin layer and corresponding rotation field θ_z .

Chapter 4. Comparison between simulation and synchrotron Laue microdiffraction experiments

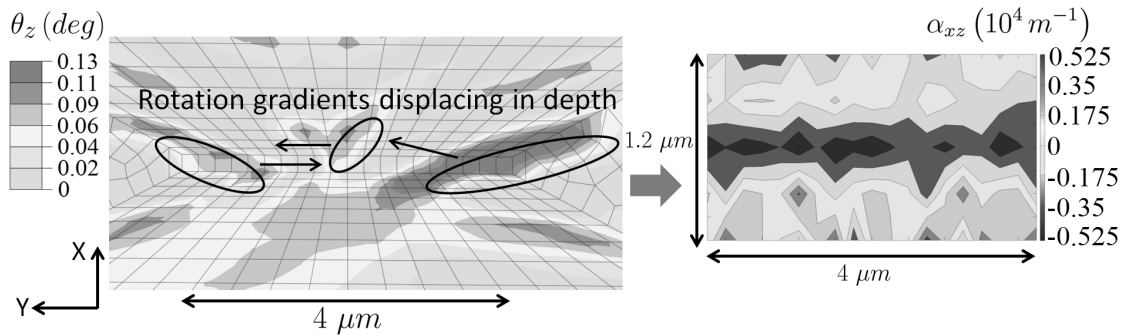


Figure 4.25 – Displacing rotation gradient, as in Fig. 4.24, and consequent α_{xz} Nye tensor component.

In Fig. 4.24 the change of the vein position as a function of depth z is shown. Images are taken in the 200 nm elements region, between the coordinates $z = 29 \mu\text{m}$ and $z = 30 \mu\text{m}$, where dislocation structures can be clearly resolved. The vein on the right is displacing with respect to the fixed reference indicated by the line. The corresponding rotation field θ_z is correlated with the dislocation density field: regions with high dislocation density have lower rotation and vice versa, in agreement with the simulation in Fig. 4.16. The derivative $k_{zx} = \partial\theta_z/\partial x$ is positive in the circled region in Fig. 4.24. This region is elongated along the y axis and it displaces in depth along the same direction. As shown in Fig. 4.25 the same is true for the other two circled veins. Therefore, when averaged over depth, the features of the Nye tensor component α_{xz} , corresponding to k_{zx} in the approximations (4.7)-(4.11), are elongated along the y axis, corresponding to the Burgers vector direction.

In conclusion, the dislocation based model applied to the full specimen geometry can clarify the relationship between the Nye tensor components α_{yz} , α_{xz} and dislocation structures. The positive and negative features shown in Fig. 4.22 (a) and 4.23 (a) appear in correspondence of forming veins, despite of the average over depth. Similar features are present in the experiment after 100 deformation cycles in the forming highly misoriented region F in Fig. 4.7, suggesting the formation of a dislocation structure in that region.

Starting from a randomly distributed dislocation density does not allow to predict the precise position of the features of the Nye tensor components in the analyzed area of the specimen. However, the characteristic distance between positive and negative regions of α_{yz} , which is around $1 \mu\text{m}$ in the simulation in Fig. 4.22 (b), and the elongation of the α_{xz} features along the Burgers vector direction are comparable to the experiment.

The simulation results would suggest that, wherever a dislocation structure is present, both components α_{yz} and α_{xz} show positive and negative values on the two opposite sides of the structure. As observed previously, the averaging procedure along the z axis and the vein bending on the slip plane can prohibit the observation of the α_{yz} component because of the superposition of positive and negative edge GNDs on the opposite sides of the vein. This is the case in the schematic representation in Fig. 4.20, where positive and negative edge dislocations are at the same position in the x - y plane, if a projection along the z axis is made.

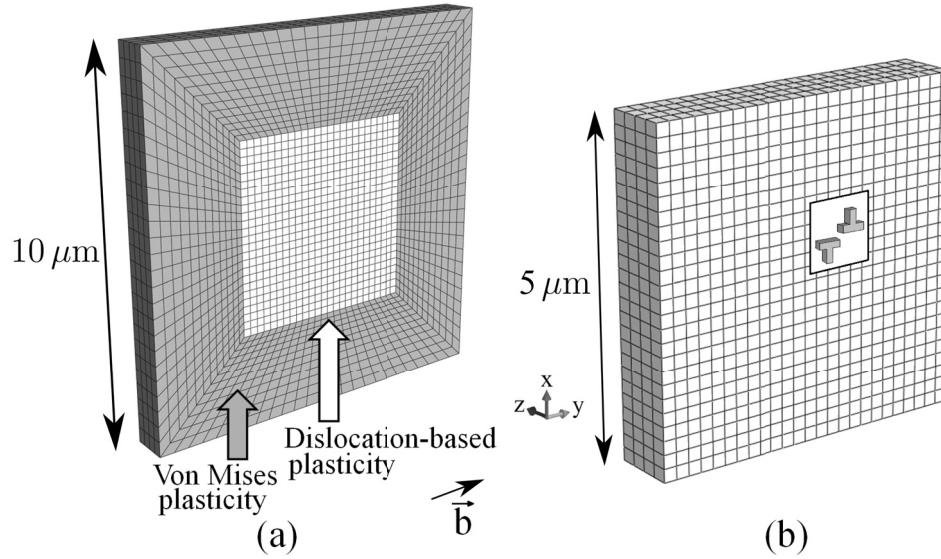


Figure 4.26 – (a) Representative volume and mesh; (b) part of the representative volume where the dislocation-based plasticity is used.

4.8 Rotation gradients surrounding different vein structures

The computational efficiency of the developed model used in the full specimen geometry does not allow to simulate the behaviour of this system up to 120 cycles. However, a cyclic deformation applied to a representative volume containing an immobile dislocation vein can clarify the nature of the highly misoriented region F in Fig. 4.7. In this section the effect of such immobile dislocation vein and its shape is tested. The rotation and Nye tensor components are compared with the experimental ones.

The representative volume used is shown in Fig. 4.26 (a). It is a parallelepiped with dimensions $10 \mu\text{m} \times 10 \mu\text{m} \times 1 \mu\text{m}$ along the x , y and z axes. The central part is modelled using the multiple slip edge-screw dislocation-based plasticity model in section 2.2, while the surrounding is described by Von Mises plasticity [Peirce et al., 1982]. The mesh size used in the central part is 200 nm. The cluster of immobile dislocations, with density ρ_{imm} , contributing to the threshold stress in (2.9), is placed inside the representative volume, as shown in Fig. 4.26 (b), and it represents an already formed vein. Periodic dislocation fluxes are used on the surface of the dislocation-based plasticity region. The displacement $U(t)$ is imposed along the external surface in order to induce pure shear in the central region, as shown in Fig. 4.27. The function $U(t)$ is chosen to simulate the experimental strain amplitude in Fig. 4.11 (b). The simulated crystal is oriented for single slip: the Burgers vector is parallel to the y axis and the slip plane normal is parallel to the x axis.

Four different shapes of the vein are compared. As shown in Fig. 4.28, the first one is parallel to the edge dislocation line (“straight”), the second one is inclined in the slip plane (“Y-inclined”), as if it is constituted of mixed edge and screw dislocations, the third one is inclined both in and out of the slip plane (“Y&X-inclined”), as if it is constituted of dislocations belonging to a

Chapter 4. Comparison between simulation and synchrotron Laue microdiffraction experiments

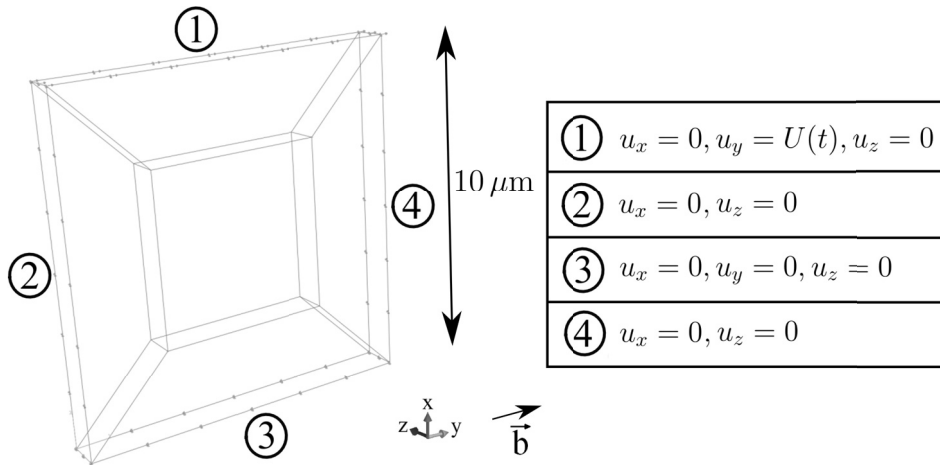


Figure 4.27 – Boundary condition used in the simulation.

| | Straight vein | Y-inclined vein | Y&X-inclined vein | Two inclined veins |
|--|-----------------------|---|--|--|
| | | | | |
| Total height (h) | 1 μm | 2 μm | 2 μm | 4 μm |
| Height of each cuboid | $h_1 = 1 \mu\text{m}$ | $h_1 = 1 \mu\text{m}$ $h_2 = 2 \mu\text{m}$ $h_3 = 1 \mu\text{m}$ | $h_1 = 1 \mu\text{m}$ $h_2 = 2 \mu\text{m}$ $h_3 = 1 \mu\text{m}$ $h_4 = 1 \mu\text{m}$ | $h_1 = 2 \mu\text{m}$ $h_2 = 2 \mu\text{m}$ |
| Total width (w) | 1 μm | 1 μm | 2 μm | 1 μm |
| Width of each cuboid | $w_1 = 1 \mu\text{m}$ | $w_1 = 1 \mu\text{m}$ $w_2 = 1 \mu\text{m}$ $w_3 = 1 \mu\text{m}$ | $w_1 = 1 \mu\text{m}$ $w_2 = 1 \mu\text{m}$ $w_3 = 2 \mu\text{m}$ $w_4 = 1 \mu\text{m}$ | $w_1 = 1 \mu\text{m}$ $w_2 = 1 \mu\text{m}$ |
| Total length (l) | 1 μm | 1 μm | 1.5 μm | 2 μm |
| Length of each cuboid | $l_1 = 1 \mu\text{m}$ | $l_1 = 0.375 \mu\text{m}$ $l_2 = 0.250 \mu\text{m}$ $l_3 = 0.375 \mu\text{m}$ | $l_1 = 0.375 \mu\text{m}$ $l_2 = 0.250 \mu\text{m}$ $l_3 = 0.375 \mu\text{m}$ $l_4 = 0.500 \mu\text{m}$ | $l_1 = 2 \mu\text{m}$ $l_2 = 2 \mu\text{m}$ |
| Y-inclination (α_y) | - | 76° | 76° | 26.5° |
| X-inclination (α_x) | - | - | 69° | - |

Figure 4.28 – Shapes of the straight, Y-inclined, Y&X-inclined and two inclined veins used in the simulation.

4.8. Rotation gradients surrounding different vein structures

secondary slip system, and the last one is constituted of two inclined clusters. The density of immobile dislocations used is $\rho_{imm} = 100 \mu\text{m}^{-2}$ and it is uniform inside the vein. The initial mobile dislocation densities are reported in Tab. 4.2 and copper parameters in Tab. 2.7 are used.

| | |
|--|--|
| $\rho_{e+}(t=0) = 5.0 \mu\text{m}^{-2}$ | $\rho_{e-}(t=0) = 5.0 \mu\text{m}^{-2}$ |
| $\rho_{s+}(t=0) = 5.0 \mu\text{m}^{-2}$ | $\rho_{s-}(t=0) = 5.0 \mu\text{m}^{-2}$ |
| $\rho_{e+,s+}(t=0) = 0.1 \mu\text{m}^{-2}$ | $\rho_{e+,s-}(t=0) = 0.1 \mu\text{m}^{-2}$ |
| $\rho_{e-,s+}(t=0) = 0.1 \mu\text{m}^{-2}$ | $\rho_{e-,s-}(t=0) = 0.1 \mu\text{m}^{-2}$ |

Table 4.2 – Initial dislocation densities for the simulations.

In the following the rotation components are averaged over depth (z axis) and the rotation gradients are calculated using these averaged values. After one full deformation cycle, the rotation field θ_z becomes non-homogeneous for the four vein geometries. This is due to the lower strain accommodated inside the vein, as explained in Fig. 4.1. The shape of this feature is related to the projected shape of the immobile dislocation vein. Therefore the Y-inclined vein has a feature in θ_z which is slightly elongated along the y axis, while for the Y&X-inclined vein it is slightly elongated along both the y and the x axes. The rotation gradients for the four cases are shown in Fig. 4.30, 4.31, 4.32 and 4.33. The following observations can be made:

- the components with the highest magnitude are k_{zx} and k_{zy} because θ_z is the main rotation component. In particular, k_{zy} corresponds to edge GNDs accumulating at the interface of the immobile vein. The value of k_{zy} is highest for the straight vein and smallest for the Y-inclined vein and for the two inclined veins. This is due to the superposition of positive and negative edge GNDs when the depth averaging is carried out;
- the component k_{yy} is related to the screw GND density, which can accumulate on the sides of the veins. Therefore, the positive and negative peaks of k_{yy} are aligned along the vein projection. For the Y-inclined vein the k_{yy} component has positive and negative peaks aligned to the y axis, while for the Y&X-inclined vein, the two central positive and negative peaks are displaced along the x axis.

The experimental images 4.4, 4.5 and 4.6 are used to calculate the rotation gradients after 120 deformation cycles, as shown in Fig. 4.34. The main features appear at the boundary of the highly misoriented area in region F of Fig. 4.7 and the values are higher than in the simulation because the experimentally observed rotation magnitude is higher, as can be found comparing Fig. 4.7 with Fig. 4.29. The following observations can be made:

- the experimental k_{zy} component has not the highest values. This indicates that the prediction given by the Y-inclined vein model or by the Y&X-inclined vein model corre-

Chapter 4. Comparison between simulation and synchrotron Laue microdiffraction experiments

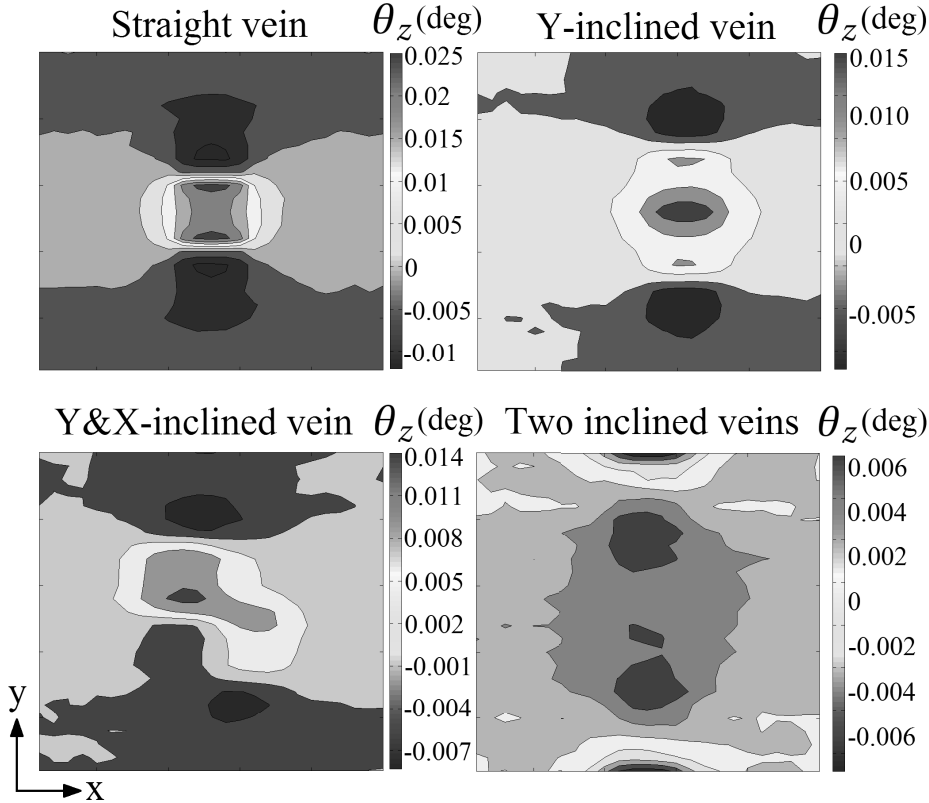


Figure 4.29 – Simulated rotation component θ_z for the four vein shapes after one cycle. Different scales are used because of the different magnitude for the four vein shapes.

4.8. Rotation gradients surrounding different vein structures

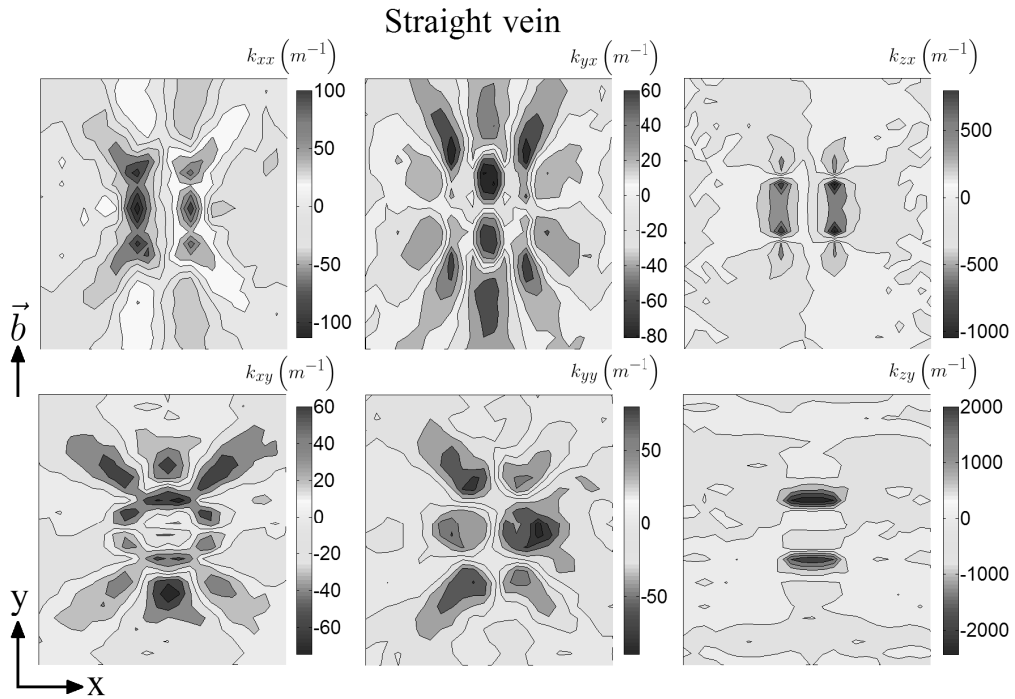


Figure 4.30 – Simulated rotation gradient components for the straight vein shape after one cycle. Different scales are used because of the different magnitude of the components.

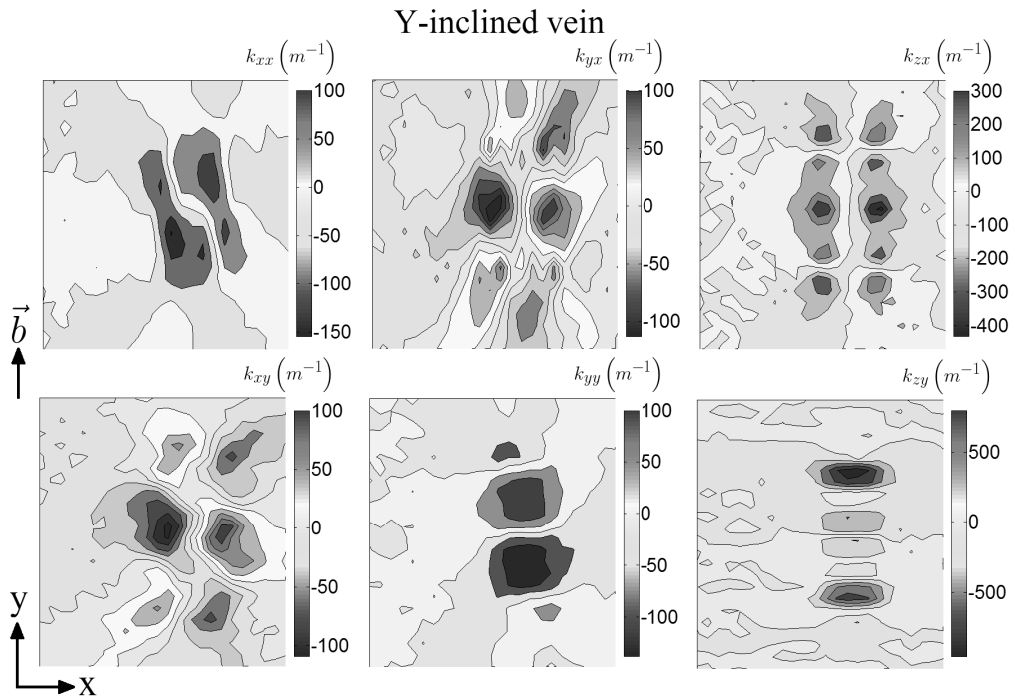


Figure 4.31 – Simulated rotation gradient components for the Y-inclined vein shape after one cycle. Different scales are used because of the different magnitude of the components.

Chapter 4. Comparison between simulation and synchrotron Laue microdiffraction experiments

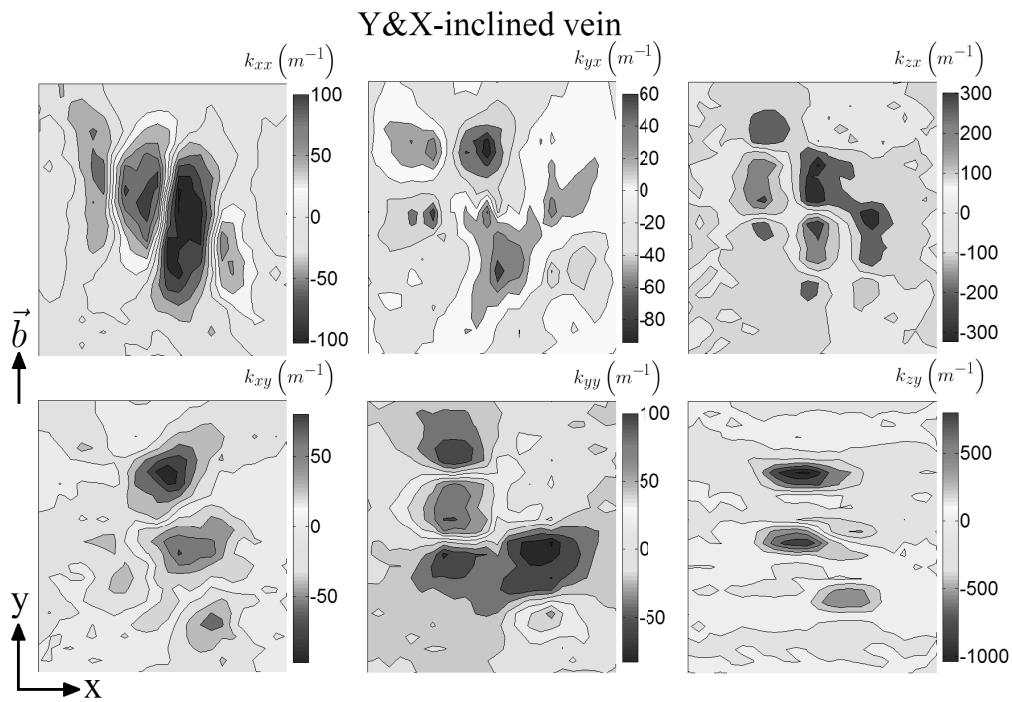


Figure 4.32 – Simulated rotation gradient components for the Y&X-inclined vein shape after one cycle. Different scales are used because of the different magnitude of the components.

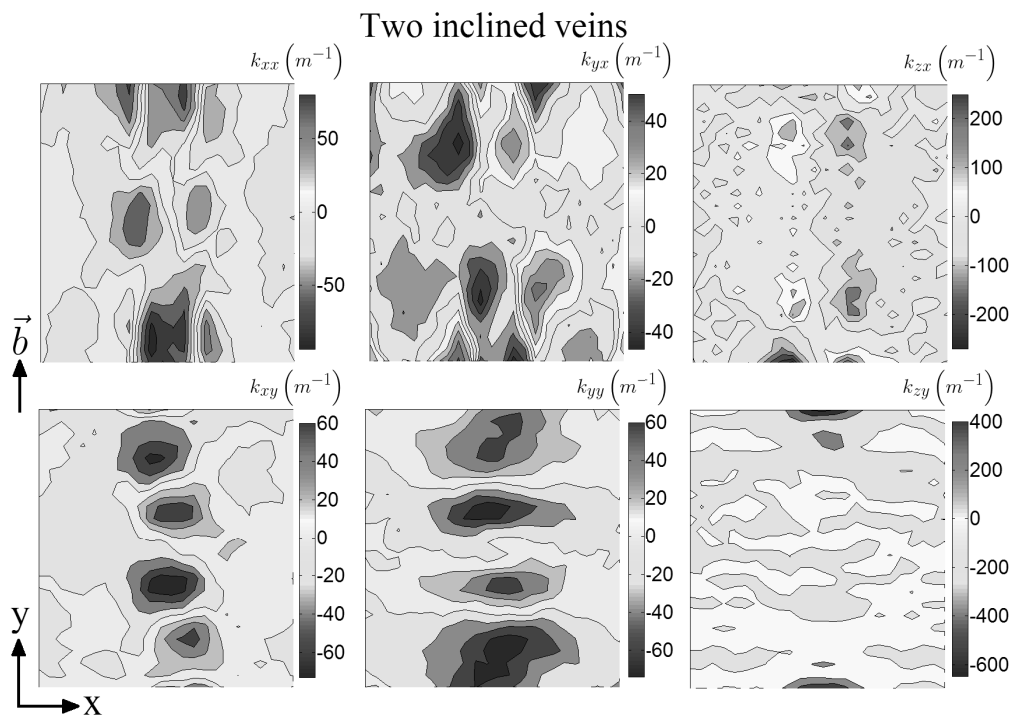


Figure 4.33 – Simulated rotation gradient components for the two inclined veins shape after one cycle. Different scales are used because of the different magnitude of the components.

4.8. Rotation gradients surrounding different vein structures

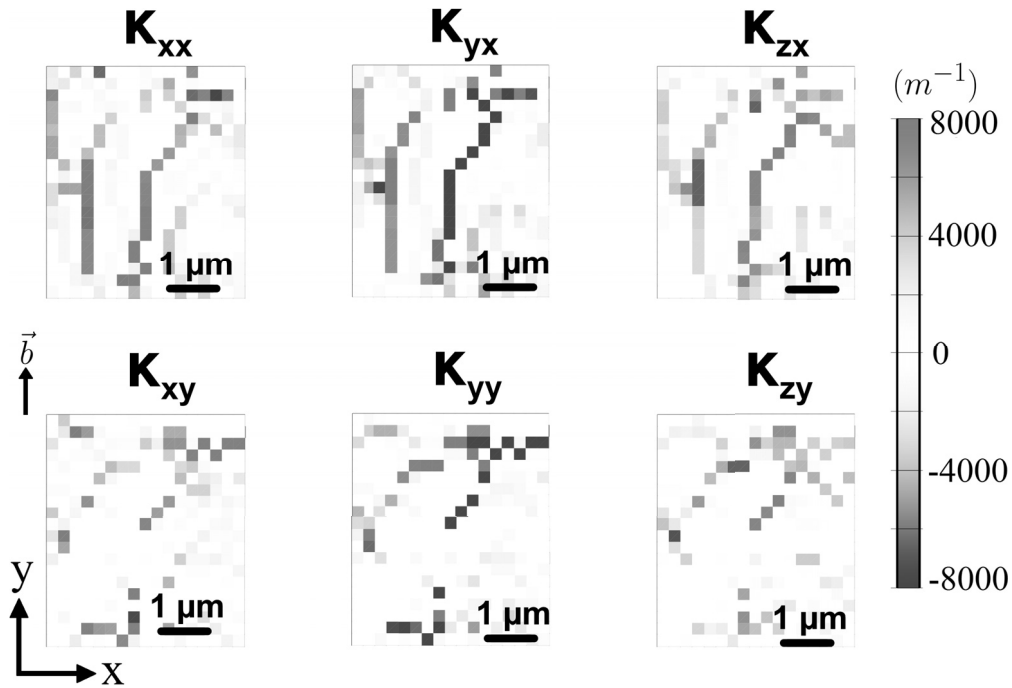


Figure 4.34 – Measured rotation gradients in radians per meter in region F of Fig. 4.7 (courtesy of Ainara Irastorza).

spond better to the experiment and a superposition of positive and negative edge GNDs is a possible explanation for the low value of k_{zy} ;

- the components k_{xx} , k_{yx} and k_{zx} have features elongated along the Burgers vector direction (y axis), while the components k_{xy} , k_{yy} and k_{zy} have features elongated along the slip plane normal (x axis). This is also observed in the experimental images in Fig. 4.34 and it is due to the sharp interface of the rotation field between the immobile vein and the surrounding area;
- in case of a straight vein, the rotation gradient components are either symmetric or antisymmetric with respect to lines parallel to the x and y axis passing through the centre of the vein. In case of a Y-inclined vein this symmetry is broken in the components k_{xx} , k_{xy} , k_{yx} and k_{yy} . The positive and negative peaks of the rotation gradients are not anymore aligned with the x and y axes, but the red and blue features appear inclined. In case of a Y&X-inclined vein this inclination is present in all the rotation gradients. The same can be observed in the upper part of the experimental rotation gradients in Fig. 4.34. This specific feature is not observed in the straight vein model and the two veins model.

Using (4.13), the apparent GND density can be calculated from the rotation gradients. The results are shown in Fig. 4.35 for the four vein shapes. For the straight and Y&X-inclined veins, ρ_{app} has a dominant contribution from α_{yz} . Therefore, mainly features elongated along the

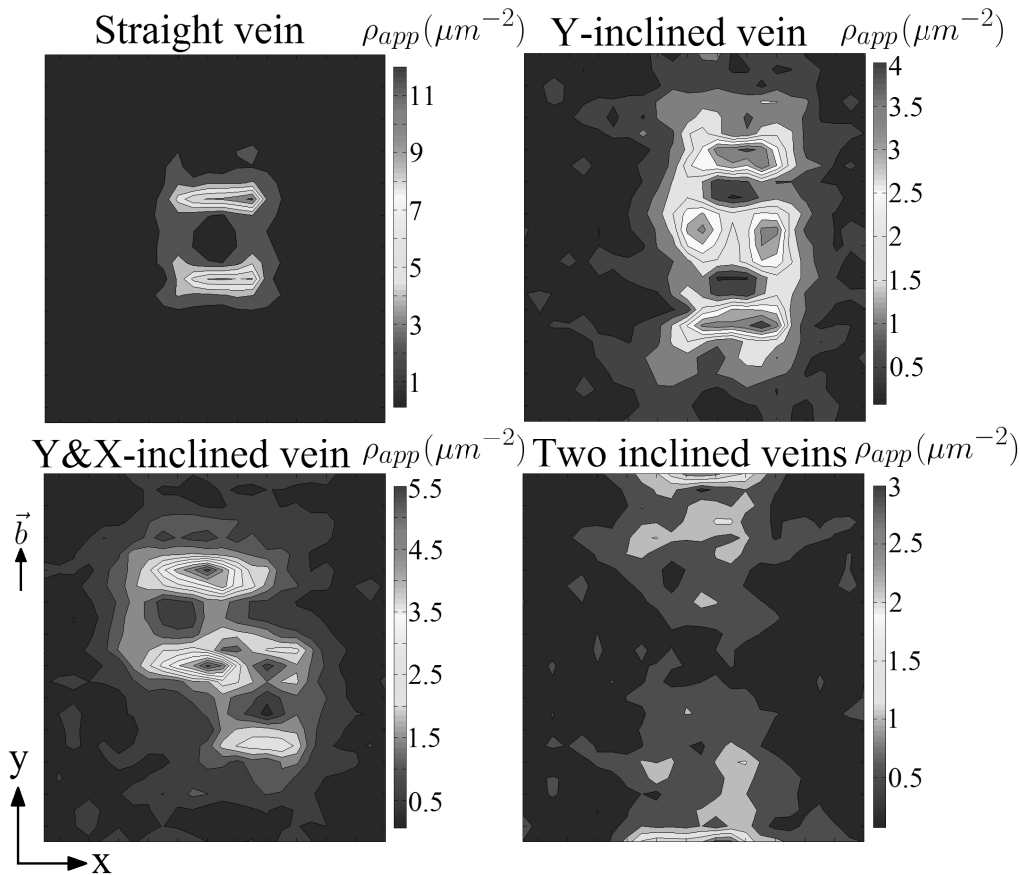


Figure 4.35 – Simulated apparent GND density after one cycle.

x axis appear. The situation is more complex for the Y-inclined vein, for which also α_{xz} is giving an important contribution. The Y-inclined vein shows features which are elongated both along the x and y axes, and which surround the projection of the vein on the x - y plane. The missing apparent GND walls parallel to the y axis for the straight, Y&X-inclined and two veins are not consistent with the experimental observation in region F of Fig. 4.8 and 4.7 at 120 cycles, where the apparent GNDs are completely surrounding the highly misoriented area.

4.9 Formation and dissociation of apparent GND density structures

In this section, the time evolution of the edge GND density has been studied by applying many deformation cycles for the straight vein shape in Fig. 4.28. The effect of the initial density of immobile dislocations in the vein and the ratio between mobile and immobile dislocation densities on the formation or dissociation of GND walls is investigated. The simulation results are compared with the behaviour of the different regions shown in Fig. 4.9.

The displacement amplitude $U(t)$ in Fig. 4.27 is chosen to simulate the experimental strain amplitudes shown in Fig. 4.11 and it varies between two extreme values depending on the

4.9. Formation and dissociation of apparent GND density structures

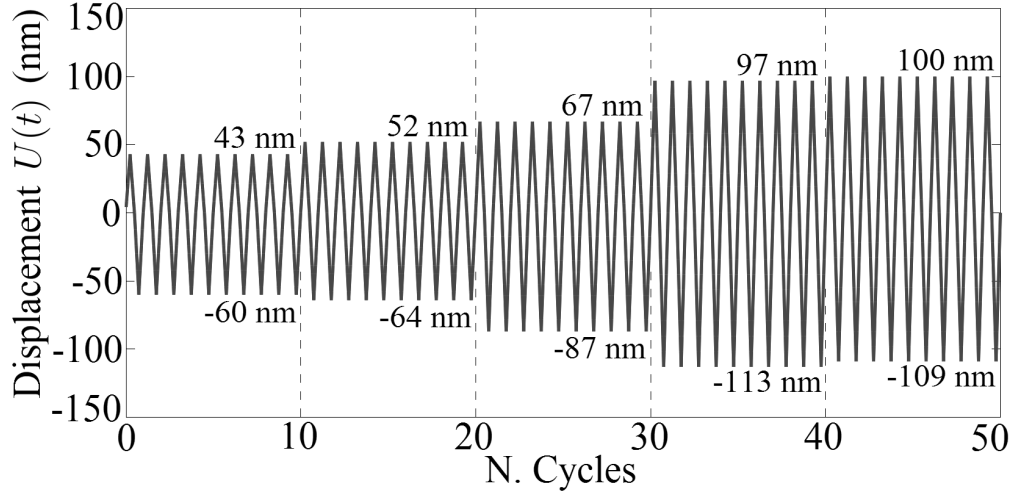


Figure 4.36 – Maximum and minimum values of the applied displacement as a function of the number of cycles N .

cycle number N in a time interval $\Delta t = 0.2$ s, as shown in Fig. 4.36. The strain rate is around $0.05 \div 0.1$ s⁻¹. To reduce the computing time, the displacement amplitude is increased every 10 cycles instead of using the experimental intervals in Fig. 4.11 (b). Simulations are carried out with different densities ρ_{imm} in the vein and different ratios of initial mobile to immobile dislocation densities, as reported in Tab. 4.3.

| | Im3-R0.33 | Im3-R0.05 | Im20-R0.05 | Im100-R0.05 |
|--|-------------------------|--------------------------|-------------------------|------------------------|
| ρ_{imm} | $3 \mu\text{m}^{-2}$ | $3 \mu\text{m}^{-2}$ | $20 \mu\text{m}^{-2}$ | $100 \mu\text{m}^{-2}$ |
| $\rho_{e+}, \rho_{e-}, \rho_{s+}, \rho_{s-} (t=0)$ | $1 \mu\text{m}^{-2}$ | $0.15 \mu\text{m}^{-2}$ | $1 \mu\text{m}^{-2}$ | $5 \mu\text{m}^{-2}$ |
| $\rho_{e+,s+}, \rho_{e+,s-}, \rho_{e-,s+}, \rho_{e-,s-} (t=0)$ | $0.02 \mu\text{m}^{-2}$ | $0.003 \mu\text{m}^{-2}$ | $0.02 \mu\text{m}^{-2}$ | $0.1 \mu\text{m}^{-2}$ |

Table 4.3 – Initial dislocation densities for the simulations.

The different simulations are indicated by “Im3-R0.33”, “Im3-R0.05”, “Im20-R0.05” and “Im100-R0.05”. The number after “Im” is the initial value of ρ_{imm} in μm^{-2} , the number after R is the ratio between mobile and immobile dislocation densities. Initial random fluctuations with a value up to 10% are added to the mobile dislocation densities.

The effect of the ratio R on the microstructural evolution is investigated by examining the edge GND density $\rho_{e,GND} = (\rho_{e+} - \rho_{e-})$ of the primary slip system during the early fatigue cycles ($N < 10$), in which the displacement amplitude is kept constant. The pre-existing vein represents an initial heterogeneity and it obstacles the motion of primary edge dislocations along the Burgers vector direction. Even if the positive and negative edge dislocations move along opposite directions when the load is reversed, the GND walls are present also after full cycles when the applied displacement is zero ($U(t) = 0$) because the formation is partially irreversible. Indeed, the dislocations in the GND walls contribute to the threshold stress

Chapter 4. Comparison between simulation and synchrotron Laue microdiffraction experiments

on the primary slip system τ_{th}^1 in (2.9), which during reverse loading prevents part of the GNDs to move to their original position. For this reason, the evolution of τ_{th}^1 during the early cycles is analyzed in parallel. Fig. 4.37 shows the evolution of the edge GND density $\rho_{e,GND} = (\rho_{e+} - \rho_{e-})$ of the primary slip system and of τ_{th}^1 for Im3-R0.33 and Im3-R0.05, where the following is observed:

- after one cycle GND walls clearly form for the Im3-R0.33 case, whose initial mobile dislocation density is higher than in Im3-R0.05. More cycles are required to observe wall formation in Im3-R0.05. In both cases τ_{th}^1 is maximum where the initial immobile vein is located. Interestingly, the region around the vein in the Im3-R0.33 case have relatively high τ_{th}^1 values. In fact, the absolute values are higher than those inside the vein in the Im3-R0.05 case.
- After 3 cycles GND walls are still visible for both cases, but the GND walls in Im3-R0.33 start dissociating. The analysis of the τ_{th}^1 spatial distribution shows that in Im3-R0.33 the region around the initial vein has patterned spots with high τ_{th}^1 values. In the Im3-R0.05 case, on the other hand, τ_{th}^1 is still maximum in the immobile vein and rather uniform in the surroundings.
- From cycles 5 to 9 the evolution in both cases is rather different. In the case of high initial mobile dislocation density (Im3-R0.33), the GND walls completely dissociate and the τ_{th}^1 pattern observed after 3 cycles evolves by increasing values and by covering larger areas. On the other hand, in the low initial mobile dislocation density case (Im3-R0.05) the GND walls become more defined and their density increases upon cycling. Besides, τ_{th}^1 shows maximum values at the interface of the immobile vein, where dislocations are being accumulated. From cycles 7 to 9, dislocation multiplication starts also getting noticeable in the surroundings (distributed spots with high τ_{th}^1 values) but the pattern is less evident than for Im3-R0.33.

These results indicate that stable GND walls form if τ_{th}^1 is higher in the immobile vein and at its interface than in the surrounding region (Im3-R0.05). If the initial mobile dislocation density is high enough (Im3-R0.33), the dislocation multiplication leads to a higher τ_{th}^1 in the surrounding region. Thus, the immobile vein is not the main structure stopping the motion of mobile dislocations but rather the forming fatigue dislocation structures are.

To determine the effect of ρ_{imm} , the microstructural evolution of all the cases in Tab. 4.3 is investigated. Fig. 4.38 shows the evolution of the edge GND density $\rho_{e,GND} = (\rho_{e+} - \rho_{e-})$ of the primary slip system from cycle 10 to 50 in the four cases and the following conclusions can be drawn:

- by comparing the values after 10 cycles, it is observed that higher initial mobile and immobile dislocation densities lead to higher GND density values.
- In all R=0.05 cases, GND walls form after 10 cycles independently of ρ_{imm} . In the Im3-R0.33 case, the walls dissociate earlier.

4.9. Formation and dissociation of apparent GND density structures

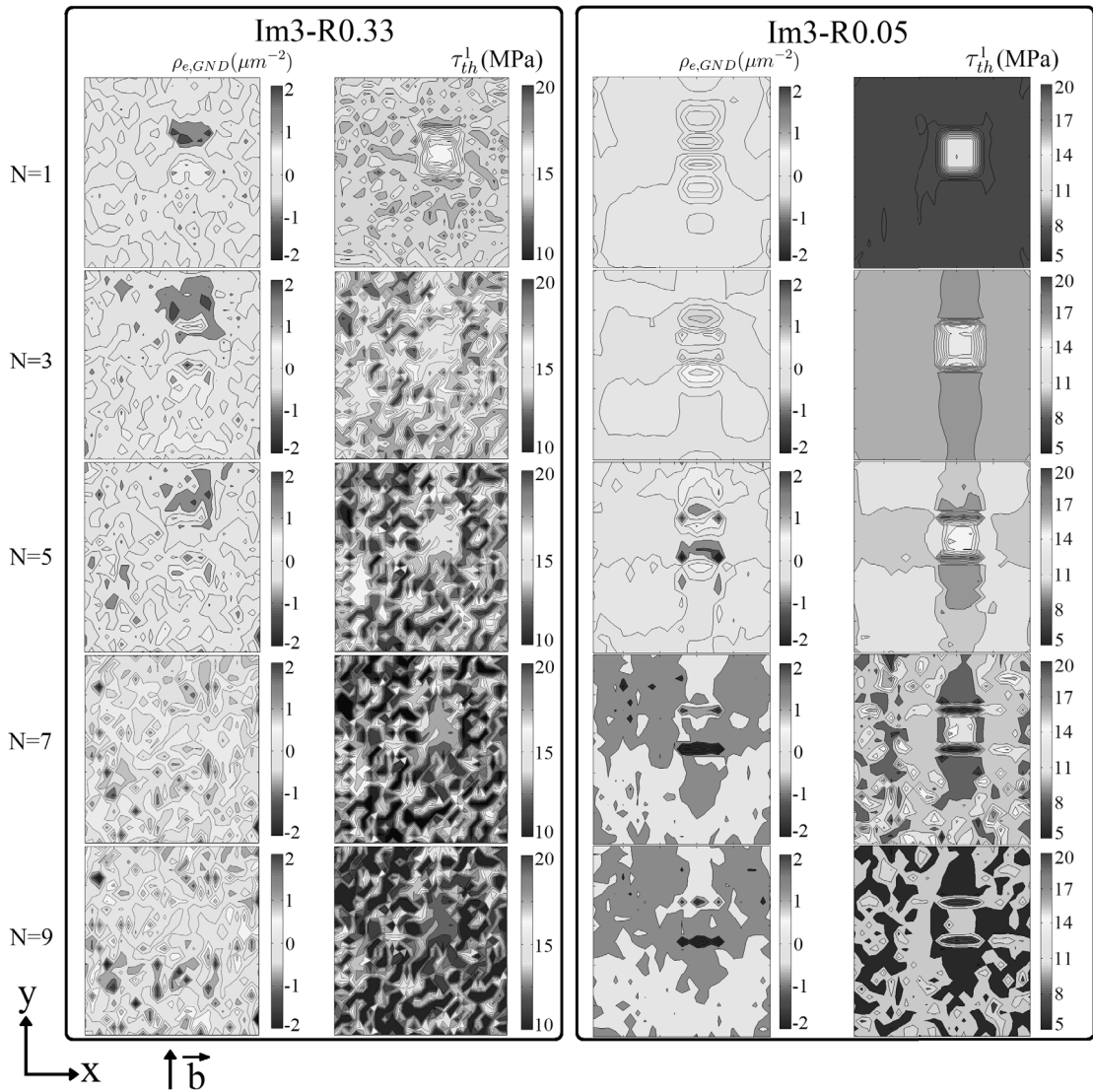


Figure 4.37 – Relationship between the geometrically necessary edge dislocation density $\rho_{e,GND} = (\rho_{e+} - \rho_{e-})$ and the threshold stress on the primary slip system for two different values of the mobile dislocation density.

Chapter 4. Comparison between simulation and synchrotron Laue microdiffraction experiments

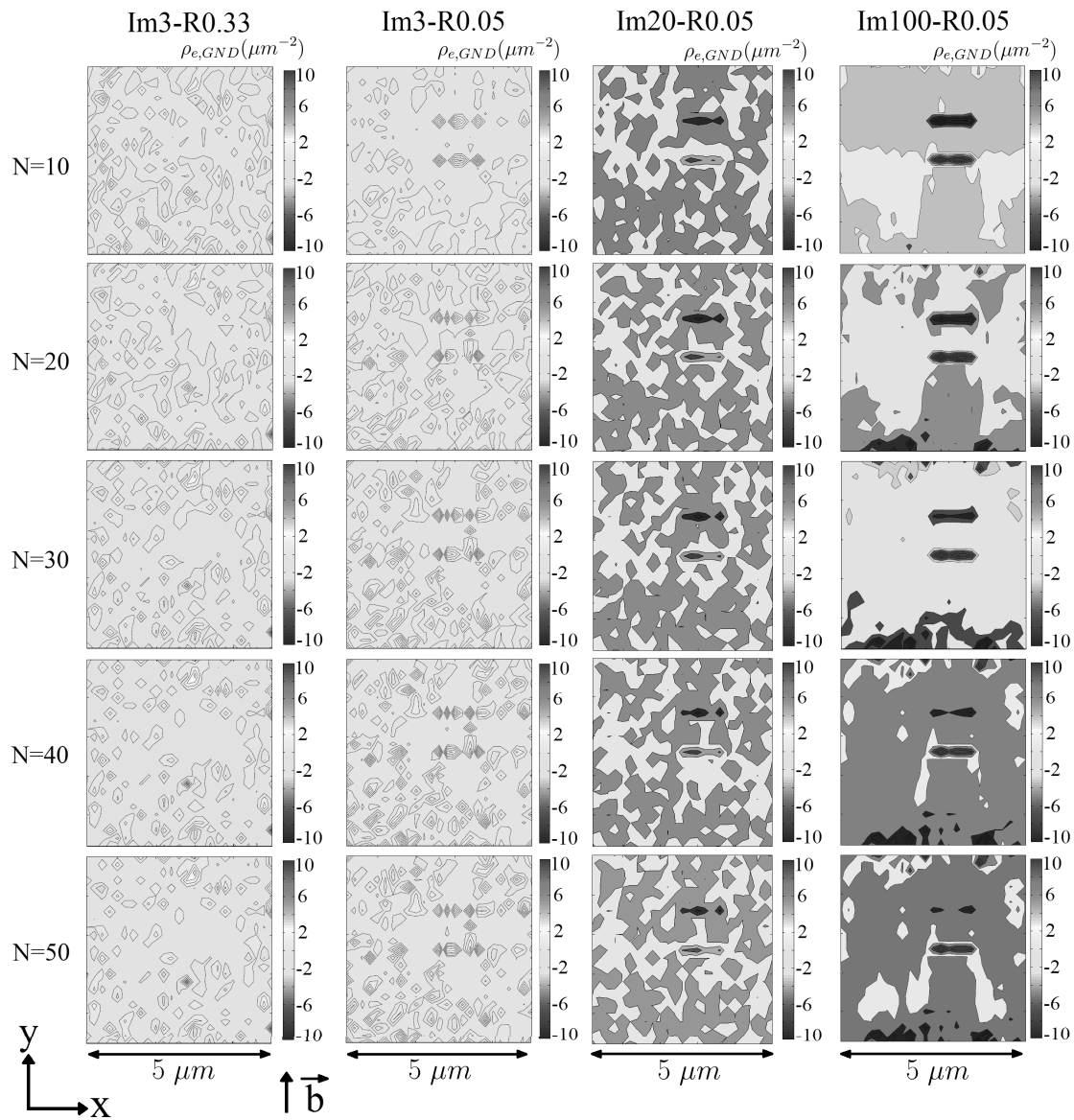


Figure 4.38 – Geometrically necessary edge dislocation density $\rho_{e,GND} = (\rho_{e+} - \rho_{e-})$, averaged over depth (z axis), at different number of cycles N and for different mobile and immobile dislocation densities.

4.9. Formation and dissociation of apparent GND density structures

- The dissociation rate of the formed GND walls is different depending on ρ_{imm} . In the case of low ρ_{imm} (Im3-R0.05), formation of a substructure of positive and negative edge dislocations in the GND walls occurs after 10 cycles, while for higher ρ_{imm} values partial dissociation of the GND walls happens after more cycles (e.g. Im100-R0.05 after 30 cycles). In the particular case of Im20-R0.05, the formed GND walls are stable during the applied cycles.
- In all four cases, the GND distribution remains stable after the displacement jump at 40 cycles.
- None of the R=0.05 cases have similar edge GND density $\rho_{e,GND} = (\rho_{e+} - \rho_{e-})$ distribution to Im3-R0.33 after 50 cycles.

These results indicate that ρ_{imm} has an effect on the evolution of GNDs.

In order to get better understanding, the τ_{th}^1 distribution is examined. Fig. 4.39 shows the threshold stress τ_{th}^1 of the primary slip system as a function of the number of cycles N for all the cases in Tab. 4.3. It is observed that:

- as it was already found in Fig. 4.37, Im3-R0.33 shows a patterned τ_{th}^1 distribution in the surrounding region of the initial vein. Upon cycling, the values increase and during the last 10 cycles the distribution does not change.
- For the same ρ_{imm} but lower initial mobile dislocation density (Im3-R0.05), τ_{th}^1 has a higher value at the interface of the immobile vein. Some pattern in the surrounding region is also observable. Due to the low mobile dislocation density ($0.15 \mu\text{m}^{-2}$), τ_{th}^1 is not sufficiently high to make stable GND structures at the interface of the vein. Therefore, the formation of a substructure of positive and negative edge dislocations in the GND walls from cycle 10 on is observed in Fig. 4.38.
- The qualitative behavior of Im20-R0.05 is analogue to the early stages of Im3-R0.05 ($N < 10$) in Fig. 4.37. Dislocations accumulate at the interface of the immobile vein, where τ_{th}^1 is highest, and therefore GND walls form. Patterning also evolves in the surrounding region. In fact, it is more evident than for Im3-R0.05 due to higher initial mobile dislocation density (see the last row in Fig. 4.39 where the same scale bar is set in the four cases for better comparison).
- In the extreme case Im100-R0.05, the behaviour of τ_{th}^1 is similar to the first 50 cycles of Im20-R0.05. The region surrounding the vein has, however, always low τ_{th}^1 . Indeed, even though the case Im100-R0.05 has higher initial mobile dislocation density, there is no pattern formation. The boundary effects are noticeable in this case due to the difference of the hardening behaviour of the two material models (dislocation based plasticity and von Mises plasticity).

The reason behind the presence or absence of pattern formation is related to the initial mobile dislocation density, which by Orowan's law (1.12) is related to the dislocation velocity. The

Chapter 4. Comparison between simulation and synchrotron Laue microdiffraction experiments

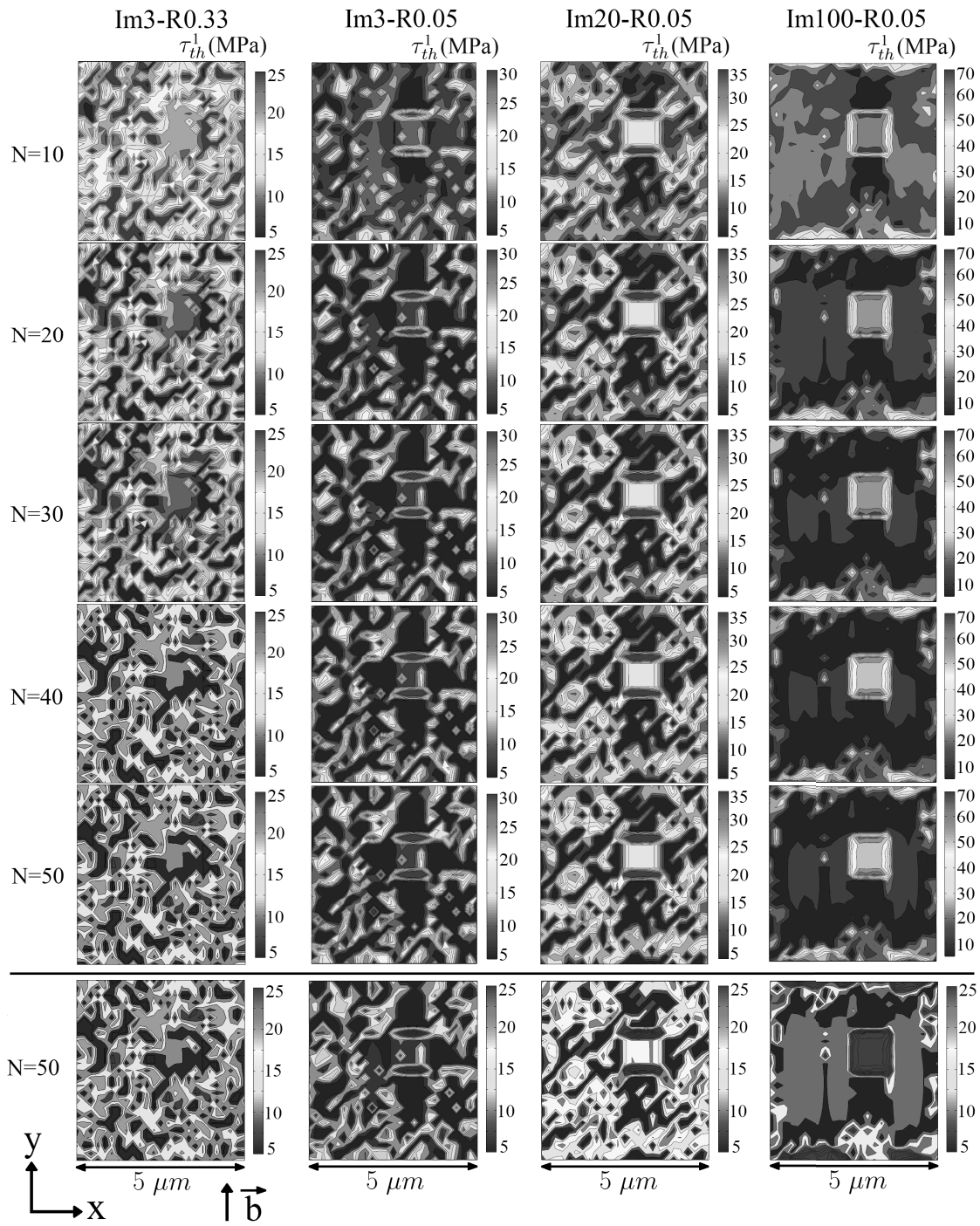


Figure 4.39 – Threshold stress τ_{th}^1 on the primary slip system at different number of cycles N and for different mobile and immobile dislocation densities. The last row shows τ_{th}^1 at cycle 50 with the same color scale.

4.9. Formation and dissociation of apparent GND density structures

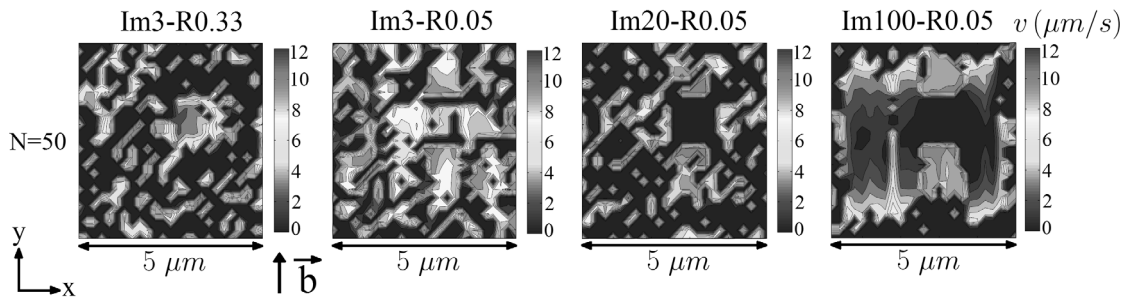


Figure 4.40 – Velocity at cycle 50 for different mobile and immobile dislocation densities.

dislocation velocity at cycle 50 is plotted for the different cases in Fig. 4.40 and the analysis shows that:

- in both Im3-R0.33 and Im3-R0.05, where the initial ρ_{imm} is low, the vein region has non-zero velocity. In Im3-R0.05, there are however more areas with higher velocity. This is in good agreement with Orowan's law (1.12) because the mobile dislocation density in that case is lower. The presence of high velocity regions at the interface of the vein in Im3-R0.05 leads to the formation of the GND walls observed in Fig. 4.38.
- The velocity field of Im20-R0.05 shows null velocity in the vein region but the velocity field in the surrounding is similar to the Im3-R0.05 case and pattern forms. Still the velocity values at the interface of the vein are high and that is why walls are formed: GNDs tend to move there.
- For Im100-R0.05, most of the simulated region has almost zero velocity field due to the high initial mobile density. This is because Orowan's law (1.12) gives a value of the dislocation velocity that decreases if the mobile dislocation density is higher. This leads to regions with lower multiplication rate and less formation of dislocation structures around the immobile vein. As a consequence, there is no pattern formation in the surroundings but only on the walls that act as main obstacle during fatigue.

These results show that the dissociation process of GND walls depends not only on the ratio R as shown before, but also on the initial conditions. For a given ratio R , the initial values determine the microstructural evolution: either the GND walls transform with further cycling (Im3-R0.05), are stable around the vein and do not prevent pattern formation (Im20-R0.05) or act as a dominant obstacle for dislocation motion and inhibit pattern formation (Im100-R0.05).

Fig. 4.41 shows the evolution of the apparent GND density as a function of the number of cycles N for all the cases in Tab. 4.3:

- in Im3-R0.33 the traces of the apparent GND density at cycle 10 are not so strong and are rather disperse. Upon cycling the density of the traces increases but the distribution is rather random. In fact the presence of the vein goes unnoticed.

Chapter 4. Comparison between simulation and synchrotron Laue microdiffraction experiments

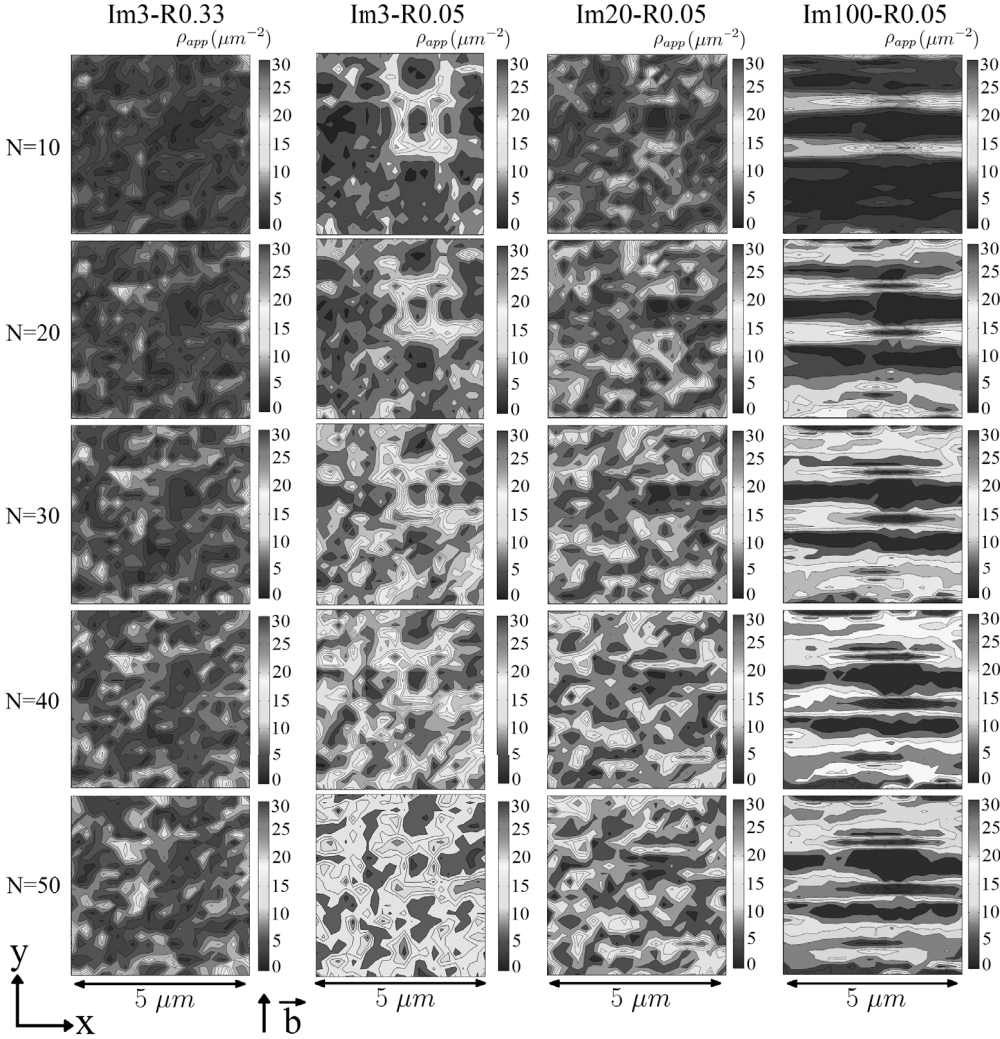


Figure 4.41 – Apparent GND density at different number of cycles N and for different values of the dislocation densities.

4.9. Formation and dissociation of apparent GND density structures

- In Im3-R0.05 the vein is dominant during the first 20 cycles: the high density apparent GND traces are mainly localized in the surrounding of the vein. During the last 30 cycles, the walls are still visible but the surrounding areas also start showing high apparent GND traces.
- In Im20-R0.05, the distribution of the initial apparent GND traces resembles the one of Im3-R0.05 at cycle 30-40. The presence of the immobile vein is visible by apparent GND walls but the surroundings have also high apparent GND traces. Upon cycling the area where the vein is located stays free of traces. Its dimension is similar to other areas where there are no apparent GNDs but where there were no initial heterogeneities.
- When the initial immobile dislocation density is high enough (Im100-R0.05) the vein is dominant during all the applied cycles. We observe that high apparent GND density walls are formed after 10 cycles and that they hardly vanish.

Tab. 4.4 summarizes the main results observed in these simulations. Briefly, the complete dissociation of edge GND walls takes place only if the ratio R is 0.33. For R=0.05, only partial dissociation is observed and generally edge GND walls are stable during cyclic deformation. The threshold stress τ_{th}^1 shows walls at the interface of the immobile vein only when stable edge GND walls form (R=0.05), while it shows only structures around the vein in the case R=0.33. The apparent GND density is strongly correlated with the threshold stress τ_{th}^1 rather than with the edge GND density. A strong pattern around the vein can form for lower values of the mobile dislocation density (Im3-R0.33, Im3-R0.05, Im20-R0.05), while for higher values of the dislocation densities (Im100-R0.05) only walls around the vein form.

| | Im3-R0.33 | Im3-R0.05 |
|----------------|--|--|
| $\rho_{e,GND}$ | Wall dissociation during the first cycles | Formation and substructuring of walls |
| τ_{th}^1 | Pattern forming around the vein | Formation of walls and pattern around the vein |
| ρ_{app} | Pattern forming around the vein | Formation of walls and pattern around the vein |
| | Im20-R0.05 | Im100-R0.05 |
| $\rho_{e,GND}$ | Formation of walls | Formation and partial dissociation of walls |
| τ_{th}^1 | Formation of walls and pattern around the vein | Walls and strong vein |
| ρ_{app} | Walls and strong pattern around the vein | Strong walls |

Table 4.4 – Summary of the results.

The simulated apparent GND density can be compared to the behaviour of the three regions of the experiment in Fig. 4.9:

- region G: the dissociation of pre-existing GND walls and the few appearing traces around them are comparable to the case Im3-R0.33.

Chapter 4. Comparison between simulation and synchrotron Laue microdiffraction experiments

- Region A: pre-existing GND walls rearrange and a pattern around the initial traces form. This is comparable to the case Im20-R0.05.
- Region B: high density initial GND traces are present; they rearrange and form permanent GND walls after 120 cycles. This is comparable to the cases Im3-R0.05 and Im100-R0.05.

4.10 Discussion and conclusion

In conclusion, the CPFE method, used with a dislocation-based constitutive model predicting patterning, can correlate the characteristics of dislocation structures with the crystal lattice rotation. This feature is not available in existing dislocation-based model for fatigue [Déprés et al., 2008] because no coupling with a FE solver is implemented. Analyses of X-ray experiments on polycrystalline structures have been compared with the CPFE method, using phenomenological constitutive laws [Obstalecki et al., 2014], however such an analysis at the micrometre length scale is not available. The main rotation components around the edge dislocation line ($[\bar{1}\bar{2}1]$) and the slip plane normal ($[111]$) observed by Mughrabi [Mughrabi, 2006] are consistent with the experimental results shown in this work. The simulations suggest that, at a larger length scale (of the order of $10\ \mu\text{m}$), these components are affected by the initial misorientation and the resulting inhomogeneity of the stiffness tensor, as shown in section 4.5. At smaller length scale (of the order of $1\ \mu\text{m}$) the specific shape of dislocation structures affect the rotation and the Nye tensor components, as shown in section 4.6. The simulations suggest that a dislocation structure that has a bending in the slip plane can better reproduce the experimental features observed, as shown in section 4.7. This is consistent with TEM observations made on the (111) slip plane shown in section 1.1. The simulations are useful to understand the relationship between GNDs and Nye tensor components, which do not always correspond to real dislocations. Highly misoriented regions can be surrounded by apparent GNDs even if the actual GND content is constituted mainly by edge dislocations, forming walls elongated along the slip plane normal, as shown in section 4.8. Initial heterogeneities at the micrometre length scale were not introduced in existing dislocation-based models for fatigue, but they turn out to affect the evolution of the lattice rotation of different regions, depending on the initial dislocation density, as shown in section 4.9. Finally, a comparison with the Kuhlmann-Wilsdorf theory [Kuhlmann-Wilsdorf, 1979a] explained in section 1.6, assuming that veins and channels are giving a similar contribution to the plastic strain in the material, can be made. The experiment and the simulations are showing highly misoriented regions, which can be caused by gradients of the plastic strain amplitude. In the Kuhlmann-Wilsdorf theory these gradients are not present. Therefore, the results obtained support the Mughrabi model [Mughrabi and Obst, 2005], in which channels accommodate a higher strain amplitude. However, Mughrabi model has to be extended to a 3D one, where veins and channels are changing their position along the specimen depth, in order to capture all the rotation components found in the experiment and in the simulations made in this work.

5 Conclusions and Outlook

In this project the possibility to describe the cyclic fatigue behaviour of FCC metals at the sub-micrometre length scale using the CPFE method has been investigated. A continuum dislocation-based constitutive model has been developed for single slip deformation of single crystals. The main step forward is the prediction of dislocation patterning appearing after many deformation cycles. This has been achieved by the introduction of a new dislocation multiplication law and a Gaussian dipole distance distribution. The multiplication law is based on the introduction of the dislocation curvature as a parameter and on the approximation that dislocation segments with specific orientations are curved. The higher dimensional dislocation theory [Hochrainer, 2015], where the dislocation density and curvature are both state variables, is suitable to find dislocation patterning during monotonic load [Sandfeld and Zaiser, 2015]. The developed model for cyclic fatigue is a special case of the higher dimensional theory, which could be used to find approximate relationships between the dislocation density and curvature. These approximations can be introduced in a model with a lower number of state variables, suitable to analyze cyclic fatigue.

A continuum local cross slip law has been developed to describe the behaviour of different materials, such as copper and aluminium. The mechanical properties and the features of dislocation patterns depend on the cross slip coefficient β . The large uncertainty on this coefficient needs further clarifications in order to develop a model that can reproduce experimental observations without fine tuning parameters. Non-local cross slip laws have been recently developed in continuum dislocation models [Xia and El-Azab, 2015] and used to simulate dislocation patterning during monotonic load. The application of these laws to cyclic fatigue needs to be further studied. The simulations carried out using the dipole-dipole interaction to reproduce persistent slip bands have shown that the introduction of small interaction terms can change the characteristics of developing dislocation patterns. A similar result was found by [Walgraef and Aifantis, 1985] introducing a threshold stress above which dislocations are liberated from veins. However, the thin PSB walls can be described only using a fine mesh, with an element size below 100 nm, and the details of the transition from veins to PSB walls need to be clarified.

In the multiple slip model, a continuum approach to describe dislocation junctions has been

Chapter 5. Conclusions and Outlook

developed. The introduction of dislocation junctions affects strongly the features of dislocation patterns, especially their shape and orientation. The recent implementation of partial dislocations and stacking faults in a continuum model [Leung and Ngan, 2016] shows that more accurate description of dislocation junctions can be achieved. The model developed in this project is able to capture the formation of dislocation junctions with the primary slip system, while a model with more state variables would be required to capture all possible dislocation junctions. The ECCI experiments provide a valuable validation method for multiple slip continuum dislocation models. However, methods to estimate the dislocation density and the depth of dislocation structures are required for quantitative comparison.

The CPFEM method is suitable to simulate the crystal lattice rotation and its relationship with dislocation structures. The comparison with transmission Laue microdiffraction experiments is limited by the volume average of this experimental technique. However, in this project, dislocation based models were able to reproduce the features of the Nye tensor in the surrounding of highly misoriented regions during cyclic fatigue. The influence of pre-existing plastic deformations due to machining has been introduced in the model in terms of initial lattice rotations. Simulations have shown that this is fundamental to predict the subsequent evolution of the rotation components. The exact position of dislocation structures during cyclic fatigue cannot be captured by the developed model if the initial dislocation distribution is not known. A combination of Laue microdiffraction and electron microscopy techniques could make it possible to reconstruct this initial dislocation distribution.

A Equation summary

A.1 Single slip model for cyclic fatigue

In this section the constitutive equations of the single slip model for cyclic fatigue, introduced in section 2.2, are summarized. The state variables used on every slip system are reported in Tab. A.1.

| | | | |
|----------------|----------------|----------------|----------------|
| ρ_{e+} | ρ_{e-} | ρ_{s+} | ρ_{s-} |
| $\rho_{e+,s+}$ | $\rho_{e+,s-}$ | $\rho_{e-,s+}$ | $\rho_{e-,s-}$ |

Table A.1 – Dislocation densities used for the single slip model for cyclic fatigue.

The rate equations for these dislocation densities on every slip system α are reported in the following. A (x, y) coordinate system is used, where the y axis is along the Burgers vector direction.

$$\dot{\rho}_{e+}^{\alpha} = \frac{F_s^{\alpha}(h_s)|v^{\alpha}|}{\bar{l}_c} (\rho_{e+,s+}^{\alpha} + \rho_{e+,s-}^{\alpha}) - 4\check{d}_e^{\alpha}|v^{\alpha}|F_e^{\alpha}(h_e)\rho_{e+}^{\alpha} (\rho_{e-}^{\alpha} + \rho_{e-,s+}^{\alpha} + \rho_{e-,s-}^{\alpha}) - \frac{\partial}{\partial y} (F_e^{\alpha}(h_e)\rho_{e+}^{\alpha}v^{\alpha}). \quad (\text{A.1})$$

$$\dot{\rho}_{e-}^{\alpha} = \frac{F_s^{\alpha}(h_s)|v^{\alpha}|}{\bar{l}_c} (\rho_{e-,s+}^{\alpha} + \rho_{e-,s-}^{\alpha}) - 4\check{d}_e^{\alpha}|v^{\alpha}|F_e^{\alpha}(h_e)\rho_{e-}^{\alpha} (\rho_{e+}^{\alpha} + \rho_{e+,s+}^{\alpha} + \rho_{e+,s-}^{\alpha}) + \frac{\partial}{\partial y} (F_e^{\alpha}(h_e)\rho_{e-}^{\alpha}v^{\alpha}). \quad (\text{A.2})$$

$$\dot{\rho}_{s+}^{\alpha} = \frac{F_e^{\alpha}(h_e)|v^{\alpha}|}{\bar{l}_c} (\rho_{e+,s+}^{\alpha} + \rho_{e-,s+}^{\alpha}) - 4\check{d}_s^{\alpha}|v^{\alpha}|F_s^{\alpha}(h_s)\rho_{s+}^{\alpha} (\rho_{s-}^{\alpha} + \rho_{e+,s-}^{\alpha} + \rho_{e-,s-}^{\alpha}) + \frac{\partial}{\partial x} (F_s^{\alpha}(h_s)\rho_{s+}^{\alpha}v^{\alpha}). \quad (\text{A.3})$$

Appendix A. Equation summary

$$\dot{\rho}_{s-}^{\alpha} = \frac{F_e^{\alpha}(h_e)|v^{\alpha}|}{\bar{l}_c} (\rho_{e+,s-}^{\alpha} + \rho_{e-,s-}^{\alpha}) - 4\check{d}_s^{\alpha}|v^{\alpha}|F_s^{\alpha}(h_s)\rho_{s-}^{\alpha} (\rho_{s+}^{\alpha} + \rho_{e+,s+}^{\alpha} + \rho_{e-,s+}^{\alpha}) - \frac{\partial}{\partial x} (F_s^{\alpha}(h_s)\rho_{s-}^{\alpha}v^{\alpha}). \quad (\text{A.4})$$

$$\begin{aligned} \dot{\rho}_{e+,s+}^{\alpha} = & -4\check{d}_e^{\alpha}|v^{\alpha}|F_e^{\alpha}(h_e)\rho_{e+,s+}^{\alpha} (\rho_{e-}^{\alpha} + \rho_{e-,s+}^{\alpha} + \rho_{e-,s-}^{\alpha}) - 4\check{d}_s^{\alpha}|v^{\alpha}|F_s^{\alpha}(h_s)\rho_{e+,s+}^{\alpha} (\rho_{s-}^{\alpha} + \rho_{e+,s-}^{\alpha} + \rho_{e-,s-}^{\alpha}) \\ & - \frac{\partial}{\partial y} (F_e^{\alpha}(h_e)\rho_{e+,s+}^{\alpha}v^{\alpha}) + \frac{\partial}{\partial x} (F_s^{\alpha}(h_s)\rho_{e+,s+}^{\alpha}v^{\alpha}) + \frac{\beta|v^{\alpha}|}{b} (\rho_{s+}^{\alpha} + \rho_{s-}^{\alpha}). \quad (\text{A.5}) \end{aligned}$$

$$\begin{aligned} \dot{\rho}_{e+,s-}^{\alpha} = & -4\check{d}_e^{\alpha}|v^{\alpha}|F_e^{\alpha}(h_e)\rho_{e+,s-}^{\alpha} (\rho_{e-}^{\alpha} + \rho_{e-,s+}^{\alpha} + \rho_{e-,s-}^{\alpha}) - 4\check{d}_s^{\alpha}|v^{\alpha}|F_s^{\alpha}(h_s)\rho_{e+,s-}^{\alpha} (\rho_{s+}^{\alpha} + \rho_{e+,s+}^{\alpha} + \rho_{e-,s+}^{\alpha}) \\ & - \frac{\partial}{\partial y} (F_e^{\alpha}(h_e)\rho_{e+,s-}^{\alpha}v^{\alpha}) - \frac{\partial}{\partial x} (F_s^{\alpha}(h_s)\rho_{e+,s-}^{\alpha}v^{\alpha}) + \frac{\beta|v^{\alpha}|}{b} (\rho_{s+}^{\alpha} + \rho_{s-}^{\alpha}). \quad (\text{A.6}) \end{aligned}$$

$$\begin{aligned} \dot{\rho}_{e-,s+}^{\alpha} = & -4\check{d}_e^{\alpha}|v^{\alpha}|F_e^{\alpha}(h_e)\rho_{e-,s+}^{\alpha} (\rho_{e+}^{\alpha} + \rho_{e+,s+}^{\alpha} + \rho_{e+,s-}^{\alpha}) - 4\check{d}_s^{\alpha}|v^{\alpha}|F_s^{\alpha}(h_s)\rho_{e-,s+}^{\alpha} (\rho_{s-}^{\alpha} + \rho_{e+,s-}^{\alpha} + \rho_{e-,s-}^{\alpha}) \\ & + \frac{\partial}{\partial y} (F_e^{\alpha}(h_e)\rho_{e-,s+}^{\alpha}v^{\alpha}) + \frac{\partial}{\partial x} (F_s^{\alpha}(h_s)\rho_{e-,s+}^{\alpha}v^{\alpha}) + \frac{\beta|v^{\alpha}|}{b} (\rho_{s+}^{\alpha} + \rho_{s-}^{\alpha}). \quad (\text{A.7}) \end{aligned}$$

$$\begin{aligned} \dot{\rho}_{e-,s-}^{\alpha} = & -4\check{d}_e^{\alpha}|v^{\alpha}|F_e^{\alpha}(h_e)\rho_{e-,s-}^{\alpha} (\rho_{e+}^{\alpha} + \rho_{e+,s+}^{\alpha} + \rho_{e+,s-}^{\alpha}) - 4\check{d}_s^{\alpha}|v^{\alpha}|F_s^{\alpha}(h_s)\rho_{e-,s-}^{\alpha} (\rho_{s+}^{\alpha} + \rho_{e+,s+}^{\alpha} + \rho_{e-,s+}^{\alpha}) \\ & + \frac{\partial}{\partial y} (F_e^{\alpha}(h_e)\rho_{e-,s-}^{\alpha}v^{\alpha}) - \frac{\partial}{\partial x} (F_s^{\alpha}(h_s)\rho_{e-,s-}^{\alpha}v^{\alpha}) + \frac{\beta|v^{\alpha}|}{b} (\rho_{s+}^{\alpha} + \rho_{s-}^{\alpha}). \quad (\text{A.8}) \end{aligned}$$

The dipole stability distances h_e^{α} and h_s^{α} , which are functions of the resolved shear stress τ^{α} , are given by:

$$h_e^{\alpha} = \frac{Gb}{8\pi(1-\nu)|\tau^{\alpha}|}, \quad (\text{A.9})$$

$$h_s^{\alpha} = \frac{Gb}{8\pi|\tau^{\alpha}|}. \quad (\text{A.10})$$

The fraction of edge and screw mobile dislocations F_e^{α} and F_s^{α} correspond to the green area below the Gaussian curve in Fig. 2.6. They are calculated using:

$$F_e^{\alpha}(h_e^{\alpha}) = \frac{1}{2} \left(1 - \operatorname{erf} \left(\frac{h_e^{\alpha} - \bar{h}_e^{\alpha}}{0.467\bar{h}_e^{\alpha}} \right) \right), \quad (\text{A.11})$$

$$F_s^{\alpha}(h_s^{\alpha}) = \frac{1}{2} \left(1 - \operatorname{erf} \left(\frac{h_s^{\alpha} - \bar{h}_s^{\alpha}}{0.467\bar{h}_s^{\alpha}} \right) \right), \quad (\text{A.12})$$

where erf is the error function. \bar{h}_e^α and \bar{h}_s^α are the mean dipole distances for edge and screw dislocations:

$$\bar{h}_e^\alpha = \frac{1}{8\pi\alpha(1-\nu)\sqrt{(\rho_{e+}^\alpha + \rho_{e-}^\alpha + \rho_{e+,s+}^\alpha + \rho_{e+,s-}^\alpha + \rho_{e-,s+}^\alpha + \rho_{e-,s-}^\alpha)}}, \quad (\text{A.13})$$

$$\bar{h}_s^\alpha = \frac{1}{8\pi\alpha(1-\nu)\sqrt{(\rho_{s+}^\alpha + \rho_{s-}^\alpha + \rho_{e+,s+}^\alpha + \rho_{e+,s-}^\alpha + \rho_{e-,s+}^\alpha + \rho_{e-,s-}^\alpha)}}. \quad (\text{A.14})$$

A.2 Multiple slip model for cyclic fatigue

In this section the constitutive equations of the multiple slip model for cyclic fatigue based on dislocation junctions, introduced in section 3.2, are summarized. The state variables used on every slip system are reported in Tab. A.2.

| | | | |
|-----------------------|-----------------------|-----------------------|-----------------------|
| $\rho_{//+}$ | $\rho_{//-}$ | $\rho_{\Gamma+}$ | $\rho_{\Gamma-}$ |
| $\rho_{//+, \Gamma+}$ | $\rho_{//+, \Gamma-}$ | $\rho_{//-, \Gamma+}$ | $\rho_{//-, \Gamma-}$ |

Table A.2 – Dislocation densities used in the junction constitutive model.

The rate equations for these dislocation densities on every slip system α are reported in the following. A (x, y) coordinate system is used, where the y axis is along the Burgers vector direction.

$$\begin{aligned} \dot{\rho}_{//+}^\alpha = & \frac{|v^\alpha|}{\bar{\Lambda}} (\rho_{//+, \Gamma+}^\alpha + \rho_{//+, \Gamma-}^\alpha) - 4\check{d}_e^\alpha |v^\alpha| \rho_{//+}^\alpha \cos\Phi (\rho_{//-}^\alpha \cos\Phi + \rho_{\Gamma+}^\alpha \sin\Phi) \\ & - 4\check{d}_s^\alpha |v^\alpha| \rho_{//+}^\alpha \sin\Phi (\rho_{\Gamma-}^\alpha \cos\Phi + \rho_{//-}^\alpha \sin\Phi) + \frac{\partial}{\partial x} (|v^\alpha| \rho_{//+}^\alpha \sin\Phi) - \frac{\partial}{\partial y} (|v^\alpha| \rho_{//+}^\alpha \cos\Phi). \end{aligned} \quad (\text{A.15})$$

$$\begin{aligned} \dot{\rho}_{//-}^\alpha = & \frac{|v^\alpha|}{\bar{\Lambda}} (\rho_{//-, \Gamma+}^\alpha + \rho_{//-, \Gamma-}^\alpha) - 4\check{d}_e^\alpha |v^\alpha| \rho_{//-}^\alpha \cos\Phi (\rho_{//+}^\alpha \cos\Phi + \rho_{\Gamma-}^\alpha \sin\Phi) \\ & - 4\check{d}_s^\alpha |v^\alpha| \rho_{//-}^\alpha \sin\Phi (\rho_{\Gamma+}^\alpha \cos\Phi + \rho_{//+}^\alpha \sin\Phi) - \frac{\partial}{\partial x} (|v^\alpha| \rho_{//-}^\alpha \sin\Phi) + \frac{\partial}{\partial y} (|v^\alpha| \rho_{//-}^\alpha \cos\Phi). \end{aligned} \quad (\text{A.16})$$

$$\begin{aligned} \dot{\rho}_{\Gamma+}^\alpha = & \frac{|v^\alpha|}{\bar{\Lambda}} (\rho_{//+, \Gamma+}^\alpha + \rho_{//-, \Gamma+}^\alpha) - 4\check{d}_e^\alpha |v^\alpha| \rho_{\Gamma+}^\alpha \sin\Phi (\rho_{//+}^\alpha \cos\Phi + \rho_{\Gamma-}^\alpha \sin\Phi) \\ & - 4\check{d}_s^\alpha |v^\alpha| \rho_{\Gamma+}^\alpha \cos\Phi (\rho_{\Gamma-}^\alpha \cos\Phi + \rho_{//-}^\alpha \sin\Phi) + \frac{\partial}{\partial x} (|v^\alpha| \rho_{\Gamma+}^\alpha \cos\Phi) + \frac{\partial}{\partial y} (|v^\alpha| \rho_{\Gamma+}^\alpha \sin\Phi). \end{aligned} \quad (\text{A.17})$$

Appendix A. Equation summary

$$\begin{aligned} \dot{\rho}_{\Gamma-}^{\alpha} &= \frac{|v^{\alpha}|}{\Lambda} (\rho_{\parallel+, \Gamma-}^{\alpha} + \rho_{\parallel-, \Gamma-}^{\alpha}) - 4\check{d}_e^{\alpha} |v^{\alpha}| \rho_{\Gamma-}^{\alpha} \sin \Phi (\rho_{\parallel-}^{\alpha} \cos \Phi + \rho_{\Gamma+}^{\alpha} \sin \Phi) \\ &- 4\check{d}_s^{\alpha} |v^{\alpha}| \rho_{\Gamma-}^{\alpha} \cos \Phi (\rho_{\Gamma+}^{\alpha} \cos \Phi + \rho_{\parallel+}^{\alpha} \sin \Phi) - \frac{\partial}{\partial x} (|v^{\alpha}| \rho_{\Gamma-}^{\alpha} \cos \Phi) - \frac{\partial}{\partial y} (|v^{\alpha}| \rho_{\Gamma-}^{\alpha} \sin \Phi) . \end{aligned} \quad (\text{A.18})$$

$$\begin{aligned} \dot{\rho}_{\parallel+, \Gamma+}^{\alpha} &= -4\check{d}_e^{\alpha} |v^{\alpha}| \rho_{\parallel+, \Gamma+}^{\alpha} [\cos \Phi (\rho_{\parallel-}^{\alpha} \cos \Phi + \rho_{\Gamma+}^{\alpha} \sin \Phi) + \sin \Phi (\rho_{\parallel+}^{\alpha} \cos \Phi + \rho_{\Gamma-}^{\alpha} \sin \Phi)] \\ &- 4\check{d}_s^{\alpha} |v^{\alpha}| \rho_{\parallel+, \Gamma+}^{\alpha} [\sin \Phi (\rho_{\Gamma-}^{\alpha} \cos \Phi + \rho_{\parallel-}^{\alpha} \sin \Phi) + \cos \Phi (\rho_{\Gamma-}^{\alpha} \cos \Phi + \rho_{\parallel-}^{\alpha} \sin \Phi)] \\ &+ \frac{\partial}{\partial x} (|v^{\alpha}| \rho_{\parallel+, \Gamma+}^{\alpha} (\sin \Phi + \cos \Phi)) - \frac{\partial}{\partial y} (|v^{\alpha}| \rho_{\parallel+, \Gamma+}^{\alpha} (\cos \Phi - \sin \Phi)) \\ &\quad + \frac{\beta |v^{\alpha}|}{b} [\cos \Phi (\rho_{\Gamma+}^{\alpha} + \rho_{\Gamma-}^{\alpha}) + \sin \Phi (\rho_{\parallel+}^{\alpha} + \rho_{\parallel-}^{\alpha})] . \end{aligned} \quad (\text{A.19})$$

$$\begin{aligned} \dot{\rho}_{\parallel+, \Gamma-}^{\alpha} &= -4\check{d}_e^{\alpha} |v^{\alpha}| \rho_{\parallel+, \Gamma-}^{\alpha} [\cos \Phi (\rho_{\parallel-}^{\alpha} \cos \Phi + \rho_{\Gamma+}^{\alpha} \sin \Phi) + \sin \Phi (\rho_{\parallel-}^{\alpha} \cos \Phi + \rho_{\Gamma+}^{\alpha} \sin \Phi)] \\ &- 4\check{d}_s^{\alpha} |v^{\alpha}| \rho_{\parallel+, \Gamma-}^{\alpha} [\sin \Phi (\rho_{\Gamma-}^{\alpha} \cos \Phi + \rho_{\parallel-}^{\alpha} \sin \Phi) + \cos \Phi (\rho_{\Gamma+}^{\alpha} \cos \Phi + \rho_{\parallel+}^{\alpha} \sin \Phi)] \\ &- \frac{\partial}{\partial x} (|v^{\alpha}| \rho_{\parallel+, \Gamma-}^{\alpha} (\cos \Phi - \sin \Phi)) - \frac{\partial}{\partial y} (|v^{\alpha}| \rho_{\parallel+, \Gamma-}^{\alpha} (\cos \Phi + \sin \Phi)) \\ &\quad + \frac{\beta |v^{\alpha}|}{b} [\cos \Phi (\rho_{\Gamma+}^{\alpha} + \rho_{\Gamma-}^{\alpha}) + \sin \Phi (\rho_{\parallel+}^{\alpha} + \rho_{\parallel-}^{\alpha})] . \end{aligned} \quad (\text{A.20})$$

$$\begin{aligned} \dot{\rho}_{\parallel-, \Gamma+}^{\alpha} &= -4\check{d}_e^{\alpha} |v^{\alpha}| \rho_{\parallel-, \Gamma+}^{\alpha} [\cos \Phi (\rho_{\parallel+}^{\alpha} \cos \Phi + \rho_{\Gamma-}^{\alpha} \sin \Phi) + \sin \Phi (\rho_{\parallel+}^{\alpha} \cos \Phi + \rho_{\Gamma-}^{\alpha} \sin \Phi)] \\ &- 4\check{d}_s^{\alpha} |v^{\alpha}| \rho_{\parallel-, \Gamma+}^{\alpha} [\sin \Phi (\rho_{\Gamma+}^{\alpha} \cos \Phi + \rho_{\parallel+}^{\alpha} \sin \Phi) + \cos \Phi (\rho_{\Gamma-}^{\alpha} \cos \Phi + \rho_{\parallel-}^{\alpha} \sin \Phi)] \\ &+ \frac{\partial}{\partial x} (|v^{\alpha}| \rho_{\parallel-, \Gamma+}^{\alpha} (\cos \Phi - \sin \Phi)) + \frac{\partial}{\partial y} (|v^{\alpha}| \rho_{\parallel-, \Gamma+}^{\alpha} (\cos \Phi + \sin \Phi)) \\ &\quad + \frac{\beta |v^{\alpha}|}{b} [\cos \Phi (\rho_{\Gamma+}^{\alpha} + \rho_{\Gamma-}^{\alpha}) + \sin \Phi (\rho_{\parallel+}^{\alpha} + \rho_{\parallel-}^{\alpha})] . \end{aligned} \quad (\text{A.21})$$

$$\begin{aligned} \dot{\rho}_{\parallel-, \Gamma-}^{\alpha} &= -4\check{d}_e^{\alpha} |v^{\alpha}| \rho_{\parallel-, \Gamma-}^{\alpha} [\cos \Phi (\rho_{\parallel+}^{\alpha} \cos \Phi + \rho_{\Gamma-}^{\alpha} \sin \Phi) + \sin \Phi (\rho_{\parallel-}^{\alpha} \cos \Phi + \rho_{\Gamma+}^{\alpha} \sin \Phi)] \\ &- 4\check{d}_s^{\alpha} |v^{\alpha}| \rho_{\parallel-, \Gamma-}^{\alpha} [\sin \Phi (\rho_{\Gamma+}^{\alpha} \cos \Phi + \rho_{\parallel+}^{\alpha} \sin \Phi) + \cos \Phi (\rho_{\Gamma+}^{\alpha} \cos \Phi + \rho_{\parallel+}^{\alpha} \sin \Phi)] \\ &- \frac{\partial}{\partial x} (|v^{\alpha}| \rho_{\parallel-, \Gamma-}^{\alpha} (\cos \Phi + \sin \Phi)) + \frac{\partial}{\partial y} (|v^{\alpha}| \rho_{\parallel-, \Gamma-}^{\alpha} (\cos \Phi - \sin \Phi)) \\ &\quad + \frac{\beta |v^{\alpha}|}{b} [\cos \Phi (\rho_{\Gamma+}^{\alpha} + \rho_{\Gamma-}^{\alpha}) + \sin \Phi (\rho_{\parallel+}^{\alpha} + \rho_{\parallel-}^{\alpha})] . \end{aligned} \quad (\text{A.22})$$

The dislocation velocity v^{α} grows linearly with the applied stress:

$$v^{\alpha} = B (|\tau^{\alpha}| - \tau_{th}^{\alpha} - \tau_p) , \quad (\text{A.23})$$

while it is zero if $(\tau_{th}^\alpha + \tau_p) > |\tau^\alpha|$. The threshold stress τ_{th}^α is given by dislocation interactions on various slip systems:

$$\tau_{th}^\alpha = Gb \sqrt{\sum_{\delta=1}^{12} \xi^{\alpha\delta} \rho^\delta}, \quad (\text{A.24})$$

where $\xi^{\alpha\delta}$ is the matrix representing the strength of interactions between dislocations of slip systems α and δ [Arsenlis and Parks, 2002].

A.3 List of symbols

| | |
|------------------|---|
| ρ_{e+} | Positive edge dislocation density |
| ρ_{e-} | Negative edge dislocation density |
| ρ_{s+} | Positive screw dislocation density |
| ρ_{s-} | Negative screw dislocation density |
| $\rho_{e+,s+}$ | Curved dislocation density with positive edge and screw components |
| $\rho_{e+,s-}$ | Curved dislocation density with positive edge and negative screw components |
| $\rho_{e-,s+}$ | Curved dislocation density with negative edge and positive screw components |
| $\rho_{e-,s-}$ | Curved dislocation density with negative edge and negative screw components |
| α | Slip system index |
| δ | Slip system index |
| F_e | Fraction of edge mobile dislocations |
| F_s | Fraction of screw mobile dislocations |
| h_e | Dipole stability distance for edge dislocations |
| h_s | Dipole stability distance for screw dislocations |
| \bar{h}_e | Mean dipole distance for edge dislocations |
| \bar{h}_s | Mean dipole distance for screw dislocations |
| τ | Resolved shear stress |
| G | Shear modulus |
| ν | Poisson ratio |
| v | Dislocation velocity |
| \bar{l}_c | Average segment length for curved dislocations |
| $\bar{\Lambda}$ | Average segment length for curved dislocations |
| \check{d}_e | Annihilation distance for edge dislocations |
| \check{d}_s | Annihilation distance for screw dislocations |
| b | Magnitude of the Burgers vector |
| β | Cross slip coefficient |
| \vec{l}_{lock} | Dislocation junction vector (see Fig. 3.3) |
| Φ | Angle between the edge dislocation line and \vec{l}_{lock} (see Fig. 3.3) |
| τ_{th} | Threshold stress |
| τ_p | Peierls stress |

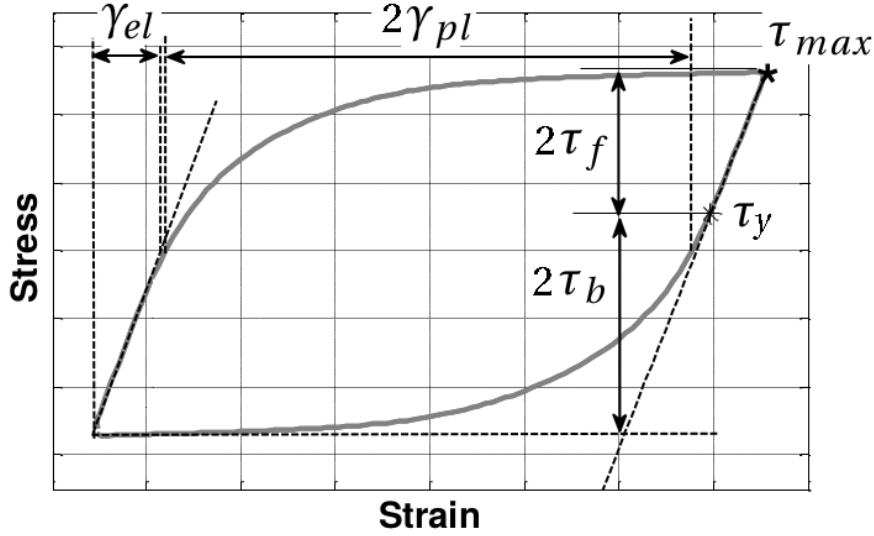


Figure A.1 – Quantities describing the stress-strain hysteresis loops.

A.4 Quantities describing the stress-strain curve

In this section the quantities used to describe the stress-strain curves during cyclic fatigue are defined. As shown in Fig. A.1, the plastic strain amplitude γ_{pl} is the halfwidth of the stress-strain hysteresis loop at zero stress. The elastic strain amplitude is found by subtracting the plastic strain amplitude from the total strain amplitude. In single slip shear experiments or simulations, the total strain is a function of time ($\gamma(t)$). The “elastic strain” and “plastic strain” (without the word “amplitude”) refer to the quantities:

$$\gamma_{el}(t) = \tau(t)/G, \quad (\text{A.25})$$

$$\gamma_{pl}(t) = \gamma(t) - \tau(t)/G, \quad (\text{A.26})$$

where $\tau(t)$ is the resolved shear stress as a function of time and G is the shear modulus. In multiple slip condition, the definitions (A.25)-(A.26) are used for every slip system. In compression experiments or simulations, the total strain amplitude refers to the relative elongation along the compression axis and the definitions (A.25)-(A.26) are used with the Young modulus E in place of G . The cumulative plastic strain $\gamma_{pl,cum}(t)$ after a time t is defined as:

$$\gamma_{pl,cum}(t) = \int_0^t |\dot{\gamma}_{pl}(\xi)| d\xi. \quad (\text{A.27})$$

In the following, the stress quantities in Fig. A.1 are defined [Kuhlmann-Wilsdorf and Laird, 1979]:

A.4. Quantities describing the stress-strain curve

- yield stress τ_y : stress value at which the material starts to deform plastically;
- maximum stress τ_{max} : maximum value of the stress reached during one cycle;
- friction stress τ_f : internal stress value necessary for the motion of dislocations;
- backstress τ_b : stress value contributing to the internal stress acting on dislocations. When the stress is reversed, the backstress continues to contribute along the same direction.

Bibliography

- J. G. Antonopoulos and A. T. Winter. Weak-beam study of dislocation structures in fatigued copper. *Philosophical Magazine*, 33(1):87–95, 1976. doi: 10.1080/14786437608221093. URL <http://dx.doi.org/10.1080/14786437608221093>.
- F. Appel, U. Messerschmidt, V. Schmidt, O.V. Klyavin, and A.V. Nikiforov. Slip structures and cross-slip of screw dislocations during the deformation of NaCl single crystals at low temperatures. *Materials Science and Engineering*, 56(3):211 – 218, 1982. ISSN 0025-5416. doi: 10.1016/0025-5416(82)90096-9.
- A Arsenlis and D.M Parks. Crystallographic aspects of geometrically-necessary and statistically-stored dislocation density. *Acta Materialia*, 47(5):1597 – 1611, 1999. ISSN 1359-6454. doi: [http://dx.doi.org/10.1016/S1359-6454\(99\)00020-8](http://dx.doi.org/10.1016/S1359-6454(99)00020-8). URL <http://www.sciencedirect.com/science/article/pii/S1359645499000208>.
- Athanasios Arsenlis and David M. Parks. Modeling the evolution of crystallographic dislocation density in crystal plasticity. *Journal of the Mechanics and Physics of Solids*, 50(9):1979 – 2009, 2002. ISSN 0022-5096. doi: 10.1016/S0022-5096(01)00134-X.
- Z.S. Basinski and S.J. Basinski. Fundamental aspects of low amplitude cyclic deformation in face-centred cubic crystals. *Progress in Materials Science*, 36(0):89 – 148, 1992. ISSN 0079-6425. doi: 10.1016/0079-6425(92)90006-S.
- Z.S. Basinski, A.S. Korbel, and S.J. Basinski. The temperature dependence of the saturation stress and dislocation substructure in fatigued copper single crystals. *Acta Metallurgica*, 28(2):191 – 207, 1980. ISSN 0001-6160. doi: [http://dx.doi.org/10.1016/0001-6160\(80\)90068-1](http://dx.doi.org/10.1016/0001-6160(80)90068-1). URL <http://www.sciencedirect.com/science/article/pii/0001616080900681>.
- E. Bitzek, C. Brandl, P. M. Derlet, and H. Van Swygenhoven. Dislocation cross-slip in nanocrystalline fcc metals. *Phys. Rev. Lett.*, 100:235501, Jun 2008. doi: 10.1103/PhysRevLett.100.235501. URL <http://link.aps.org/doi/10.1103/PhysRevLett.100.235501>.
- J Bonneville, B Escaig, and J.L Martin. A study of cross-slip activation parameters in pure copper. *Acta Metallurgica*, 36(8):1989 – 2002, 1988. ISSN 0001-6160. doi: 10.1016/0001-6160(88)90301-X.

Bibliography

- J. Bretschneider, C. Holste, and B. Tippelt. Cyclic plasticity of nickel single crystals at elevated temperatures. *Acta Materialia*, 45(9):3775 – 3783, 1997. ISSN 1359-6454. doi: [http://dx.doi.org/10.1016/S1359-6454\(97\)00030-X](http://dx.doi.org/10.1016/S1359-6454(97)00030-X). URL <http://www.sciencedirect.com/science/article/pii/S135964549700030X>.
- Leopold Buchinger, Stefanie Stanzl, and Campbell Laird. Dislocation structures in copper single crystals fatigued at low amplitudes. *Philosophical Magazine A*, 50(2):275–298, 1985. doi: 10.1080/01418618408244227.
- C. Buque. Dislocation structures and cyclic behaviour of [011] and [1-11]-oriented nickel single crystals. *International Journal of Fatigue*, 23(8):671 – 678, 2001. ISSN 0142-1123. doi: [http://dx.doi.org/10.1016/S0142-1123\(01\)00032-9](http://dx.doi.org/10.1016/S0142-1123(01)00032-9). URL <http://www.sciencedirect.com/science/article/pii/S0142112301000329>.
- D. Caillard and J.L. Martin. Some aspects of cross-slip mechanisms in metals and alloys. *J. Phys. France*, 50(18):2455–2473, 1989. doi: <http://dx.doi.org/10.1051/jphys:0198900500180245500>.
- S. Catalao, X. Feaugas, Ph. Pilvin, and M.-Th. Cabrillat. Dipole heights in cyclically deformed polycrystalline AISI 316L stainless steel. *Materials Science and Engineering: A*, 400–401(0): 349 – 352, 2005. ISSN 0921-5093. doi: 10.1016/j.msea.2005.03.094.
- Alex S. Cheng and Campbell Laird. Mechanisms of fatigue hardening in copper single crystals: The effects of strain amplitude and orientation. *Materials Science and Engineering*, 51(1): 111 – 121, 1981. ISSN 0025-5416. doi: [http://dx.doi.org/10.1016/0025-5416\(81\)90112-9](http://dx.doi.org/10.1016/0025-5416(81)90112-9). URL <http://www.sciencedirect.com/science/article/pii/0025541681901129>.
- L. F. Jr. Coffin. A study of the effects of cyclic thermal stresses on a ductile metal. *Transactions of the ASME*, 76:931 – 950, 1954.
- R. Courant, K. Friedrichs, and H. Lewy. Über die partiellen Differenzgleichungen der mathematischen Physik. *Mathematische Annalen*, 100:32–74, 1928. doi: 10.1007/BF01448839.
- E Van der Giessen and A Needleman. Discrete dislocation plasticity: a simple planar model. *Modelling and Simulation in Materials Science and Engineering*, 3(5):689, 1995. URL <http://stacks.iop.org/0965-0393/3/i=5/a=008>.
- B. Devincere and L.P. Kubin. Mesoscopic simulations of dislocations and plasticity. *Materials Science and Engineering: A*, 234–236:8 – 14, 1997. ISSN 0921-5093. doi: [http://dx.doi.org/10.1016/S0921-5093\(97\)00146-9](http://dx.doi.org/10.1016/S0921-5093(97)00146-9). URL <http://www.sciencedirect.com/science/article/pii/S0921509397001469>.
- B. Devincere, L. Kubin, and T. Hoc. Physical analyses of crystal plasticity by DD simulations. *Scripta Materialia*, 54(5):741 – 746, 2006. ISSN 1359-6462. doi: 10.1016/j.scriptamat.2005.10.066.

- Benoit Devincere, Thierry Hoc, and Ladislav P. Kubin. Collinear interactions of dislocations and slip systems. *Materials Science and Engineering: A*, 400–401:182 – 185, 2005. ISSN 0921-5093. doi: 10.1016/j.msea.2005.02.071.
- G. Dewel, P. Borckmans, and D. Walgraef. Nonequilibrium phase transitions and chemical instabilities. *Journal of Statistical Physics*, 24(1):119–137. ISSN 1572-9613. doi: 10.1007/BF01007639. URL <http://dx.doi.org/10.1007/BF01007639>.
- J.I. Dickson, J. Boutin, and G. L'Esperance. An explanation of labyrinth walls in fatigued f.c.c. metals. *Acta Metallurgica*, 34(8):1505 – 1514, 1986a. ISSN 0001-6160. doi: 10.1016/0001-6160(86)90095-7.
- J.I. Dickson, L. Handfield, and G. L'Esperance. Geometrical factors influencing the orientations of dipolar dislocation structures produced by cyclic deformation of f.c.c. metals. *Materials Science and Engineering*, 81(0):477 – 492, 1986b. ISSN 0025-5416. doi: 10.1016/0025-5416(86)90285-5. Proceedings of the International Conference on Low Energy Dislocation Structures.
- Martin Diehl, Pratheek Shanthraj, Philip Eisenlohr, and Franz Roters. Neighborhood influences on stress and strain partitioning in dual-phase microstructures. *Meccanica*, 51(2):429–441, 2016. ISSN 1572-9648. doi: 10.1007/s11012-015-0281-2. URL <http://dx.doi.org/10.1007/s11012-015-0281-2>.
- Olga Dmitrieva, Patrick W. Dondl, Stefan Müller, and Dierk Raabe. Lamination microstructure in shear deformed copper single crystals. *Acta Materialia*, 57(12):3439 – 3449, 2009. ISSN 1359-6454. doi: <http://dx.doi.org/10.1016/j.actamat.2009.03.035>. URL <http://www.sciencedirect.com/science/article/pii/S1359645409001943>.
- D. Drouin, A. R. Couture, D. Joly, X. Tastet, V. Aimez, and R. Gauvin. CASINO v2.42 - a fast and easy-to-use modeling tool for scanning electron microscopy and microanalysis users. *Wiley Periodicals*, 29:92–101, 2007. doi: 10.1002/sca.20000.
- C. Déprés. *Modélisation physique des stades précurseurs de l'endommagement en fatigue dans l'acier inoxydable austénitique 316L*. PhD thesis, Institut national polytechnique de Grenoble, 2004.
- C. Déprés, C. F. Robertson *, and M. C. Fivel. Low-strain fatigue in AISI 316L steel surface grains: a three-dimensional discrete dislocation dynamics modelling of the early cycles i. dislocation microstructures and mechanical behaviour. *Philosophical Magazine*, 84(22): 2257–2275, 2004. doi: 10.1080/14786430410001690051. URL <http://dx.doi.org/10.1080/14786430410001690051>.
- C. Déprés, M. Fivel, and L. Tabourot. A dislocation-based model for low-amplitude fatigue behaviour of face-centred cubic single crystals. *Scripta Materialia*, 58(12):1086 – 1089, 2008. ISSN 1359-6462. doi: <http://dx.doi.org/10.1016/j.scriptamat.2008.02.027>. URL <http://www.sciencedirect.com/science/article/pii/S1359646208001632>.

Bibliography

- Kroener E. *Zeitschr. Phys.*, 142:463–475, 1955.
- F. Eberl, S. Forest, G. Cailletaud, T. Wroblewski, and J. L. Lebrun. Finite-element calculations of the lattice rotation field of a tensile-loaded nickel-based alloy multicrystal and comparison with topographical X-ray diffraction measurements. *Metallurgical and Materials Transactions A*, 33(9):2825–2833, 2002. ISSN 1543-1940. doi: 10.1007/s11661-002-0268-1. URL <http://dx.doi.org/10.1007/s11661-002-0268-1>.
- B. Escaig. Sur le glissement dévié des dislocations dans la structure cubique à faces centrées. *Journal de Physique*, 29(1):225, 1968.
- Y. Estrin. Dislocation density-related constitutive modeling. In A. S. Krausz and K. Krausz, editors, *Unified Constitutive Laws of Plastic Deformation*, pages 69–106. Academic Press, New York, 1996.
- Y. Estrin, H. Braasch, and Y. Brechet. A dislocation density based constitutive model for cyclic deformation. *Journal of Engineering Materials and Technology*, 118(4):441 – 447, 1996. ISSN 0921-5093. doi: <http://dx.doi.org/10.1115/1.2805940>.
- Marc C. Fivel. Discrete dislocation dynamics: an important recent break-through in the modelling of dislocation collective behaviour. *Comptes Rendus Physique*, 9(3–4):427 – 436, 2008. ISSN 1631-0705. doi: 10.1016/j.crhy.2007.11.005.
- A. G. Gasparyan and V. K. Ohanyan. Orientation-dependent distribution of the length of a random segment and covariogram. *Journal of Contemporary Mathematical Analysis*, 50(2): 90–97, 2015. doi: 10.3103/S1068362315020053.
- H. Goldstein, C. P. Poole, and J. L. Safko. *Classical Mechanics*. Addison Wesley, 2000.
- J. I. Goldstein, D. E. Newbury, P. Echlin, and D. C. Joy. *Scanning Electron Microscopy and X-Ray Microanalysis*. Springer, 2005.
- S. Groh, E.B. Marin, M.F. Horstemeyer, and H.M. Zbib. Multiscale modeling of the plasticity in an aluminum single crystal. *International Journal of Plasticity*, 25(8):1456 – 1473, 2009. ISSN 0749-6419. doi: 10.1016/j.ijplas.2008.11.003.
- I. Groma. Link between the microscopic and mesoscopic length-scale description of the collective behavior of dislocations. *Phys. Rev. B*, 56:5807–5813, Sep 1997. doi: 10.1103/PhysRevB.56.5807.
- I. Groma and P. Balogh. Investigation of dislocation pattern formation in a two-dimensional self-consistent field approximation. *Acta Materialia*, 47(13):3647 – 3654, 1999. ISSN 1359-6454. doi: 10.1016/S1359-6454(99)00215-3.
- I. Groma, F.F. Csikor, and M. Zaiser. Spatial correlations and higher-order gradient terms in a continuum description of dislocation dynamics. *Acta Materialia*, 51(5):1271 – 1281, 2003. ISSN 1359-6454. doi: [http://dx.doi.org/10.1016/S1359-6454\(02\)00517-7](http://dx.doi.org/10.1016/S1359-6454(02)00517-7). URL <http://www.sciencedirect.com/science/article/pii/S1359645402005177>.

- A. Guitton, A. Irastorza-Landa, R. Broennimann, D. Grolimund, S. Van Petegem, and H. Van Swygenhoven. Picosecond pulsed laser for microscale sample preparation. *Materials Letters*, 160:589 – 591, 2015. ISSN 0167-577X. doi: <http://dx.doi.org/10.1016/j.matlet.2015.06.119>. URL <http://www.sciencedirect.com/science/article/pii/S0167577X15301816>.
- Vipul K. Gupta and Sean R. Agnew. A simple algorithm to eliminate ambiguities in ebsd orientation map visualization and analyses: Application to fatigue crack-tips/wakes in aluminum alloys. *Microscopy and Microanalysis*, 16:831–841, 12 2010. ISSN 1435-8115. doi: 10.1017/S1431927610093992. URL http://journals.cambridge.org/article_S1431927610093992.
- J. H. Halton. Algorithm 247: Radical-inverse quasi-random point sequence. *Commun. ACM*, 7(12):701–702, December 1964. ISSN 0001-0782. doi: 10.1145/355588.365104. URL <http://doi.acm.org/10.1145/355588.365104>.
- J.R Hancock and J.C Grosskreutz. Mechanisms of fatigue hardening in copper single crystals. *Acta Metallurgica*, 17(2):77 – 97, 1969. ISSN 0001-6160. doi: 10.1016/0001-6160(69)90130-8. URL <http://www.sciencedirect.com/science/article/pii/0001616069901308>.
- J. P. Hirth. On dislocation interactions in the fcc lattice. *Journal of Applied Physics*, 32(4), 1961.
- J. P. Hirth and J. Lothe. *Theory of Dislocations*. Krieger Publishing, 1982.
- T. Hochrainer. Multipole expansion of continuum dislocations dynamics in terms of alignment tensors. *Philosophical Magazine*, 95(12):1321–1367, 2015. doi: 10.1080/14786435.2015.1026297. URL <http://dx.doi.org/10.1080/14786435.2015.1026297>.
- T. Hochrainer, M. Zaiser, and P. Gumbsch. A three-dimensional continuum theory of dislocation systems: kinematics and mean-field formulation. *Philosophical Magazine*, 87(8-9): 1261–1282, 2007. doi: 10.1080/14786430600930218.
- Thomas Hochrainer, Stefan Sandfeld, Michael Zaiser, and Peter Gumbsch. Continuum dislocation dynamics: Towards a physical theory of crystal plasticity. *Journal of the Mechanics and Physics of Solids*, 63:167 – 178, 2014. ISSN 0022-5096. doi: <http://dx.doi.org/10.1016/j.jmps.2013.09.012>. URL <http://www.sciencedirect.com/science/article/pii/S0022509613001877>.
- Felix Hofmann, Xu Song, Brian Abbey, Tea-Sung Jun, and Alexander M. Korsunsky. High-energy transmission Laue micro-beam X-ray diffraction: a probe for intra-granular lattice orientation and elastic strain in thicker samples. *Journal of Synchrotron Radiation*, 19(3): 307–318, May 2012. doi: 10.1107/S0909049512003044. URL <http://dx.doi.org/10.1107/S0909049512003044>.
- M. Hollmann. Strain localization in nickel single crystals cyclically deformed at 77 K. *Philosophical Magazine Letters*, 80(9):613–619, 2000. doi: 10.1080/09500830050134327. URL <http://dx.doi.org/10.1080/09500830050134327>.
- David L. Holt. Dislocation cell formation in metals. *Journal of Applied Physics*, 41(8), 1970.

Bibliography

- U. Holzwarth and U. Eßmann. The evolution of persistent slip bands in copper single crystals. *Applied Physics A*, 57(2):131–141. ISSN 1432-0630. doi: 10.1007/BF00331434. URL <http://dx.doi.org/10.1007/BF00331434>.
- Y. M. Hu and Z. G. Wang. Nucleation stresses for persistent slip band formation in fatigued copper bicrystals. *Journal of Materials Science Letters*, 16(6):500–504. ISSN 1573-4811. doi: 10.1023/A:1018532914474. URL <http://dx.doi.org/10.1023/A:1018532914474>.
- Y.M. Hu and Z.G. Wang. Cyclic stress-strain response and dislocation structure of a [345]/[117] copper bicrystal. *Acta Materialia*, 45(7):2655 – 2670, 1997. ISSN 1359-6454. doi: [http://dx.doi.org/10.1016/S1359-6454\(96\)00410-7](http://dx.doi.org/10.1016/S1359-6454(96)00410-7). URL <http://www.sciencedirect.com/science/article/pii/S1359645496004107>.
- Y.M. Hu, Z.G. Wang, and G.Y. Li. Cyclic deformation behavior of copper bicrystals. *Materials Science and Engineering: A*, 208(2):260 – 269, 1996. ISSN 0921-5093. doi: [http://dx.doi.org/10.1016/0921-5093\(95\)10061-X](http://dx.doi.org/10.1016/0921-5093(95)10061-X). URL <http://www.sciencedirect.com/science/article/pii/092150939510061X>.
- J. W. Hutchinson. Bounds and self-consistent estimates for creep of polycrystalline materials. *Proceedings of the Royal Society of London A: Mathematical, Physical and Engineering Sciences*, 348(1652):101–127, 1976. ISSN 0080-4630. doi: 10.1098/rspa.1976.0027. URL <http://rspa.royalsocietypublishing.org/content/348/1652/101>.
- A. Irastorza-Landa, H. Van Swygenhoven, S. Van Petegem, N. Grilli, A. Bollhalder, S. Brandstetter, and D. Grolimund. Following dislocation patterning during fatigue. *Acta Materialia*, 112:184 – 193, 2016. ISSN 1359-6454. doi: <http://dx.doi.org/10.1016/j.actamat.2016.04.011>. URL <http://www.sciencedirect.com/science/article/pii/S1359645416302671>.
- N. Y. Jin. Dislocation structures in fatigued copper single crystals oriented for double-slip. *Philosophical Magazine A*, 48(5):L33–L38, 1983. doi: 10.1080/01418618308236534. URL <http://dx.doi.org/10.1080/01418618308236534>.
- N.Y. Jin and A.T. Winter. Dislocation structures in cyclically deformed [001] copper crystals. *Acta Metallurgica*, 32(8):1173 – 1176, 1984. ISSN 0001-6160. doi: [http://dx.doi.org/10.1016/0001-6160\(84\)90123-8](http://dx.doi.org/10.1016/0001-6160(84)90123-8). URL <http://www.sciencedirect.com/science/article/pii/0001616084901238>.
- C. Kords. *On the role of dislocation transport in the constitutive description of crystal plasticity*. PhD thesis, RWTH Aachen, 2013.
- D. Kuhlmann-Wilsdorf and C. Laird. Dislocation behavior in fatigue. *Materials Science and Engineering*, 27(2):137 – 156, 1977. ISSN 0025-5416. doi: [http://dx.doi.org/10.1016/0025-5416\(77\)90166-5](http://dx.doi.org/10.1016/0025-5416(77)90166-5). URL <http://www.sciencedirect.com/science/article/pii/0025541677901665>.
- D. Kuhlmann-Wilsdorf, J.H. van der Merwe, and H. Wilsdorf. Lix. elementary structure and slip band formation in aluminium. *The London, Edinburgh, and Dublin Philosophical*

- Magazine and Journal of Science*, 43(341):632–644, 1952. doi: 10.1080/14786440608520219. URL <http://dx.doi.org/10.1080/14786440608520219>.
- Doris Kuhlmann-Wilsdorf. Dislocation behavior in fatigue iii. properties of loop patches — do they participate in fatigue cycling? *Materials Science and Engineering*, 39(1):127 – 139, 1979a. ISSN 0025-5416. doi: [http://dx.doi.org/10.1016/0025-5416\(79\)90178-2](http://dx.doi.org/10.1016/0025-5416(79)90178-2). URL <http://www.sciencedirect.com/science/article/pii/0025541679901782>.
- Doris Kuhlmann-Wilsdorf. Dislocation behavior in fatigue iv. quantitative interpretation of friction stress and back stress derived from hysteresis loops. *Materials Science and Engineering*, 39(2):231 – 245, 1979b. ISSN 0025-5416. doi: [http://dx.doi.org/10.1016/0025-5416\(79\)90062-4](http://dx.doi.org/10.1016/0025-5416(79)90062-4). URL <http://www.sciencedirect.com/science/article/pii/0025541679900624>.
- Doris Kuhlmann-Wilsdorf. Q: Dislocations structures — how far from equilibrium? a: Very close indeed. *Materials Science and Engineering: A*, 315(1–2):211 – 216, 2001. ISSN 0921-5093. doi: [http://dx.doi.org/10.1016/S0921-5093\(01\)01204-7](http://dx.doi.org/10.1016/S0921-5093(01)01204-7). URL <http://www.sciencedirect.com/science/article/pii/S0921509301012047>.
- Doris Kuhlmann-Wilsdorf and Campbell Laird. Dislocation behavior in fatigue ii. friction stress and back stress as inferred from an analysis of hysteresis loops. *Materials Science and Engineering*, 37(2):111 – 120, 1979. ISSN 0025-5416. doi: 10.1016/0025-5416(79)90074-0. URL <http://www.sciencedirect.com/science/article/pii/0025541679900740>.
- Doris Kuhlmann-Wilsdorf and Campbell Laird. Dislocation behavior in fatigue v: Breakdown of loop patches and formation of persistent slip bands and of dislocation cells. *Materials Science and Engineering*, 46(2):209 – 219, 1980. ISSN 0025-5416. doi: [http://dx.doi.org/10.1016/0025-5416\(80\)90176-7](http://dx.doi.org/10.1016/0025-5416(80)90176-7). URL <http://www.sciencedirect.com/science/article/pii/0025541680901767>.
- J.W. Kysar, Y. Saito, M.S. Oztop, D. Lee, and W.T. Huh. Experimental lower bounds on geometrically necessary dislocation density. *International Journal of Plasticity*, 26(8):1097 – 1123, 2010. ISSN 0749-6419. doi: <http://dx.doi.org/10.1016/j.ijplas.2010.03.009>. URL <http://www.sciencedirect.com/science/article/pii/S0749641910000574>. Special Issue In Honor of Lallit Anand.
- Campbell Laird, Philip Charsley, and Haël Mughrabi. Low energy dislocation structures produced by cyclic deformation. *Materials Science and Engineering*, 81:433 – 450, 1986. ISSN 0025-5416. doi: [http://dx.doi.org/10.1016/0025-5416\(86\)90281-8](http://dx.doi.org/10.1016/0025-5416(86)90281-8). URL <http://www.sciencedirect.com/science/article/pii/0025541686902818>. Proceedings of the International Conference on Low Energy Dislocation Structures.
- B. C. Larson, J. Z. Tischler, Anter El-Azab, and Wenjun Liu. Dislocation density tensor characterization of deformation using 3D X-ray microscopy. *Journal of Engineering Materials and Technology*, 130:021024, 2008. ISSN 0094-4289. doi: 10.1115/1.2884336. URL <http://dx.doi.org/10.1115/1.2884336>.

Bibliography

- J. Lemaitre and J. L. Chaboche. *Mechanics of solid materials*. Cambridge University Press, 2002.
- T. Lepistö, V.-T. Kuokkala, and P. Kettunen. The PSB structure in multiple-slip oriented copper single crystals. *Scripta Metallurgica*, 18(3):245 – 248, 1984. ISSN 0036-9748. doi: [http://dx.doi.org/10.1016/0036-9748\(84\)90516-7](http://dx.doi.org/10.1016/0036-9748(84)90516-7). URL <http://www.sciencedirect.com/science/article/pii/0036974884905167>.
- G. L'Esperance, J.B. Vogt, and J.I. Dickson. The identification of labyrinth wall orientations in cyclically deformed AISI-SAE 316 stainless steel. *Materials Science and Engineering*, 79(2): 141 – 147, 1986. ISSN 0025-5416. doi: 10.1016/0025-5416(86)90397-6.
- H.S. Leung and A.H.W. Ngan. Dislocation-density function dynamics – an all-dislocation, full-dynamics approach for modeling intensive dislocation structures. *Journal of the Mechanics and Physics of Solids*, 91:172 – 203, 2016. ISSN 0022-5096. doi: <http://dx.doi.org/10.1016/j.jmps.2016.03.008>. URL <http://www.sciencedirect.com/science/article/pii/S0022509615302507>.
- P. Li, Z.F. Zhang, S.X. Li, and Z.G. Wang. Effect of orientations on cyclic deformation behavior of Ag and Cu single crystals: Cyclic stress–strain curve and slip morphology. *Acta Materialia*, 56(10):2212 – 2222, 2008. ISSN 1359-6454. doi: <http://dx.doi.org/10.1016/j.actamat.2008.01.006>. URL <http://www.sciencedirect.com/science/article/pii/S1359645408000414>.
- P. Li, S.X. Li, Z.G. Wang, and Z.F. Zhang. Formation mechanisms of cyclic saturation dislocation patterns in [0 0 1], [0 1 1] and copper single crystals. *Acta Materialia*, 58(9):3281 – 3294, 2010. ISSN 1359-6454. doi: <http://dx.doi.org/10.1016/j.actamat.2010.02.002>. URL <http://www.sciencedirect.com/science/article/pii/S1359645410000881>.
- P. Li, S.X. Li, Z.G. Wang, and Z.F. Zhang. Fundamental factors on formation mechanism of dislocation arrangements in cyclically deformed fcc single crystals. *Progress in Materials Science*, 56(3):328 – 377, 2011. ISSN 0079-6425. doi: <http://dx.doi.org/10.1016/j.pmatsci.2010.12.001>. URL <http://www.sciencedirect.com/science/article/pii/S007964251000068X>.
- S. X. Li, X. W. Li, Z. F. Zhang, Z. G. Wang, and K. Lu. On the formation of deformation bands in fatigued copper single crystals. *Philosophical Magazine A*, 82(16):3129–3147, 2002. doi: 10.1080/01418610208239637. URL <http://dx.doi.org/10.1080/01418610208239637>.
- Xiao-Wu Li, Yang Zhou, Wei-Wei Guo, and Guang-Ping Zhang. Characterization of dislocation structures in copper single crystals using electron channelling contrast technique in SEM. *Crystal Research and Technology*, 44(3):315–321, 2009. ISSN 1521-4079. doi: 10.1002/crat.200800346. URL <http://dx.doi.org/10.1002/crat.200800346>.
- Yuanfeng Li and Campbell Laird. Masing behavior observed in monocrystalline copper during cyclic deformation. *Materials Science and Engineering: A*, 161(1):23 – 29, 1993. ISSN 0921-5093. doi: [http://dx.doi.org/10.1016/0921-5093\(93\)90471-P](http://dx.doi.org/10.1016/0921-5093(93)90471-P). URL <http://www.sciencedirect.com/science/article/pii/092150939390471P>.

- Yuanfeng Li and Campbell Laird. Cyclic response and dislocation structures of AISI 316L stainless steel. part 1: single crystals fatigued at intermediate strain amplitude. *Materials Science and Engineering: A*, 186(1–2):65 – 86, 1994. ISSN 0921-5093. doi: [http://dx.doi.org/10.1016/0921-5093\(94\)90306-9](http://dx.doi.org/10.1016/0921-5093(94)90306-9). URL <http://www.sciencedirect.com/science/article/pii/S0921509394903069>.
- Binglin Lu and S. Torquato. Lineal-path function for random heterogeneous materials. *Phys. Rev. A*, 45:922–929, Jan 1992. doi: 10.1103/PhysRevA.45.922.
- R. Madec, B. Devincre, L. Kubin, T. Hoc, and D. Rodney. The role of collinear interaction in dislocation-induced hardening. *Science*, 301(5641):1879–1882, 2003. doi: 10.1126/science.1085477.
- S. S. Manson. Behavior of materials under conditions of thermal stress. *NACA Technical Report 1170*, 1954. URL <http://ntrs.nasa.gov/search.jsp?R=19930092197>.
- E. Martínez, J. Marian, A. Arsenlis, M. Victoria, and J.M. Perlado. Atomistically informed dislocation dynamics in fcc crystals. *Journal of the Mechanics and Physics of Solids*, 56(3): 869 – 895, 2008. ISSN 0022-5096. doi: <http://dx.doi.org/10.1016/j.jmps.2007.06.014>. URL <http://www.sciencedirect.com/science/article/pii/S0022509607001408>.
- Peter E. McHugh. *Mechanics of Microstructured Materials*, chapter Introduction to Crystal Plasticity Theory, pages 125–171. Springer Vienna, Vienna, 2004. ISBN 978-3-7091-2776-6. doi: 10.1007/978-3-7091-2776-6_5. URL http://dx.doi.org/10.1007/978-3-7091-2776-6_5.
- K. Mecke, C. Blochwitz, and V. Kremling. The development of the dislocation structures during the fatigue process of f.c.c. single crystals. *Crystal Research and Technology*, 17(12):1557–1570, 1982. ISSN 1521-4079. doi: 10.1002/crat.2170171219. URL <http://dx.doi.org/10.1002/crat.2170171219>.
- H. Mecking and U.F. Kocks. Kinetics of flow and strain-hardening. *Acta Metallurgica*, 29(11): 1865 – 1875, 1981. ISSN 0001-6160. doi: [http://dx.doi.org/10.1016/0001-6160\(81\)90112-7](http://dx.doi.org/10.1016/0001-6160(81)90112-7). URL <http://www.sciencedirect.com/science/article/pii/0001616081901127>.
- U Messerschmidt and M Bartsch. Generation of dislocations during plastic deformation. *Materials Chemistry and Physics*, 81(2–3):518 – 523, 2003. ISSN 0254-0584. doi: [http://dx.doi.org/10.1016/S0254-0584\(03\)00064-6](http://dx.doi.org/10.1016/S0254-0584(03)00064-6). URL <http://www.sciencedirect.com/science/article/pii/S0254058403000646>.
- Ashok Misra, R.C. Prasad, Vishal S. Chauhan, and Rajeev Kumar. Effect of peierls’ stress on the electromagnetic radiation during yielding of metals. *Mechanics of Materials*, 42(5):505 – 521, 2010. ISSN 0167-6636. doi: <http://dx.doi.org/10.1016/j.mechmat.2010.01.005>. URL <http://www.sciencedirect.com/science/article/pii/S0167663610000128>.
- H. Mughrabi. The cyclic hardening and saturation behaviour of copper single crystals. *Materials Science and Engineering*, 33(2):207 – 223, 1978. ISSN 0025-5416. doi: [http://dx.doi.org/10.1016/0025-5416\(78\)90001-2](http://dx.doi.org/10.1016/0025-5416(78)90001-2).

Bibliography

- [//dx.doi.org/10.1016/0025-5416\(78\)90174-X](http://dx.doi.org/10.1016/0025-5416(78)90174-X). URL <http://www.sciencedirect.com/science/article/pii/002554167890174X>.
- H. Mughrabi. Dual role of deformation-induced geometrically necessary dislocations with respect to lattice plane misorientations and/or long-range internal stresses. *Acta Materialia*, 54(13):3417 – 3427, 2006. ISSN 1359-6454. doi: <http://dx.doi.org/10.1016/j.actamat.2006.03.047>. URL <http://www.sciencedirect.com/science/article/pii/S1359645406002527>. Selected Papers from the Meeting “Micromechanics and Microstructure Evolution: Modeling, Simulation and Experiments” held in Madrid/Spain, 11–16 September 2005.
- H. Mughrabi and B. Obst. Misorientations and geometrically necessary dislocations in deformed copper crystals: A microstructural analysis of X-ray rocking curves. *Zeitschrift für Metallkunde*, 96:688–697, jul 2005. doi: 10.3139/146.101088.
- H. Mughrabi, F. Ackermann, and K. Herz. Persistent slip bands in fatigued face-centered and body-centered cubic metals. In J. T. Fong, editor, *Fatigue mechanisms*, page 69. ASTM, 1979.
- J. Nellessen, S. Sandlöbes, and D. Raabe. Effects of strain amplitude, cycle number and orientation on low cycle fatigue microstructures in austenitic stainless steel studied by electron channelling contrast imaging. *Acta Materialia*, 87(0):86 – 99, 2015. ISSN 1359-6454. doi: 10.1016/j.actamat.2014.12.024.
- P Neumann. Dislocation dynamics in fatigue. *Physica Scripta*, 1987(T19B):537, 1987. URL <http://stacks.iop.org/1402-4896/1987/i=T19B/a=035>.
- Mark Obstalecki, Su Leen Wong, Paul R. Dawson, and Matthew P. Miller. Quantitative analysis of crystal scale deformation heterogeneity during cyclic plasticity using high-energy X-ray diffraction and finite-element simulation. *Acta Materialia*, 75:259 – 272, 2014. ISSN 1359-6454. doi: <http://dx.doi.org/10.1016/j.actamat.2014.04.059>. URL <http://www.sciencedirect.com/science/article/pii/S1359645414003103>.
- W. C. Overton and John Gaffney. Temperature variation of the elastic constants of cubic elements. i. copper. *Phys. Rev.*, 98:969–977, May 1955. doi: 10.1103/PhysRev.98.969. URL <http://link.aps.org/doi/10.1103/PhysRev.98.969>.
- W. Pantleon. Resolving the geometrically necessary dislocation content by conventional electron backscattering diffraction. *Scripta Materialia*, 58(11):994 – 997, 2008. ISSN 1359-6462. doi: <http://dx.doi.org/10.1016/j.scriptamat.2008.01.050>. URL <http://www.sciencedirect.com/science/article/pii/S1359646208000912>.
- D. Peirce, R.J. Asaro, and A. Needleman. An analysis of nonuniform and localized deformation in ductile single crystals. *Acta Metallurgica*, 30(6):1087 – 1119, 1982. ISSN 0001-6160. doi: [http://dx.doi.org/10.1016/0001-6160\(82\)90005-0](http://dx.doi.org/10.1016/0001-6160(82)90005-0). URL <http://www.sciencedirect.com/science/article/pii/0001616082900050>.

- M.S. Pham, C. Solenthaler, K.G.F. Janssens, and S.R. Holdsworth. Dislocation structure evolution and its effects on cyclic deformation response of AISI 316L stainless steel. *Materials Science and Engineering: A*, 528(7–8):3261 – 3269, 2011. ISSN 0921-5093. doi: 10.1016/j.msea.2011.01.015.
- M.S. Pham, S.R. Holdsworth, K.G.F. Janssens, and E. Mazza. Cyclic deformation response of AISI 316L at room temperature: Mechanical behaviour, microstructural evolution, physically-based evolutionary constitutive modelling. *International Journal of Plasticity*, 47:143 – 164, 2013. ISSN 0749-6419. doi: <http://dx.doi.org/10.1016/j.ijplas.2013.01.017>. URL <http://www.sciencedirect.com/science/article/pii/S0749641913000272>.
- J. Polák. Electrical resistivity of cyclically deformed copper. *Czechoslovak Journal of Physics B*, 19(3):315–322, 1969. ISSN 1572-9486. doi: 10.1007/BF01712868. URL <http://dx.doi.org/10.1007/BF01712868>.
- J. Pontes, D. Walgraef, and E.C. Aifantis. On dislocation patterning: Multiple slip effects in the rate equation approach. *International Journal of Plasticity*, 22(8):1486 – 1505, 2006. ISSN 0749-6419. doi: <http://dx.doi.org/10.1016/j.ijplas.2005.07.011>. URL <http://www.sciencedirect.com/science/article/pii/S0749641905001786>. Special issue in honour of Dr. Kirk ValanisValanis Issue.
- D. Raabe, M. Sachtleber, Z. Zhao, F. Roters, and S. Zaefferer. Micromechanical and macromechanical effects in grain scale polycrystal plasticity experimentation and simulation. *Acta Materialia*, 49(17):3433 – 3441, 2001. ISSN 1359-6454. doi: [http://dx.doi.org/10.1016/S1359-6454\(01\)00242-7](http://dx.doi.org/10.1016/S1359-6454(01)00242-7). URL <http://www.sciencedirect.com/science/article/pii/S1359645401002427>.
- R. P. Reed and T. Horiuchi. *Austenitic Steels at Low Temperatures*. Plenum Press, 1983.
- F. Roters. Advanced material models for the crystal plasticity finite element method, 2011.
- F. Roters, D. Raabe, and G. Gottstein. Work hardening in heterogeneous alloys—a microstructural approach based on three internal state variables. *Acta Materialia*, 48(17):4181 – 4189, 2000. ISSN 1359-6454. doi: [http://dx.doi.org/10.1016/S1359-6454\(00\)00289-5](http://dx.doi.org/10.1016/S1359-6454(00)00289-5). URL <http://www.sciencedirect.com/science/article/pii/S1359645400002895>.
- F. Roters, P. Eisenlohr, C. Kords, D.D. Tjahjanto, M. Diehl, and D. Raabe. DAMASK: the Düsseldorf Advanced MATERIAL Simulation Kit for studying crystal plasticity using an FE based or a spectral numerical solver. *Procedia IUTAM*, 3:3 – 10, 2012. ISSN 2210-9838. doi: <http://dx.doi.org/10.1016/j.piutam.2012.03.001>. URL <http://www.sciencedirect.com/science/article/pii/S2210983812000028>. {IUTAM} Symposium on Linking Scales in Computations: From Microstructure to Macro-scale Properties.
- Stefan Sandfeld and Michael Zaiser. Pattern formation in a minimal model of continuum dislocation plasticity. *Modelling and Simulation in Materials Science and Engineering*, 23(6): 065005, 2015. doi: 10.1088/0965-0393/23/6/065005.

Bibliography

- M. Sauzay and L.P. Kubin. Scaling laws for dislocation microstructures in monotonic and cyclic deformation of fcc metals. *Progress in Materials Science*, 56(6):725 – 784, 2011. ISSN 0079-6425. doi: <http://dx.doi.org/10.1016/j.pmatsci.2011.01.006>. URL <http://www.sciencedirect.com/science/article/pii/S0079642511000077>. Festschrift Vaclav Vitek.
- C. Schiller and D. Walgraef. Numerical simulation of persistent slip band formation. *Acta Metallurgica*, 36(3):563 – 574, 1988. ISSN 0001-6160. doi: 10.1016/0001-6160(88)90089-2.
- Gunther Schoeck and Maciej Krystian. The peierls energy and kink energy in fcc metals. *Philosophical Magazine*, 85(9):949–966, 2005. doi: 10.1080/14786430412331314654. URL <http://dx.doi.org/10.1080/14786430412331314654>.
- A. Schwab, J. Bretschneider, C. Buque, C. Blochwitz, and C. Holste. Application of electron channelling contrast to the investigation of strain localization effects in cyclically deformed fcc crystals. *Philosophical Magazine Letters*, 74(6):449–454, 1996. doi: 10.1080/095008396179986. URL <http://dx.doi.org/10.1080/095008396179986>.
- B.A Simkin and M.A Crimp. An experimentally convenient configuration for electron channeling contrast imaging. *Ultramicroscopy*, 77(1–2):65 – 75, 1999. ISSN 0304-3991. doi: [http://dx.doi.org/10.1016/S0304-3991\(99\)00009-1](http://dx.doi.org/10.1016/S0304-3991(99)00009-1). URL <http://www.sciencedirect.com/science/article/pii/S0304399199000091>.
- S. Suresh. *Fatigue of Materials*. Cambridge University Press, 1998.
- J. Vallin, M. Mongy, K. Salama, and O. Beckman. Elastic constants of aluminum. *Journal of Applied Physics*, 35(6), 1964.
- H. Van Swygenhoven and S. Van Petegem. The use of laue microdiffraction to study small-scale plasticity. *JOM*, 62(12):36–43, 2010. ISSN 1543-1851. doi: 10.1007/s11837-010-0178-4. URL <http://dx.doi.org/10.1007/s11837-010-0178-4>.
- T. Vegge, T. Rasmussen, T. Leffers, O. B. Pedersen, and K. W. Jacobsen. Determination of the rate of cross slip of screw dislocations. *Phys. Rev. Lett.*, 85:3866–3869, Oct 2000. doi: 10.1103/PhysRevLett.85.3866.
- Marianne Videm and Nils Ryum. Cyclic deformation of [001] aluminium single crystals. *Materials Science and Engineering: A*, 219(1–2):1 – 10, 1996. ISSN 0921-5093. doi: 10.1016/S0921-5093(96)10261-6.
- Daniel Walgraef and Elias C. Aifantis. Dislocation patterning in fatigued metals as a result of dynamical instabilities. *Journal of Applied Physics*, 58(2), 1985.
- Daniel Walgraef and Elias C. Aifantis. Dislocation patterning in fatigued metals: Labyrinth structures and rotational effects. *International Journal of Engineering Science*, 24(12):1789 – 1798, 1986. ISSN 0020-7225. doi: [http://dx.doi.org/10.1016/0020-7225\(86\)90127-8](http://dx.doi.org/10.1016/0020-7225(86)90127-8). URL <http://www.sciencedirect.com/science/article/pii/0020722586901278>.

- R. Wang and Q.F. Fang. Core structure and mobility of an edge dislocation in aluminum. *Journal of Alloys and Compounds*, 310(1–2):80 – 84, 2000. ISSN 0925-8388. doi: [http://dx.doi.org/10.1016/S0925-8388\(00\)00991-9](http://dx.doi.org/10.1016/S0925-8388(00)00991-9). URL <http://www.sciencedirect.com/science/article/pii/S0925838800009919>. Intern. Conf. Internal Friction and Ultrasonic Attenuation in Solids (ICIFUAS-12).
- Z.G. Wang, Z.F. Zhang, X.W. Li, W.P. Jia, and S.X. Li. Orientation dependence of the cyclic deformation behavior and the role of grain boundaries in fatigue damage in copper crystals. *Materials Science and Engineering: A*, 319–321:63 – 73, 2001. ISSN 0921-5093. doi: [http://dx.doi.org/10.1016/S0921-5093\(01\)01055-3](http://dx.doi.org/10.1016/S0921-5093(01)01055-3). URL <http://www.sciencedirect.com/science/article/pii/S0921509301010553>.
- A. T. Winter. A model for the fatigue of copper at low plastic strain amplitudes. *Philosophical Magazine*, 30(4):719–738, 1974. doi: 10.1080/14786437408207230. URL <http://dx.doi.org/10.1080/14786437408207230>.
- A. T. Winter. Nucleation of persistent slip bands in cyclically deformed copper crystals. *Philosophical Magazine, Part A*, 37:457–463, April 1978. doi: 10.1080/01418617808239182.
- A.T. Winter, O.R. Pedersen, and K.V. Rasmussen. Dislocation microstructures in fatigued copper polycrystals. *Acta Metallurgica*, 29(5):735 – 748, 1981. ISSN 0001-6160. doi: [http://dx.doi.org/10.1016/0001-6160\(81\)90117-6](http://dx.doi.org/10.1016/0001-6160(81)90117-6). URL <http://www.sciencedirect.com/science/article/pii/0001616081901176>.
- A. Wöhler. Über die festigkeitsversuche mit eisen und stahl. *Zeitschrift für Bauwesen*, 20: 73–106, 1870.
- Shengxu Xia and Anter El-Azab. Computational modelling of mesoscale dislocation patterning and plastic deformation of single crystals. *Modelling and Simulation in Materials Science and Engineering*, 23(5):055009, 2015. URL <http://stacks.iop.org/0965-0393/23/i=5/a=055009>.
- Stefan Zaefferer and Nahid-Nora Elhami. Theory and application of electron channelling contrast imaging under controlled diffraction conditions. *Acta Materialia*, 75(0):20 – 50, 2014. ISSN 1359-6454. doi: 10.1016/j.actamat.2014.04.018.
- T. Zhai, J.W. Martin, and G.A.D. Briggs. Fatigue damage at room temperature in aluminium single crystals—ii. TEM. *Acta Materialia*, 44(5):1729 – 1739, 1996. ISSN 1359-6454. doi: [http://dx.doi.org/10.1016/1359-6454\(95\)00330-4](http://dx.doi.org/10.1016/1359-6454(95)00330-4). URL <http://www.sciencedirect.com/science/article/pii/S1359645495003304>.
- Z.F. Zhang, Z.G. Wang, and Z.M. Sun. Evolution and microstructural characteristics of deformation bands in fatigued copper single crystals. *Acta Materialia*, 49(15):2875 – 2886, 2001. ISSN 1359-6454. doi: [http://dx.doi.org/10.1016/S1359-6454\(01\)00219-1](http://dx.doi.org/10.1016/S1359-6454(01)00219-1). URL <http://www.sciencedirect.com/science/article/pii/S1359645401002191>.

Curriculum Vitae

PERSONAL INFORMATION

Name, Surname: Nicolò Grilli

Date of birth: July 17th, 1988

Place of birth: Parma, Italy

EDUCATION

09/2012 – Present: **École Polytechnique Fédérale de Lausanne**

Paul Scherrer Institut

Switzerland

PhD in Materials Science and Engineering

09/2007 – 07/2012 : **University of Pisa**

Scuola Normale Superiore

Italy

Bachelor degree in Physics

Master degree in Condensed Matter Physics

01/2010 - 07/2010 : **NEST Laboratories**

Italy

Bachelor thesis

09/2011 - 07/2012 : **Virgo GW Detector**

Italy

Master thesis

PUBLICATIONS

Irastorza-Landa A., Van Swygenhoven H., Van Petegem S., **Grilli N.** et al. (2016) “Following dislocation patterning during fatigue”, *Acta Materialia* 112 (2016) 184-193.

Grilli N., Janssens K., Van Swygenhoven H. (2015) “Crystal plasticity finite element modelling of low cycle fatigue in fcc metals”, *Journal of the Mechanics and Physics of Solids* 84 (2015) 424-435.

Grilli N. (2013) “A sensitive and compact inclinometer for Virgo”, *European Gravitational Observatory Newsletter* 23 (2013).

SUBMITTED PUBLICATIONS

Grilli N., Janssens K., Nellessen J., Sandlöbes S., Raabe D. “Multiple slip dislocation patterning in a dislocation-based crystal plasticity finite element method”

Irastorza-Landa A., **Grilli N.**, Van Swygenhoven H. “Laue micro-diffraction and crystal plasticity finite element simulations to reveal a vein structure in fatigued Cu”

Irastorza-Landa A., **Grilli N.**, Van Swygenhoven H. “Effect of pre-existing immobile dislocations on the evolution of geometrically necessary dislocations during fatigue”

CONFERENCES/WORKSHOPS

9th European Solid Mechanics Conference, ESMC15, Madrid, Spain, July 6-10, 2015. Oral presentation: “Cyclic fatigue simulation of polycrystals using dislocation-based CPFEM”.

12th International Conference on the Mechanical Behaviour of Materials, Karlsruhe, Germany, May 10-14, 2015. Oral presentation: “Dislocation-based modelling of low cycle fatigue in fcc single and polycrystals”.

International Symposium on Plasticity and Its Current Applications, Montego Bay, Jamaica, January 4-9, 2015. Oral presentation: “Cyclic crystal plasticity constitutive modelling of dislocation structures in fatigued fcc metals”.

Multiscale Material Modelling Conference, MMM, Berkeley, US, October 6-10, 2014. Oral presentation: “Low cycle fatigue modelling of fcc metals in single and multiple slip by crystal plasticity finite element method”.

Junior EUROMAT, Lausanne, Switzerland, July 21-25, 2014. Oral presentation: “Finite element modelling of mechanical properties and dislocation patterning of fcc metals during cyclic plastic fatigue”.

Computational Mechanics of Polycrystals symposium, CMCn2014, Düsseldorf, Germany, July 14-15, 2014. Oral presentation: “Modification of the dislocation-based model in DAMASK for cyclic plasticity”.

Dislocation-based Plasticity symposium, Schöntal, Germany, February 24-28, 2014. Oral presentation: “Modified equations for crystal plasticity finite element modelling of low cycle fatigue in single crystal fcc metals”.

143rd TMS Annual Meeting & Exhibition, San Diego, US, February 16-20, 2014. Oral presentation: “Modified constitutive equations for crystal plasticity finite element modelling of low cycle fatigue in single crystal fcc metals”.

EUROMAT 2013, Sevilla, Spain, September 8-13, 2013. Poster presentation: “Physics-based constitutive modelling of cyclic plasticity in fatigue”.

EDMX Research day, Lausanne, Switzerland, September 6, 2013. Poster presentation: “Physics-based constitutive modelling for crystal plasticity finite element computation of cyclic plasticity in fatigue”.

CNRS Mecano General Meeting 2013, Düsseldorf, Germany, July 18-19, 2013. Poster¹⁵⁰ presentation: “Physics-based constitutive modelling of cyclic plasticity in fatigue”.

